Model-based reconstruction of magnetisation distributions in nanostructures from electron optical phase images

Jan Caron

JÜLICH
Forschungszentrum

Model-based reconstruction of magnetisation distributions in nanostructures from electron optical phase images

Von der Fakultät für Mathematik, Informatik und Naturwissenschaften der RWTH Aachen University zur Erlangung des akademischen Grades eines Doktors der Naturwissenschaften genehmigte Dissertation

vorgelegt von

M.Sc. Jan Caron

aus Mönchengladbach

Model-based reconstruction of magnetisation distributions in nanostructures from electron optical phase images

Jan Caron

Abstract

**Model-based reconstruction of magnetisation distributions
in nanostructures from electron optical phase images**

Off-axis electron holography is a powerful technique for recording the phase shift of high-energy electron waves that pass through a thin specimen in the transmission electron microscope. Information about the electromagnetic field in and around the specimen is encoded in the phase, according to the Aharonov-Bohm equations. In this thesis, a model-based iterative reconstruction (MBIR) algorithm was developed, which allows the retrieval of the projected in-plane magnetisation distribution from individual magnetic phase images or a complete tomographic reconstruction of the three-dimensional magnetisation distribution from two ideally orthogonal tilt series of phase images. To guarantee efficient model-based reconstructions, an optimised forward model implementation for fast and accurate simulations of magnetic phase images from a given magnetisation distribution was derived. This new approach utilises sparse matrix multiplications and fast convolutions in Fourier space with pre-calculated convolution kernels based on known analytic solutions for the phase contribution of simple geometries. As the inverse problem of retrieving the magnetisation distribution is ill-posed, regularisation techniques had to be applied, that guarantee the existence of a solution and its uniqueness. Modelled after the minimisation of the exchange energy, Tikhonov regularisation of first order is used to apply smoothness constraints to the solution of the reconstruction. In addition, *a priori* knowledge about the position and size of the magnetised regions is utilised in the form of a three-dimensional mask to significantly reduce the number of retrieval targets. Optimal estimation diagnostic tools were adapted for the assessment of the quality of the reconstruction results. The MBIR algorithm was successfully applied to simulated phase images for the reconstruction of two-and three-dimensional magnetisation distributions. External sources of magnetisation outside the field of view were addressed by linear phase ramp and offset fits, as well as with buffer pixels that increase the number of degrees of freedom for the MBIR algorithm. A method to account for the perturbed reference wave of the electron hologram was provided and other artefacts in the magnetic phase images were tackled by excluding them from the reconstruction process. In three dimensions, studies about the influence of the maximum tilt angle and angular sampling were performed. The MBIR algorithm was successfully used to reconstruct a projected in-plane magnetisation distribution from a magnetic phase image of a lithographically patterned cobalt structure. Finally, a three-dimensional magnetisation distribution was reconstructed from a set of simulated phase images with limited angular range under the influence of Gaussian noise and random phase offsets and ramps, proving the feasibility of the algorithm for future three-dimensional experimental studies.

Kurzfassung

Modellbasierte Rekonstruktion von Magnetisierungsverteilungen in Nanostrukturen aus elektronenoptischen Phasenbildern

Off-Axis-Elektronenholographie ist eine leistungsfähige Technik zur Erfassung der Phasenverschiebung von hochenergetischen Elektronenwellen, die eine dünne Probe im Transmissionselektronenmikroskop passieren. Informationen über das elektromagnetische Feld in und um die Probe werden in der Phase nach den Aharonov-Bohm-Gleichungen kodiert. In dieser Arbeit wurde ein modellbasierter iterativer Rekonstruktionsalgorithmus (MBIR) entwickelt, der die Rekonstruktion der projizierten Magnetisierungsverteilung aus einzelnen Phasenbildern oder eine vollständige tomographische Rekonstruktion der dreidimensionalen Verteilung aus zwei orthogonalen Kippserien von Phasenbildern ermöglicht. Um effiziente modellbasierte Rekonstruktionen zu gewährleisten, wurde ein optimiertes Vorwärtsmodell zur schnellen und genauen Simulation von Phasenbildern aus einer gegebenen Magnetisierungsverteilung implementiert. Das Modell nutzt Multiplikationen dünn besetzter Matrizen und schnelle Faltungen im Fourier-Raum mit vorberechneten Faltungskernen, die auf bekannten analytischen Lösungen für den Phasenbeitrag einfacher Geometrien basieren. Da das inverse Problem der Rekonstruktion der Magnetisierung schlecht gestellt ist, werden Regularisierungstechniken angewendet, welche die Existenz einer Lösung und deren Einzigartigkeit garantieren. Basierend auf der Minimierung der Austauschenergie wird Tikhonov-Regularisierung erster Ordnung verwendet, um die Glattheit der Lösungen zu fordern. Zusätzlich wird *a priori* Wissen über die Position und Größe der magnetisierten Bereiche in Form einer dreidimensionalen Maske genutzt, um die Anzahl der Unbekannten zu reduzieren. Zur Beurteilung der Qualität der Rekonstruktionsergebnisse wurden diagnostische Größen eingeführt. Der MBIR-Algorithmus wurde erfolgreich auf simulierte Phasenbilder zur Rekonstruktion von zwei- und dreidimensionalen Magnetisierungsverteilungen angewendet. Externe Magnetisierungsquellen außerhalb des Sichtfeldes wurden durch Anpassung linearer Phasenrampen und Offsets, sowie durch Pufferpixel berücksichtigt. Methoden zur Berücksichtigung der gestörten Referenzwelle des Elektronenhologramms, sowie zum Ausschluss anderer Artefakte aus dem Rekonstruktionsprozess wurden eingeführt. Studien über den Einfluss des maximalen Neigungswinkels und der Winkelabtastung in 3D wurden durchgeführt. Der MBIR-Algorithmus wurde erfolgreich eingesetzt, um aus dem Phasenbild einer lithographisch aufgetragenen Kobaltstruktur eine projizierte Magnetisierungsverteilung zu rekonstruieren. Schließlich wurde eine dreidimensionale Magnetisierungsverteilung aus einer simulierten Kippserie mit limitiertem Winkelbereich, Gauß'schem Rauschen, zufälligen Phasenverschiebungen und Rampen rekonstruiert, was die Anwendbarkeit des Algorithmus für zukünftige dreidimensionale experimentelle Studien zeigt.

Contents

List of figures

List of tables

Nomenclature

Abbreviations

ART   Algebraic reconstruction technique

CG   Conjugate gradient

CT   Computed tomography

FBP   Filtered backprojection

FDFC   Fourier space discretisation, Fourier space convolution

FFT   Fast Fourier transform

FOV   Field of view

FWHM   Full width at half maximum

LES   Linear equation system

MBIR   Model based iterative reconstruction

PDF   Probability density function

RDFC   Real space discretisation, Fourier space convolution

RDRC   Real space discretisation, real space convolution

RMS   Root mean square

SIRT   Simultaneous iterative reconstruction technique

STEM   Scanning transmission electron microscopy

SVD   Singular value decomposition

TEM   Transmission electron microscopy

Universal constants

e	Elementary charge (1.602×10^{-19} C)
$\hbar$	Reduced Planck constant (6.582×10^{-16} eVs)
m_e	Electron rest mass (9.109×10^{-31} kg $=$ 0.511 MeV/c²)
μ_0	Vacuum permeability ($4\pi \times 10^{-7}$ Tm/A)
μ_B	Bohr magneton (9.274×10^{-24} J/T)
Φ_0	Magnetic flux quantum (2.067×10^{-15} Tm²)

Indices and coordinates

x, y, z	Euclidean coordinates in three-dimensional space
i, j, k	Indices of the three-dimensional coordinates x, y and z
u, v	Euclidean coordinates in a two-dimensional projection
p, q	Indices of the two-dimensional coordinates u and v
ρ, ϕ, z	Cylindrical coordinates in three-dimensional space
a	Index denoting an *a priori* quantity
b	Index iterating over all phase images
el	Index denoting an electrostatic quantity
mag	Index denoting a magnetic quantity
obj	Index denoting the object wave
pr	Index denoting a projected quantity
rec	Index denoting a reconstructed quantity
ref	Index denoting a reference quantity
s	Index denoting a weighted sum along the projection direction
sat	Index denoting a saturated magnetisation state
t	Index denoting a true, error-free quantiy

XVIII

Scalar quantities

a	Grid spacing
A	Amplitude modulation of an electron wave
C	Cost function
f	Fourier frequency
I	Intensity distribution
k	Wave number
L	Dimension along a grid axis
m	Number of measurements
N	Number of pixels/voxels along a grid axis
R	Radius
t	Thickness
V	Electrostatic potential
α	Superposition angle
β	Magnetisation angle in the projection plane
η	Zero padding number
Γ	Confidence array
γ	Lorentz factor
λ	Electron wavelength
λ	Regularisation parameter
φ	Phase shift
Ψ	Electron wave function
Ξ	Mask
ϵ	Root mean square error

Vector quantities

$\boldsymbol{A}$	Magnetic vector potential
$\boldsymbol{B}$	Magnetic flux density
$\boldsymbol{F}$	Forward model
$\boldsymbol{k}$	Wave vector
$\boldsymbol{M}$	Magnetisation
$\boldsymbol{m}$	Relative magnetisation
$\boldsymbol{P}$	Projection function
$\boldsymbol{Q}$	Phase mapping function
$\boldsymbol{r}$	Three-dimensional coordinate vector (x, y, z)
$\boldsymbol{x}$	Input state vector
$\boldsymbol{y}$	Measurement vector
$\boldsymbol{\epsilon}$	Vector of measurement errors

Matrix quantities

$\mathbf{A}$	Averaging kernel
$\mathbf{F}$	Complete system matrix / Jacobi matrix
$\mathbf{G}$	Gain matrix
$\mathbf{I}$	Identity matrix
$\mathbf{P}$	Projection matrix
$\mathbf{Q}$	Phase mapping matrix
$\mathbf{S}$	Covariance matrix
$\mathbf{W}$	Weighting matrix

Other symbols

$\imath$	Imaginary unit
∂	Partial derivative
∇	Nabla operator
$\mathcal{F}_2$	Two-dimensional Fourier transform
$\mathcal{F}_3$	Three-dimensional Fourier transform
$\mathcal{O}$	Computational complexity
$\Im$	Imaginary part of a complex number
$\Re$	Real part of a complex number
Θ	Boxcar/rectangular function

1. Introduction

Modern technology relies heavily on magnetic materials and, with today's increasing tendency towards miniaturisation, smaller magnetic structures are required. Magnetic nanostructures, ranging from single-domain particles [1] to more complex structures such as skyrmions [2–4], are promising candidates with attractive properties for a wide range of fields. Implementations are prevalent in industrial and technological sectors such as data storage and processing [5, 6] or catalysis [7]. Further applications can be found in the life sciences, *e.g.* in biomedicine [8, 9], cancer treatment [10, 11], genetic engineering [12] and as contrast agents for imaging techniques such as magnetic resonance imaging (MRI) [13]. Magnetic nanoparticles are also of biological importance, *e.g.* as magnetosome chains in magnetotactic bacteria [14]. Due to their scale, magnetic nanoparticles can exhibit vastly different properties compared to their macroscopic counterparts. Tailoring them to the specific needs of the aforementioned fields necessitates the development of methods that are able to reliably characterise their magnetic structures.

Highly sophisticated measurement instruments such as electron microscopes enable access to the microstructure, chemical composition and functional properties of nanoscale materials. Based on the development of electromagnetic lenses by Hans Busch in 1926, the first prototype of an electron microscope was constructed by Ernst Ruska and Max Knoll in 1931. After obtaining a patent in the same year and in close cooperation with Ruska, Siemens made the technology commercially available in 1938. In electron microscopy (EM), accelerated electrons are used for the illumination of samples. The resolution of conventional light microscopes is inherently limited to around 300 nm by the wavelength of visible light. In contrast, the de Broglie wavelength of the relativistic electrons that are used in EM would theoretically, according to the Rayleigh criterion, allow resolutions in the range of picometers (10^{-12} m). However, in analogy to light optics, aberrations occur for electron optical lenses. As a result, the theoretical resolution limit has not yet been reached[1]. In 1997, progress was made with the introduction of a hardware correction system for spherical aberration by Rose, Haider and Urban [15]. With this technology, modern electron microscopes are able to resolve structures smaller than one Ångström (0.1 nm).

Modern transmission electron microscopy (TEM) offers a wide variety of phase contrast techniques that are sensitive to the magnetic induction within and around a

---

[1]The image blurring due to, mainly, spherical aberration is often compared to a view through the bottom of a glass bottle, which conveys the strength of this effect.

sample. These techniques include off-axis electron holography [16–24], differential phase contrast imaging in the scanning TEM (STEM) [25–30], ptychography [31, 32] and the Fresnel and Foucault modes of Lorentz TEM [33–37]. The TEM mode of off-axis electron holography is particularly powerful for characterising the magnetic states of nanoscale materials and devices [14, 38, 39]. Electron holography was first proposed by Gabor in 1948 [40, 41]. The most prominent operational mode is the off-axis scheme, which was introduced by Leith and Upatnieks [42] in 1962. This mode uses an electrostatic biprism [43] to overlap an electron wave that has passed through a region of interest on the sample with a reference wave, thereby creating an interference pattern, or hologram, in the image plane that enables recording of the phase shift of the electron wave in addition to its intensity. The phase shift can be recorded quantitatively and directly across all spatial frequencies and is sensitive to the electromagnetic field within and around the sample. Figure 1.1 shows a contemporary electron microscope that is capable of conducting electron holography measurements.

Figure 1.1.: Picture of the FEI Titan G2 60-300 HOLO, installed in the Ernst Ruska-Centre for Microscopy and Spectroscopy with Electrons (ER-C) in the Jülich research centre. This fourth generation TEM is optimised for the investigation of electromagnetic fields in materials using off-axis electron holography. Image taken from [44].

The quantum mechanical relationship between the magnetisation distribution in a nanostructure and the magnetic phase shift that it induces in an electron wave is based on the Aharonov-Bohm effect [45], which was first proposed by Ehrenberg and Siday in 1949 [46]. For characterisation of the magnetisation, the inverse problem of reconstructing the underlying spatial distribution of magnetic moments from one or more phase images has to be solved. In three dimensions, this equates to a vector field electron tomography problem. Standard methods for electron tomographic reconstruction include filtered backprojection (FBP), the algebraic reconstruction technique (ART) and the simultaneous iterative reconstruction technique (SIRT) [47, 48]. These techniques are all affected by missing wedge artefacts, which occur when the experimental images do not cover a full tilt range of 180°, as well as by the influence of non-linear recorded intensities caused by diffraction effects [21, 49]. Other strategies such as geometric [50] and discrete [51, 52] tomography are able to overcome some of these problems, *e.g.* by employing *a priori* knowledge about the object geometry. However, they are often limited to convex structures and a discrete number of grey levels. An evaluation of different geometric tomography algorithms has been presented by Alpers et al. [48]. Additional complications arise from the fact that magnetic properties are vector fields and thus have to be reconstructed using algorithms for vector field tomography instead of scalar field tomography. Backprojection-based formulae for electron vector field tomography have been described by Lade et al. [53, 54].

When reconstructing a magnetic field using off-axis electron holography, projections of two components of $\boldsymbol{B}$ are proportional to the gradients of two-dimensional recorded phase images. Both components can therefore, in principle, be reconstructed separately, using scalar FBP from two orthogonal tilt series of phase images, while the third component can then be derived from the Maxwell equations (*cf. e.g.* Lai et al. [55]). Other approaches for tackling the reconstruction of $\boldsymbol{B}$ can be found *e.g.* in [56–67]. Instead of focusing on $\boldsymbol{B}$, one can also reconstruct the magnetic vector potential $\boldsymbol{A}$ [68–70]. Theoretically, $\boldsymbol{A}$ can be reconstructed from two orthogonal tilt series. However, due to inaccuracies and instabilities in the presence of noise, either a third tilt series or a limitation to divergence-free fields is necessary [54, 61, 69].

Instead of reconstructing the magnetic field $\boldsymbol{B}$ or the magnetic vector potential $\boldsymbol{A}$, this thesis goes one step further by reconstructing the magnetisation distribution $\boldsymbol{M}$, which is the source of $\boldsymbol{A}$ and in turn also $\boldsymbol{B}$. $\boldsymbol{A}$ and $\boldsymbol{B}$ generally extend outside the boundaries of a magnetic particle, while $\boldsymbol{M}$ is a material property and thus implicitly restricted by an object's shape. If this shape is known or can be approximated, then it can be used as *a priori* knowledge, which significantly reduces the number of unknown variables during the reconstruction process and also reduces the influence of the missing wedge problem, just as for shape constraints used in geometric tomography.

This thesis presents a novel model-based iterative reconstruction (MBIR) technique, which enables the retrieval of either the projected magnetisation distribution of the in-plane components of $\boldsymbol{M}$ inside a sample from a single recorded magnetic phase

image or the three-dimensional distribution of the vector field M from a series of magnetic phase images recorded as a function of sample tilt angle. The advantage of using such a model-based approach is that each trial solution is guaranteed to satisfy known physical laws. At the same time, it allows the inclusion of additional *a priori* knowledge and constraints, which are of great benefit for the analysis of noisy datasets [71]. MBIR techniques are currently employed in a wide variety of fields, ranging from the km scale in atmospheric tomography by using plane-mounted infrared sounders [72] to the mm scale in X-ray computed tomography (CT) [73]. In this thesis, the principle is adapted to the nanoscale for the reconstruction of magnetisation distributions from electron optical phase images recorded in the TEM.

As a consequence of their iterative nature and the size of the matrices involved in their calculation, MBIR techniques have the disadvantage of being slower and more memory intensive than direct reconstruction techniques such as FBP. This problem is overcome in this thesis by employing a range of optimisation strategies. Pre-computed, known analytical solutions for the phase contributions of simple geometries are employed to avoid costly full matrix calculations in favour of a novel operator-based approach. Together with an efficient use of Fourier space convolution, this approach significantly speeds up the reconstruction process, while minimising memory consumption. The inherent ill-posed nature of the reconstruction problem poses an additional challenge of finding the best solution from a pool of possible distributions. In this thesis, this problem is solved by employing the known location of the sample in the form of a mask and by constraining the spatial frequencies that can be present in the recovered magnetisation distribution as physical constraints.

This thesis achieves two main goals:

1. The development of a fast and accurate forward model, which maps an arbitrary three-dimensional magnetisation distribution onto one or more phase images.

2. Integration of this forward model into an iterative model-based algorithm for the retrieval of two-dimensional and three-dimensional magnetisation distributions from either single phase images or tilt series of phase images, respectively.

The following questions are addressed:

- How good is the newly developed forward model in comparison to other approaches, in terms of speed and susceptibility to artefacts?

- How can *a priori* knowledge about magnetisation distributions and physical constraints be utilised to find the best solution using the model-based reconstruction algorithm?

- What influence on the reconstructed magnetisation distribution do these constraints have and how is their effect quantifiable?

- Which artefacts can occur during the reconstruction of two- or three- dimensional magnetisation distributions and what measures can be employed to deal with them?

- Are there magnetisation distributions that are not retrievable using the new reconstruction approach and, if yes, what is their nature?

Chapter 2 begins with an overview of the principles of off-axis electron holography and the acquisition of phase images. The basic equation for the forward model, which links a magnetisation distribution to the phase shift that it induces in a passing electron wave, is derived. Analytical simplifications that can be made for the phase shifts of simple magnetic geometries are described. The fundamental aspects of solving inverse problems are then outlined and concretised for the problem of magnetisation reconstruction.

An efficient model-based reconstruction algorithm necessitates a fast and accurate implementation of a forward model, due to its iterative application during retrieval. Chapter 3 describes existing implementations, which are based on simple integration techniques. Discretisation approaches in Fourier space are discussed, in order to point out problems and sources of artefacts. A new approach based on real space discretisation, which utilises known analytical solutions for simple geometries in the form of look-up tables, is then introduced. This chapter concludes with a comparison of the different implementations in terms of computational time and accuracy.

Chapter 4 utilises the new forward model for the retrieval of two- and three- dimensional magnetisation distributions using an MBIR algorithm. The ill-posed problem of magnetisation retrieval is approximated by a discrete least squares minimisation problem. *A priori* knowledge of the location of the magnetic object, as well as other constraints, are employed to find the best reconstructed solution. Furthermore, diagnostic measurements are derived, in order to provide a critical analysis of the reconstruction results.

After introducing the reconstruction algorithm, Chapters 5 and 6 contain examples of the reconstruction of two- and three-dimensional magnetisation distributions, respectively. Particular emphasis is placed on the influence of noise, constraints and *a priori* information on the retrieval process.

In Chapter 7, the results of this thesis are summarised and future perspectives are outlined.

2. Fundamentals and basic principles

This chapter presents the basic principles of the measurement technique of off-axis electron holography and the reconstruction of a phase image from an electron hologram. The basic equation for the forward model that links phase images to a magnetisation distribution is derived and analytical solutions for basic geometries are described. This formulation of the forward model leads to the inverse problem of retrieving the magnetisation distribution from a set of phase images and to an illustration of the concepts of inverse problems in general.

2.1. Off-axis electron holography

The principle of electron holography was proposed by Gabor in 1948 [40, 41] as a measurement technique that can be used to record not only the intensity of an electron wave but also its phase. As the phase is only measurable if it can be compared to a reference wave, the electron beam has to interfere with a "coherent background". In the off-axis holography scheme, the beam is split into two parts. One half, the object wave, is sent through the sample and accumulates a phase shift through interaction with its electromagnetic field. The second half bypasses the sample, ideally through vacuum, and acts as a reference wave. In the image plane, the two waves are then recombined to produce an interference pattern: the hologram.

Modern implementations of the off-axis holography scheme in electron microscopy utilise an electrostatic biprism, which was first introduced by Möllenstedt and Düker in 1955 [43] as a beam splitter. The biprism consists of a metal-coated quartz filament or a thin metal wire with a diameter of less than a micrometer and two grounded electrodes on either side of the filament with an applied (usually positive) voltage of between a few tens and a few hundreds of Volts. A schematic diagram of the instrumental setup for a single biprism is shown in Fig. 2.1. More complex setups with more than one biprism also exist and are described *e.g.* in [74]. The applied voltage causes both the object wave and the reference wave to be deflected towards the biprism, which results in two partially coherent, virtual electron sources in the backfocal plane of the objective lens [75]. An electron hologram is formed in the overlap region of the waves in the image plane (*cf.* Fig. 2.1). The superposition angle α is approximately proportional to the applied voltage [76].

electron source

condenser lens

object plane   sample

reference wave   object exit-wave

back focal plane   objective lens

virtual   virtual
electron   electron
source   source

α

biprism

image   reference
wave   wave

image
plane
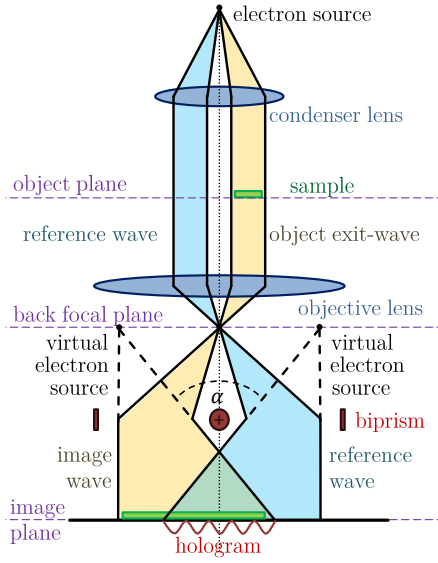
hologram

Figure 2.1.: Schematic diagram showing the electron optical setup for the TEM mode
of off-axis electron holography. The electron beam is produced by an electron source at
the top of the microscope. After primary beam formation in the condenser lens system,
part of the electron beam passes through the sample, while the rest is used as a reference
beam. Both waves are imaged by the objective lens and tilted towards each other by a
biprism. In the image plane, they interfere to form a hologram.

The reference wave in the object plane is assumed to be a normalised plane wave with wave vector $\boldsymbol{k}$, wave number $k = |\boldsymbol{k}| = \frac{2\pi}{\lambda}$ and electron wavelength λ. Writing the coordinate vector $\boldsymbol{r} = (x, y, z)$ and the scalar product $\boldsymbol{k}\boldsymbol{r} = k_x x + k_y y + k_z z$, the reference wave can be expressed in the form

$$\Psi_{\text{ref}}\left(\boldsymbol{r}\right) = e^{\imath \boldsymbol{k}\boldsymbol{r}}, \tag{2.1}$$

while the object wave is modulated in amplitude A and phase φ by the specimen according to the expression

$$\Psi_{\text{obj}}\left(\boldsymbol{r}\right) = A\left(x, y\right) e^{\imath \left[\boldsymbol{k}\boldsymbol{r} + \varphi(x,y)\right]}. \tag{2.2}$$

The biprism tilts the two waves towards each other by angles of $\pm\frac{\alpha}{2}$, which changes their $\boldsymbol{k}$ vectors to $\boldsymbol{k}_{\text{obj}}$ for the object wave and $\boldsymbol{k}_{\text{ref}}$ for the reference wave, respectively[1], leading to the expressions

$$\Psi_{\text{ref}}\left(\boldsymbol{r}\right) = e^{\imath \boldsymbol{k}_{\text{ref}}\boldsymbol{r}} \tag{2.3}$$

and

$$\Psi_{\text{obj}}\left(\boldsymbol{r}\right) = A\left(x, y\right) e^{\imath \left[\boldsymbol{k}_{\text{obj}}\boldsymbol{r} + \varphi(x,y)\right]}. \tag{2.4}$$

The hologram intensity distribution $I\left(x, y\right)$ is then:

$$I\left(x, y\right) = \|\Psi_{\text{ref}} + \Psi_{\text{obj}}\|^2 = \Psi_{\text{ref}}^2 + \Psi_{\text{obj}}^2 + \Psi_{\text{ref}}^* \Psi_{\text{obj}} + \Psi_{\text{ref}} \Psi_{\text{obj}}^* \tag{2.5}$$

$$= 1 + A^2\left(x, y\right)$$

$$+ A\left(x, y\right) \left(e^{\imath \left[\left(\boldsymbol{k}_{\text{obj}} - \boldsymbol{k}_{ref}\right)\boldsymbol{r} + \varphi(x,y)\right]} + e^{-\imath \left[\left(\boldsymbol{k}_{\text{obj}} - \boldsymbol{k}_{\text{ref}}\right)\boldsymbol{r} + \varphi(x,y)\right]}\right) \tag{2.6}$$

$$= 1 + A^2\left(x, y\right) + 2A\left(x, y\right) \cos\left(\left(\boldsymbol{k}_{\text{obj}} - \boldsymbol{k}_{\text{ref}}\right)\boldsymbol{r} + \varphi\left(x, y\right)\right) \tag{2.7}$$

$$\approx 1 + A^2\left(x, y\right) + 2A\left(x, y\right) \cos\left(2\pi q_{\text{c}} x + \varphi\left(x, y\right)\right). \tag{2.8}$$

In the last step, with the help of the small angle approximation, the following relation was used:

$$\left(\boldsymbol{k}_{\text{obj}} - \boldsymbol{k}_{\text{ref}}\right)\boldsymbol{r} = k \sin\left(\alpha\right) x \approx k\alpha x \approx 2\pi q_{\text{c}} x. \tag{2.9}$$

The term $q_{\text{c}} \equiv \frac{1}{\Delta x} \approx \frac{k\alpha}{2\pi}$ is referred to as the carrier spatial frequency [75] and corresponds to the inverse of the interference fringe spacing in the hologram, as derived in the appendix in Section A.1. It carries phase information about the object wave and can be generalised to a two-dimensional vector $\boldsymbol{q}_{\text{c}} \approx \frac{k\alpha}{2\pi}$ for an arbitrary biprism orientation parallel to the projection plane.

---

[1]The effects of the remaining objective lens aberrations of the electron microscope [20], which can be described as a convolution of the object wave with a point spread function [75], further influence the transfer of amplitude and phase from the object to the image plane, but are neglected here.

Both the phase and the amplitude are encoded in the cosinusoidal interference term of the intensity distribution $I\left(x,y\right)$ in Eq. 2.8, thereby providing access to information about the complete object wave. Extracting this information from the intensity distribution is best performed in Fourier space. A two-dimensional Fourier transformation is defined by the expression

$$\tilde{f}\left(q_x, q_y\right) \equiv \mathcal{F}_2\left\{f\left(x,y\right)\right\} = \iint f\left(x,y\right) e^{-\imath(q_x x + q_y y)} dx dy, \tag{2.10}$$

where the two-dimensional spatial frequency is $\boldsymbol{q} = \left(q_x, q_y\right)$. The Fourier transform of Eq. 2.8 then consists of three terms [75]:

$$
\begin{aligned}
\mathcal{F}_2\left\{I\left(x,y\right)\right\} = \quad &\delta\left(\boldsymbol{q}\right) \quad &&+ \mathcal{F}_2\left\{A^2\left(x,y\right)\right\} \quad &&\text{centreband} \\
&+\delta\left(\boldsymbol{q} - \boldsymbol{q}_c\right) * \mathcal{F}_2\left\{A\left(x,y\right) e^{\imath\varphi(x,y)}\right\} \quad &&+1 \text{ sideband} \\
&+\delta\left(\boldsymbol{q} + \boldsymbol{q}_c\right) * \mathcal{F}_2\left\{A\left(x,y\right) e^{-\imath\varphi(x,y)}\right\} \quad &&-1 \text{ sideband.} \tag{2.11}
\end{aligned}
$$

The centreband term consists of the contribution of electrons that did not interact with the sample (resulting in a peak at the zero frequency $\boldsymbol{q} = 0$) and the Fourier transform of the object wave intensity, *i.e.*, of the image that would be obtained using conventional bright-field TEM [76]. The two sidebands represent the Fourier spectra of the complete, complex image wave and its conjugate [75]. Both sidebands contain the same information because the hologram intensity $I\left(x,y\right)$ is a real-valued function and therefore has a Hermitian-symmetric Fourier transform. An example of a simulated off-axis electron hologram of a homogeneously magnetised disc with a purely magnetic phase contribution and its Fourier transform are shown in Figs. 2.2a and 2.2b, respectively.

Numerically masking the +1 sideband, centering it in Fourier space (*cf.* Fig 2.2c) and subsequent back-transformation into real space allows reconstruction of the complex object wave $\Psi_{\text{obj,rec}}\left(x,y\right) = A\left(x,y\right) e^{\imath\varphi(x,y)}$ from the hologram[2]. The phase, which can then be extracted from the complex object wave, is initially restricted to the range $[-\pi, \pi]$ and can be unwrapped digitally before further processing. It should be noted that the phase of the electron wave can only ever be determined to an arbitrary offset. If a vacuum region can be identified in the image that is sufficiently far away from the object and any fields associated with it, then it can be used as a zero reference for the phase to correct this offset. The resulting phase image allows examination of the electromagnetic properties of the object, as described in the next section.

---

[2] The size of the sideband mask determines the number of pixels in the resulting phase image. The mask size has to be sufficiently small to not include parts of the centreband.
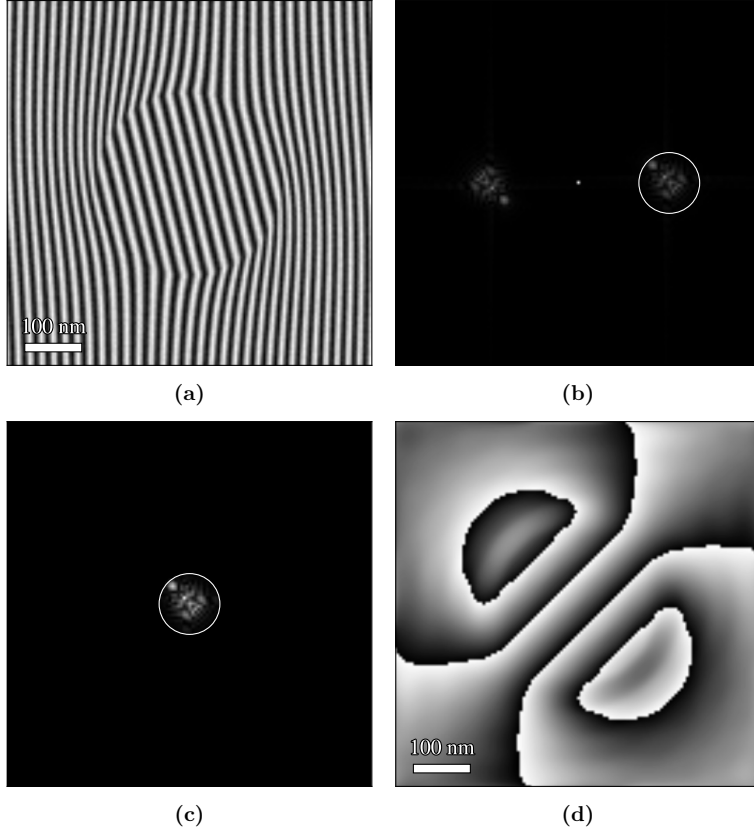
Figure 2.2.: Steps in phase reconstruction from an off-axis electron hologram. **(a)** The intensity distribution of a simulated hologram corresponding to the magnetic contribution to the phase of a disc with a radius of 160 nm. The disc is homogeneously magnetised at an angle of 45° with respect to the x axis. **(b)** The Fourier transform of the hologram with the central point of the power spectrum and two distinct sidebands. The right +1 sideband is cut out, centred, masked outside the marked circle and shown in **(c)**. **(d)** The extracted phase, which is calculated in two steps: First, the inverse Fourier transform of the centred sideband is calculated, resulting in the reconstructed complex object wave $\Psi_{\text{obj,rec}}(x, y)$. Then, the phase can be calculated from $\varphi(x, y) = \arctan(\Re\{\Psi_{\text{obj,rec}}(x, y)\}/\Im\{\Psi_{\text{obj,rec}}(x, y)\})$.

2.2. Phase shifts of magnetisation distributions

The phase shift $\varphi(x, y)$ of an electron wave that has passed through a sample in the TEM can be expressed, in the projection approximation, as a sum of two contributions [77]:

$$\varphi(x, y) = \varphi_{\mathrm{el}}(x, y) + \varphi_{\mathrm{mag}}(x, y) \tag{2.12}$$

$$= C_{\mathrm{el}} \int V(\boldsymbol{r}) dz - \frac{\pi}{\Phi_0} \int A_z(\boldsymbol{r}) dz, \tag{2.13}$$

where $\varphi_{\mathrm{el}}(x, y)$ and $\varphi_{\mathrm{mag}}(x, y)$ are the electrostatic and magnetic contributions to the phase shift, respectively. The incident electron beam direction is parallel to the z axis, $C_{\mathrm{el}} = \frac{\gamma m_{\mathrm{el}} e \lambda}{\hbar^2}$ is an interaction constant, $\Phi_0 = \pi \hbar / e$ is the magnetic flux quantum, γ is the Lorentz factor (used due to the relativistic velocity of the electrons), m_{el} is the electron rest mass, λ is the electron wavelength and $A_z(\boldsymbol{r})$ with $\boldsymbol{r} = (x, y, z)$ is the z component of the magnetic vector potential $\boldsymbol{A}$ [45, 46]. The electrostatic potential V typically comprises both the mean inner potential of the sample V_0 [78–83] and additional variations in potential associated with longer-range charge redistribution in the sample [84–94] and electrostatic stray fields outside it [95–106].

It is primarily the magnetic contribution to the phase φ_{mag} that is of interest in this thesis. Compared to other phase contrast techniques, which typically record either only some spatial frequencies of the phase or a signal that is approximately proportional to the first or second derivative of the phase [77, 107], off-axis electron holography provides direct access to complete phase information. Several different experimental approaches, which are not described here, can be used to separate the desired (but often very weak) magnetic contribution from the total recorded phase shift.

The magnetic vector potential $\boldsymbol{A}(\boldsymbol{r})$ in Eq. 2.13 is linked to the magnetisation distribution $\boldsymbol{M}(\boldsymbol{r})$ in the sample by the convolution integral [108]

$$\boldsymbol{A}(\boldsymbol{r}) = \frac{\mu_0}{4\pi} \int \boldsymbol{M}(\boldsymbol{r}') \times \frac{\boldsymbol{r} - \boldsymbol{r}'}{|\boldsymbol{r} - \boldsymbol{r}'|^3} d\boldsymbol{r}', \tag{2.14}$$

where μ_0 is the vacuum permeability. According to Eq. 2.14, the magnetisation distribution $\boldsymbol{M}(\boldsymbol{r})$ is convolved with the kernel $\frac{\mu_0}{4\pi} \frac{\boldsymbol{r}}{|\boldsymbol{r}|^3}$ by a vector product. Equations 2.13 and 2.14 can be combined to provide a formula that links the magnetic phase shift $\varphi_{\mathrm{mag}}(x, y)$ to the components $\boldsymbol{M}(\boldsymbol{r}) = (M_x(\boldsymbol{r}), M_y(\boldsymbol{r}), M_z(\boldsymbol{r}))$ of the

magnetisation distribution in the sample in the form

$$\varphi_{\text{mag}}(x,y) = -\frac{\mu_0}{4\Phi_0} \int \left[\int \boldsymbol{M}(\boldsymbol{r}') \times \frac{\boldsymbol{r} - \boldsymbol{r}'}{|\boldsymbol{r} - \boldsymbol{r}'|^3} d\boldsymbol{r}' \right]_z dz \tag{2.15}$$

$$= -\frac{\mu_0}{4\Phi_0} \iint \frac{(y - y') M_x(\boldsymbol{r}') - (x - x') M_y(\boldsymbol{r}')}{|\boldsymbol{r} - \boldsymbol{r}'|^3} d\boldsymbol{r}' dz \tag{2.16}$$

$$= -\frac{\mu_0}{2\Phi_0} \int \frac{(y - y') M_x(\boldsymbol{r}') - (x - x') M_y(\boldsymbol{r}')}{(x - x')^2 + (y - y')^2} d\boldsymbol{r}'. \tag{2.17}$$

In this way, the vector product convolution is split into two separate additive convolutions, each of which depends on only one component of the magnetisation ($M_x(\boldsymbol{r})$ or $M_y(\boldsymbol{r})$). The integration over z can be executed in the last step because only the denominator $|\boldsymbol{r} - \boldsymbol{r}'|$ depends on it, yielding a factor of 2 [76]. Because of the vector product in Eq. 2.14, only the components of the magnetisation that are perpendicular to the electron beam direction contribute to φ_{mag} and no information about the z component $M_z(\boldsymbol{r})$ is contained in the magnetic contribution to the phase shift..

Equation 2.17 is the fundamental equation that describes the forward problem. Unfortunately, it can only be solved analytically for a small number of simple object geometries, a few of which are described in the following subsections. In Chapter 3, numerical strategies for solving Eq. 2.17 are assessed and analytical solutions for simple geometries are revisited and utilised for optimisation purposes.

2.2.1. Real space calculations of homogeneous distributions

For most magnetisation distributions $\boldsymbol{M}(\boldsymbol{r})$, it is very difficult, if not impossible, to evaluate the integral in Eq. 2.17 analytically. However, it is possible to obtain analytical solutions for homogeneously magnetised objects that have simple geometries. Such objects can be described by a material-dependent saturation magnetisation M_{sat} and an angle β in the magnetisation plane, resulting in the following expression for the magnetisation

$$\boldsymbol{M}_{\text{hom}}(\boldsymbol{r}) = \begin{cases} M_{\text{sat}}(\cos(\beta), \sin(\beta), 0), & \boldsymbol{r} \in V \\ 0, & \boldsymbol{r} \notin V, \end{cases} \tag{2.18}$$

where V is the volume of the homogeneously-magnetised object. For a projection along the z axis, the z component of $\boldsymbol{M}$ does not contribute to φ_{mag} (as shown in Eq. 2.17) and can be set to zero without loss of generality.

By inserting Eq. 2.18 into Eq. 2.17, a simplified formula for the magnetic contribution to the phase shift can be obtained [76, 109]. The integrand no longer depends on z' and the integration yields the thickness of the object in the electron beam direction $t(x', y')$, which is defined by the integration boundaries of the object volume V.

In terms of the magnetic saturation induction $B_{\text{sat}} = \mu_0 M_{\text{sat}}$, Eq. 2.17 can then be rewritten in the form

$$\varphi_{\text{mag}}(x, y) = \frac{-B_{\text{sat}}}{2\Phi_0} \iint \frac{(y - y') \cos(\beta) - (x - x') \sin(\beta)}{(x - x')^2 + (y - y')^2} t(x', y') \, dx'dy'. \quad (2.19)$$

For simple object geometries, analytical solutions to Eq. 2.19 exist [109, 110]. For example, the magnetic phase shift of a uniformly in-plane-magnetised disc of radius R and thickness t oriented with its axis parallel to the z axis is given by the expression

$$\varphi_{\text{mag}}(x, y) = \begin{cases} -\pi t \frac{B_{\text{sat}}}{2\Phi_0} & (y \cos(\beta) - x \sin(\beta)), \quad r \leq R \\ -\pi t \frac{B_{\text{sat}}}{2\Phi_0} \left(\frac{R}{r}\right)^2 (y \cos(\beta) - x \sin(\beta)), \quad r > R. \end{cases} \quad (2.20)$$

Analytical solutions also exist for more complicated object geometries, such as polyhedra [111, 112] and tilted slabs [76, 109].

2.2.2. Fourier space calculations of homogeneous distributions

By applying the convolution theorem, the magnetic vector potential $\boldsymbol{A}(\boldsymbol{r})$ can also be calculated in Fourier space. When applied to Eq. 2.14, the convolution of $\boldsymbol{A}(\boldsymbol{r})$ with the kernel $\frac{\mu_0}{4\pi} \frac{\boldsymbol{r}}{|\boldsymbol{r}|^3}$ becomes [108]

$$\mathcal{F}_3\{\boldsymbol{A}(\boldsymbol{r})\} = \frac{\mu_0}{4\pi} \mathcal{F}_3\{\boldsymbol{M}(\boldsymbol{r})\} \times \mathcal{F}_3\left\{\frac{\boldsymbol{r}}{|\boldsymbol{r}|^3}\right\} \quad (2.21)$$

$$\Leftrightarrow \quad \boldsymbol{A}(\boldsymbol{r}) = -\mu_0 \mathcal{F}_3^{-1}\left\{\mathcal{F}_3\{\boldsymbol{M}(\boldsymbol{r})\} \times \imath \frac{\boldsymbol{k}}{|\boldsymbol{k}|^2}\right\}, \quad (2.22)$$

where the three-dimensional Fourier transform is defined according to the expression

$$\mathcal{F}_3\{f(\boldsymbol{r})\} = \int f(\boldsymbol{r}) \exp(-2\pi \imath \boldsymbol{r}\boldsymbol{k}) \, d\boldsymbol{r} = \tilde{f}(\boldsymbol{k}). \quad (2.23)$$

The tilde symbol is used to represent a Fourier transformed function and the transformed convolution kernel is $\mathcal{F}_3\left\{\frac{\boldsymbol{r}}{|\boldsymbol{r}|^3}\right\} = -4\pi \imath \frac{\boldsymbol{k}}{|\boldsymbol{k}|^2}$ [108].

In 1991, Mansuripur used this approach to calculate the phase shifts of magnetised objects of constant thickness and periodicity in the x and y directions. Subsequently, Beleggia and Zhu [111, 112] proposed a way to apply the Fourier space approach to homogeneously magnetised objects. The magnetisation distribution in such an object can be expressed in the form $\boldsymbol{M}_{\text{hom}}(\boldsymbol{r}) = M_{\text{sat}} \boldsymbol{e}_{\text{mag}} D(\boldsymbol{r})$, where the unit vector $\boldsymbol{e}_{\text{mag}}$ points in the magnetisation direction and the shape function $D(\boldsymbol{r})$ represents the region of space that is bounded by the magnetised object (taking a value of zero outside it and unity inside it). The Fourier transform of the magnetisation distribution is then $\tilde{\boldsymbol{M}}_{\text{hom}}(\boldsymbol{k}) = M_{\text{sat}} \boldsymbol{e}_{\text{mag}} \tilde{D}(\boldsymbol{k})$. By making use of Eq. 2.22,

the magnetic vector potential can be written in terms of the magnetic saturation induction $B_{\text{sat}} = \mu_0 M_{\text{sat}}$ in the form

$$\tilde{\boldsymbol{A}}\left(\boldsymbol{k}\right) = -\mu_0 \tilde{\boldsymbol{M}}(\boldsymbol{k}) \times \imath \frac{\boldsymbol{k}}{\left|\boldsymbol{k}\right|^2} \tag{2.24}$$

$$= -\imath B_{\text{sat}} \tilde{D}\left(\boldsymbol{k}\right) \left(\boldsymbol{e}_{\text{mag}} \times \frac{\boldsymbol{k}}{\left|\boldsymbol{k}\right|^2}\right). \tag{2.25}$$

For a projection along the z axis, the magnetic phase shift can then be written

$$\tilde{\varphi}_{\text{mag}}\left(k_x, k_y\right) = \frac{\imath \pi B_{\text{sat}}}{\Phi_0} \frac{\tilde{D}\left(k_x, k_y, 0\right)}{\left(k_x^2 + k_y^2\right)} \left(\boldsymbol{e}_{\text{mag}} \times \boldsymbol{k}\right)|_z. \tag{2.26}$$

If the saturation magnetisation, the magnetisation direction and the shape function $D\left(\boldsymbol{r}\right)$ are all known and the Fourier transform $\tilde{D}\left(\boldsymbol{k}\right)$, which is referred to as the shape amplitude, can be calculated, then it is straightforward to find an analytical solution for $\tilde{\varphi}_{\text{mag}}$. However, transforming this solution back to real space analytically is then often much more difficult. Nevertheless, in [111] analytical solutions for rectangular, cylindrical and spherical object geometries were reported. The same concept was applied to polyhedral particles in [112].

2.2.3. Phase of a magnetic vortex state

It is also possible to analytically calculate φ_{mag} for a circular disc of radius R and height t that is oriented with its axis parallel to the z axis and supports an infinitely sharp magnetic vortex state. In cylindrical coordinates (ρ, ϕ, z), the magnetisation distribution is given by the expression

$$\boldsymbol{M}_{\text{vortex}}\left(\rho, \phi, z\right) = M_{\text{sat}} \boldsymbol{e}_{\text{mag}}\left(\phi\right) \Theta\left(R - \rho\right) \Theta\left(\frac{t}{2} - |z|\right), \tag{2.27}$$

where the unit vector $\boldsymbol{e}_{\text{mag}}\left(\phi\right) = \left(-\sin\left(\phi\right), \cos\left(\phi\right), 0\right)$ for the magnetisation direction depends on the angle ϕ in the magnetisation plane and Θ is the box function. The magnetic contribution to the phase shift is then simply [111]

$$\varphi_{\text{mag}}\left(\rho\right) = \begin{cases} \frac{\pi B_{\text{sat}} t}{\Phi_0}\left(R - \rho\right), & \rho \leq R \\ 0, & \rho > R. \end{cases} \tag{2.28}$$

In practise, a vortex core is never infinitely sharp. According to Humphrey and de Graef [71], a better approximation can be made by modifying the magnetisation vector to smoothly transition to be pointing out-of-plane in the centre, according to the expression

$$\boldsymbol{M}_{\text{vortex}}\left(\rho, \phi, z\right) = M_{\text{sat}} \begin{pmatrix} -\sin\left(\phi\right)\sqrt{1 - \nu\left(\rho\right)} \\ \cos\left(\phi\right)\sqrt{1 - \nu\left(\rho\right)} \\ \nu\left(\rho\right) \end{pmatrix} \Theta\left(R - \rho\right) \Theta\left(\frac{t}{2} - |z|\right), \tag{2.29}$$

where $\nu\left(\rho\right) \equiv 1 - \frac{2}{\pi}\arcsin\left(\tanh\left(\frac{\pi\rho}{R_\nu}\right)\right)$ and R_ν is the vortex core radius. However, an easy analytical solution for the resulting magnetic contribution to the phase shift is not available and numerical methods are required.

2.2.4. Projected magnetisation distributions

An arbitrary magnetisation distribution can be described relative to a material-dependent saturation magnetisation M_{sat}, in the form of a relative magnetisation distribution

$$\boldsymbol{m}\left(\boldsymbol{r}\right) \equiv \boldsymbol{M}\left(\boldsymbol{r}\right)/M_{\mathrm{sat}}, \tag{2.30}$$

that is dimensionless. Making use of this definition, Eq. 2.17 can be further simplified to

$$\varphi_{\mathrm{mag}}(x,y) = \frac{-\mu_0 M_{\mathrm{sat}}}{2\Phi_0}\int\frac{\left(y-y'\right)m_x(\boldsymbol{r}') - \left(x-x'\right)m_y(\boldsymbol{r}')}{\left(x-x'\right)^2 + \left(y-y'\right)^2}d\boldsymbol{r}' \tag{2.31}$$

$$= \frac{-B_{\mathrm{sat}}}{2\Phi_0}\iint\frac{\left(y-y'\right)m_{\mathrm{pr},x}(x',y') - \left(x-x'\right)m_{\mathrm{pr},y}(x',y')}{\left(x-x'\right)^2 + \left(y-y'\right)^2}dx'dy'. \tag{2.32}$$

In the second step, the fact that only $\boldsymbol{m}\left(\boldsymbol{r}\right)$ depends on the z coordinate is used to evaluate the integral over the z coordinate first. The resulting projection (which has physical units of length) makes use of the relation

$$\boldsymbol{m}_{\mathrm{pr}}\left(x,y\right) \equiv \int\boldsymbol{m}\left(\boldsymbol{r}\right)dz, \tag{2.33}$$

which describes the areal density of magnetic moments in the projection plane. Without loss of generality, this definition can be extended to arbitrary projection directions onto any two-dimensional plane with axis coordinates u and v:

$$\varphi_{\mathrm{mag}}(u,v) = \frac{-B_{\mathrm{sat}}}{2\Phi_0}\iint\frac{\left(v-v'\right)m_{\mathrm{pr},u}(u',v') - \left(u-u'\right)m_{\mathrm{pr},v}(u',v')}{\left(u-u'\right)^2 + \left(v-v'\right)^2}du'dv'. \tag{2.34}$$

In general, u and v do not have to be aligned with x and y. In this way, Eq. 2.34 separates the calculation of φ_{mag} into two steps:

- A calculation of the areal magnetisation distribution $\boldsymbol{m}_{\mathrm{pr}}$ by projecting $\boldsymbol{m}\left(\boldsymbol{r}\right)$ along the beam direction.

- A convolution of the two components of this projection with the convolution kernels $\frac{v}{u^2+v^2}$ and $\frac{-u}{u^2+v^2}$, in order to calculate the magnetic contribution to the phase shift.

This separation is used in Chapter 3, with Eq. 2.34 providing an analytical foundation for an optimised forward model.

The transformation of Eq. 2.34 into Fourier space then turns the convolutions into simple multiplications that lead to the following analytical formula for the magnetic contribution to the phase shift [113]:

$$\tilde{\varphi}_{\mathrm{mag}}\left(k_u, k_v\right) = \frac{\imath \pi B_{\mathrm{sat}}}{\Phi_0} \frac{\tilde{m}_{\mathrm{pr},u}\left(k_u, k_v\right) \cdot k_v - \tilde{m}_{\mathrm{pr},v}\left(k_u, k_v\right) \cdot k_u}{k_u^2 + k_v^2}, \qquad (2.35)$$

where the Fourier transformations are two-dimensional.

It should be noted that for a very thick sample (or a very rapidly varying magnetisation distribution) it may not be valid to approximate the propagation of the electron beam through the sample by a simple integration along the beam direction, *i.e.* the projection approximation is no longer valid. Electron scattering then needs to be taken into account, *e.g.*, by using a multislice approach [114]. In such a situation, the order in which the electron beam traverses through the sample matters and a simple projection cannot be used.

2.3. Basic concepts of inverse problems

After establishing the mathematical link between the magnetisation distribution $\boldsymbol{M}\left(\boldsymbol{r}\right)$ and the magnetic contribution to the phase shift $\varphi_{\mathrm{mag}}\left(u, v\right)$, the inverse problem of reconstructing $\boldsymbol{M}\left(\boldsymbol{r}\right)$ from a set of phase images has to be tackled. This section provides a brief introduction to the solution of inverse problems and applies its formalisms to the specific case of magnetisation reconstruction from electron optical phase images. The interdependence between the forward and inverse problems is illustrated schematically in Fig. 2.3.
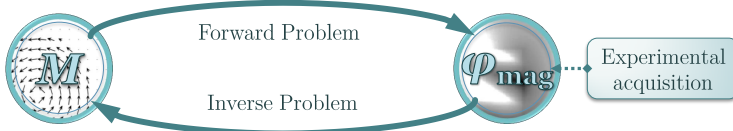
Figure 2.3.: Illustration of the forward and inverse problems that link the magnetisation distribution $\boldsymbol{M}$ and the magnetic contribution to the phase shift φ_{mag}.

In general, if a function $\boldsymbol{F} : \mathbb{R}^n \mapsto \mathbb{R}^m$, which defines a forward model, maps a physical quantity onto a set of observable data, then the reconstruction of the quantity from the data is referred to as an inverse problem. In this thesis, the function $\boldsymbol{F}$ maps the magnetisation distribution $\boldsymbol{M}\left(\boldsymbol{r}\right)$ onto a set of magnetic phase images $\varphi_{\mathrm{mag}}\left(u, v\right)$.

A forward model can be defined mathematically in such a way that it operates on vectorised quantities $\boldsymbol{x}$ and $\boldsymbol{y}$ instead of multi-dimensional fields such as the magnetisation or the phase. For the specific case of the reconstruction of a magnetisation

distribution, the so-called input state vector $\boldsymbol{x} \in \mathbb{R}^n$ is the vectorised form of the magnetisation distribution $\boldsymbol{M}$. The n entries of the input state vector $\boldsymbol{x}$ correspond to the degrees of freedom of the reconstruction, which are determined by the vector components of each magnetised voxel in the magnetisation distribution. The so-called measurement vector $\boldsymbol{y} \in \mathbb{R}^m$ contains the vectorised concatenation of all of the measured phase images φ_{mag}, whose pixels correspond to m individual measurements. The exact vectorisation formalism, which is needed to set up $\boldsymbol{x}$ and $\boldsymbol{y}$ from $\boldsymbol{M}$ and φ_{mag}, is further explained in Chapter 3. With these quantities defined, the forward model can be expressed as

$$\boldsymbol{F}\left(\boldsymbol{M}\right) = \varphi_{\mathrm{mag}} \qquad \overset{\text{vectorisation}}{\rightarrow} \qquad \boldsymbol{F}\left(\boldsymbol{x}\right) = \boldsymbol{y}. \tag{2.36}$$

If the forward model describes the underlying physical process accurately and completely, then $\boldsymbol{F}$ can be used to create a "true", error-free simulation $\boldsymbol{y}_{\mathrm{t}} \in \mathbb{R}^m$. However, in reality, measurements are usually affected by errors $\boldsymbol{\epsilon} \in \mathbb{R}^m$ originating from different sources. If the true state is denoted $\boldsymbol{x}_{\mathrm{t}} \in \mathbb{R}^n$, then the error-afflicted measurements $\boldsymbol{y} \in \mathbb{R}^m$ can be expressed in the form

$$\boldsymbol{y} = \boldsymbol{y}_{\mathrm{t}} + \boldsymbol{\epsilon} = \boldsymbol{F}\left(\boldsymbol{x}_{\mathrm{t}}\right) + \boldsymbol{\epsilon}. \tag{2.37}$$

The errors $\boldsymbol{\epsilon}$ cannot be separated from the measurements $\boldsymbol{y}$ after acquisition, *i.e.* it is usually impossible to reconstruct the true state $\boldsymbol{x}_{\mathrm{t}}$. Nevertheless, it is often still possible to reconstruct at least an approximation $\boldsymbol{x}_{\mathrm{rec}} \in \mathbb{R}^n$ and the inverse problem can be expressed as in the form

$$\boldsymbol{x}_{\mathrm{rec}} = \boldsymbol{F}^{-1}\left(\boldsymbol{y}\right). \tag{2.38}$$

If the inverse problem is well-posed, then this equation is usually solvable. A well-posed problem is defined by three fundamental conditions [115]:

- A solution to the problem exists.
- The solution is unique.
- The solution depends continuously on the data.

If any one of these conditions is not met, then the problem is ill-posed and more sophisticated strategies have to be employed to try to solve it. If $\boldsymbol{F}$ is not injective, *i.e.*, there is no "one-to-one" mapping, then the inverse problem does not necessarily have a unique solution. If $\boldsymbol{F}$ is not surjective, *i.e.*, there is no "onto" mapping, then the inverse problem may have no solution, *e.g.*, because of errors shifting $\boldsymbol{y}$ outside the range (or image / target set) of $\boldsymbol{F}$. In both cases, $\boldsymbol{F}^{-1}$ does not exist and direct inversion is impossible.

In order to solve an ill-posed inverse problem, it can be approximated by a well-posed problem. This process is referred to as regularisation and is described in depth

in [115–118]. First, the inverse problem (Eq. 2.38) is replaced by a minimisation problem, which searches for a solution to the expression

$$\min_x \| \boldsymbol{F} \left(\boldsymbol{x} \right) - \boldsymbol{y} \|_2^2 . \tag{2.39}$$

This relaxation ensures that at least one solution can be found. In order to further ensure that exactly one unique solution is found, a regularisation term $R_\lambda \left(\boldsymbol{x} \right)$ is added to the minimisation problem. This term operates on the state vector $\boldsymbol{x}$ and usually acts as a penalty on the complexity of $\boldsymbol{x}$. $R_\lambda \left(\boldsymbol{x} \right)$ can be used to model physical constraints that describe *a priori* knowledge about the system. The sum of the norm of the residual vector $\boldsymbol{F} \left(\boldsymbol{x} \right) - \boldsymbol{y}$ and the regularisation term $R_\lambda \left(\boldsymbol{x} \right)$ is termed the cost function

$$C \left(\boldsymbol{x} \right) \equiv \| \boldsymbol{F} \left(\boldsymbol{x} \right) - \boldsymbol{y} \|_2^2 + R_\lambda \left(\boldsymbol{x} \right) . \tag{2.40}$$

The minimisation in Eq. 2.39 is replaced by a minimisation of the cost function $C : \mathbb{R}^n \mapsto \mathbb{R}$. The regularisation term $R_\lambda \left(\boldsymbol{x} \right)$ depends on a regularisation parameter λ, which controls the importance of $R_\lambda \left(\boldsymbol{x} \right)$ in comparison to the norm of the residual vector. Basically, λ is used to balance the trade-off between the compliance with the measurements (the first term in Eq. 2.40) and adherence to the regularisation (the second term in Eq. 2.40)[3]. As $\lambda \to 0$, the regularisation term vanishes and the minimisation of the cost function converges to its unregularised form. $R_\lambda \left(\boldsymbol{x} \right)$ is often given by a norm that operates on the state vector $\boldsymbol{x}$. A simple example is the Euclidean norm $\| \boldsymbol{x} \|_2$. If a pool of possible solutions exists for the unregularised problem, then a regularisation term $R_\lambda \left(\boldsymbol{x} \right) = \| \boldsymbol{x} \|_2$ will choose the smallest and simplest solution, effectively applying Occam's razor. The basics of the reconstruction process are summarised in Fig. 2.4.

Minimisation of the cost function depends not only on the forward model $\boldsymbol{F} \left(\boldsymbol{x} \right)$, but also on its derivative $\boldsymbol{F}' \left(\boldsymbol{x} \right)$ and its adjoint[4] $\boldsymbol{F}' \left(\boldsymbol{x} \right)^\dagger$. Because this minimisation is usually executed in an iterative fashion, these quantities have to be calculated several hundreds if not thousands of times. The next chapter therefore focuses on an optimised implementation of the forward model, which can be used to map a magnetisation distribution to a set of phase images, as well as on its derivative and adjoint. Subsequently, Chapter 4 is dedicated to the application of the forward model in an efficient MBIR algorithm and to the modelling of a fitting regularisation term, following the steps presented in this section.

---

[3]In more complex cases, $\boldsymbol{R}_\lambda \left(\boldsymbol{x} \right)$ can be a sum of different regularisation terms, each with a separate regularisation parameter λ, in order to balance them against each other and the measurements.

[4]The adjoint is usually denoted by a dagger †. As an example, the adjoint of a linear operator $\mathbf{F}$ is the complex conjugate (denoted by ∗) of its transpose (denoted by T): $\mathbf{F}^\dagger = \left(\mathbf{F}^* \right)^T$.
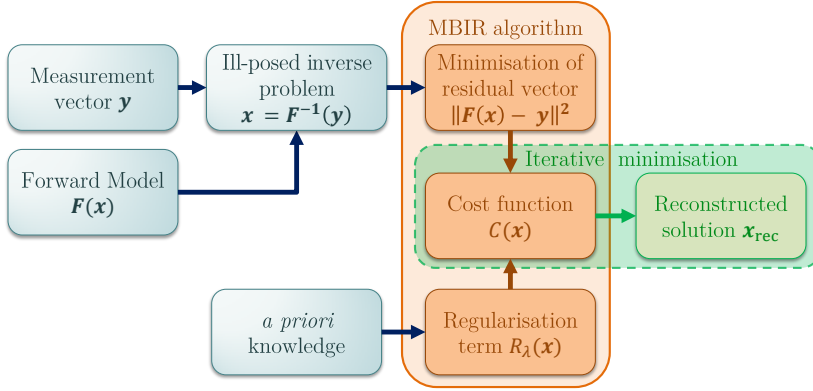
Figure 2.4.: Illustration of the reconstruction process. A forward model $F(x)$ maps a physical quantity x onto a set of observable data described by the measurement vector y. The inverse problem is ill-posed and has to be substituted by a minimisation problem. Together with a regularisation term $R_\lambda(x)$, which can be based on *a priori* knowledge about the system, a cost function $C(x)$ is constructed and minimised iteratively in an MBIR algorithm to find the best-fitting solution x_{rec}.

2.4. Summary

In this chapter, the basic principles of off-axis electron holography were described. It was shown that the electromagnetic phase shift is encoded in electron holograms and can be extracted from the sidebands of their Fourier transforms. If the magnetisation distribution of a sample is known, then the magnetic contribution to the phase shift can be expressed as a convolution integral. In the projection approximation, only the components of the magnetisation that are perpendicular to the electron beam direction contribute to the phase shift. The resulting integral equation can only be solved analytically for simple geometries and magnetisation configurations; some of which were outlined in this chapter. Solutions for the integral can be obtained either in real space or in Fourier space. The integral can be simplified further by performing a projection along the electron beam direction, on the assumption that the sample is sufficiently thin. This concept constitutes the basis of the optimised implementation of a forward model in Chapter 3. Finally, the mathematical basis for inverse problem solving was introduced. This approach is developed into an MBIR algorithm for the reconstruction of magnetisation distributions from electron optical phase images in Chapter 4.

3. A forward model for the calculation of the magnetic phase

This chapter is adapted from [P1] in the list of own publications, submitted to Ultramicroscopy.

In comparison to direct tomographic reconstruction techniques such as FBP, MBIR techniques have the disadvantage that their iterative approach is often much more costly in terms of computation time and memory space. In this thesis, the computational bottleneck is the forward model, which maps a chosen magnetisation distribution onto the corresponding phase images. This forward model is invoked up to several thousand times per reconstruction. It also has to reflect the underlying physics (described in Section 2.2) as accurately and completely as possible. If this is not the case, then one risks introducing additional artefacts into the reconstruction. In addition, an efficient MBIR algorithm requires not only the forward model itself, but also its derivative and adjoint, to be known.

The mathematical basis for the forward model that is used in this thesis is given by Eq. 2.34. This equation shows that the forward model can be split into a projection along the electron beam direction and a subsequent phase mapping operation that is described by convolutions. Whereas the projection is relatively straightforward, the phase mapping step proves to be more complicated. An analytical solution to Eq. 2.34 only exists for a few selected magnetisation distributions, as shown in Section 2.2. For an arbitrary magnetisation distribution, the integral therefore has to be solved numerically. Two approaches currently exist to tackle this problem:

- Direct solution of Eq. 2.34 in real space by applying the trapezium rule to discretise the convolution integral. This approach yields an accurate phase image, but the computation is very slow, as the convolutions are executed in real space.

- Discretisation of the analytical equation in Fourier space (*cf.* Eq. 2.35), where the two convolutions are expressed as multiplications. The result must then be transformed back to real space to calculate the phase image. This approach is much faster, but it suffers from artefacts that are linked to Fourier space discretisation.

Both approaches have desirable aspects but also downsides. The goal of this chapter is to introduce a novel phase mapping approach that combines the accuracy of real space integration with the speed of the Fourier space approach. Together with an efficient projection scheme, this phase mapping approach leads to an overall optimised forward model and provides all of the tools that are necessary for an MBIR algorithm.

The first part of this chapter provides a mathematical formulation of the forward model as a nested matrix equation. As a prerequisite, the three-dimensional space of the magnetisation distribution and the two-dimensional spaces of the phase images are discretised so that they can be used in numerical calculations. A magnetisation state vector and a measurement vector are introduced (*cf.* Section 2.3). The forward model can then be expressed as a matrix equation, because projections and convolutions are linear transformations. For the projection, special emphasis is placed on the intricacies of vector fields. Techniques that are applicable to sparse matrices, *i.e.*, matrices that have relatively few non-zero entries, are used for computational optimisation. The second part of this chapter focuses on an efficient phase mapping implementation. First, prevailing approaches for numerically calculating the phase are illuminated. A novel and improved combined approach is then introduced. Finally, this new approach is compared with the currently more prevalent Fourier space approach, with regard to computational speed and accuracy.

3.1. Matrix formalism of the forward model

3.1.1. Discretisation

The starting point for a numerical calculation of the magnetic contribution to the phase shift φ_{mag} of a magnetisation distribution $\boldsymbol{M}$ is a suitable discretisation of the relevant physical quantities. The three-dimensional magnetisation distribution can be discretised on a Cartesian grid of edge length a (defining the grid spacing) by assigning a local magnetisation $\boldsymbol{M}[i,j,k] = (M_x[i,j,k], M_y[i,j,k], M_z[i,j,k])$ to each grid point $\boldsymbol{r}[i,j,k]$. The grid points divide the three-dimensional space into cubic voxels of volume $V_{\mathrm{vx}} = a^3$, which are labelled by three indices[1] i, j and k. Each voxel is represented by its centre positions along the x, y and z axes (*cf.* Fig. 3.1), such that

$$\boldsymbol{r}[i,j,k] = (x[i], y[j], z[k]) = a\left(i + \frac{1}{2}, j + \frac{1}{2}, k + \frac{1}{2}\right).\qquad(3.1)$$

---

[1]In all of the following discussions, spatial indices are always denoted by square brackets to separate them from other parameters.
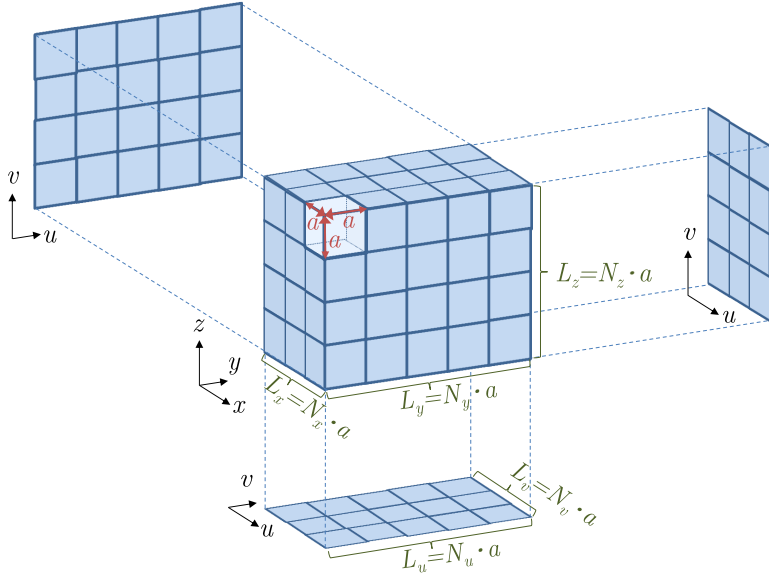
Figure 3.1.: Definition of the coordinate system used to discretise a three-dimensional magnetisation distribution with spatial coordinates x, y and z, shown alongside three exemplary two-dimensional projections with spatial coordinates u and v. Such projections are used to discretise the projected magnetisation distributions and phase images. One such coordinate system exists for each projection direction. For simplification, only coordinate systems along the three major axes (x, y and z) are shown.

The total dimensions of the grid are $L_x \times L_y \times L_z$, with $L_x = N_x a$, $L_y = N_y a$ and $L_z = N_z a$. The number of grid points along the x, y and z directions is then denoted N_x, N_y and N_z. $\boldsymbol{M}[i,j,k]$ can always be described relative to a (material-dependent) saturation magnetisation M_{sat} in the form of a relative magnetisation distribution[2]

$$\boldsymbol{m}[i,j,k] \equiv \boldsymbol{M}[i,j,k] / M_{\text{sat}}, \qquad (3.2)$$

which is the discretised form of Eq. 2.30.

Application of the forward model to a magnetisation distribution results in a set of N_b discretised magnetic phase images $\varphi_{\text{mag},b}[p,q]$, which are labelled with two spatial indices[3] p and q. The parameter b specifies the index of the image. The coordinate system uv of each magnetic phase image (*cf.* Fig. 3.1) does not need to be aligned with the xyz coordinates of the magnetisation distribution. Each magnetic phase image contains $N_{u,b} \times N_{v,b}$ pixels. Here, the grid spacing a of the two-dimensional coordinate systems is chosen to be the same as that of the three-dimensional space, with each pixel having an area of $A_{\text{px}} = a^2$. Just as for the three-dimensional discretisation (*cf.* Eq. 3.1), each pixel is represented by its centre position along the u and v axes (*cf.* Fig. 3.1), such that

$$(u[p], v[q]) = a\left(p + \frac{1}{2}, q + \frac{1}{2}\right). \qquad (3.3)$$

In general, each magnetic phase image could vary in the number of pixels in the field of view. Here, it is assumed that all sizes are the same, *i.e.*, $N_{u,b} \equiv N_u$ and $N_{v,b} \equiv N_v$. The sizes of the phase images can be selected during the reconstruction of the phase from the corresponding hologram (*cf.* Section 2.1). This size is usually chosen to be the same for all of the phase images in a tilt series. The chosen simplification is therefore justified in nearly all cases.

In addition to the discretisation of the three-dimensional magnetisation distribution $\boldsymbol{m}[i,j,k]$ and the phase images $\varphi_{\text{mag},b}[p,q]$, the intermediate result for the projected magnetisation distribution $\boldsymbol{m}_{\text{pr}}$ is needed. In the simple case of a projection along the z direction, $\boldsymbol{m}_{\text{pr}}$ can be discretised by turning the projection integral $\boldsymbol{m}_{\text{pr}}(x,y) = \int \boldsymbol{m}(\boldsymbol{r})\,dz$ (*cf.* Eq. 2.33) into a sum[4] over all of the voxels along the z axis, which results in the expression

$$\boldsymbol{m}_{\text{pr}}[i,j] = \sum_k \boldsymbol{m}[i,j,k] \cdot a \equiv a \cdot \boldsymbol{m}_{\text{s}}[i,j]. \qquad (3.4)$$

---

[2] M_{sat} is factored out to simplify the following formulas and calculations. In general, M_{sat} can vary across the field of view if, *e.g.*, different magnetic materials are present. If this is the case, M_{sat} can just be set to $1\,\frac{\text{A}}{\text{m}}$, so that $\boldsymbol{m}[i,j,k]$ is numerically equal to $\boldsymbol{M}[i,j,k]$, just without units.

[3] The indices p and q were chosen for the two-dimensional coordinate systems to distinguish them from the three-dimensional coordinate system, indexed by i, j and k.

[4] All of the sums in the following discussions implicitly go from 0 to the corresponding number of pixels $N_{x/y/z}$, or $N_{u/v}$ minus one, respectively.

The infinitesimal term dz in the integral is thereby to the grid spacing a during discretisation. For convenience, a new measure $\boldsymbol{m}_\mathrm{s}[i,j]$ is used to represent the sum, so that a can be factored out[5]. Although Eq. 3.4 is only valid for a projection along z, without loss of generality, the projection can be generalised to the established coordinate systems uv for arbitrary projection directions. The resulting generalised form $\boldsymbol{m}_{\mathrm{s},b}[p,q]$ also includes the image index b, so that different projection directions can be distinguished. The mapping $\boldsymbol{m}[i,j,k] \rightarrow \boldsymbol{m}_{\mathrm{s},b}[p,q]$ between the three-dimensional magnetisation distribution and its projection is then no longer as simple as a sum along a major axis and is described in depth in Section 3.1.3. The same coordinate system is used below for the projected magnetisation distributions and the resulting phase images, $i.e.$, both have image dimensions $N_u \times N_v$. The grid spacing a is used by all discretised quantities.

3.1.2. Vectorisation

The formulation of the forward model, which is described in Eq. 2.36, necessitates vectorisation of the discretised quantities $\boldsymbol{m}[i,j,k]$, $\boldsymbol{m}_{\mathrm{s},b}[p,q]$ and $\varphi_\mathrm{mag}[p,q]$. Vectorisation in this sense means that a multi-dimensional field is reduced to a one-dimensional field by listing all of the entries in a single vector. The inverse operation is referred to as reshaping and returns an appropriate vector to its multi-dimensional shape.

Here, the magnetisation state vector $\boldsymbol{x} \in \mathbb{R}^{3N_x N_y N_z}$, which serves as input for the forward model, is the vectorised form of the three-dimensional magnetisation distribution $\boldsymbol{m}[i,j,k]$. It is constructed by separately vectorising the three components $m_x[i,j,k]$, $m_y[i,j,k]$ and $m_z[i,j,k]$, and concatenating them to create a single vector:

$$\boldsymbol{x} = \begin{pmatrix} \boldsymbol{x}_x \\ \boldsymbol{x}_y \\ \boldsymbol{x}_z \end{pmatrix} = \begin{pmatrix} m_x[0,0,0], \dots, m_x[N_x-1, N_y-1, N_z-1], \\ m_y[0,0,0], \dots, m_y[N_x-1, N_y-1, N_z-1], \\ m_z[0,0,0], \dots, m_z[N_x-1, N_y-1, N_z-1] \end{pmatrix}^T . \tag{3.5}$$

For each component sub-vector $\boldsymbol{x}_x$, $\boldsymbol{x}_y$ and $\boldsymbol{x}_z$, the first index i of the x coordinate changes the fastest, while the last index k of the z coordinate changes the slowest[6]. This means that $\boldsymbol{x}_x[1,0,0]$ follows $\boldsymbol{x}_x[0,0,0]$ and so on. The same principle is applied to all of the following vectorisations.

Similarly, both components $m_{\mathrm{s},b,u}$ and $m_{\mathrm{s},b,v}$ of each projected relative magnetisation distribution $\boldsymbol{m}_{\mathrm{s},b}[p,q]$ can be vectorised to form the two sub-vectors $\boldsymbol{x}_{\mathrm{pr},b,u}$ and

---

[5]Whereas $\boldsymbol{m}_s$ has no units (it is a sum of unit-less relative magnetisation voxels), $\boldsymbol{m}_\mathrm{pr}$ contains the grid spacing a and has units of length.

[6]In an algorithmic implementation, this order is in accordance with the memory order of most "row-major" programming languages, $e.g.$ C or Python. A counter-example is Fortran, which is a "column-major" language.

$\boldsymbol{x}_{\mathrm{pr},b,v}$. Their concatenation $\boldsymbol{x}_{\mathrm{pr},b} \in \mathbb{R}^{2N_u N_v}$ can be written

$$\boldsymbol{x}_{\mathrm{pr},b} = \begin{pmatrix} \boldsymbol{x}_{\mathrm{pr},b,u} \\ \boldsymbol{x}_{\mathrm{pr},b,v} \end{pmatrix} = \begin{array}{l} \left(m_{\mathrm{s},b,u}\left[0,0\right], \ldots, m_{\mathrm{s},b,u}\left[N_u - 1, N_v - 1\right], \right. \\ \left. m_{\mathrm{s},b,v}\left[0,0\right], \ldots, m_{\mathrm{s},b,v}\left[N_u - 1, N_v - 1\right] \right)^T . \end{array} \tag{3.6}$$

Overall, there are N_b projection vectors $\boldsymbol{x}_{\mathrm{pr},b}$, one corresponding to each measured phase image. These projection vectors can be concatenated to form one collective vector $\boldsymbol{x}_{\mathrm{pr}} \in \mathbb{R}^{N_b 2 N_u N_v}$, with

$$\boldsymbol{x}_{\mathrm{pr}} = \begin{pmatrix} \boldsymbol{x}_{\mathrm{pr},1} \\ \vdots \\ \boldsymbol{x}_{\mathrm{pr},N_b} \end{pmatrix} . \tag{3.7}$$

In vectorised form, the projection of the three-dimensional magnetisation distribution $\boldsymbol{x}$ onto the collection of projected distributions $\boldsymbol{x}_{pr}$ can be expressed as a projection function

$$\boldsymbol{P}\left(\boldsymbol{x}\right) \equiv \boldsymbol{x}_{\mathrm{pr}}. \tag{3.8}$$

The vector $\boldsymbol{y} \in \mathbb{R}^{N_b N_u N_v}$ contains the vectorised magnetic phase images $\varphi_{\mathrm{mag},b}\left[p,q\right]$ in order of ascending image number b:

$$\boldsymbol{y} = \begin{pmatrix} \boldsymbol{y}_1 \\ \vdots \\ \boldsymbol{y}_{N_b} \end{pmatrix} = \begin{array}{l} \left(\varphi_{\mathrm{mag},1}\left[0,0\right], \ldots, \varphi_{\mathrm{mag},1}\left[N_u - 1, N_v - 1\right], \right. \\ \cdots, \\ \left. \varphi_{\mathrm{mag},N_b}\left[0,0\right], \ldots, \varphi_{\mathrm{mag},N_b}\left[N_u - 1, N_v - 1\right] \right)^T . \end{array} \tag{3.9}$$

For the inverse problem of reconstructing a magnetisation distribution, which is the goal of this thesis, $\boldsymbol{y}$ describes the measured phase images and is referred to as the "measurement vector" below. The measurement vector $\boldsymbol{y}$ can be related to the collection of projected distributions $\boldsymbol{x}_{\mathrm{pr}}$ by a "phase mapping" function

$$\boldsymbol{Q}\left(\boldsymbol{x}_{\mathrm{pr}}\right) = \boldsymbol{y}, \tag{3.10}$$

which describes the two convolutions that appear in Eq. 2.34.

After all of the relevant quantities have been vectorised, an equation for the forward model can be defined. Starting from the general equation (*cf.* Eq. 2.36) and utilising Eqs. 3.8 and 3.10, the expression for the forward model is

$$\boldsymbol{F}\left(\boldsymbol{x}\right) = \boldsymbol{y} = \boldsymbol{Q}\left(\boldsymbol{x}_{\mathrm{pr}}\right) = \boldsymbol{Q}\left(\boldsymbol{P}\left(\boldsymbol{x}\right)\right). \tag{3.11}$$

The two steps of projection and phase mapping are described in the following sections, with the goal of finding a complete system matrix that describes the forward model.

3.1.3. Projection matrix

The projection $\boldsymbol{P}\left(\boldsymbol{x}\right)$ is a linear transformation and can therefore be expressed as a matrix operation

$$\boldsymbol{P}\left(\boldsymbol{x}\right) = \mathbf{P}\boldsymbol{x} = \begin{pmatrix} \mathbf{P}_1 \\ \vdots \\ \mathbf{P}_{N_b} \end{pmatrix} \begin{pmatrix} \boldsymbol{x}_x \\ \boldsymbol{x}_y \\ \boldsymbol{x}_z \end{pmatrix} \equiv \begin{pmatrix} \boldsymbol{x}_{\mathrm{pr},1} \\ \vdots \\ \boldsymbol{x}_{\mathrm{pr},N_b} \end{pmatrix} = \boldsymbol{x}_{\mathrm{pr}}, \tag{3.12}$$

where $\mathbf{P} \in \mathbb{R}^{N_b 2 N_u N_v \times 3 N_x N_y N_z}$ is the projection matrix, which itself consists of N_b sub-matrices that correspond to the projection directions of the individual images. The projection sub-matrices

$$\mathbf{P}_b = \begin{pmatrix} c_{b,ux}\mathbf{W}_b & c_{b,uy}\mathbf{W}_b & c_{b,uz}\mathbf{W}_b \\ c_{b,vx}\mathbf{W}_b & c_{b,vy}\mathbf{W}_b & c_{b,vz}\mathbf{W}_b \end{pmatrix}, \tag{3.13}$$

where $\mathbf{P}_b \in \mathbb{R}^{2 N_u N_v \times 3 N_x N_y N_z}$, describe the parallel projection of a three-dimensional three-component vector field onto a two-dimensional two-component vector field. They consist of six entries, which are themselves expressed as products of six coefficients (*e.g.* $c_{b,ux} \in \mathbb{R}$) and a weighting matrix $\mathbf{W}_b \in \mathbb{R}^{N_u N_v \times N_x N_y N_z}$. The weighting matrix $\mathbf{W}_b$ describes the weighting impact of the 3D voxels on the 2D pixels of the projection. The coefficients determine the contributions of the three-dimensional magnetisation components xyz (columns) to the projected magnetisation components uv (rows).

The projection sub-matrix $\mathbf{P}_b$ is best illustrated by a simple example of a small volume of $2 \times 2 \times 2$ voxels. For a simple projection along the z direction, the matrix is given by the expression

$$\mathbf{P}_b = \begin{pmatrix} \mathbf{W}_b & \mathbf{0} & \mathbf{0} \\ \mathbf{0} & \mathbf{W}_b & \mathbf{0} \end{pmatrix}. \tag{3.14}$$

Here, the x component is mapped onto the u component, the y component is mapped onto the v component and the z component of the three-dimensional magnetisation is lost during the projection. All of the coefficients are zero, except for $c_{b,ux} = c_{b,vy} = 1$. The weighting matrix is then

$$\mathbf{W}_b = \begin{pmatrix} \mathbf{I}_4 & \mathbf{I}_4 \end{pmatrix} = \begin{pmatrix} 1 & 0 & 0 & 0 & 1 & 0 & 0 & 0 \\ 0 & 1 & 0 & 0 & 0 & 1 & 0 & 0 \\ 0 & 0 & 1 & 0 & 0 & 0 & 1 & 0 \\ 0 & 0 & 0 & 1 & 0 & 0 & 0 & 1 \end{pmatrix}. \tag{3.15}$$

In this case, the weighting matrix consists of two 4×4 identity matrices $\mathbf{I}_4$. They are each applied to one of the two slices in the z direction. In this simple example, both slices are just summed up without being modified. Therefore, $\mathbf{W}_b$ is essentially just a matrix representation of the summation that was already described in Eq. 3.4.

For different projection directions, the calculation is more complicated. The two vector field components of the projection are then given by a linear combination of the three-dimensional components. This linear combination is determined by the coefficients, *e.g.* $c_{b,ux}$ and the complexity of the weighting matrix also increases. Nonetheless, some general characteristics of $\mathbf{W}_b$ can be noted:

- Each column of $\mathbf{W}_b$ has to add up to one, *i.e.*, no magnetisation is lost during the projection[7]. If the projection of a voxel centre does not coincide with the centre of a pixel in the two-dimensional coordinate system uv, then the entry in the corresponding column of $\mathbf{W}_b$ has a value between 0 and 1, indicating that the magnetisation inside the voxel is redistributed between several pixels upon projection. This redistribution increases the number of non-zero entries in $\mathbf{W}_b$, in comparison to a projection along a major axis.

- The row sum of $\mathbf{W}_b$ is an indicator of the number of voxels that are projected onto a specific pixel. In the example of a z projection described above, each row sum has to be equal to the number of pixels N_z along the z direction. As above, the row sum can in general also be fractional when a voxel only contributes part of its magnetisation to a pixel upon projection.

$\mathbf{W}_b$ has to be set up only once at the beginning of the reconstruction process. The construction of the weighting matrices is rather verbose and is not discussed in depth in this chapter. Section A.2 in the appendix describes implementations for projections along the three major axes (xyz) and for projections with a tilt about the x or the y axis. It should be noted that $\mathbf{W}_b$ and therefore also $\mathbf{P}_b$ are very sparse matrices, *i.e.*, they have very few non-zero entries. By storing only the non-zero entries in combination with their location in the matrix, memory consumption can be reduced to a tiny fraction of that for a naive implementation. As an additional benefit, matrix vector multiplications can be carried out several orders of magnitude faster. The sparse nature of $\mathbf{P}_b$ therefore enables efficient implementation for the thousands of projections that are necessary for the execution of an MBIR algorithm[8].

3.1.4. Phase mapping matrix

The second part of the forward model is described by the function $\boldsymbol{Q}\left(\boldsymbol{x}_{\mathrm{pr}}\right) = \boldsymbol{y}$, whose implementation involves a convolution of the components of the projected magnetisation $\boldsymbol{x}_{\mathrm{pr}}$ by two convolution kernels. This convolution process is referred to as "phase mapping" below. As the convolutions are linear operations, phase mapping

---

[7]The exceptions for slanted projections are voxels at the edges and corners of the three-dimensional volume, whose projection rays can "miss" the projected coordinate systems. If the magnetised volume is located in the centre of the three-dimensional space, then no magnetisation is lost.

[8]All of the methods that are described here can also be applied to scalar fields. The weighting matrix then directly describes the projection with $\mathbf{P}_b = \mathbf{W}_b$.

can therefore also be expressed in terms of a matrix operation $\mathbf{Q} \in \mathbb{R}^{N_b N_u N_v \times N_b 2 N_u N_v}$. As a result of the independence of the individual phase images, $\mathbf{Q}$ has a block diagonal structure:

$$
\boldsymbol{Q}\left(\boldsymbol{x}_{\mathrm{pr}}\right) = \boldsymbol{y} = \mathbf{Q} \boldsymbol{x}_{\mathrm{pr}} = \begin{pmatrix} \mathbf{Q}_1 & \mathbf{0} & \cdots & \mathbf{0} \\ \mathbf{0} & \ddots & & \vdots \\ \vdots & & \ddots & \mathbf{0} \\ \mathbf{0} & \cdots & \mathbf{0} & \mathbf{Q}_{N_b} \end{pmatrix} \begin{pmatrix} \boldsymbol{x}_{\mathrm{pr},1} \\ \vdots \\ \boldsymbol{x}_{\mathrm{pr},N_b} \end{pmatrix} = \begin{pmatrix} \mathbf{Q}_1 \boldsymbol{x}_{\mathrm{pr},1} \\ \vdots \\ \mathbf{Q}_{N_b} \boldsymbol{x}_{\mathrm{pr},N_b} \end{pmatrix}.
$$

$$(3.16)$$

Every sub-matrix $\mathbf{Q}_b \in \mathbb{R}^{N_u N_v \times 2 N_u N_v}$ describes the convolution process for a single projection $\boldsymbol{x}_{\mathrm{pr},b}$. $\mathbf{Q}_b$, in turn, is a block matrix that is composed of two square sub-matrices $\mathbf{Q}_{b,u} \in \mathbb{R}^{N_u N_v \times N_u N_v}$ and $\mathbf{Q}_{b,v} \in \mathbb{R}^{N_u N_v \times N_u N_v}$, which separate the convolutions of the two projected magnetisation components in the u and v directions:

$$
\mathbf{Q}_b \boldsymbol{x}_{\mathrm{pr},b} = \begin{pmatrix} \mathbf{Q}_{b,u} & \mathbf{Q}_{b,v} \end{pmatrix} \begin{pmatrix} \boldsymbol{x}_{\mathrm{pr},b,u} \\ \boldsymbol{x}_{\mathrm{pr},b,v} \end{pmatrix} = \mathbf{Q}_{b,u} \boldsymbol{x}_{\mathrm{pr},b,u} + \mathbf{Q}_{b,v} \boldsymbol{x}_{\mathrm{pr},b,v} \tag{3.17}
$$

$$
\equiv \boldsymbol{y}_{b,u} + \boldsymbol{y}_{b,v} = \boldsymbol{y}_b. \tag{3.18}
$$

In contrast to the sparse projection matrix $\mathbf{P}$, the phase mapping matrices $\mathbf{Q}_b$ for single images are dense. For non-trivial forward models containing many projections it is thus infeasible to compute all entries of $\mathbf{Q}_b$ or store the matrices $\mathbf{Q}_b$ in memory. The entire second half of this chapter (*cf.* Section 3.2) is consequently dedicated to finding the most efficient implementation of the operation $\mathbf{Q}_b \boldsymbol{x}_{\mathrm{pr},b}$.

3.1.5. Complete system matrix

In summary, the (very nested) complete system system matrix $\mathbf{F} \in \mathbb{R}^{N_b N_u N_v \times 3 N_x N_y N_z}$ of the forward model, which is illustrated in Fig. 3.2, is given by the expression

$$
\mathbf{F} = \mathbf{Q} \mathbf{P} = \begin{pmatrix} \mathbf{Q}_1 & \mathbf{0} & \cdots & \mathbf{0} \\ \mathbf{0} & \ddots & & \vdots \\ \vdots & & \ddots & \mathbf{0} \\ \mathbf{0} & \cdots & \mathbf{0} & \mathbf{Q}_{N_b} \end{pmatrix} \cdot \begin{pmatrix} \mathbf{P}_1 \\ \vdots \\ \mathbf{P}_{N_b} \end{pmatrix} = \begin{pmatrix} \mathbf{Q}_1 \mathbf{P}_1 \\ \vdots \\ \mathbf{Q}_{N_b} \mathbf{P}_{N_b} \end{pmatrix}. \tag{3.19}
$$

Because of the block diagonal nature of this matrix, the measurement vector $\boldsymbol{y}_b$ of each magnetic phase image can be calculated separately by splitting the forward model into N_b individual sub-problems $\mathbf{Q}_b \mathbf{P}_b \equiv \mathbf{F}_b \in \mathbb{R}^{N_u N_v \times 3 N_x N_y N_z}$. This formulation results in a complete model description as a linear problem:

$$
\boldsymbol{y} = \mathbf{F} \boldsymbol{x} = \mathbf{Q} \mathbf{P} \boldsymbol{x} = \begin{pmatrix} \boldsymbol{y}_1 \\ \vdots \\ \boldsymbol{y}_{N_b} \end{pmatrix} = \begin{pmatrix} \mathbf{Q}_1 \mathbf{P}_1 \boldsymbol{x} \\ \vdots \\ \mathbf{Q}_{N_b} \mathbf{P}_{N_b} \boldsymbol{x} \end{pmatrix} \equiv \begin{pmatrix} \mathbf{F}_1 \boldsymbol{x} \\ \vdots \\ \mathbf{F}_{N_b} \boldsymbol{x} \end{pmatrix}. \tag{3.20}
$$

System matrix $\mathbf{F}$ ¦ Single image matrix $\mathbf{F}_b$
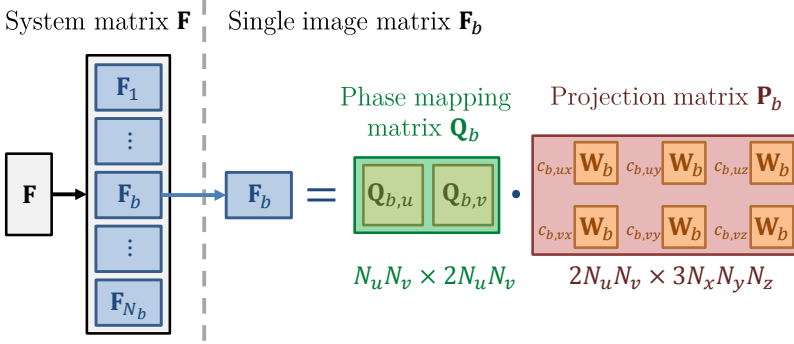
Figure 3.2.: Illustration of the nested nature of the system matrix $\mathbf{F}$, which consists of a stack of N_b sub-matrices $\mathbf{F}_b$, each of which describes the forward model for a single image and can be expressed as a matrix product $\mathbf{F}_b = \mathbf{Q}_b \mathbf{P}_b$. The projection matrix $\mathbf{P}_b \in \mathbb{R}^{2N_uN_v \times 3N_xN_yN_z}$ can be further decomposed into six entries of a weighting matrix $\mathbf{W}_b \in \mathbb{R}^{N_uN_v \times N_xN_yN_z}$ with different coefficients. In contrast, the phase mapping matrix $\mathbf{Q}_b \in \mathbb{R}^{N_uN_v \times 2N_uN_v}$ consists of two sub-matrices, which describe convolutions of the u and v components of the projected magnetisation distribution, respectively.

Splitting the forward model into N_b independent sub-problems for each phase image is important, as it can be used in a parallelised implementation in the future. In the case of a reconstruction of the projected in-plane magnetisation from a single phase image, *i.e.* $N_b = 1$, $\mathbf{F}$ can be simplified to:

$$y = \mathbf{F}_1 x = \mathbf{Q}_1 \mathbf{P}_1 x. \tag{3.21}$$

3.1.6. Derivatives and adjoints

An efficient solution to the inverse problem requires that the derivative of the forward model, *i.e.*, the Jacobi matrix $\frac{\partial \boldsymbol{F}(\boldsymbol{x})}{\partial \boldsymbol{x}}$, must be known (*cf.* Section 2.3). Although finite differences are often used to calculate $\frac{\partial F(x)}{\partial x}$ for non-linear models [72], for the linear problem at hand the Jacobi matrix is just equal to the system matrix itself:

$$\frac{\partial \boldsymbol{F}(\boldsymbol{x})}{\partial \boldsymbol{x}} = \frac{\partial}{\partial \boldsymbol{x}}(\mathbf{F}\boldsymbol{x}) = \mathbf{F} = \mathbf{QP}. \tag{3.22}$$

In practice, only the product of the Jacobi matrix $\mathbf{F}$ with a vector $\boldsymbol{x}$ is needed. This product is trivial and reduces to an evaluation of the forward model itself:

$$\frac{\partial \boldsymbol{F}(\boldsymbol{x})}{\partial \boldsymbol{x}} \cdot \boldsymbol{x} = \mathbf{F}\boldsymbol{x} = \boldsymbol{F}(\boldsymbol{x}) \tag{3.23}$$

In addition, the adjoint of the Jacobi matrix $\mathbf{F}^\dagger$ is needed, in order to map the measurements back onto the underlying model. The adjoint of a matrix $\mathbf{F}$ is defined as its conjugate transpose

$$\mathbf{F}^\dagger = (\mathbf{F}^*)^T. \tag{3.24}$$

An adjoint operation can be interpreted as a "back-propagation" of information [119]. As the system matrix $\mathbf{F}$ and its sub-matrices are all real-valued, the adjoint $\mathbf{F}^\dagger$ is equal to the transposed $\mathbf{F}^T$ and can be expressed as

$$\mathbf{F}^T = (\mathbf{Q}\mathbf{P})^T = \mathbf{P}^T\mathbf{Q}^T. \tag{3.25}$$

The adjoint phase mapping matrix takes the form

$$\mathbf{Q}^T = \begin{pmatrix} \mathbf{Q}_1^T & \mathbf{0} & \cdots & \mathbf{0} \\ \mathbf{0} & \ddots & & \vdots \\ \vdots & & \ddots & \mathbf{0} \\ \mathbf{0} & \cdots & \mathbf{0} & \mathbf{Q}_{N_b}^T \end{pmatrix}, \tag{3.26}$$

with

$$\mathbf{Q}_b^T = \begin{pmatrix} \mathbf{Q}_{b,u}^T \\ \mathbf{Q}_{b,u}^T \end{pmatrix}. \tag{3.27}$$

The adjoint projection matrix is

$$\mathbf{P}^T = \begin{pmatrix} \mathbf{P}_1^T & \cdots & \mathbf{P}_{N_b}^T \end{pmatrix}, \tag{3.28}$$

with

$$\mathbf{P}_b^T = \begin{pmatrix} c_{b,ux}\mathbf{W}_b^T & c_{b,vx}\mathbf{W}_b^T \\ c_{b,uy}\mathbf{W}_b^T & c_{b,vy}\mathbf{W}_b^T \\ c_{b,uz}\mathbf{W}_b^T & c_{b,vz}\mathbf{W}_b^T \end{pmatrix}. \tag{3.29}$$

In analogy to $\mathbf{P}_b$, matrix-vector multiplications with $\mathbf{P}_b^T$ can be efficiently executed by using sparse matrix techniques.

3.2. Phase mapping strategies

Whereas the sparse projection matrix $\mathbf{P}$ can be implemented efficiently by using sparse matrix multiplications (*cf.* Section 3.1.3), the phase mapping matrix $\mathbf{Q}$ poses additional challenges because of its high density. As discussed in Section 3.1.5, the complete forward model can be split into N_b independent sub-problems. It therefore makes sense to address the phase mapping matrix $\mathbf{Q}_b$ for each sub-problem separately.

In general, $\mathbf{Q}_b$ can be interpreted as an operator, *i.e.*, a mathematical relation that maps a vectorised projected magnetisation distribution $\boldsymbol{x}_{\mathrm{pr},b}$ onto a vectorised phase image $\boldsymbol{y}_b$. What is crucial for the efficiency of the algorithm is the concrete implementation of this operator. A trivial approach would be to set up the complete matrix $\mathbf{Q}_b \in \mathbb{R}^{N_u N_v \times 2 N_u N_v}$ and to evaluate the matrix-vector calculation $\mathbf{Q}_b \boldsymbol{x}_{\mathrm{pr},b}$. However, as $\mathbf{Q}_b$ scales as $\mathcal{O}\left(2N^4\right)$, this strategy is extremely memory-inefficient. Even for a relatively small number of pixels along each axis, *e.g.*, $N = 128$, $4\,\mathrm{GB}$ would be needed if $\mathbf{Q}_b$ is saved as a standard 64 bit floating point array. In the worst case, if each phase image requires a different matrix $\mathbf{Q}_b$, the overall memory consumption further increases by a factor of N_b.

The goal of this section is the derivation of a more efficient operator implementation of $\mathbf{Q}_b$. The convolutions that are involved in calculating the phase are best understood and executed on two-dimensional arrays instead of their vectorisations. Therefore, it makes sense to implicitly assume the reshaping of the projected magnetisation $\boldsymbol{x}_{\mathrm{pr},b} \rightarrow \boldsymbol{m}_{s,b}\left[p,q\right]$ as the first mathematical step of the operator $\mathbf{Q}_b$. Independent of how the convolutions are executed, the result will then always be a two-dimensional phase image $\varphi_{\mathrm{mag},b}\left[p,q\right]$. Analogously, the last mathematical step of the operator $\mathbf{Q}_b$ has to be a re-vectorisation $\varphi_{\mathrm{mag},b}\left[p,q\right] \rightarrow \boldsymbol{y}_b$. After all of the phase images $\boldsymbol{y}_b$ have been calculated separately, they can be concatenated to create a complete measurement vector $\boldsymbol{y}$ (*cf.* Eq. 3.9). In summary, the order of mathematical operations is:

$$\boldsymbol{x}_{\mathrm{pr},b} \overset{\text{reshaping}}{\rightarrow} \boldsymbol{m}_{\mathrm{s},b}\left[p,q\right] \overset{\text{phase mapping}}{\rightarrow} \varphi_{\mathrm{mag},b}\left[p,q\right] \overset{\text{vectorisation}}{\rightarrow} \boldsymbol{y}_b. \tag{3.30}$$

The starting point for an efficient phase mapping operator is always the formula for the magnetic phase shift (*cf.* Eq. 2.34)

$$\varphi_{\mathrm{mag}}(x,y) = \frac{-B_{\mathrm{sat}}}{2\Phi_0} \iint \frac{\left(y-y'\right)m_{\mathrm{pr},x}(x',y') - \left(x-x'\right)m_{\mathrm{pr},y}(x',y')}{\left(x-x'\right)^2 + \left(y-y'\right)^2} dx'dy'. \tag{3.31}$$

For an arbitrary magnetisation distribution, discretised numerical approaches have to be used to calculate the phase. The choice of discretisation strategy for the calculation of the phase is very important, as it determines factors such as computational speed and accuracy and therefore the overall efficiency of the forward model. The space in which discretisation takes place is particularly important. Both a real space discretisation (RD) strategy (based on Eq. 2.34) and a Fourier space discretisation (FD) strategy (based on Eq. 2.35) are discussed in this section. The computationally most expensive parts of this calculation are the convolutions themselves. They can also be performed either in real space (RC) or in Fourier space (FC). Fourier space convolution is significantly faster than real space convolution. The advantages and disadvantages of each strategy are discussed, before introducing a novel approach that combines the benefits of both approaches[9].

---

[9]For the sake of simplicity, the image indices b of the phase images $\varphi_{\mathrm{mag},b}\left[p,q\right]$ and the projected magnetisation distributions $\boldsymbol{m}_{\mathrm{s},b}\left[p,q\right]$ are dropped in the following discussions.

3.2.1. Existing real space approach (RDRC)

The most simple approach to calculate a phase image from an arbitrary projected magnetisation distribution is to directly solve Eq. 2.34 in real space by applying the trapezium rule to discretise the convolution integral. The direct implementation of Eqs. 3.3 and 3.4 results in the following formula for the discretised magnetic contribution to the phase shift at a given pixel with indices (p, q):

$$\varphi_{\text{mag}}[p, q] = \frac{-B_{\text{sat}}}{2\Phi_0} \sum_{p'q'} \left(\frac{(v[q] - v[q']) \, m_{\text{pr},u}[p', q']}{(u[p] - u[p'])^2 + (v[q] - v[q'])^2} \right.$$
$$\left. - \frac{(u[p] - u[p']) \, m_{\text{pr},v}[p', q']}{(u[p] - u[p'])^2 + (v[q] - v[q'])^2} \right) \cdot a^2 \tag{3.32}$$

$$= -\frac{B_{\text{sat}} a^2}{2\Phi_0} \sum_{p'q'} \frac{(q - q') \, m_{\text{s},u}[p', q'] - (p - p') \, m_{\text{s},v}[p', q']}{(p - p')^2 + (q - q')^2}. \tag{3.33}$$

For a complete phase image, Eq. 3.33 has to be evaluated separately for every pixel (p, q), which corresponds to $N_u \times N_v$ integral calculations. It should be noted that Eq. 3.33 differentiates between pixels in the phase image that are denoted by unprimed indices (p, q) and pixels in the projected magnetisation distribution that are denoted by primed indices (p', q'). The sum iterates over the latter indices and effectively collects the phase contributions of all $N_u \times N_v$ magnetised pixels at (p', q') to the current pixel (p, q) in the phase image.

Therefore, a simple numerical algorithm scales as $\mathcal{O}(N^4)$, which can become very time-consuming for larger grids. Keimpema et al. have shown that, despite the computational effort, this numerical approach results in excellent agreement with analytical results for known object geometries [109]. Furthermore, it avoids artefacts, which are introduced by discretising in Fourier space according to Eq. 2.35. These artefacts are explained in Section 3.2.3. As a result of the fact that both the discretisation and the convolution are performed in real space, this simple numerical algorithm is referred to as RDRC.

3.2.2. Existing Fourier space approach (FDFC)

An alternative numerical approach for calculating the magnetic contribution to the phase shift uses discretisation in Fourier space. The starting point for this approach is Eq. 2.35, in which discretisation takes the form

$$\tilde{\varphi}_{\text{mag}}[p, q] = \frac{\imath \pi B_0}{\Phi_0} \frac{\tilde{m}_{\text{pr},u}[p, q] \cdot k_v[q] - \tilde{m}_{\text{pr},v}[p, q] \cdot k_u[p]}{k_u^2[p] + k_v^2[q]} \tag{3.34}$$

$$= \frac{\imath B_0 a^2}{2\Phi_0} \frac{\tilde{m}_{\text{s},u}[p, q] \cdot \hat{f}_v[q] - \tilde{m}_{\text{s},v}[p, q] \cdot \hat{f}_u[p]}{\hat{f}_u^2[p] + \hat{f}_v^2[q]}. \tag{3.35}$$

Because the magnetisation distribution is a real-valued quantity, the Fourier transformed components $\tilde{m}_{\mathrm{s},u}[p,q]$ and $\tilde{m}_{\mathrm{s},u}[p,q]$ can be calculated using a real-valued fast Fourier transform (RFFT). As a result, half of the computational cost can be saved when compared to using a complex fast Fourier transformation (FFT). The discrete frequencies that are used in the convolution kernels in Fourier space have to reflect this choice. The frequencies are given by the expressions

$$k_u[p] = 2\pi f_u[p] = 2\pi f_a \hat{f}_u[p] = \frac{2\pi}{a} \cdot \hat{f}_u[p] \tag{3.36}$$

$$k_v[q] = 2\pi f_v[q] = 2\pi f_a \hat{f}_v[q] = \frac{2\pi}{a} \cdot \hat{f}_v[q] \tag{3.37}$$

$$\hat{f}_u[p] = \begin{cases} \left[0,1,...,\ \frac{N_u}{2}\ -1,\ \frac{N_u}{2}\ \right]/N_u, & N_u \text{ even} \\ \left[0,1,...,\frac{N_u-1}{2}-1,\frac{N_u-1}{2}\right]/N_u, & N_u \text{ odd} \end{cases} \tag{3.38}$$

$$\hat{f}_v[p] = \begin{cases} \left[0,1,...,\frac{N_v}{2}-1,\ -\frac{N_v}{2}\ ,...,-1\right]/N_v, & N_v \text{ even} \\ \left[0,1,...,\frac{N_v-1}{2}\ ,-\frac{N_v-1}{2},...,-1\right]/N_v, & N_v \text{ odd.} \end{cases} \tag{3.39}$$

In Eqs. 3.36–3.39, $\hat{f}_u$ and $\hat{f}_v$ are normalised frequencies with respect to the sampling frequency f_a, which is defined as the inverse of the grid spacing a. Eqs. 3.35–3.39 provide a numerical approach for calculating the magnetic phase shift based on Fourier space discretisation. As a result of the use of a fast Fourier transformation, the calculation scales as $\mathcal{O}\left(N^2 \log N\right)$, which is significantly faster than the RDRC approach. Several software packages for simulating magnetic contributions to phase images from magnetisation distributions (*e.g.*, MALTS [120] and ATHLETICS [121]) implement this numerical scheme. As the kernels are discretised in Fourier space and the convolution is also performed in Fourier space, this approach is referred to as FDFC.

3.2.3. Artefacts introduced by discrete Fourier transformations

Despite the significantly faster computational time, the FDFC approach has several shortcomings. The zero frequency contribution is undefined as a result of the divergence of the convolution kernel $\boldsymbol{k}/|\boldsymbol{k}|^2$ at $\boldsymbol{k} = 0$ (*i.e.*, for the indices $p = q = 0$). The average phase within the field of view (FOV) is therefore not known and is implicitly set to zero. This missing information can lead to phase offset errors, which are in general not difficult to deal with (see *e.g.* Section 5.4.1).

A more serious limitation results from the presence of wrap-around artefacts, which are introduced by Fourier space discretisation (FD) of the kernel. The discretisation of a continuous function, in its simplest form, is performed by multiplication with a Dirac comb, which represents perfect sampling and is illustrated in Fig. 3.3. A Dirac comb, which is also known as an "impulse train", is a periodic distribution of Dirac delta functions. It is a fixed point of the Fourier transformation, *i.e.*, a transform of a Dirac comb is also a Dirac comb, although the spacing between the delta functions

Figure space

Real space

IFFT

FFT

k

k_a

x

$1/k_a$

$\tilde{f}(k) \ * \ \sum_{n\in\mathbb{Z}} \delta(k - nk_a)$

$f(x) \ \cdot \ \dfrac{1}{k_a}\sum_{n\in\mathbb{Z}} \delta\left(x - \dfrac{n}{k_a}\right)$
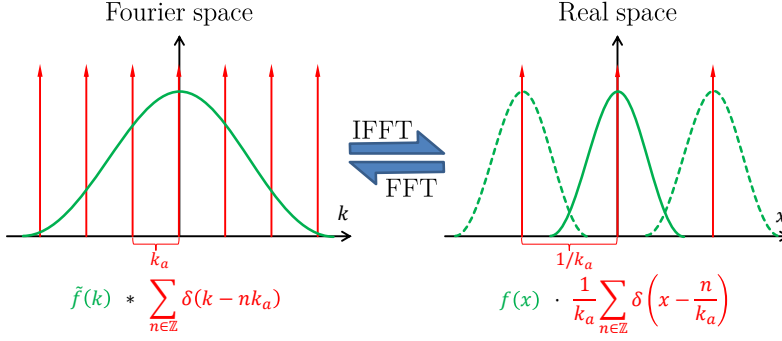
Figure 3.3.: Schematic diagram illustrating the fact that perfect sampling of a function $\tilde{f}(k)$ (marked in green) in Fourier space can be expressed as a multiplication with a Dirac comb (marked in red), *i.e.*, a distribution of Dirac delta functions with periodicity k_a. In real space, this multiplication corresponds to a convolution of the inverse Fourier transformed function $f(x)$ with a Dirac comb that has inverted periodic length $1/k_a$, leading to a periodic repetition of $f(x)$ in real space. If $f(x)$ does not decay to zero fast enough, then an overlap of these periodic distributions (marked by dashed green lines) leads to aliasing artefacts. This illustration does not consider the finite size of an image, which is taken into account separately, in the main text below.

is inverted after transformation. The transformation of a Dirac comb with a small periodic length in one space has a large periodic length in the other space and vice versa. If discretisation is performed in Fourier space, then the real space function is convolved with a Dirac comb, resulting in periodic repetition of the kernel in real space at its edges. The periodic length depends on the sampling interval (denoted k_a in Fig. 3.3) in Fourier space. The real space kernel does not decay to zero at its borders ($\propto \boldsymbol{r}/|\boldsymbol{r}|^3$) and is also not band-limited in Fourier space ($\propto \boldsymbol{k}/|\boldsymbol{k}|^2$). Therefore, discretisation in one space always leads to aliasing in the other space.

In the case of FD, periodic repetition of the kernel occurs in real space and contributions from "phantom" kernels spill into the original kernel. After the convolution with the magnetisation distribution, this situation leads to artefacts, which can be described as periodic "phantom" magnetisation distributions, whose phase contributions spill into the FOV. In the case of RD, corresponding artefacts can occur in Fourier space, whereas the phase in real space is free of aliasing artefacts. RD implicitly sets the magnetisation outside the FOV to zero, which is often much closer to reality, *e.g.*, for samples such as isolated nanoparticles. In contrast, FD assumes periodicity in real space, which leads to the artefacts that are described above.

As a result of the fact that the kernel never decays completely to zero and is not band-limited, the Nyquist–Shannon sampling theorem cannot be satisfied. Therefore, aliasing artefacts cannot be avoided completely. However, their influence can be minimised by zero-padding the magnetisation distribution in real space. Zero-

padding increases the effective FOV by extending it with zeros at the borders until a chosen size is reached. The result of zero-padding is a finer frequency sampling in Fourier space, which equates to a decrease in the periodic length between the delta peaks of the Dirac comb in Fourier space. The convolution kernels must be discretised in Fourier space with the same Dirac comb to enable element-wise multiplication with the transformed magnetisation distribution. The finer frequency sampling results in a larger periodic length in real space, *i.e.*, in an increase in the distance between the "phantom" distributions. Therefore, the kernel decays further before reaching the edge of the FOV, which decreases the phase contributions of overlapping repetitions at the kernel borders. Zero-padding of the magnetisation implicitly assumes zero magnetisation in the padded regions and subsequent periodic repetition due to FD of the convolution kernels. This assumption is a weaker form of the assumption used in the RDRC approach that no magnetisation resides outside the FOV. An increase in zero-padding can decrease wrap-around artefacts, but it does not eliminate them completely. The use of an increased FOV also requires more memory to store the kernels and magnetisation distributions and the element-wise multiplication takes longer.
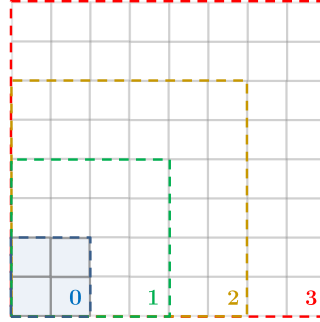
Figure 3.4.: Schematic diagram illustrating the definition of the zero-padding number η. The example shows a FOV of 2×2 pixels, which is marked in blue. If no padding is used, then the FOV stays the same size and the padding number is $\eta = 0$. For a padding number of $\eta = 1$, the axes are extended by the length of the FOV in each direction (4×4 pixels). A number of $\eta = 2$ adds twice the length of the FOV (6×6 pixels) and so on.

In order to quantify the effect of the increase in FOV, a zero-padding number η is introduced. A value of $\eta = 0$ means no padding is applied, a value of $\eta = 1$ means that both axes are extended by the length of the original FOV (quadrupling its area), a value of $\eta = 2$ means that both axes are extended by twice the length of the original FOV, etc. (*cf.* Fig. 3.4 for an illustration).

A discrete approach must also cut off at some point, which is equivalent to multiplication by a windowing box function. Windowing of the kernel by a box function in Fourier space corresponds to convolution by a cardinal sine function (sinc) in

real space and vice versa, with a broader box resulting in a narrower sinc function. Higher frequencies are then cut off, leading to ringing due to the Gibbs phenomenon at sharp boundaries and edges. The highest available frequency is the Nyquist frequency, which is given by half of the sampling frequency $f_a = \frac{1}{a}$, which is in turn determined by the inverse of the grid spacing a in real space. Gibbs ringing can be reduced by choosing a finer grid spacing and thus including higher frequencies in Fourier space. If discretisation takes place in real space instead of Fourier space, then windowing results in frequency-domain ripples that are similar to Gibbs ringing. However, because only the real space phase image is of interest here, the artefacts in Fourier space can be neglected without further consequences.

All of these effects are summarised in Tab. 3.1. In the following section, a new approach for magnetic phase calculation is introduced. The new approach makes use of discretisation in real space and circumvents the artefacts that are linked to Fourier space discretisation, while maintaining high computational speed.

Table 3.1.: Overview of artefacts resulting from discretisation and windowing in real space and in Fourier space.

Operation	Resulting operation and artefacts in target space
Windowing with a box-function in real space	Convolution with a sinc function in Fourier space: frequency-domain ripple
Windowing with a box-function in Fourier space	Convolution with a sinc function in real space: Gibbs phenomenon / ringing in real space
Discretisation in real space	Convolution with a Dirac comb in Fourier space: aliasing in the frequency domain
Discretisation in Fourier space	Convolution with a Dirac comb in real space: periodic repetition in real space

3.2.4. Introduction of a novel and optimised approach (RDFC)

Despite the accuracy of the RDRC approach described by Eq. 3.33, the scaling as $\mathcal{O}\left(N^4\right)$ makes its practical use unfeasible for larger grids. In contrast, the FDFC approach suffers from a range of artefacts as a result of discretisation in Fourier space. In this section, a novel approach that combines the benefits of both approaches is introduced. The approach is termed RDFC, as it combines the accuracy of real space discretisation (RD) with the fast computational speed and scaling as $\mathcal{O}\left(N^2 \log\left(N\right)\right)$ of Fourier space convolution (FC). The starting point is real space discretisation. However, it is approached from a different perspective than for the RDRC approach, thereby allowing for several optimisations, which are used to speed up the calculation without loss of accuracy.

In Eq. 3.33, the collective magnetic phase shift for each pixel (p, q) in a phase image $\varphi_{\text{mag}}[p, q]$ is calculated sequentially by integrating the contributions of all magnetised pixels (p', q') in the FOV to each pixel (p, q). Instead, the order can be reversed. First, the phase contribution of each magnetised pixel (p', q') to the whole FOV can be calculated. These contributions are denoted $\varphi_{p'q'}[p, q]$ and are added up to form the collective magnetic phase shift $\varphi_{\text{mag}}[p, q]$. The magnetic phase shift can then be expressed as a sum over the contributions of all magnetised pixels in the form

$$
\begin{aligned}
\varphi_{\text{mag}}[p, q] &= \sum_{p'q'} \varphi_{p'q'}[p, q] \\
&= \sum_{p'q'} \varphi_u[p - p', q - q'] \cdot m_{\text{s},u}[p', q'] \\
&\quad + \sum_{p'q'} \varphi_v[p - p', q - q'] \cdot m_{\text{s},v}[p', q'] \\
&= (m_{\text{s},u} * \varphi_u)[p, q] + (m_{\text{s},v} * \varphi_v)[p, q],
\end{aligned}
$$

(3.40)

(3.41)

(3.42)

where φ_{mag}, $\varphi_{p'q'}$ and $\varphi_{u/v}$ are all arrays of size $N_u \times N_v$. The contribution to the phase of a specific magnetised pixel at position (p', q') can be expressed as the linear combination

$$
\varphi_{p'q'}[p, q] = \varphi_u[p - p', q - q'] \cdot m_{\text{s},u}[p', q'] + \varphi_v[p - p', q - q'] \cdot m_{\text{s},v}[p', q'].
$$

(3.43)

The phase contribution components $\varphi_u[p, q]$ and $\varphi_v[p, q]$ can be identified from Eq. 3.33 as the convolution kernels and can be interpreted as the phase shifts of single magnetic dipoles that are normalised relative to M_{sat} and oriented perpendicular to each other. With $C_{\text{mag}} = -\frac{B_{\text{sat}} a^2}{2\phi_0}$, the kernels $\varphi_{u/v}[p, q]$ can be expressed in the form

$$
\varphi_u[p, q] \equiv C_{\text{mag}} \frac{q}{p^2 + q^2}, \qquad \varphi_v[p, q] \equiv C_{\text{mag}} \frac{-p}{p^2 + q^2}.
$$

(3.44)

In order to avoid the problem that the kernels are not well defined at $p = q = 0$, they are interpreted here as two orientations of homogeneously magnetised discs, for which the analytical solution was presented in Section 2.2. The discretised expression for Eq. 2.20 is given by:

$$
\varphi_{\circ}[p, q, \beta] = \begin{cases} -\pi t \frac{B_{\text{sat}}}{2\Phi_0} a \left(q \cos(\beta) - p \sin(\beta)\right), & p^2 + q^2 \leq R \\ -\pi t \frac{B_{\text{sat}}}{2\Phi_0} \frac{R^2}{a} \frac{(q \cos(\beta) - p \sin(\beta))}{p^2 + q^2}, & p^2 + q^2 > R. \end{cases}
$$

(3.45)

The thickness t of the disc is set to the size of a single pixel ($t = a$). Each pixel on the two-dimensional grid is represented by such a disc with a base area of πR^2 and the radius R of the disc is chosen so that the area A_{px} and thus the magnetisation is preserved:

$$
A_{\text{px}} \equiv a^2 \stackrel{!}{=} \pi R^2 \quad \Leftrightarrow \quad R = \frac{a}{\sqrt{\pi}} < a.
$$

(3.46)

The centres of neighbouring pixels are separated by a distance of at least $a > R$. The condition $p^2 + q^2 \leq R$ of the first part of Eq. 3.45 is therefore only fulfilled for the centre of the homogeneously magnetised disc at $p = q = 0$, for which the phase is zero. The second part of Eq. 3.45 then describes the contribution of the pixel at position (p, q) to every other pixel (p', q') except to itself, leading to the expression

$$\varphi_\circ [p, q, \beta] = \begin{cases} 0, & p = q = 0 \\ C_{\mathrm{mag}} \frac{(q\cos(\beta) - p\sin(\beta))}{p^2 + q^2} & \text{else.} \end{cases} \tag{3.47}$$

For orientations of the homogeneously magnetised discs along the u or v axes and for all pixels except $p = q = 0$ where the phase is zero, Eq. 3.44 is recovered, including the resolved discontinuity:

$$\varphi_u [p, q] \equiv \varphi_\circ [p, q, \beta = 0] \quad = C_{\mathrm{mag}} \frac{q}{p^2 + q^2} \tag{3.48}$$

$$\varphi_v [p, q] \equiv \varphi_\circ [p, q, \beta = \pi/2] = C_{\mathrm{mag}} \frac{-p}{p^2 + q^2}. \tag{3.49}$$

$$\varphi_{p'q'}[p, q] = m_{\mathrm{s},u}[p', q'] \cdot \varphi_u[p - p', q - q'] + m_{\mathrm{s},v}[p', q'] \cdot \varphi_v[p - p', q - q']$$
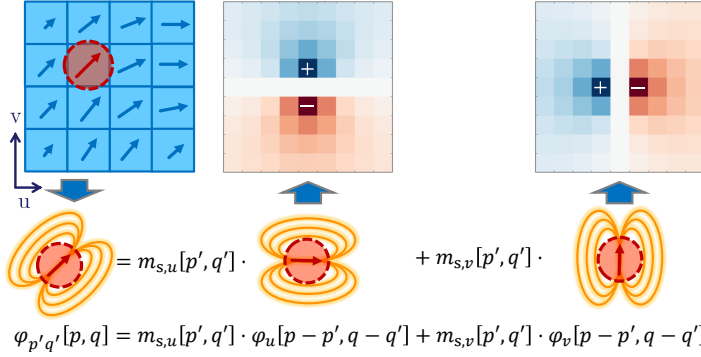
Figure 3.5.: Schematic diagram illustrating the magnetic phase contribution of each magnetised pixel in the RDFC approach. The contribution of each pixel can be expressed as a linear combination of two convolution kernels (oriented in the u and v directions), with the projected relative magnetisation distribution components as coefficients.

The representation of a single magnetised pixel by a disc is further illustrated in Fig. 3.5. Both convolution kernels can be pre-computed in advance and stored in look-up arrays. The magnetisation components $m_{\mathrm{s},u}$ and $m_{\mathrm{s},v}$ are arrays of size $N_u \times N_v$. The lookup arrays of the convolution kernels must therefore have sizes $(2N_u - 1) \times (2N_v - 1)$, so that the appropriate sub-arrays for each position of a magnetised pixel can be used. These sub-arrays are illustrated in Fig. 3.6.

Pre-calculation of the look-up arrays and iterating over the contributing magnetised pixels instead of the affected pixels in the phase image saves calculation time and
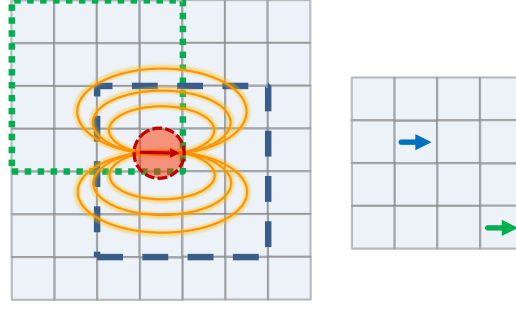
Figure 3.6.: Schematic diagram illustrating the approach used to determine the u component of φ_{mag} from a look-up array (left side). The look-up array must have size $(2N_u - 1) \times (2N_v - 1)$. Different "cut-out" sub-arrays are used, depending on the position of the magnetised pixel, as shown for two pixels at different positions. The sub-arrays are chosen so that the centre of the convolution kernel coincides with the position of the current magnetised pixel.

memory space. However, it does not change the overall scaling as $\mathcal{O}\left(N^4\right)$. Performing the convolutions in Eq. 3.42 in Fourier space (FC), where they take the form of simple multiplications, reduces the computational complexity to $\mathcal{O}\left(N^2 \log\left(N\right)\right)$. In order to perform these element-wise multiplications, the magnetisation components and the convolution kernels must have the same size. This criterion can be satisfied by applying zero-padding at their borders until their sizes match. As illustrated in Fig. 3.7, all of the involved arrays are padded to a size of $2N_u \times 2N_v$ pixels[10].

In the new approach, both the magnetisation distributions $m_{\mathrm{s},u}[p,q]$ and $m_{\mathrm{s},v}[p,q]$ and the convolution kernels $\varphi_{u/v}[p,q]$ are discretised in real space, instead of just the magnetisation distribution, as in the FDFC approach. The use of real space discretisation avoids the artefacts that are associated with discretisation in Fourier space, as discussed in Section 3.2.2. Zero-padding is applied in both approaches. However, in the FDFC approach it is used to diminish the Fourier-space-related artefacts, without eliminating them completely. In the new approach, it is just used to enable element-wise multiplication by equalizing the array sizes. Therefore, in contrast to the FDFC approach, an upper zero-padding boundary of $2N_u \times 2N_v$ exists, for which the solution is free of the aforementioned artefacts.

In summary, the calculation of a magnetic phase image using the novel approach can be described in terms of a linear combination of two Fourier space convolutions, where the tilde represents Fourier transformed quantities:

$$\varphi_{\mathrm{mag}}[p,q] = \mathcal{F}_2^{-1}\left\{\tilde{m}_{\mathrm{s},u} \cdot \tilde{\varphi}_u\right\}[p,q] + \mathcal{F}_2^{-1}\left\{\tilde{m}_{\mathrm{s},v} \cdot \tilde{\varphi}_v\right\}[p,q]. \tag{3.50}$$

---

[10]FFT algorithms usually operate best on arrays with dimensions that are powers of two. If N_u and N_v were already chosen accordingly, then $2N_u$ and $2N_v$ automatically satisfy this criterion. Otherwise, additional zero-padding to the next power of two may be necessary.

Kernel   FOV
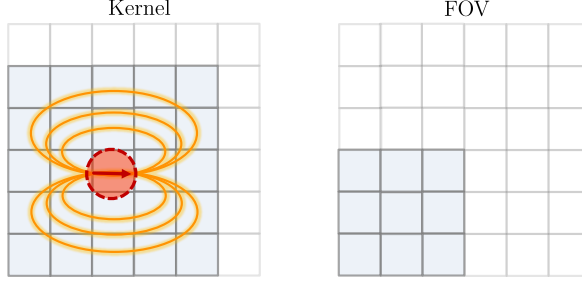
Figure 3.7.: Schematic diagram illustrating the zero-padding procedure used for the RDFC approach. The example shows a FOV of $N_u \times N_v = 3 \times 3$ pixels, marked in blue on the right. The convolution kernel of the u component is shown on the left, has size $2N_u - 1 \times 2N_v - 1 = 5 \times 5$ pixels and is also marked in blue. Both arrays must be zero-padded so that they have the same size $2N_u \times 2N_v = 6 \times 6$ pixels, in order to allow element-wise array-multiplications. The even axis length is chosen for faster FFT calculations. Zero-padding is indicated by white pixels. For the kernel, this procedure is very computationally efficient as only one pixel has to be added to each axis.

The vectorised form of the two terms in Eq. 3.50 corresponds to the two matrix-vector products $\mathbf{Q}_{b,u}\boldsymbol{x}_{\mathrm{pr},b,u}$ and $\mathbf{Q}_{b,v}\boldsymbol{x}_{\mathrm{pr},b,v}$ in Eq. 3.17. Each column of $\mathbf{Q}_{b,u}$ and $\mathbf{Q}_{b,v}$ consists of a vectorised sub-array of the convolution kernel φ_u or φ_v, as described in Fig. 3.6. From left to right, the columns correspond to the entries of $\boldsymbol{x}_{\mathrm{pr},b,u}$ and $\boldsymbol{x}_{\mathrm{pr},b,v}$, respectively. The entire procedure is illustrated[11] in Fig. 3.8.

As the convolution kernel does not decay completely to zero, the matrices $\mathbf{Q}_{b,u} \in \mathbb{R}^{N_u N_v \times N_u N_v}$ and $\mathbf{Q}_{b,v} \in \mathbb{R}^{N_u N_v \times N_u N_v}$ and therefore $\mathbf{Q}_b$ are very dense. The high density of $\mathbf{Q}_b$ prohibits the use of sparse matrix operations, while its large size makes it unfeasible for it to be set up and stored in memory efficiently. However, during the reconstruction process, only the product of $\mathbf{Q}_b$ with a vector and never the full matrix itself is required. Despite its high density, the information in $\mathbf{Q}_b$ in fact has a high level of redundancy. The RDFC approach exploits this fact by only keeping the significantly smaller convolution kernels φ_u and φ_v, or rather their Fourier transforms, in memory. The convolutions are carried out in Fourier space by using a sophisticated FFT implementation[12] (*cf.* Fig. 3.9 for an illustration). The workflow that describes the action of $\mathbf{Q}_b$ as an operator on the input vector $\boldsymbol{x}_{\mathrm{pr},b}$ can be broken down into the following steps:

---

[11]The pixel-by-pixel description of the RDRC algorithm (*cf.* Section 3.2.1) can also be illustrated using Fig. 3.8. For a chosen pixel (p,q), Eq. 3.33 corresponds to one row of $\mathbf{Q}_b$. Each row is calculated on demand, without ever setting up the full matrix $\mathbf{Q}_b$ completely.

[12]*e.g.*, the FFTW library ("The Fastest Fourier Transform of the West" [122]), which was used in this thesis.
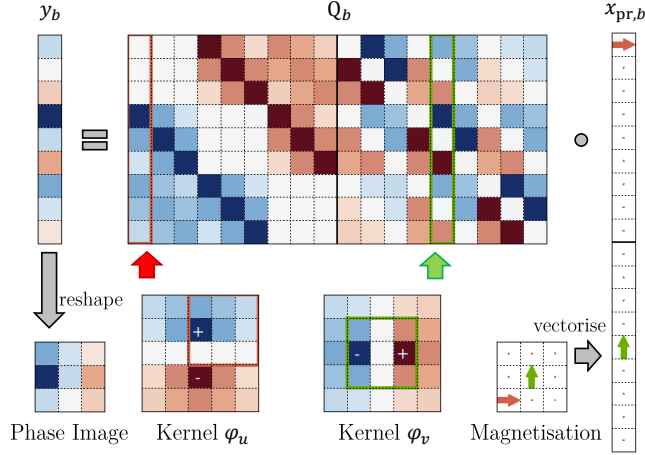
Figure 3.8.: Schematic diagram illustrating the magnetic phase mapping process for a 3×3 pixel magnetisation distribution by full matrix multiplication with $\mathbf{Q}_b$. Equation 3.17 is represented at the top. The matrix $\mathbf{Q}_b$ and the vector $\boldsymbol{x}_{\mathrm{pr},b}$ are both split into their u and v parts, as indicated by bold black lines. The sub-matrices $\mathbf{Q}_{b,u}$ and $\mathbf{Q}_{b,v}$ represent the convolution with the kernels φ_u and φ_v, respectively. $\boldsymbol{x}_{\mathrm{pr},b}$ is the vectorised form (*cf.* Eq. 3.6) of the projected magnetisation distribution (bottom right). In this case, it has one pixel magnetised in the u direction (red) and one in the v direction (green). Two columns of $\mathbf{Q}_{b,u}$ are coloured. They show the relevant sub-arrays of the convolution kernels, which are used for the two magnetised pixels. The resulting vector $\boldsymbol{y}_b$ can be reshaped to the resulting magnetic phase image (bottom left).

1. The input vector $\boldsymbol{x}_{\mathrm{pr},b}$ is separated into its components $\boldsymbol{x}_{\mathrm{pr},b,u}$ and $\boldsymbol{x}_{\mathrm{pr},b,u}$.

2. Both components are reshaped into two-dimensional arrays $m_{\mathrm{s},b,u}$ and $m_{\mathrm{s},b,u}$ of size $N_u \times N_v$ and zero-padded to size $2N_u \times 2N_v$.

3. $m_{\mathrm{s},b,u}$ and $m_{\mathrm{s},b,u}$ are Fourier transformed using an RFFT algorithm[13].

4. They are multiplied by the pre-computed Fourier transforms of the convolution kernels φ_u and φ_v.

5. The results of the two products are transformed back into real space.

6. The zero-padding is inverted by cutting out[14] a sub-array of size $N_u \times N_v$.

7. Both results are added together to calculate a phase image $\varphi_{\mathrm{mag},b}$.

8. The phase image $\varphi_{\mathrm{mag},b}$ is vectorised to obtain the measurement vector $\boldsymbol{y}_b$.

For the reconstruction process, the adjoint operator $\mathbf{Q}_b^T$, as defined in Eq. 3.27, is needed in addition to $\mathbf{Q}_b$. The discrete Fourier transformation employed in $\mathbf{Q}_b$ is a unitary linear operator, $i.e.$, its adjoint is equal to its inverse. Just as for $\mathbf{Q}_b$, the description of $\mathbf{Q}_b^T$ as an operator improves the performance of the calculation significantly, in comparison to setting up the full matrix. The workflow of $\mathbf{Q}_b^T$ can be broken down into the following steps ($cf.$ Fig. 3.10 for an illustration of the process):

1. The input vector for adjoint phase mapping is reshaped into an array of size $N_u \times N_v$ and zero-padded to size $2N_u \times 2N_v$.

2. This array is Fourier transformed and multiplied by the complex conjugates of the Fourier transforms of the convolution kernels φ_u and φ_v.

3. The resulting arrays are then transformed back into real space and sub-arrays of shape $N_u \times N_v$ are extracted.

4. These arrays are combined to obtain the u and v components of a two-dimensional vector field, which is vectorised in the last step.

---

[13]The RFFT algorithm can be used because $m_{\mathrm{s},b,u}$ and $m_{\mathrm{s},b,u}$ only contain real values, which results in an improvement in speed of a factor of two.

[14]Due to the kernel centre being at pixel $[N_u - 1, N_v - 1]$ instead of at the origin, the cut-out region has to be shifted to $[N_u - 1 : 2N_u - 1, N_u - 1 : 2N_v - 1]$.
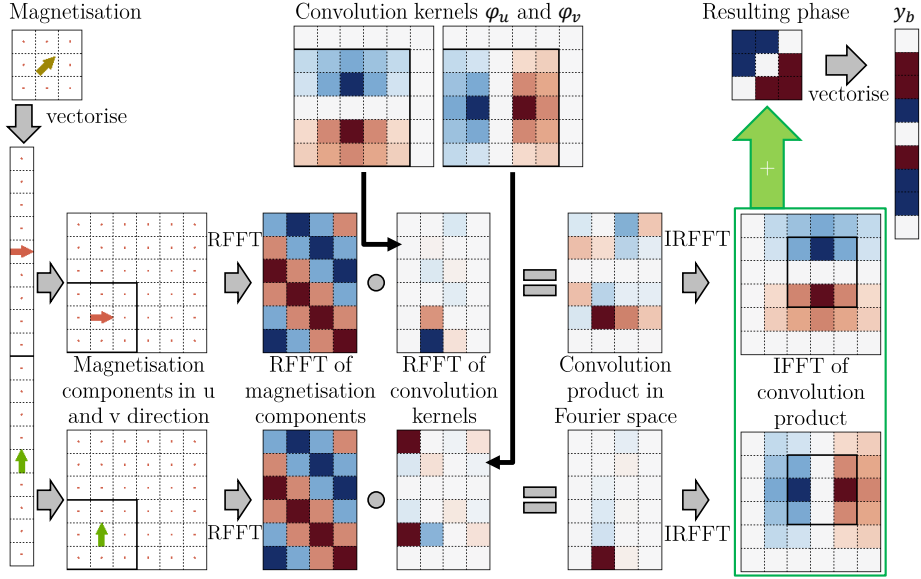
Figure 3.9.: Schematic diagram illustrating the magnetic phase mapping process for a 3×3 pixel magnetisation distribution using Fourier space convolution. Only the real parts of imaginary numbers are shown, where applicable. The left side shows the input vector $\boldsymbol{x}_{\mathrm{pr},b}$ for a single image, which is split into its two components $\boldsymbol{x}_{\mathrm{pr},b,u}$ and $\boldsymbol{x}_{\mathrm{pr},b,v}$. These components are reshaped into two-dimensional arrays, then zero-padded (bold outline) and Fourier transformed by an RFFT. They are then multiplied by Fourier transforms of the pre-computed convolution kernels. Both products are converted back to real space by an IRFFT, in order to recover the complete phase contribution of each magnetisation component. Appropriate sub-arrays of size $N_u \times N_v$ are extracted to reverse the zero-padding. The sub-arrays are added to calculate the magnetic phase image, which is then vectorised into the measurement vector $\boldsymbol{y}_b$ (shown on the right).
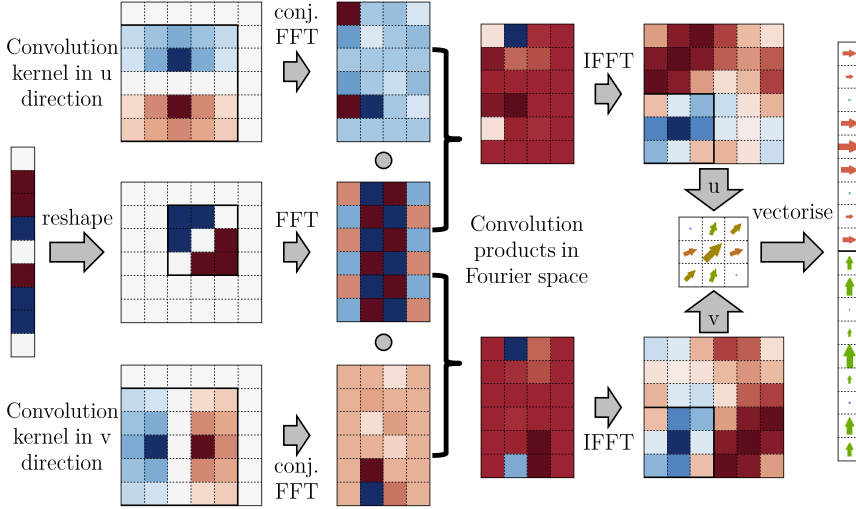
Figure 3.10.: Schematic diagram illustrating the adjoint magnetic phase mapping process using Fourier space convolution. The phase input shown is the result from Fig. 3.9. Again, only the real parts of imaginary numbers are shown, where applicable. The input vector on the left is reshaped into an array of size $N_u \times N_v$. This array and the two convolution kernels are zero-padded. Tracing back the steps of the procedure described in Fig. 3.9, the input array is placed into a zero array of size $2N_u \times 2N_v$ at position $[N_u - 1 : 2N_u - 1, N_u - 1 : 2N_v - 1]$. The input array is Fourier transformed and multiplied by the complex conjugates of the Fourier transforms of the convolution kernels φ_u and φ_v. Both convolution products are then transformed back into real space. Before proceeding, sub-arrays $[0 : N_u, 0 : N_v]$ are extracted (shown using bold outlines), in order to reverse the zero-padding. These two sub-arrays are combined as the u and v components of a two-dimensional vector field, which is vectorised in a final step (shown on the right).

## 3.3. Comparison of the RDFC and FDFC approaches

In this section, the RDFC and FDFC approaches for magnetic phase image calculation are evaluated with regard to computational speed and accuracy by comparing their results with known solutions for simple geometrical objects[15]. The RDRC approach is not addressed here, because it was already compared with the FDFC approach by Keimpema et al. [109]. Furthermore, the FDFC approach is currently more prevalent due to its significantly faster scaling. For a comparison of the two algorithms, two different test magnetisation distributions for which analytical solutions are available are considered:

- A homogeneously magnetised disc in the xy plane with its magnetisation directed along the positive y axis, corresponding to an angle of $\pi/2$ from the x axis (*cf.* Eq. 2.20).

- A disc magnetised in a counter-clockwise vortex state, with the centre of the vortex corresponding to the centre of the disc (*cf.* Eq. 2.28).

Each disc has a radius of $32\,\text{nm}$, a thickness of $8\,\text{nm}$ and is placed in a volume of size $128 \times 128 \times 16\,\text{nm}^3$, with the z axis being the symmetry axis. The resulting grid spacing is $a = 1\,\text{nm}$ and the saturation magnetic induction is $B_{\text{sat}} = 1\,\text{T}$. Slices through the xy plane at $z = 0$ are shown in Fig. 3.11. The z axis is also the projection axis. Therefore, the coordinate axes u and v of the projection coincide with the x and y axes of the three-dimensional distribution.

Figure 3.12 shows the analytical solutions for φ_{mag} for the two test distributions (Figs. 3.12a and 3.12c) and the corresponding holographic contour maps (Figs. 3.12b and 3.12d). The contour maps are generated by taking the cosine of the amplified phase φ_{mag}, in this case by a gain factor of 100. The colours that are superimposed on the magnetic induction maps are determined from the gradient of φ_{mag}. This gradient is an indicator for the direction of the projected in-plane magnetic flux density. The chosen colour scheme, which is used for holographic contour maps and vector plots, is derived in the appendix in Section A.5.

The two test distributions have distinctly different magnetic vector potentials $\boldsymbol{A}$ and magnetic contributions to the phase shift. Whereas the vortex state generates no vector potential outside the disc, $\boldsymbol{A}$ decreases slowly outside the homogeneously magnetised disc without reaching zero at the edge of the FOV. In both distributions, the disc occupies only a quarter of the FOV, so that the phase outside the discs due to the different stray fields can be assessed for both numerical approaches.

---

[15]All of the simulation scripts that are used in these sections were written in the Python programming language (version 3.5) and executed on a Lenovo T430 Thinkpad with 16GB RAM, Intel Core i7-3520M CPU on Windows 64bit OS.
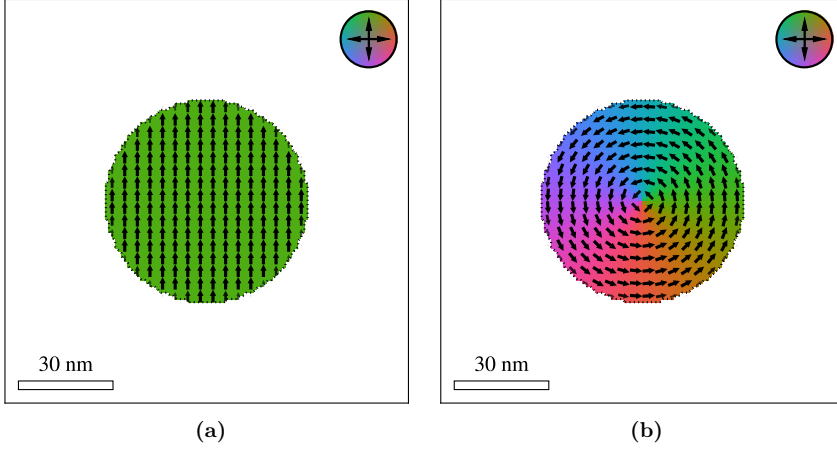
Figure 3.11.: Slice in the xy plane through the centres of the magnetisation distributions of discs that are (**a**) homogeneously magnetised and (**b**) support a magnetic vortex state. For visualisation purposes, each arrow represents an average over an area of $2 \times 2\,\mathrm{nm}^2$. The discs each have a radius of $32\,\mathrm{nm}$, a thickness of $8\,\mathrm{nm}$ and are placed in a volume of size $128 \times 128 \times 16\,\mathrm{nm}^3$. The magnetisation direction is colour-coded according to a colour scheme that is derived in the appendix in Section A.5.

3.3.1. Assessment of the FDFC approach

In order to assess the results of the FDFC approach described by Eq. 3.35, they are compared with "true" analytical solutions, which are shown in Fig. 3.12. For this purpose, a line profile of φ_{mag} through the centre of each disc is extracted for the analytical solution and for numerical solutions calculated for different grid spacings a (*cf.* [71]). The position of the line profile is marked by a red dashed line in the phase images shown in Fig. 3.12. The resulting comparison is shown in Fig. 3.13.

To assess the accuracy of the FDFC approach across the entire FOV, the root mean square (RMS) value $\Delta\varphi_{\mathrm{RMS}}$ of the pixel-wise difference between the numerical results and the analytical solution is evaluated. The resulting difference images and $\Delta\varphi_{\mathrm{RMS}}$ values are shown for both test objects in Fig. 3.14. The FDFC approach assumes periodic repetition of each magnetisation distribution, thereby introducing the artefacts that were discussed in Section 3.2.3. These artefacts influence φ_{mag}, as shown in Figs. 3.13 and 3.14.

For the homogeneously magnetised disc, the magnetic vector potential $\boldsymbol{A}$ and the magnetic contribution to the phase φ_{mag} are not zero at the edges of the FOV. The phase therefore "overlaps" onto the other side of the image, resulting in a sloped difference between the numerical and analytical solutions (*cf.* Figs. 3.13a and 3.14a). Due to the symmetry of the image, the phase at the edges of the FOV becomes zero.
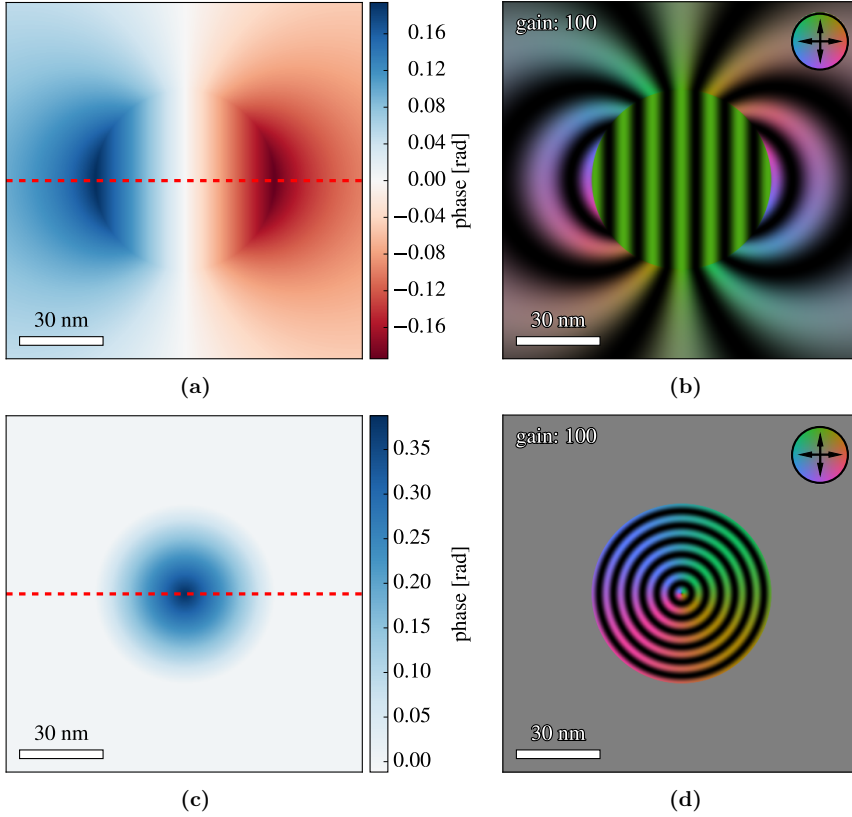
Figure 3.12.: Analytical solutions for φ_{mag} for discs that are (**a**) homogeneously magnetised and (**c**) support a magnetic vortex state. (**b**) and (**d**) show the corresponding magnetic induction maps generated by taking the cosine of the amplified phase φ_{mag} (gain factor: 100). The red dashed lines in (**a**) and (**c**) indicate the positions to extract line profiles of the phase, which are shown in Figs. 3.13 and 3.16. The FOV used for each calculation is 128×128 nm².
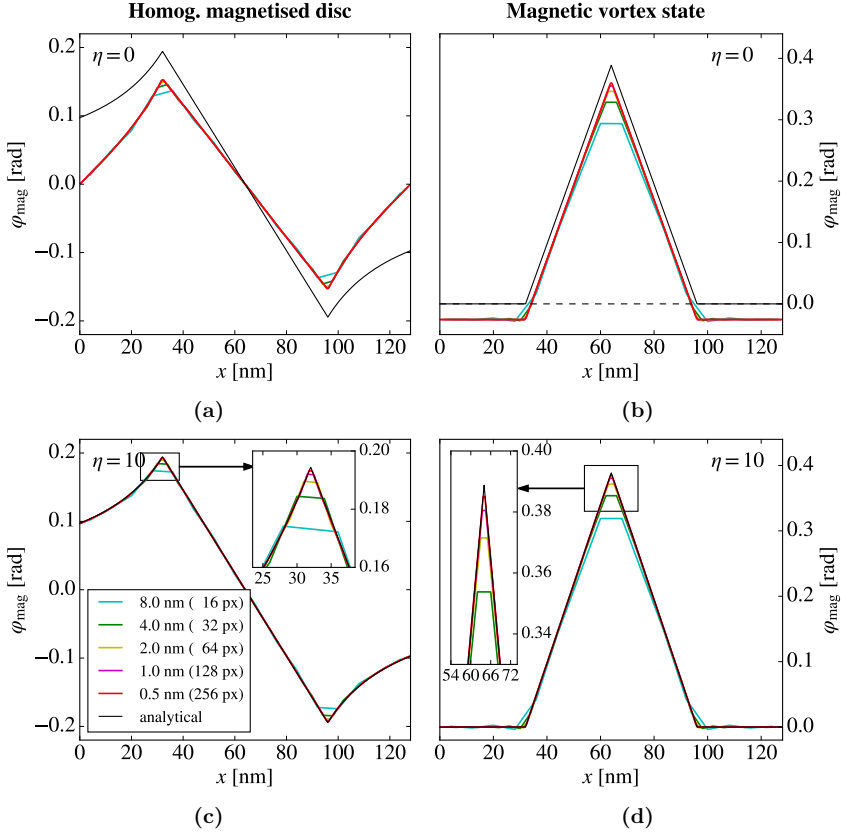
Figure 3.13.: Line profiles of φ_{mag} obtained from Fourier space FDFC calculations performed for discs that are (**a**, **c**) homogeneously magnetised and (**b**, **d**) support a magnetic vortex state for different sampling grid spacings, as well as for the analytical solution for each disc. (**a**) and (**b**) are calculated for an unpadded FOV, while (**c**) and (**d**) are calculated for a zero-padding number of $\eta = 10$. The insets show magnified regions, in order to better illustrate the behaviours of the numerical solutions for different grid spacings a at the borders (**c**) or the centres (**d**) of the discs. The number of pixels along the 128 nm length of the image is stated in parentheses for each grid spacing.

49
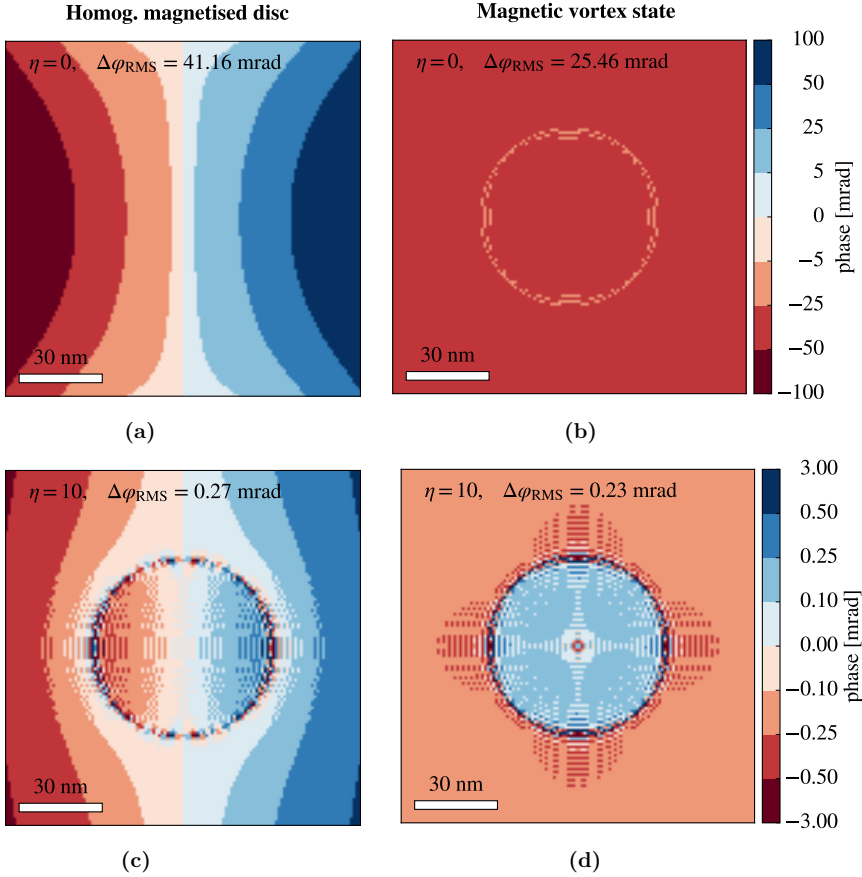
Figure 3.14.: Difference between FDFC and analytical solutions for φ_{mag} for discs that are (**a**, **c**) homogeneously magnetised and (**b**, **d**) support a magnetic vortex state. The grid spacing is $a = 1\,\mathrm{nm}$. (**a**) and (**b**) are calculated for an unpadded FOV, while (**c**) and (**d**) are calculated for a zero-padding number of $\eta = 10$. The colour scale is not linear and is used to emphasise different magnitudes of error. The maximum error is much higher for the unpadded case in (**a**) and (**b**). The annotation at the top of each image gives the RMS difference $\Delta\varphi_{\mathrm{RMS}}$ of the pixel-wise difference between the numerical result and the analytical solution for each calculation.

Zero-padding is commonly used to reduce such artefacts, as discussed in Section 3.2.2 (*cf.* Fig. 3.4 for an illustration). The amount of zero-padding needed depends on the fraction of the FOV that is occupied by the magnetic object and on the decay behaviour of $\boldsymbol{A}$ outside the object, which is often not known beforehand. The extent of zero-padding should be chosen so that $\boldsymbol{A}$ is sufficiently small at the edges of the padded FOV. Figures 3.13c and 3.14c show the influence of a zero-padding number of $\eta = 10$ on the phase calculated using the FDFC approach. The aliasing artefacts are suppressed and the underlying slope vanishes.

For the vortex state, the magnetic vector potential $\boldsymbol{A}$ is zero outside the magnetisation distribution and therefore no phase overlap occurs (*cf.* Fig. 3.13b). As mentioned in Section 3.2.3, the zero frequency coefficient is implicitly set to zero for the FDFC approach. The zero frequency coefficient corresponds to the average value of the calculated phase image, which can be interpreted as a global phase offset. Implicitly pinning this value to zero means that a phase image calculated using the FDFC approach is phase shifted relative to the analytical solution, as it must always have an average value of zero. For the homogeneously magnetised disc, whose phase is symmetric about zero, no artefact is introduced. In contrast, the analytical solution for the magnetic phase of the vortex disc is positive across the entire FOV. This situation results in a negative global offset, which dominates the RMS difference $\Delta\varphi_{\mathrm{RMS}}$, as can be seen in Fig. 3.14b. It should be noted that, in contrast to aliasing artefacts, this global offset can usually be corrected after the phase is calculated. Zero-padding can be used to reduce the influence of this artefact, as can be seen in Fig. 3.14d for a zero-padding number of $\eta = 10$. Padding the magnetisation distribution in real space with empty space brings the average phase asymptotically closer to zero, which is in accordance with the implicit assumption of the FDFC approach, therefore reducing $\Delta\varphi_{\mathrm{RMS}}$. The only remaining artefact is Gibbs ringing at the edges of the disc. The Gibbs ringing is parallel to the grid axes, as a result of the windowing of the convolution kernels in Fourier space (*cf.* Section 3.2.3).

In Fig. 3.15, the RMS difference $\Delta\varphi_{\mathrm{RMS}}$ and the computation time t_{comp} are assessed for both test distributions for a pixel size of $a = 1\,\mathrm{nm}$ and a FOV of 128×128 pixels, as a function of the padding number η. Figure 3.15b shows that zero-padding drastically increases the computation time. Furthermore, the increasing grid size can also cause memory problems if the original FOV was already large. Figure 3.15a shows the development of $\Delta\varphi_{\mathrm{RMS}}$ with increasing zero-padding for both objects. For the calculation of $\Delta\varphi_{\mathrm{RMS}}$, only pixels in the original FOV and not those added by zero-padding are considered. For both distributions, the Fourier-specific artefacts and therefore $\Delta\varphi_{\mathrm{RMS}}$ decrease rapidly with increased zero-padding. The trade-off in both cases is a significant increase in computation time.
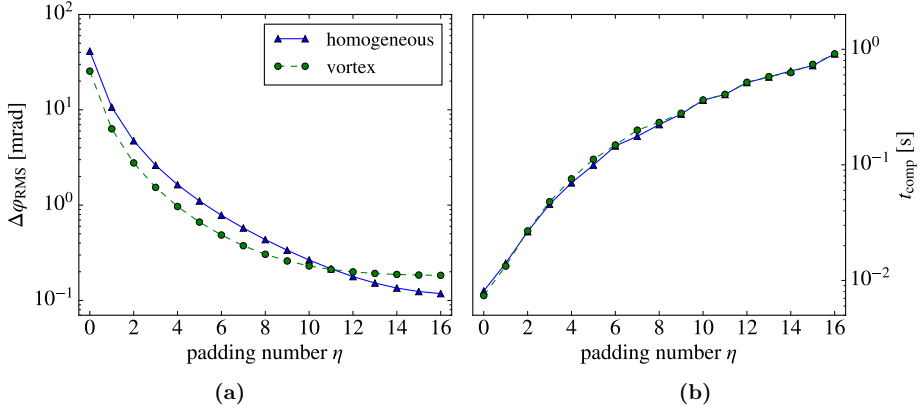
Figure 3.15.: (**a**) Dependence of the RMS difference $\Delta\varphi_{\mathrm{RMS}}$ on zero-padding number η for the FDFC approach for the homogeneously magnetised disc (blue triangles and dashed line) and the disc containing a magnetic vortex state (green circles and solid line). (**b**) Corresponding computation times t_{comp}, which are virtually identical for both objects.

3.3.2. Assessment of the RDFC approach

The same assessments were performed for the RDFC approach described in Section 3.2.4. The resulting comparison is shown in Figs. 3.16 and 3.17. The RDFC approach matches the analytical solutions to a very high degree, without being influenced by Fourier-related artefacts. For finer grid spacings, even the sharp peaks in the phase at the edges of the homogeneously magnetised disc and the centre of the vortex disc are reproduced (see the insets in Fig. 3.16).

The RMS difference $\Delta\varphi_{\mathrm{RMS}}$ is shown for both test objects in Fig. 3.17 for a grid spacing a of 1 nm and a field of view of 128×128 pixels. The line profiles in Fig. 3.16 show that the grid spacing has to be sufficiently small to accurately describe regions such as the boundaries of a magnetised object or points where the magnetisation direction changes rapidly (*e.g.*, at the centre of a magnetic vortex). The RMS difference $\Delta\varphi_{\mathrm{RMS}}$ for both objects is approximately 0.2 mrad, which is 3 orders of magnitude smaller than the maximum phase shift shown in Fig. 3.12. This assessment further confirms the accuracy of the RDFC approach.

3.3.3. RDFC and FDFC comparison for different grid spacings

In this section, the RDFC and FDFC approaches are compared for different grid sizes, with regard to both computation time and accuracy. Four different zero-padding numbers η are used for the FDFC approach and are listed in Tab. 3.2a.
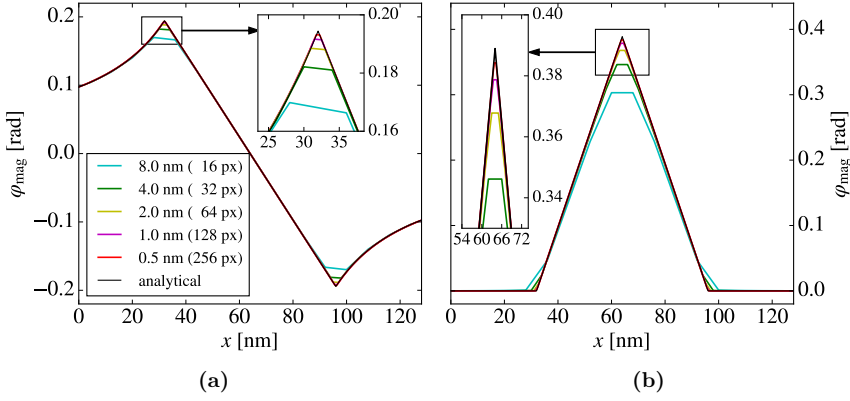
Figure 3.16.: Line profiles of φ_{mag} obtained from RDFC calculations performed for discs that are (**a**) homogeneously magnetised and (**b**) support a vortex state for different grid spacings, as well as for the analytical solution for each disc. The insets show magnified regions, in order to better illustrate the behaviours of the numerical solutions for different grid spacings a at the border (**a**) and the centre (**b**) of the disc. The number of pixels along the 128 nm length of the image is stated in parentheses for each grid spacing.
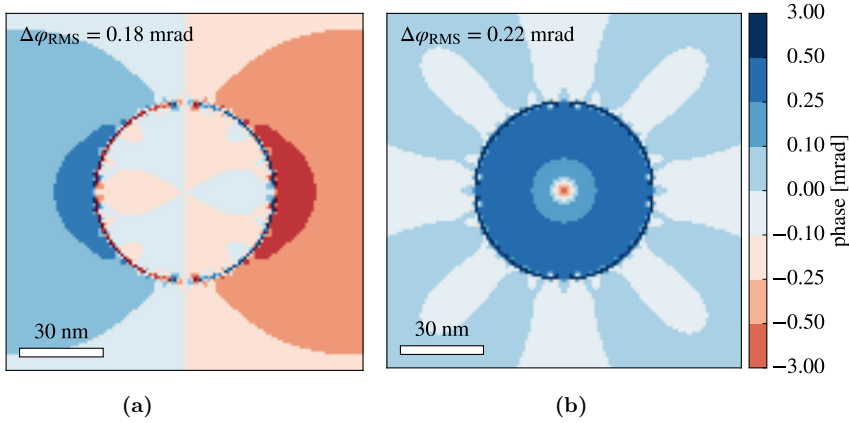
Figure 3.17.: Difference between RDFC and analytical solutions for φ_{mag} for discs that are (**a**) homogeneously magnetised and (**b**) support a magnetic vortex state. The grid spacing is $a = 1\,\mathrm{nm}$. The colour scale is not linear and is used to emphasise different magnitudes of error. The annotation at the top of each image gives the RMS difference $\Delta\varphi_{\mathrm{RMS}}$ of the pixel-wise difference between the numerical result and the analytical solution for each calculation.

Each value guarantees that the dimensions of the padded field of view are a power of two, which is beneficial for the FFT computation for both approaches. At the same time, the grid spacing a is varied, starting from $a = 0.5\,\text{nm}$ and doubling in steps up to a value of $a = 4\,\text{nm}$. The corresponding grid sizes range from $256 \times 256 \times 32$ voxels to $32 \times 32 \times 4$ voxels. An overview of the calculations is given in Tab. 3.2b. As before, the projection direction is always parallel to the z axis.

Table 3.2.: (**a**) Overview of the different zero-padding numbers η that are used in the following discussions and the resulting FOV, relative to a starting image size of $N \times N$ pixels. (**b**) Overview of the different grid spacings a that are used and the corresponding grid size, which is chosen so that the three-dimensional volume is fixed to be $128 \times 128 \times 64\,\text{nm}^3$.

<div>

(**a**) Variation of zero-padding η

Zero-padding η	Field of view
0	$N \times N$
1	$2N \times 2N$
3	$4N \times 4N$
7	$8N \times 8N$

(**b**) Variation of grid spacing a

Grid spacing a	Grid size
0.5 nm	$256 \times 256 \times 32$ voxels
1 nm	$128 \times 128 \times 16$ voxels
2 nm	$64 \times 64 \times 8$ voxels
4 nm	$32 \times 32 \times 4$ voxels

</div>

The results of the comparison are shown in Fig. 3.18 on a logarithmic scale in the form of plots of computation time t_{comp} (Figs. 3.18a and 3.18b) and RMS difference $\Delta\varphi_{\text{RMS}}$ (Figs. 3.18c and 3.18d). Both quantities are plotted as a function of grid spacing a.

The results indicate that the Fourier space method without zero-padding is the fastest numerical approach because the convolution operates on arrays of size $N \times N$. For a zero-padding number of $\eta = 1$, the convolution operates on a FOV of size $2N \times 2N$, which is also the size that is used for the RDFC approach. As a result of the fact that the RDFC approach pre-computes the convolution kernels, it is closer to the FDFC approach with $\eta = 0$ than to $\eta = 1$, with regard to the computational speed. Furthermore, it is significantly faster than the FDFC approach for higher zero-padding numbers.

For the homogeneously magnetised disc, $\Delta\varphi_{\text{RMS}}$ for the FDFC approach is dominated by aliasing artefacts resulting from the periodic repetition in real space. The RMS difference $\Delta\varphi_{\text{RMS}}$ decreases with increasing zero-padding and only depends slightly on grid size for higher values of η, which increasingly suppress aliasing artefacts. $\Delta\varphi_{\text{RMS}}$ is determined by both η and the distance of the object from the edge of the field of view. For the RDFC approach, $\Delta\varphi_{\text{RMS}}$ is many orders of magnitudes lower than for the FDFC approach because it does not suffer from such artefacts. The primary factor that determines the accuracy of the RDFC approach, as expressed by the RMS difference $\Delta\varphi_{\text{RMS}}$, is the grid spacing and therefore the sampling density of the discretisation. For the disc that supports a magnetic vortex, similar results are obtained. However, the dominating artefact for this distribution
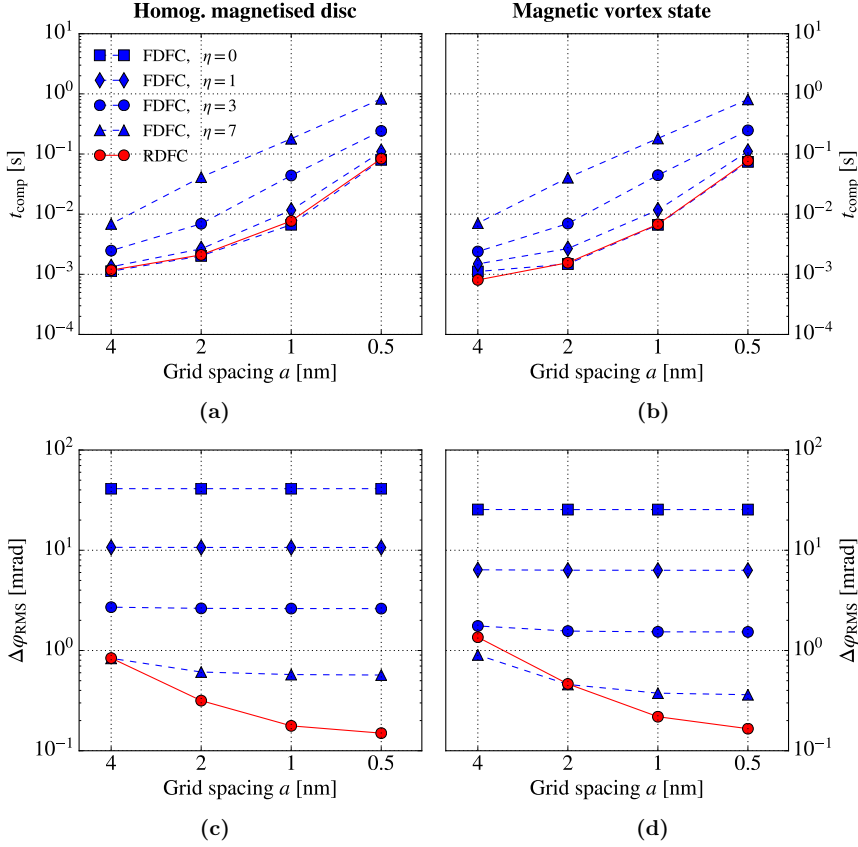
Figure 3.18.: (**a**) Computation time t_{comp} plotted for the different approaches for the homogeneously magnetised disc as a function of grid spacing a. (**c**) RMS difference $\Delta\varphi_{\text{RMS}}$ plotted for the different approaches. (**b**) and (**d**) show corresponding plots for the vortex disc. FDFC results are shown using dashed lines and in blue. RDFC results are shown using solid lines and in red.

when using the FDFC approach is not aliasing due to periodic repetition, but the missing zero frequency, which results in a phase offset. Aliasing does not occur because the periodic distributions outside the FOV produce no stray fields and are therefore disjoint.

The two test distributions represent different behaviours that a magnetisation distribution can exhibit. The difference between these behaviours is similar in some respects to the Helmholtz decomposition, which separates a vector field into a curl-free and a divergence-free part. Whereas homogeneously magnetised objects have slowly decaying stray fields that produce a phase shift outside the object, vortex states produce more localised phase shift distributions. In an experimental sample of unknown magnetic configuration, in general both contributions may be expected. The FDFC approach is prone to Fourier-specific artefacts, which can only be circumvented by using extensive zero-padding. In contrast, the novel RDFC approach produces very accurate phase images for arbitrary magnetisation distributions without having to trade off computational speed, as in the RDRC approach. This makes the RDFC approach the ideal implementation for the phase mapping matrix $\mathbf{Q}_b$ in the forward model for an MBIR algorithm, for which accuracy and computational speed are essential.

3.4. Summary

In this chapter, a forward model for calculating the magnetic contribution to the electron optical phase shift from a three-dimensional magnetisation distributions has been developed and assessed. The forward model was initially expressed as a matrix equation. To this end, the involved quantities had to be discretised and vectorised. The nested nature of the system matrix $\mathbf{F}$ was explored, resulting in a separation of the forward model into sub-problems for each phase image. Each of these sub-problems was split further into a projection matrix $\mathbf{P}_b$ and a phase mapping matrix $\mathbf{Q}_b$. An optimised implementation of the projection matrix was realised by using sparse matrix calculations. In contrast, the dense nature of the phase mapping matrix required a more complex approach. Existing phase mapping strategies were then explored. It was established that the RDRC ("real space discretisation, real space convolution") approach calculates phase images that are in accordance with analytical solutions, but is very slow and scales as $\mathcal{O}\left(N^4\right)$. The FDFC ("Fourier space discretisation, Fourier space convolution") approach is significantly faster and scales as $\mathcal{O}\left(N^2 \log N\right)$. However, as a result of the implicit assumption of periodic repetition of the magnetisation distribution at the borders of the FOV, it exhibits deviations from analytical results in the case of slowly decaying fields outside a magnetised object. In order to combine the advantages of both approaches, an optimised phase mapping strategy was proposed. The resulting RDFC approach is based on convolution kernels that are discretised in real space and pre-calculated from a known analytical solution for a homogeneously magnetised disc. The RDFC

approach was compared with the currently prevalent FDFC approach and was shown to minimise artefacts, while maximising computational speed. Table 3.3 shows an overview of all three approaches, their scaling and their assumptions about the magnetisation distribution. In the next chapter, the optimised forward model is employed in an MBIR algorithm to reconstruct magnetisation distributions from magnetic phase images.

Table 3.3.: Comparison of the different phase mapping approaches, with regard to the assumption that is implicitly made about the magnetisation distribution and the scaling with axis length N.

Approach	Implicit assumption	Scaling
RDRC	No magnetisation outside the FOV	$\mathcal{O}\left(N^4\right)$
FDFC	Periodic magnetisation outside the FOV	$\mathcal{O}\left(N^2 \log N\right)$
RDFC	No magnetisation outside the FOV	$\mathcal{O}\left(N^2 \log N\right)$

4. Solving the inverse problem of magnetisation retrieval

In this chapter, the retrieval of a magnetisation distribution $\boldsymbol{M}$ from one or more magnetic phase images, *i.e.*, the inverse problem to the forward model, is discussed. The system matrix $\mathbf{F} \in \mathbb{R}^{m \times n}$ of the forward model with $n = 3N_x N_y N_z$ retrieval targets and $m = N_b N_u N_v$ measurements is, in general, rank-deficient (*i.e.*, singular) and a simple inversion of the form

$$\boldsymbol{x} = \mathbf{F}^{-1} \boldsymbol{y} \tag{4.1}$$

is not possible. $\mathbf{F}$ is most likely not a square matrix (*i.e.*, $n = m$), because the number of images N_b is generally a lot smaller than any of the spatial dimensions (N_x, N_y or N_z). In an underdetermined system with more retrieval targets than individual measurements ($n > m$), the system matrix $\mathbf{F}$ is rank deficient and the resulting linear equation system (LES)

$$\boldsymbol{y} = \mathbf{F}\boldsymbol{x} \tag{4.2}$$

is not uniquely solvable.

The use of a coarser grid spacing a reduces the number of voxels and can potentially result in N_b being larger than N_x, N_y or N_z. In this way, an overdetermined situation involving fewer unknowns than measurements ($n < m$) can be ensured. However, if a coarse grid is used, then information about magnetic structures that have higher spatial frequencies cannot be reconstructed.

In the rare case of a square matrix $\mathbf{F}$, *i.e.*, $n = m$, the invertibility of $\mathbf{F}$ is still not guaranteed, because a non-trivial null space $\text{null}(\mathbf{F})$ of $\mathbf{F}$ can exist. The null space of a matrix is defined by the expression

$$\text{null}(\mathbf{F}) = \{\boldsymbol{x} \in \mathbb{R}^n | \mathbf{F}\boldsymbol{x} = \mathbf{0}\}. \tag{4.3}$$

Here, it describes all magnetisation state vectors[1] $\boldsymbol{x}$ that map onto the zero measurement vector $\boldsymbol{y} = \mathbf{0}$, *i.e.*, they produce no magnetic phase. If the null space is non-trivial, then there exist magnetisation states $\boldsymbol{x} \in \text{null}(\mathbf{F})$ that are "invisible" to the measurement technique of off-axis electron holography and to the corresponding

---

[1]If the null space only contains the zero vector, then it is referred to as trivial. If it contains additional vectors, it is called non-trivial.

forward model. An arbitrary linear combination of such states could then be added to a magnetisation distribution without changing the resulting magnetic contribution to the phase. The solution to the inverse problem is then not unique and the rank of $\mathbf{F}$ is decreased according to the rank-nullity theorem

$$\text{rank}\,(\mathbf{F}) = n - \text{rank}\,(\text{null}\,(\mathbf{F}))\,. \tag{4.4}$$

The term $\text{rank}\,(\text{null}\,(\mathbf{F}))$, the so-called nullity, denotes the dimension of the null space $\text{null}\,(\mathbf{F})$. An illustration of the null space is presented in Fig. 4.1.
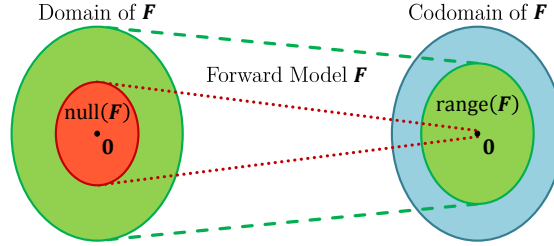
Figure 4.1.: null space and range (or image) of the forward model described by the system matrix $\mathbf{F}$. Here, the domain of $\mathbf{F}$ is the set of all magnetisation state vectors $\boldsymbol{x}$, while the codomain is the set of all possible measurement vectors $\boldsymbol{y}$. The null space $\text{null}\,(\mathbf{F})$ is the set of all magnetisation states $\boldsymbol{x}$ that are mapped onto the zero vector $\boldsymbol{y} = \boldsymbol{0}$, *i.e.*, no phase is produced. The $\text{range}\,(\mathbf{F})$ is the image of the forward model. It contains all measurement vectors $\boldsymbol{y}$ that can be produced by all magnetisation state vectors $\boldsymbol{x}$. Not all measurements $\boldsymbol{y}$ in the codomain necessarily have to be attainable by $\mathbf{F}$. For example, if they are noisy, they can lie outside of $\text{range}\,(\mathbf{F})$. No magnetisation state $\boldsymbol{x}$ then exists, which would be able to produce the corresponding phase images.

Furthermore, calculation of the magnetic contribution to the electron optical phase shift for a given magnetisation distribution involves the calculation of projection and convolution integrals. The latter integrals act as smoothing low-pass filters. The inverse to an integral is a derivative which acts as a high-pass filter and is sensitive to errors, effectively amplifying noise in the data. Whenever a forward model has smoothing properties, the appearance of strong oscillations resulting from small data perturbations with high frequencies is to be expected in the solution to the inverse problem [115]. An error-affected measurement $\boldsymbol{y}$ could lie outside the image[2] of $\mathbf{F}$. No magnetisation state $\boldsymbol{x}$ with $\{\boldsymbol{x} \in \mathbb{R}^n | \mathbf{F}\boldsymbol{x} = \boldsymbol{y}\}$ could produce the measured phase images $\boldsymbol{y}$.

All of the issues that are described above contribute to the ill-posed nature of the inverse problem. As outlined in Section 2.3, a number of steps have to be taken to tackle magnetisation reconstruction. In Section 4.1, the original ill-posed inverse problem is first replaced by a least squares minimisation problem. In Section 4.2,

---

[2]The image of $\mathbf{F}$ is often also called $\text{range}\,(\mathbf{F})$ and is illustrated in Fig. 4.1.

regularisation is introduced. Minimisation of the resulting cost function to retrieve the best fitting solution is discussed in Section 4.3. Diagnostic measures to evaluate the quality of the reconstructed magnetisation distribution are illuminated in Section 4.4. An in-depth analysis of the null space of $\mathbf{F}$, which is deeply linked to the question of whether all arbitrary magnetisation distributions can be retrieved, is conducted in Section 4.5.

4.1. Approximation by least squares minimisation

The problem of solving $\mathbf{F}\boldsymbol{x} = \boldsymbol{y}$ for $\boldsymbol{x}$, which is in general ill-posed for the reasons stated above, can be approximated by a least squares minimisation problem (*cf.* Eq. 2.39) in the form

$$\min_{\boldsymbol{x}} \|\mathbf{F}\boldsymbol{x} - \boldsymbol{y}\|^2_{\mathbf{S}_\epsilon^{-1}} = \min_{\boldsymbol{x}} \left[(\mathbf{F}\boldsymbol{x} - \boldsymbol{y})^T \mathbf{S}_\epsilon^{-1} (\mathbf{F}\boldsymbol{x} - \boldsymbol{y}) \right]. \tag{4.5}$$

Such a minimisation guarantees the existence of at least one solution. The least squares term of the residual vector $\mathbf{F}\boldsymbol{x} - \boldsymbol{y}$ uses a Euclidean norm that is weighted by the inverse of the covariance matrix of the measurement errors $\mathbf{S}_\epsilon \in \mathbb{R}^{m \times m}$. The covariance matrix $\mathbf{S}_\epsilon$ is included based on optimal estimation theory [116], as discussed further in Section 4.4 and Section A.3. It is assumed to be diagonal [72]. Its inverse $\mathbf{S}_\epsilon^{-1}$, which is used in Eq. 4.5, has the same sparse structure and essentially determines the weights of different entries in the residual vector $\mathbf{F}\boldsymbol{x} - \boldsymbol{y}$ in the overall "cost" of the minimisation. Inverse variances can be used as the diagonal entries of $\mathbf{S}_\epsilon^{-1}$ if statistical error estimates are available for all of the pixels in the measured phase images. Alternatively, $\mathbf{S}_\epsilon^{-1}$ can be interpreted in terms of the confidence in the measurements $\boldsymbol{y}$ by introducing a "confidence array" $\Gamma_b[p, q]$ for each magnetic phase image. Each entry in Γ_b then acts as a weight, with which the associated pixel in the phase image contributes to the reconstruction and can lie between 0 and 1. An example of Γ_b is shown in Fig. 4.3d. $\mathbf{S}_\epsilon^{-1}$ is then constructed as a diagonal matrix with

$$\begin{aligned} \operatorname{diag}\left(\mathbf{S}_\epsilon^{-1}\right) = \Big(&\Gamma_1\left[0, 0\right], \dots, \Gamma_1\left[N_u - 1, N_v - 1\right], \\ &\cdots, \\ &\Gamma_{N_b}\left[0, 0\right], \dots, \Gamma_{N_b}\left[N_u - 1, N_v - 1\right], \Big). \end{aligned} \tag{4.6}$$

A confidence value of 0 in $\mathbf{S}_\epsilon^{-1}$ translates to a variance that goes to ∞ in $\mathbf{S}_\epsilon$, *i.e.*, the corresponding measurement is not trustworthy and that pixel is ignored. Values of 0 could*, e.g.*, be assigned to clearly identifiable artefacts, such as dead pixels or phase unwrapping errors. Values of 1 denote full contributions and complete trust in the corresponding pixels in the phase images.

4.2. Regularisation

Even though substitution of the original problem by a least squares minimisation ensures the existence of a solution, its uniqueness is not guaranteed. In order to ensure uniqueness, regularisation techniques are required. As explained in Section 2.3, regularisation refers to the approximation of an ill-posed problem by a solvable better-posed one. The most simple regularisation technique, which has already been applied implicitly, is the discretisation of the magnetisation distribution and the magnetic phase images, without which a matrix formulation could not have been used. Discretisation reduces an infinite-dimensional problem to a finite-dimensional one. The choice of a coarser grid spacing a during discretisation reduces the complexity of the problem. However, it also limits the maximum spatial frequency, with which features in the magnetisation distribution can be represented. Another regularisation strategy is the introduction of additional *a priori* information, which often amounts to the application of Occam's razor and results in selecting the most sensible solution from a pool of possible solutions. Two regularisation techniques are described below.

4.2.1. Tikhonov regularisation

One of the most commonly used regularisation techniques is Tikhonov regularisation [123], of which a first order variant is used in this thesis. Generalised Tikhonov regularisation utilises a weighted Euclidean norm which operates on differences between a state vector $\boldsymbol{x}$ and an *a priori* state $\boldsymbol{x}_a$ that can represent expectations about the state that should be retrieved. The regularisation term $R_\lambda(\boldsymbol{x})$ in Eq. 2.40 takes the form

$$R_\lambda(\boldsymbol{x}) = \|\boldsymbol{x} - \boldsymbol{x}_a\|_{\mathbf{S}_a^{-1}}^2 = (\boldsymbol{x} - \boldsymbol{x}_a)^T \mathbf{S}_a^{-1} (\boldsymbol{x} - \boldsymbol{x}_a) \tag{4.7}$$

in the minimisation process. The matrix $\mathbf{S}_a \in \mathbb{R}^{n \times n}$, which contains the dependency on the regularisation parameters (*cf.* λ in Section 2.3), can be interpreted as the covariance matrix of the *a priori* state $\boldsymbol{x}_a$. Its inverse $\mathbf{S}_a^{-1}$ is referred to as the precision matrix [72] and directly dictates the physical constraints that should be applied to the solution $\boldsymbol{x}$. For a Tikhonov regularisation of zeroth order, the precision matrix $\mathbf{S}_a^{-1}$ is a diagonal matrix. In its simplest implementation, $\mathbf{S}_a^{-1}$ is a scaled identity matrix $\lambda \mathbf{I}_n \in \mathbb{R}^{n \times n}$, which favours solutions with a small Euclidean norm $\|\boldsymbol{x} - \boldsymbol{x}_a\|^2$, *i.e.*, solutions that are close to $\boldsymbol{x}_a$. For a simple Tikhonov regularisation with $\mathbf{S}_a^{-1} = \lambda \mathbf{I}_n$ and $\boldsymbol{x}_a = \boldsymbol{0}$, the regularisation favours overall small magnetisation distributions [115, 117].

The general expression for a Tikhonov regularisation that also constrains first order derivatives takes the form [72, 124]:

$$\mathbf{S}_a^{-1} = \lambda_0 \mathbf{D}^T \mathbf{D} + \lambda_x \boldsymbol{\nabla}_x^T \boldsymbol{\nabla}_x + \lambda_y \boldsymbol{\nabla}_y^T \boldsymbol{\nabla}_y + \lambda_z \boldsymbol{\nabla}_z^T \boldsymbol{\nabla}_z, \tag{4.8}$$

where $\mathbf{D}$ is a diagonal matrix (often the identity matrix) and the other terms include simple positive semi-definite Tikhonov regularisation matrices of first order, *e.g.*,

$$\boldsymbol{\nabla}_x = \begin{pmatrix} -1 & 1 & 0 & \cdots & 0 \\ 0 & -1 & 1 & \ddots & 0 \\ \vdots & \ddots & \ddots & \ddots & \vdots \\ 0 & \cdots & 0 & -1 & 1 \\ 0 & \cdots & 0 & 0 & 0 \end{pmatrix}. \tag{4.9}$$

The last three terms in Eq. 4.8 apply smoothness constraints to the solution $\boldsymbol{x}$ by applying gradients in all three spatial directions x, y and z. The regularisation parameters λ_0, λ_x, λ_y and λ_z are used to weight the different contributions against each other and against the norm in Eq. 4.5 describing the measurement residuals.

Enforcing the smoothness of the magnetisation can be physically motivated by relating it to the minimisation of the exchange energy. The exchange energy can be expressed in the continuum approximation [125] by an integral form

$$E_{\text{exch.}} = J \int_V (\nabla \boldsymbol{M})^2 \, dV = J \int_V \left((\nabla M_x)^2 + (\nabla M_y)^2 + (\nabla M_z)^2 \right) dV, \tag{4.10}$$

where J is a phenomenological exchange constant. A regularisation which selects a solution with minimised exchange energy is very reasonable from a physical point of view and is modelled by comparing Eq. 4.8 with Eq. 4.10. The squared partial derivatives of the magnetisation in Eq. 4.10 correspond to the Tikhonov regularisation matrices of first order in Eq. 4.8. All of the partial derivatives in Eq. 4.10 are equally weighted. The regularisation parameters for the first order derivatives in Eq. 4.8 are therefore chosen to be the same, *i.e.*,

$$\lambda_x = \lambda_y = \lambda_z \equiv \lambda. \tag{4.11}$$

The diagonal matrix in Eq. 4.8 is not present in Eq. 4.10. The parameter λ_0, which is associated with the zero order term in Eq. 4.8, is therefore set to zero. The resulting precision matrix $\mathbf{S}_{\text{a}}^{-1}$ then depends linearly on a single regularisation parameter[3] λ and can be expressed in the form

$$\mathbf{S}_{\text{a}}^{-1}(\lambda) = \lambda \left(\boldsymbol{\nabla}_x^T \boldsymbol{\nabla}_x + \boldsymbol{\nabla}_y^T \boldsymbol{\nabla}_y + \boldsymbol{\nabla}_z^T \boldsymbol{\nabla}_z \right). \tag{4.12}$$

Furthermore, the derivatives in Eq. 4.10 operateon the magnetisation directly and not on differences to another magnetisation state. For the regularisation to accurately reflect the exchange energy minimisation, the *a priori* state $\boldsymbol{x}_{\text{a}}$ should therefore be set to the zero vector, so that with $\boldsymbol{x}_{\text{a}} = \boldsymbol{0}$ in Eq. 4.7, the derivatives in $\mathbf{S}_{\text{a}}^{-1}$ operate on the unbiased magnetisation state $\boldsymbol{x}$.

---

[3]The regularisation parameter λ and the exchange constant J are not equivalent. While λ is a flexible parameter that is used to control the strength of the regularisation, J is a fixed property of the magnetisation state.

In summary, the constructed regularisation term in Eq. 4.7 is a measure of the smoothness of the solution and penalises its discontinuities. The chosen Tikhonov regularisation effectively selects the magnetisation state that has minimal exchange energy from the pool of all possible solutions.

4.2.2. Regularisation by applying a mask

In addition to Tikhonov regularisation, another regularisation method involves the application of a mask $\Xi\,[i,j,k]$. This mask is a boolean array that has the same shape as the magnetisation distribution $\boldsymbol{M}\,[i,j,k]$. It describes the known positions of magnetised regions in the vector field space and greatly reduces the number n of retrieval targets in $\boldsymbol{x}$ by fixing values outside of Ξ to zero. The state vector $\boldsymbol{x}$ is shortened to a smaller number of entries, which is equivalent to the number of voxels that are masked by Ξ. Figure 4.3c shows an example of a mask Ξ for a two-dimensional case. The precision matrix $\mathbf{S}_\mathrm{a}^{-1}\,(\lambda,\Xi)$ has to account for the mask Ξ to ensure that derivatives are only calculated inside its boundaries. Otherwise, sudden drops to zero of the magnetisation at these boundaries would be erroneously punished by the smoothness constraint.

In contrast to, *e.g.*, the $\boldsymbol{B}$ field, which can continue smoothly outside a magnetised region, the magnetisation $\boldsymbol{M}$ is usually more localised and is characterised by the mask Ξ. The mask therefore has a significant influence on the reconstruction and the correct identification of the magnetised regions before a reconstruction is attempted is therefore of great importance. This point is discussed further in Chapter 5.

4.3. Minimisation of the cost function

Figure 4.2 provides a summary of the listed steps that are required to solve the inverse problem. Taking into account that the *a priori* state was set to zero in Section 4.2.1, these methods lead to a cost function $C : \mathbb{R}^n \mapsto \mathbb{R}$ that is given by the expression

$$C\,(\boldsymbol{x}) = \|\mathbf{F}\boldsymbol{x} - \boldsymbol{y}\|^2_{\mathbf{S}_\epsilon^{-1}} + \|\boldsymbol{x}\|^2_{\mathbf{S}_\mathrm{a}^{-1}} \tag{4.13}$$

$$= (\mathbf{F}\boldsymbol{x} - \boldsymbol{y})^T\,\mathbf{S}_\epsilon^{-1}\,(\mathbf{F}\boldsymbol{x} - \boldsymbol{y}) + \boldsymbol{x}^T\mathbf{S}_\mathrm{a}^{-1}\boldsymbol{x}, \tag{4.14}$$

where the aim is to find the minimum $\min_{\boldsymbol{x}}\,[C\,(\boldsymbol{x})]$ of the cost function.

The regularisation parameter λ, on which the precision matrix $\mathbf{S}_\mathrm{a}^{-1}$ depends linearly, is used to balance the compliance of the solution to the measurements (the first term in Eq. 4.13) and its compliance to the physical constraints that are imposed by the regularisation (the second term in Eq. 4.13). The regularisation parameter can also be interpreted as a Lagrange multiplier, whereby Eq. 4.5 is minimised while being subjected to the physical constraint that is described by Eq. 4.7 [118].
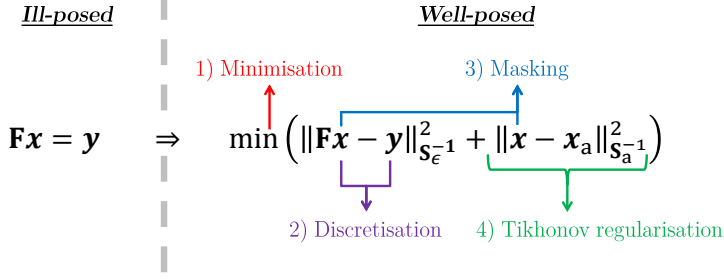
Figure 4.2.: Summary of the steps which are taken to replace the ill-posed inverse problem by a better posed one. 1) The linear equation system is replaced by a least squares minimisation, which ensures at least one solution. 2) The magnetisation state and the measured phase images are discretised, so the problem is finite-dimensional. 3) A mask is used to locate magnetised regions, which sets the magnetisation to zero outside and thus reduces the amount of retrieval targets. 4) Tikhonov regularisation of first order is applied to minimise the exchange energy of the system and choose a smooth solution.

As mentioned above, minimisation of only the norm of the residual vector $\|\mathbf{F}\boldsymbol{x} - \boldsymbol{y}\|^2_{\mathbf{S}^{-1}_\epsilon}$ does not provide a unique solution for $\boldsymbol{x}$ if $\mathbf{F}$ is rank deficient, *i.e.*, it has non-trivial null space [118]. However, the addition of a non-degenerate regularisation term in quadratic form $\boldsymbol{x}^T \mathbf{S}^{-1}_a \boldsymbol{x}$, where $\mathbf{S}^{-1}_a$ is a positive definite matrix, guarantees overall non-degeneracy. Minimisation of the cost function $C(\boldsymbol{x})$ then leads to a unique solution[4].

The final rows of $\boldsymbol{\nabla}_{x/y/z}$ contain only zeros, in order to guarantee the square $n \times n$ shape. Because of these rows, $\mathbf{S}^{-1}_a$ has a single zero eigenvalue, effectively reducing its rank to $n - 1$. $\mathbf{S}^{-1}_a$ is therefore only semi-positive definite. Its null space is non-trivial according to the rank-nullity theorem (*cf.* Eq. 4.4) and consists of all homogeneously-magnetised distributions. Because the amplitudes and directions of those distributions are the same everywhere[5], they are "invisible" to the derivatives that are applied by $\mathbf{S}^{-1}_a$. Even though a homogeneous magnetisation distribution passes through the regularisation without penalty, its characteristic phase contribution makes it easy to determine its orientation and amplitude from the measurements $\boldsymbol{y}$. Examples of a homogeneous magnetisation distribution (4.3a) and the magnetic phase image that it produces (4.3b) are shown in Fig. 4.3.

In order to find the best-fitting solution $\boldsymbol{x}_{\mathrm{rec}}$ to the inverse problem, the cost function $C(\boldsymbol{x})$ has to be minimised. The minimum must be a root of the first derivative of $C(\boldsymbol{x})$. Therefore, identification of the roots of the gradient vector $\boldsymbol{C}'(\boldsymbol{x}) \in \mathbb{R}^n$

---

[4]Taken from "Numerical Recipes: The art of scientific computing" (2007) [118]: "When a quadratic minimization principle is combined with a quadratic constraint, and both are positive, only *one* of the two need be non-degenerate for the overall problem to be well-posed."

[5]Or at least the same for every disjoint magnetised region.
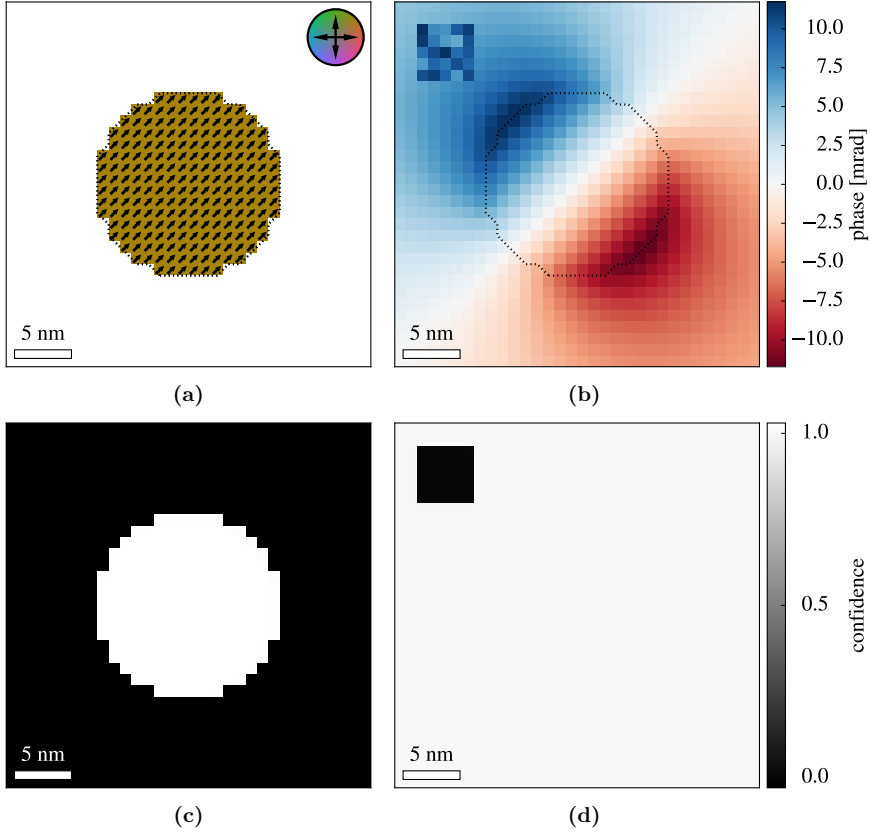
Figure 4.3.: Illustration of a simulated phase image and corresponding arrays. (**a**) shows a projected magnetisation distribution for a simple $t = 1\,\text{nm}$ thick homogeneously-magnetised disc with a radius of $R = 8\,\text{nm}$ and a grid spacing of $a = 1\,\text{nm}$, magnetised at an angle of $\beta = 45°$. The resulting magnetic phase image in rad is shown in (**b**). Both images show the projection of the mask Ξ, which determines the localisation of the magnetised disc, as a dotted outline. The two-dimensional projection of Ξ is shown separately in (**c**) as a boolean image, with white corresponding to "True". The phase image contains a simulated artefact in the upper left corner, which is not taken into account in the reconstruction of $\boldsymbol{M}$ by setting the corresponding values in the confidence array Γ in (**d**) to zero (black pixels). The value everywhere else is set to unity, which means the corresponding pixels go into the reconstruction with full weight.

allows identification of candidate solutions according to the expression:

$$\boldsymbol{C}'\left(\boldsymbol{x}\right) = 2\mathbf{F}^T\mathbf{S}_\epsilon^{-1}\left(\mathbf{F}\boldsymbol{x} - \boldsymbol{y}\right) + 2\mathbf{S}_\mathrm{a}^{-1}\boldsymbol{x} \overset{!}{=} 0. \tag{4.15}$$

The sufficient condition for a minimum in $C\left(\boldsymbol{x}\right)$ is fulfilled if the Hessian matrix $\mathbf{C}'' \in \mathbb{R}^{n\times n}$, which is given by the expression

$$\mathbf{C}'' = 2\mathbf{F}^T\mathbf{S}_\epsilon^{-1}\mathbf{F} + 2\mathbf{S}_\mathrm{a}^{-1}, \tag{4.16}$$

is positive semi-definite. As $\mathbf{S}_\epsilon^{-1}$ is a positive diagonal matrix, the first term $\mathbf{F}^T\mathbf{S}_\epsilon^{-1}\mathbf{F}$ in Eq. 4.16 can be written as a Gramian matrix $\left(\mathbf{S}_\epsilon^{-1/2}\mathbf{F}\right)^T\left(\mathbf{S}_\epsilon^{-1/2}\mathbf{F}\right)$ and, as such, is positive semi-definite. As stated above, the precision matrix $\mathbf{S}_\mathrm{a}^{-1}$ is also positive semi-definite. Therefore, the Hessian matrix $\mathbf{C}''$ always satisfies the sufficient condition for a minimum to be found. It should be noted that $\mathbf{S}_\mathrm{a}$ and $\mathbf{S}_\epsilon$ do not have to be known explicitly, as only their inverses are used in the present equations. An alternative Bayesian interpretation of these matrices is given in the appendix in Section A.3.

In order to find the root $\boldsymbol{x}_\mathrm{rec}$ from $\boldsymbol{C}'\left(\boldsymbol{x}\right)$, Newton's method [126] is utilised by employing a Taylor expansion about an arbitrary starting point $\boldsymbol{x}_0$ in the form

$$\boldsymbol{C}'\left(\boldsymbol{x}_\mathrm{rec}\right) = \boldsymbol{C}'\left(\boldsymbol{x}_0\right) + \mathbf{C}'' \cdot \left(\boldsymbol{x}_\mathrm{rec} - \boldsymbol{x}_0\right) \overset{!}{=} 0. \tag{4.17}$$

$$\Leftrightarrow \mathbf{C}''\left(\boldsymbol{x}_0 - \boldsymbol{x}_\mathrm{rec}\right) = \boldsymbol{C}'\left(\boldsymbol{x}_0\right) \tag{4.18}$$

$$\Leftrightarrow \mathbf{C}''\boldsymbol{x}_\mathrm{rec} = \mathbf{C}''\boldsymbol{x}_0 - \boldsymbol{C}'\left(\boldsymbol{x}_0\right) \tag{4.19}$$

$$\Leftrightarrow \boldsymbol{x}_\mathrm{rec} = \boldsymbol{x}_0 - \mathbf{C}''^{-1}\boldsymbol{C}'\left(\boldsymbol{x}_0\right). \tag{4.20}$$

As a result of the linearity of the forward model, the Hessian matrix $\mathbf{C}''$ does not depend on $\boldsymbol{x}$. Therefore, no higher orders are present in the Taylor expansion. Equation 4.20 can be identified as the Newton iteration scheme. Because the cost function is quadratic in $\boldsymbol{x}$, it converges in only one step. The choice of starting point is therefore not important and it can be set to the zero vector $\boldsymbol{x}_0 = \boldsymbol{0}$ without loss of generality, *i.e.*, the reconstruction starts with an "empty" magnetisation distribution.

The dimensions of $\boldsymbol{C}'' \in \mathbb{R}^{n\times n}$ scale as $\mathcal{O}\left(n^2\right) = \mathcal{O}\left(N^6\right)$ for an axis length of N pixels. A large Hessian matrix results in a very high computation time and memory consumption. Direct matrix inversion (as implied by Eq. 4.20) is therefore unfeasible. Instead, by inserting Eq. 4.15 and Eq. 4.16 into Eq. 4.18 while using $\boldsymbol{x}_0 = \boldsymbol{0}$, the linear system of equations

$$\left(2\mathbf{F}^T\mathbf{S}_\epsilon^{-1}\mathbf{F} + 2\mathbf{S}_\mathrm{a}^{-1}\right)\left(\boldsymbol{x}_0 - \boldsymbol{x}_\mathrm{rec}\right) = 2\mathbf{F}^T\mathbf{S}_\epsilon^{-1}\left(\mathbf{F}\boldsymbol{x}_0 - \boldsymbol{y}\right) + 2\mathbf{S}_\mathrm{a}^{-1}\boldsymbol{x}_0 \tag{4.21}$$

$$\Leftrightarrow \left(\mathbf{F}^T\mathbf{S}_\epsilon^{-1}\mathbf{F} + \mathbf{S}_a^{-1}\right)\boldsymbol{x}_\mathrm{rec} = \mathbf{F}^T\mathbf{S}_\epsilon^{-1}\boldsymbol{y} \tag{4.22}$$

can be constructed and interpreted as the weighted $\left(\mathbf{S}_\epsilon^{-1}\right)$ and regularised $\left(\mathbf{S}_\mathrm{a}^{-1}\right)$ normal equations of the original LES $\mathbf{F}\boldsymbol{x} = \boldsymbol{y}$. Equation 4.22 can then be solved

iteratively for $\boldsymbol{x}_{\text{rec}}$ by employing a conjugate gradient (CG) scheme. CG is the industry standard for solving equation systems with a symmetric positive definite matrix [127]. As stated above, the Hessian matrix fulfils this condition[6]. The conjugate gradient scheme does not require a full Hessian matrix, but instead only the result of its product with a vector [129]. This product is itself a concatenation of different matrix-vector products. With the aid of the optimised forward model implementation derived in Chapter 3, the product of the Hessian matrix and a vector $\boldsymbol{x}$ can be expressed in the form

$$\mathbf{C}''\boldsymbol{x} = 2\mathbf{P}^T\left(\mathbf{Q}^T\left(\mathbf{S}_\epsilon^{-1}\left(\mathbf{Q}\left(\mathbf{P}\boldsymbol{x}\right)\right)\right)\right) + 2\mathbf{S}_\text{a}^{-1}\boldsymbol{x}. \tag{4.23}$$

Equation 4.23 emphasises the importance of the adjoint operators $\mathbf{Q}^T$ and $\mathbf{P}^T$. They are executed once every CG iteration and therefore necessitate the efficient implementation derived in Section 3.2.4. Whereas $\mathbf{Q}$ and $\mathbf{Q}^T$ employ sophisticated Fourier space convolutions with pre-computed kernels, $\mathbf{P}$, $\mathbf{P}^T$, $\mathbf{S}_\text{a}^{-1}$ and $\mathbf{S}_\epsilon^{-1}$ utilise sparse matrix multiplications. Instead of having to set up the full Hessian matrix $\mathbf{C}''$, only the sparse matrices and lookup kernels for the phase mapping and its adjoint in $\mathbf{Q}$ and $\mathbf{Q}^T$ have to be kept in memory. These measures enable very efficient iteration steps during the CG calculations. The optimised forward model, which uses dedicated data structures for its operations, thereby reduces both memory consumption and computation time for an efficient reconstruction.

4.4. Diagnostics

A reconstruction result should not only consist of a reconstructed magnetisation distribution, but also diagnostic measures that can be used to assess its quality. Linear diagnostic tools are presented below, in order to allow an evaluation of the goodness of fit of specific parts of a retrieved solution and overall measures of quality. Root-mean-square diagnostics, which can be used to assess the overall closeness of a solution to a "true" magnetisation state are also introduced.

4.4.1. Optimal estimation linear diagnostics

In this section, optimal estimation linear diagnostics based on Bayes theorem are illuminated. These diagnostics make use of the interpretation of the norm weights $\mathbf{S}_\epsilon^{-1}$ and $\mathbf{S}_\text{a}^{-1}$ as inverse covariance matrices (*cf.* Eq. 4.14). This Bayesian interpretation is derived in depth in the appendix in Section A.3. It leads to the same reconstruction formula as Eq. 4.20. However, instead of only delivering an optimal solution $\boldsymbol{x}_{\text{rec}}$, it provides a complete probability density function (PDF) with an

---

[6]$\mathbf{C}''$ is, strictly speaking, only positive *semi*-definite with rank $n-1$. In practice, the single zero eigenvalue due to $\mathbf{S}_\text{a}^{-1}$ does not cause problems during the CG scheme [128].

expected value $\boldsymbol{x}_{\text{rec}}$ and a covariance matrix $\mathbf{S}_x$. This covariance matrix allows assertions to be made about the statistics of a reconstructed magnetisation state. The covariance matrix $\mathbf{S}_x$ can be identified as twice the inverse of the Hessian matrix of the cost function (*cf.* Eq. A.40):

$$\mathbf{S}_x = 2\left(\mathbf{C}''\right)^{-1} = \left(\mathbf{F}^T\mathbf{S}_\epsilon^{-1}\mathbf{F} + \mathbf{S}_{\text{a}}^{-1}\right)^{-1}. \tag{4.24}$$

It should be noted that the inverse of the covariance matrix $\mathbf{S}_x^{-1}$ is a linear function of the inverse covariance matrix of the measurements $\mathbf{S}_\epsilon^{-1}$ and the inverse covariance matrix of the *a priori* information $\mathbf{S}_{\text{a}}^{-1}$ [116]. $\mathbf{S}_x^{-1}$ should not be interpreted statistically, because $\mathbf{S}_\epsilon^{-1}$ and $\mathbf{S}_{\text{a}}^{-1}$ are generated *ad hoc* to describe the confidence in the measurements (*cf.* Eq. 4.6) and the precision matrix of the regularisation (*cf.* Eq. 4.12), respectively. However, it can be used as a diagnostic tool [72], as shown below.

In order to assess how a reconstructed magnetisation state $\boldsymbol{x}_{\text{rec}}$ depends on the true solution $\boldsymbol{x}_{\text{t}}$ and on the measurement errors $\boldsymbol{\epsilon}$ (*cf.* Eq. 2.37), Eq. 4.22 is solved for $\boldsymbol{x}_{\text{rec}}$ according to the expressions

$$\boldsymbol{x}_{\text{rec}} = \left(\mathbf{F}^T\mathbf{S}_\epsilon^{-1}\mathbf{F} + \mathbf{S}_{\text{a}}^{-1}\right)^{-1}\mathbf{F}^T\mathbf{S}_\epsilon^{-1}\boldsymbol{y} \tag{4.25}$$

$$= \mathbf{S}_x\mathbf{F}^T\mathbf{S}_\epsilon^{-1}\boldsymbol{y} \tag{4.26}$$

$$= \mathbf{S}_x\mathbf{F}^T\mathbf{S}_\epsilon^{-1}\left(\mathbf{F}\boldsymbol{x}_{\text{t}} + \boldsymbol{\epsilon}\right) \tag{4.27}$$

$$\equiv \mathbf{G}\left(\mathbf{F}\boldsymbol{x}_{\text{t}} + \boldsymbol{\epsilon}\right) \tag{4.28}$$

$$\equiv \mathbf{A}\boldsymbol{x}_{\text{t}} + \mathbf{G}\boldsymbol{\epsilon}, \tag{4.29}$$

where Eq. 2.37 was used in the second step to include a dependency on $\boldsymbol{x}_{\text{t}}$. Equation 4.29 introduces two important matrices [72, 116]: the gain matrix $\mathbf{G} \in \mathbb{R}^{n \times m}$ given by the expression

$$\mathbf{G} = \mathbf{S}_x\mathbf{F}^T\mathbf{S}_\epsilon^{-1} = \left(\mathbf{F}^T\mathbf{S}_\epsilon^{-1}\mathbf{F} + \mathbf{S}_{\text{a}}^{-1}\right)^{-1}\mathbf{F}^T\mathbf{S}_\epsilon^{-1} \tag{4.30}$$

and the averaging kernel $\mathbf{A} \in \mathbb{R}^{n \times n}$ given by the expression

$$\mathbf{A} = \mathbf{G}\mathbf{F}. \tag{4.31}$$

$\mathbf{G}$ and $\mathbf{A}$ are independent of the actual measurements $\boldsymbol{y}$ and depend only on the chosen forward model $\mathbf{F}$, the mask Ξ, the covariance matrix of the measurements $\mathbf{S}_\epsilon$ and the precision matrix $\mathbf{S}_{\text{a}}$ of the regularisation.

The gain matrix $\mathbf{G}$ maps perturbations in measured magnetic phase images onto differences in the reconstructed magnetisation state $\boldsymbol{x}_{\text{rec}}$. It can be interpreted as the regularised Moore-Penrose pseudo-inverse of the system matrix $\mathbf{F}$. Each $\text{row}_i\left(\mathbf{G}\right) \in \mathbb{R}^m$ in the gain matrix can be reshaped into a series of N_b images, one for each measured magnetic phase image. These so-called gain maps show the amplification with which the magnetic phase images and their corresponding errors

are mapped onto the magnetic vector component that is determined by each row index i. The units of the gain maps are given in 1/rad, because the normalised magnetisation distribution $\boldsymbol{m}$ is dimensionless.

The averaging kernel $\mathbf{A}$ describes how a true solution $\boldsymbol{x}_{\mathrm{t}}$ would be distorted by the reconstruction procedure. It is calculated as the product of the gain matrix $\mathbf{G}$ and the system matrix $\mathbf{F}$. As stated above, the former matrix can be interpreted as the pseudo-inverse of the latter. In the ideal case, $\mathbf{A}$ should be the identity matrix, which would correspond to perfect recovery of the true state $\boldsymbol{x}_{\mathrm{t}}$ through the reconstruction. However, as a result of rank deficiencies in $\mathbf{F}$ and because of the regularisation, this is generally not the case. A $\mathrm{row}_i\,(\mathbf{A}) \in \mathbb{R}^n$ in the averaging kernel corresponds to one of the three vector components of one voxel (specified by the row index i). It can be reshaped into a three-dimensional vector field of the same shape as the reconstructed magnetisation distribution and then describes the smoothing properties of the reconstruction. For perfect retrieval, only one component of a single voxel, which is determined by the row index i, should be non-zero, similar to a multi-dimensional delta-peak. In practice, information about the magnetisation that is contained in one vector component of one voxel will "leak" into neighbouring voxels, while possibly also diffusing into the other two vector components. Because Tikhonov regularisation of first order and not zeroth order is employed, no damping occurs in addition to the smoothing. Without damping and for an *a priori* distribution of $\boldsymbol{x}_{\mathrm{a}} = \boldsymbol{0}$, a given $\mathrm{row}_i\,(\mathbf{A})$ should always sum to one (apart from small numerical errors). Information about the true state is therefore just diffused during reconstruction and no information is lost[7]. The spatial distribution of this diffusion can be assessed by placing line scans throughout the reshaped volume of the averaging kernel distribution in different spatial directions (*cf.* Fig. 4.4). The full width at half maximum (FWHM) of these line scans can be used as a directionally dependent indicator of the resolution of the reconstruction algorithm. Structures that are smaller than the FWHM are not resolved properly. The vector field of a reshaped averaging kernel row (*cf.* Fig. 4.4a) resembles the field of a magnetic dipole with closed field line loops on both sides of the orientation axis. The negative values of the line scan in the y direction for the x component in Fig. 4.4b indicates regions where those field lines loop around and point in negative x direction.

It is also of interest to assess how measurement perturbations, which can be described by a covariance matrix $\mathbf{S}_{\mathrm{in}}$, are propagated to perturbations of a reconstructed magnetisation state (*i.e.*, reconstruction noise), as described by a covariance matrix $\mathbf{S}_{\mathrm{out}}$. The relationship between both matrices can be expressed in terms of

---

[7]In particular for an *a priori* distribution $\boldsymbol{x}_{\mathrm{a}} \neq \boldsymbol{0}$, information loss can occur because the reconstruction also partly contains the *a priori* state. For an *a priori* state that is different to the zero vector, Eq. 4.29 contains an additional term: $\boldsymbol{x}_{\mathrm{rec}} = \mathbf{A}\boldsymbol{x}_{\mathrm{t}} + (\mathbf{I}_n - \mathbf{A})\,\boldsymbol{x}_{\mathrm{a}} + \mathbf{G}\boldsymbol{\epsilon}$.
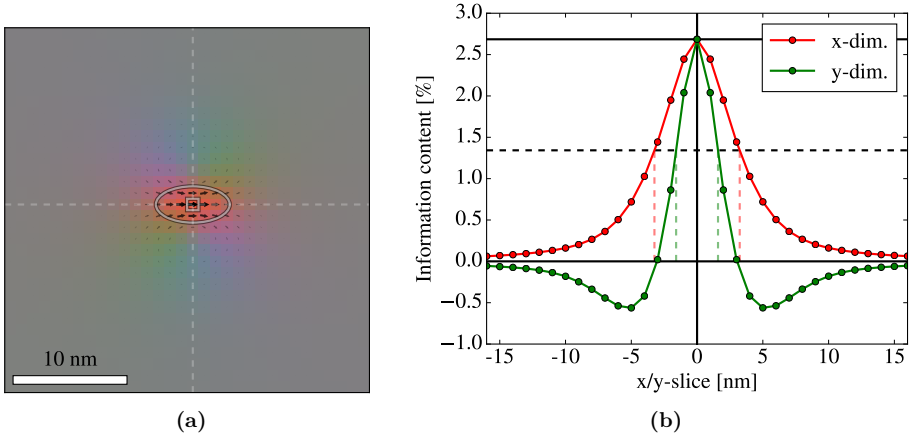
Figure 4.4.: (**a**) In-plane vector field of the reshaped averaging kernel row for the x component of a voxel located in the centre (indicated by the rectangle) of a FOV of size 32×32 pixels and $\lambda = 10^{-5}$. The position of the line scans are indicated by dashed lines in the x and y directions and shown in (**b**) in the form of linear plots. The line scans are centred on the analysed voxel at position 0, where the maximum information content (solid black line at the top) is contained. A dotted horizontal line indicates half of this value. The values of FWHM for both spatial directions are marked with coloured dashed vertical lines, whose positions are determined by linear interpolation between the nearest points. The FWHM values are indicators of the resolution in each spatial direction and are illustrated in (**a**) as the minor and major axes of an ellipse. The negative values for the variation of the x component in y direction (green plot in (**b**)), result from the closed field lines of the averaging kernel on both sides of the orientation axis. The averaging kernel for the y component at the same spatial position would deliver the same result, but rotated by 90°.

the gain matrix $\mathbf{G}$ as

$$\mathbf{S}_{\text{out}} = \mathbf{G}\mathbf{S}_{\text{in}}\mathbf{G}^T \tag{4.32}$$

$$= \mathbf{S}_x\mathbf{F}^T\mathbf{S}_\epsilon^{-1}\mathbf{S}_{\text{in}}\left(\mathbf{S}_x\mathbf{F}^T\mathbf{S}_\epsilon^{-1}\right)^T \tag{4.33}$$

$$= \mathbf{S}_x\mathbf{F}^T\mathbf{S}_\epsilon^{-1}\mathbf{S}_{\text{in}}\mathbf{S}_\epsilon^{-1}\mathbf{F}\mathbf{S}_x. \tag{4.34}$$

Equating $\mathbf{S}_{\text{in}}$ and $\mathbf{S}_\epsilon$ is only valid if $\mathbf{S}_\epsilon$ truly represents an estimate of the statistics of the measurements. However, as stated above, $\mathbf{S}_\epsilon$ is usually generated *ad hoc* by the confidence arrays Γ_b and therefore has no rigorous statistical meaning. On the assumption of uniform and uncorrelated errors in the phase images, the covariance matrix of the measurements can instead be set to $\mathbf{S}_{\text{in}} = \sigma_\epsilon^2\mathbf{I}_m$ with a measurement error variance of σ_ϵ^2, leading to the simplified formula

$$\mathbf{S}_{\text{out}} = \sigma_\epsilon^2 \cdot \mathbf{G}\mathbf{G}^T. \tag{4.35}$$

which allows a simple estimate of the reconstruction noise to be obtained. Similarly, $\mathbf{S}_{\text{in}}$ can be set up as a diagonal matrix with variances σ_b^2 for each phase image denoted by the index b, or alternatively as a full statistical description of the measurement errors, if this is available. Stronger regularisation leads to lower noise in the reconstruction because the regularisation acts like a low-pass-filter [118]. Caution is therefore advised, because stronger regularisation leads to the suppression of higher-frequency features in the true magnetic state.

All of these diagnostics depend on the calculation of the covariance matrix $\mathbf{S}_x$, which is given by Eq. 4.24 and requires the inverse of the Hessian of the cost function. Just as for the reconstruction itself, inverting $\mathbf{C}''$ is complicated, if not impossible. Instead, a set of linear equation systems

$$\mathbf{C}''\mathbf{S}_x = 2\mathbf{I}_n \tag{4.36}$$

can be constructed. Each pair of columns $\text{col}_i\left(\mathbf{I}_n\right) \in \mathbb{R}^n$ and $\text{col}_i\left(\mathbf{S}_x\right) \in \mathbb{R}^n$ represents a single LES $\mathbf{C}''\text{col}_i\left(\mathbf{S}_x\right) = 2\text{col}_i\left(\mathbf{I}_n\right)$. Each of these equation systems can be solved separately by using the conjugate gradient scheme in the same way as for the original reconstruction described in Eq. 4.23. Each column of $\text{col}_i\left(\mathbf{I}_n\right)$ corresponds to one vector component of one reconstructed voxel of the magnetisation distribution (determined by the column index i). Therefore, n LES would have to be solved by using CG methods to calculate the covariance matrix $\mathbf{S}_x$. A complete calculation is generally not desirable as a result of time and memory constraints. Instead, it is more sensible to apply the above diagnostic concepts to only selected points of interest in the reconstruction $\boldsymbol{x}_{\text{rec}}$, especially as the characteristics of neighbouring points are strongly correlated. For each point of interest, only a single row of the averaging kernel $\mathbf{A}$ or the gain matrix $\mathbf{G}$ is needed [72]:

$$\text{row}_i\left(\mathbf{G}\right) = \text{row}_i\left(\mathbf{S}_x\right)\mathbf{F}^T\mathbf{S}_\epsilon^{-1} = \text{col}_i\left(\mathbf{S}_x\right)\mathbf{F}^T\mathbf{S}_\epsilon^{-1} \tag{4.37}$$

$$\text{row}_i\left(\mathbf{A}\right) = \text{row}_i\left(\mathbf{S}_x\right)\mathbf{F}^T\mathbf{S}_\epsilon^{-1}\mathbf{F} = \text{col}_i\left(\mathbf{S}_x\right)\mathbf{F}^T\mathbf{S}_\epsilon^{-1}\mathbf{F}. \tag{4.38}$$

The rows and columns of $\mathbf{S}_x$ are identical, *i.e.*, $\text{row}_i\left(\mathbf{S}_x\right) = \text{col}_i\left(\mathbf{S}_x\right)$, because $\mathbf{S}_x$ is a covariance matrix and therefore symmetric and positive semi-definite. The reconstruction noise in a single point of interest can be calculated from the expression

$$\text{row}_i\left(\mathbf{S}_{\text{out}}\right) = \text{row}_i\left(\mathbf{G}\right)\mathbf{S}_{\text{in}}\left(\text{row}_i\left(\mathbf{G}\right)\right)^T. \tag{4.39}$$

In this way, diagnostic properties can be calculated for individual points in the reconstruction. However, their numerical complexity is similar to that of the reconstruction itself. Both the resolution of the reconstruction and the reconstruction noise depend heavily on the chosen regularisation strength (defined by the parameter λ). The choice of λ determines how well a solution fits the measurements and if it is artificially "oversmoothed" by the regularisation, as discussed in more detail below.

4.4.2. Root mean square diagnostics

Whereas the diagnostics described above allow for the detailed assessment of the statistical properties of localised points and the resolution of the reconstructed distributions $\boldsymbol{x}_{\text{rec}}$, it is often advantageous to have a global measure of the the goodness of fit of the entire distribution. If a reference magnetisation state $\boldsymbol{x}_{\text{ref}}$ exists, then simple root mean square (RMS) metrics can be used to quantify deviations of the reconstruction from the reference solution. An example of a reference solution is a "true" analytical solution $\boldsymbol{x}_{\text{t}}$, assuming this is known. In the following definitions, the non-vectorised forms of $\boldsymbol{x}_{\text{rec}}$ and $\boldsymbol{x}_{\text{ref}}$, *i.e.*, the three-dimensional magnetisation distributions $\boldsymbol{m}_{\text{rec}}$ and $\boldsymbol{m}_{\text{ref}}$ are used. For the reconstruction of an arbitrary scalar field $s_{\text{rec}}\left[i,j,k\right]$, errors from a reference $s_{\text{ref}}\left[i,j,k\right]$ can be described by using a single metric

$$\epsilon_{\text{tot}} = \sqrt{\frac{\sum_{i,j,k}\left\|s_{\text{rec}}\left[i,j,k\right] - s_{\text{ref}}\left[i,j,k\right]\right\|^2}{\sum_{i,j,k}\left\|s_{\text{ref}}\left[i,j,k\right]\right\|^2}}. \tag{4.40}$$

In contrast, errors in a vector field can be described either by their direction or by their magnitude. A decision about which of these parameters is more important depends on the application at hand. Appropriate RMS metrics for these properties have been described by Kemp et al. [70] and take the forms

$$\epsilon_{\text{mag}} = \sqrt{\frac{\sum_{i,j,k}\left(\left\|\boldsymbol{m}_{\text{rec}}\left[i,j,k\right]\right\| - \left\|\boldsymbol{m}_{\text{ref}}\left[i,j,k\right]\right\|\right)^2}{\sum_{i,j,k}\left\|\boldsymbol{m}_{\text{ref}}\left[i,j,k\right]\right\|^2}} \tag{4.41}$$

for the normalised errors in magnitude[8] and

$$\epsilon_{\text{dir}} = \frac{1}{\pi}\sqrt{\frac{1}{N_x N_y N_z}\sum_{i,j,k}\left[\cos^{-1}\left(\frac{\boldsymbol{m}_{\text{ref}}\left[i,j,k\right] \cdot \boldsymbol{m}_{\text{rec}}\left[i,j,k\right]}{\left\|\boldsymbol{m}_{\text{ref}}\left[i,j,k\right]\right\|\left\|\boldsymbol{m}_{\text{rec}}\left[i,j,k\right]\right\|}\right)\right]^2} \tag{4.42}$$

---

[8]The index "mag" in this case has a double meaning as both "magnitude" and "magnetisation".

for the directional error. The latter error is defined as the RMS of the angle between the reference vector and the reconstructed vector at each voxel, divided by π to reflect a fractional error and not an angle in radians. These metrics are useful for investigating the different artefacts that can influence a reconstruction in a controlled, simulated environment, if an unperturbed reference state $\boldsymbol{x}_{\mathrm{ref}}$ is known. Some of these artefacts are discussed in Chapters 5 and 6.

4.5. Reconstructibility and null spaces

As mentioned in Section 4.3, the null spaces of the forward model and its sub-matrices play an important role in determining which magnetisation states can be retrieved and which are "invisible" to the reconstruction, as they do not produce a magnetic phase shift. In this section, the null spaces of the projection matrix $\mathbf{P}$ and the phase mapping matrix $\mathbf{Q}$ are illuminated.

4.5.1. The null space of the projection matrix

The null space of the complete projection matrix $\mathbf{P}$ depends directly on the null spaces of the sub-matrices $\mathbf{P}_b$ for each projection direction and can be understood in an intuitive way. The projection process that is described by each sub-matrix $\mathbf{P}_b$ can be split into two steps. Each step results in a loss of information, which leads to a contribution to the null space, as follows:

First, the vector field is projected in three-dimensional space (xyz) along a chosen projection direction. The resulting projected vector field resides in a two-dimensional subspace of three-dimensional space. The projection plane is oriented perpendicular to the projection direction and all of the information about the distribution along this direction is lost upon projection. The resulting vector field still possesses three vector components (xyz). The null space contains all of the vector field distributions that sum up to zero along the projection direction.

A transformation from the three-dimensional coordinate system (xyz) to a two-dimensional coordinate system (uv), which is specific to the current projection, is then performed. The third component of the vector field, which is perpendicular to the projection plane uv, is dropped. The perpendicular component does not contribute to the phase mapping (*cf.* Eq. 2.34) and always lies in the null space of the phase mapping matrix $\mathbf{Q}$. Dropping this component during the projection instead of keeping it as input for $\mathbf{Q}$ is computationally efficient[9]. The null space therefore also includes all distributions with vectors that are solely oriented along the projection direction.

---

[9]This procedure effectively reduces the dimension of $\boldsymbol{x}_{\mathrm{pr}}$ by one third from $3N_uN_v$ to $2N_uN_v$ and "shifts the blame" for the information loss of the third vector component from the phase mapping $\mathbf{Q}$ to the projection $\mathbf{P}$.

This split into two steps is purely theoretical and is used to illustrate the two contributions to the null space. In practice, it is performed in one step during the projection using $\mathbf{P}_b$. A mathematical description of both steps can be found in Section A.4 in the appendix, where $\mathbf{P}_b$ is split into two sub-matrices.

A magnetisation distribution therefore lies in the null space of the projection if the magnetisation vectors are either parallel to the projection direction or zero, when they are summed up along the projection direction. The null space of $\mathbf{P}_b \in \mathbb{R}^{2N_u N_v \times 3N_x N_y N_z}$ has nullity $\operatorname{rank}\left(\operatorname{null}\left(\mathbf{P}_b\right)\right) = 3N_x N_y N_z - 2N_u N_v$. An illustrative example of such a null space is shown in Fig. 4.5a.

(a)   **(b)**
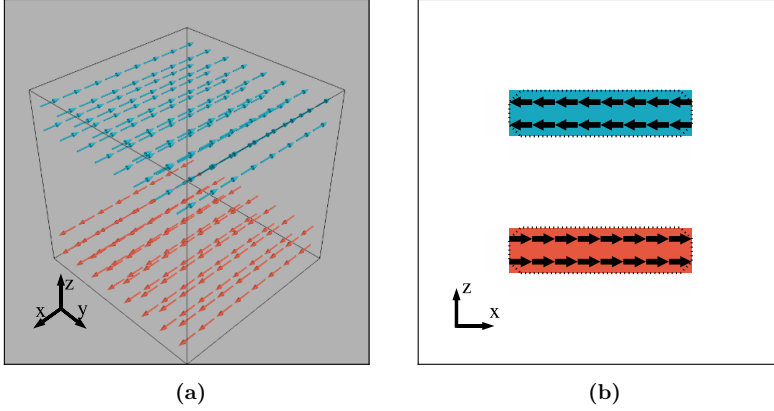
Figure 4.5.: (**a**) shows two slabs that are magnetised in the positive and negative x directions, respectively. The distribution lies in the null space of a projection along the z direction, due to its moments cancelling in the projection direction. It also lies in the null space of a projection along the x direction because the projected moments are parallel to the projection direction. Of the three main axes, only a projection along the y direction, which is shown in (**b**) is in the range of the corresponding projection matrix $\mathbf{P}_b$, *i.e.*, $\boldsymbol{x} \in \operatorname{range}\left(\mathbf{P}_b\right)$.

A distribution that is invisible in one specific projection direction, specified by $\mathbf{P}_b$, is not necessarily invisible for *all* projection directions. The complete projection matrix $\mathbf{P}$ (defined in Eq. 3.12) incorporates b projection directions, each of which has its own projection sub-matrix $\mathbf{P}_b$ and null space $\operatorname{null}\left(\mathbf{P}_b\right)$. In order to guarantee that a magnetisation state $\boldsymbol{x}$ lies outside the null space of the complete projection matrix $\mathbf{P}$, *i.e.* that it is not completely invisible for the forward model, $\boldsymbol{x}$ has to lie in the range (or image) of at least one sub-matrix[10] $\mathbf{P}_b$, *i.e.*, $\boldsymbol{x} \in \operatorname{range}\left(\mathbf{P}_b\right)$.

---

[10]$\boldsymbol{x} \in \operatorname{range}\left(\mathbf{P}\right)$ only means that information about $\boldsymbol{x}$ can be obtained with the projection matrix $\mathbf{P}$ *at all* and that the distribution is not completely invisible. However, it does not automatically guarantee a satisfactory reconstruction result.

For a scalar field, a complete[11] series of projections around one tilt axis can be described by the Radon transformation [130]. An inverse Radon transformation can then be used to reconstruct the original three-dimensional distribution analytically. The null space for a single tilt series is trivial in the scalar case, as a complete tilt series around one tilt axis guarantees that all distributions are visible. Vector field reconstructions are more complicated. They have been examined by Hauck [131] for two-dimensional vector fields. A generalisation to three-dimensional fields can be made by applying the rules for the two-dimensional case for each slice that is perpendicular to the tilt axis. Although the projection of a scalar field can be expressed intuitively as a simple integral along the projection direction, two kinds of interactions have to be distinguished for a vector field [53]:

- A longitudinal interaction, which can be expressed mathematically as a scalar product of the vector field and the tangential vector of the projection direction.

- A transversal interaction, which can be expressed as a vector product of the vector field and the tangential vector of the projection direction.

Using a Helmholtz decomposition [132], a fundamental theorem of vector calculus, any three-dimensional, rapidly decaying and smooth vector field[12] can be expressed as a sum of a curl-free ("irrotational") and a divergence-free ("solenoidal") vector field. For the two-dimensional case, Hauck was able to show that, for a longitudinal interaction with a vector field and a complete tilt series, only the solenoidal contribution can be reconstructed [131]. In contrast, for a transversal interaction only the irrotational contribution can be reconstructed, while no information about the curls in the vector field are contained in the projections.

As mentioned above, when executing a set of projections described by $\mathbf{P}$, the vector component along the projection direction vanishes and only components that lie perpendicular to it are relevant. Therefore, $\mathbf{P}$ has to describe a set of transversal interactions. An example that showcases the inability to map the curls of a vector field is shown in Fig. 4.6a. A magnetised cylinder supports a vortex distribution that is aligned along its symmetry axis. For a tilt series acquired perpendicular to the cylinder axis, the sum of the magnetisation vectors is zero for all of the projection directions. The distribution lies in the null space of all single image projection matrices $\mathbf{P}_b$ and is therefore invisible for the complete projection matrix $\mathbf{P}$. In general, a single tilt series will always be insensitive to any curls in the vector field around the tilt axis.

In order to circumvent this limitation, a second tilt axis, which is ideally perpendicular to the first tilt axis, is required. Any curl that is invisible in the first series appears as an irrotational contribution in the second tilt series and *vice versa*. The

---

[11]Here, "complete" means that the projection is known for every angle around the chosen tilt axis. In practice, only a finite number of projections is available, which leads to artefacts in the reconstruction.

[12]This assumption is justified for localised magnetisation distributions.

(a)   (b)
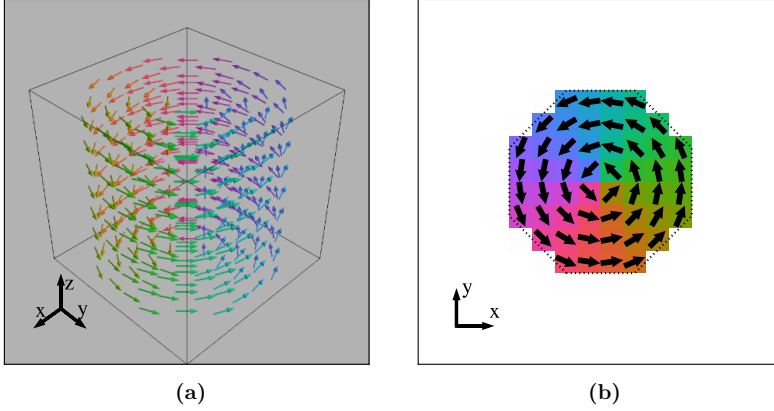
Figure 4.6.: (a) shows a magnetised disc, which supports a vortex distribution that is oriented along the z axis. A slice in the xy plane is illustrated in **(b)**. This distribution is invisible to all projections that are perpendicular to the z direction because all of the moments along these lines add up to zero or are oriented along the projection direction.

null space of the complete projection matrix $\mathbf{P}$ therefore becomes trivial when two orthogonal tilt series are available.

The results of this section can be summarised as follows:

- A single projection $\mathbf{P}_b$ is insensitive to a magnetisation distribution if the vectors that are summed along the projection direction are zero or have no components in the projection plane.

- A complete projection matrix $\mathbf{P}$ corresponding to a single tilt series is insensitive to curls of the vector field around the tilt axis.

- A complete projection matrix $\mathbf{P}$ describing two (ideally orthogonal) tilt series has a trivial null space. No non-zero magnetisation distribution is mapped onto the zero vector.

4.5.2. The null space of the phase mapping matrix

Even after guaranteeing that the null space of the projection matrix $\mathbf{P}$ is trivial, a projected magnetisation distribution $\boldsymbol{x}_{\mathrm{pr}} \neq \mathbf{0}$ can still be mapped onto the zero vector by the phase mapping matrix $\mathbf{Q}$. If a projected distribution $\boldsymbol{x}_{\mathrm{pr}} = \mathbf{P}\boldsymbol{x} \neq \mathbf{0}$ lies in the null space of the phase mapping matrix $\mathbf{Q}$, then the original distribution $\boldsymbol{x}$ automatically lies in the null space of the complete system matrix $\mathbf{F}$. The mathematical expression for this relation is:

$$\mathbf{P}\boldsymbol{x} = \boldsymbol{x}_{\mathrm{pr}} \in \mathrm{null}\,(\mathbf{Q}) \Leftrightarrow \mathbf{Q}\mathbf{P}\boldsymbol{x} = \mathbf{0} \Leftrightarrow \boldsymbol{x} \in \mathrm{null}\,(\mathbf{Q}\mathbf{P}) \Leftrightarrow \boldsymbol{x} \in \mathrm{null}\,(\mathbf{F})\,. \quad (4.43)$$

The matrix $\mathbf{Q}$ and its null space are described in this section. As $\mathrm{null}\,(\mathbf{Q})$ is not as intuitive as the null space for the projection, it is analysed by singular value decomposition (SVD). A SVD is only feasible for matrices that are not too large. Without loss of generality, it can be assumed that all of the axes have the same size $(N_x = N_y = N_z = N_u = N_v \equiv N)$ so that the phase mapping matrix takes the form $\mathbf{Q} \in \mathbb{R}^{N^2 \times 2N^2}$ and the number of entries scales as $\mathcal{O}\,(N^4)$. A SVD of the phase mapping matrix can be expressed in the form

$$\mathbf{Q} = \mathbf{U}\boldsymbol{\Sigma}\mathbf{V}^T, \tag{4.44}$$

where $\boldsymbol{\Sigma} \in \mathbb{R}^{N^2 \times 2N^2}$ is a diagonal matrix with the singular values on its diagonal, while $\mathbf{U} \in \mathbb{R}^{N^2 \times N^2}$ and $\mathbf{V} \in \mathbb{R}^{2N^2 \times 2N^2}$ are unitary matrices, whose columns contain the left and right singular vectors, respectively. The null space of $\mathbf{Q}$ cannot be trivial because it maps from the two-dimensional vector field onto a two-dimensional scalar field, $i.e.$, there are twice as many unknowns as there are measurements. According to the rank-nullity theorem ($cf.$ Eq. 4.4), the null space and range (or image) must therefore have equal sizes, as reflected in the singular value matrix

$$\boldsymbol{\Sigma} = \begin{pmatrix} \sigma_1 & \cdots & 0 & 0 & \cdots & 0 \\ \vdots & \ddots & \vdots & \vdots & \ddots & \vdots \\ 0 & \cdots & \sigma_{N^2} & 0 & \cdots & 0 \end{pmatrix}. \tag{4.45}$$

$\boldsymbol{\Sigma}$ has exactly N^2 unique non-zero singular values on its diagonal and N^2 zero columns afterwards. Similarly, the first N^2 columns of $\mathbf{V}$ represent the singular vectors, while the second half of column vectors comprise a basis of the null space, $i.e.$, that every element of the null space can be expressed as a linear combination of these basis vectors. All of the column vectors of $\mathbf{V}$ can be reshaped into two-dimensional projected magnetisation distributions. These distributions can be used to illustrate the range and the null space of the phase mapping matrix $\mathbf{Q}$. They determine which parts of a magnetisation distribution contribute the most to the phase and which parts do not generate a contribution to the phase.

Figure 4.7 shows the singular values for a phase mapping matrix $\mathbf{Q} \in \mathbb{R}^{256 \times 512}$ that operates on a FOV of 16×16 pixels. Each singular value has a corresponding singular vector, which can be reshaped into an in-plane vector field of size 16×16 pixels. Applying the phase mapping matrix $\mathbf{Q}$ to each of these vector fields reveals the phase contribution of the corresponding singular value. The maximum of the absolute value of the phase is also shown in Fig. 4.7. Both curves exhibit the same monotonically decreasing trend, with high singular values being linked to distributions which produce larger phase differences. Figure 4.8 illustrates examples of the projected magnetisation distributions, into which the singular vectors can be reshaped. Familiar shapes such as vortex structures or largely uniformly magnetised distributions can be recognised as the main contributors (in the first row of Fig. 4.8). With decreasing singular value, the phase contribution diminishes. At the same time, the spatial frequency with which the magnetisation distribution varies across the FOV
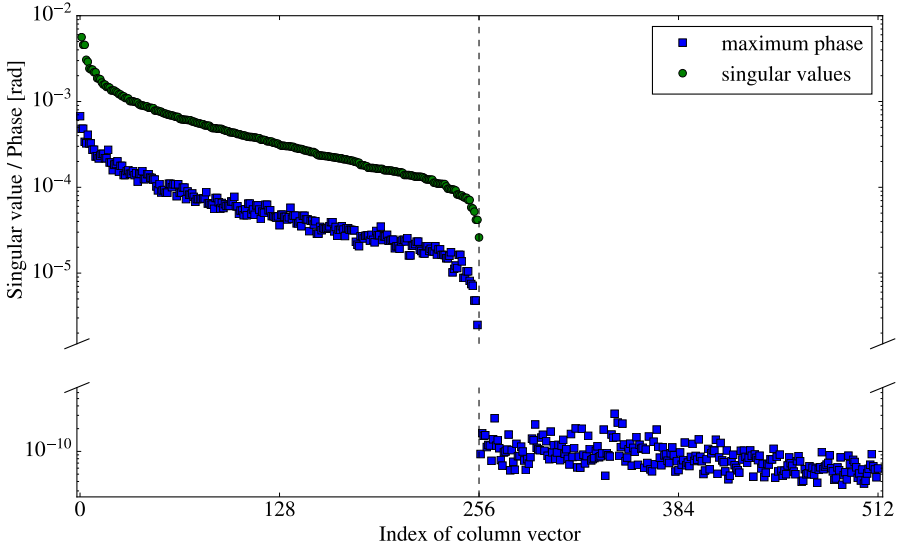
Figure 4.7.: Singular value decomposition of a phase mapping matrix $\mathbf{Q} \in \mathbb{R}^{256 \times 512}$ for an axis length of $N = 16$. The 256 singular values are shown as green circles. The maximum of the absolute phase contribution that the corresponding singular vector distribution generates is shown as blue squares on the left. Similarly, the phase contribution of all 256 null space basis vector distributions is shown. They are labelled with indices from 257 to 512 and only generate numerical noise in the range of 10^{-10} rad, which is effectively zero, as expected.

increases. The frequency of the spatial variation eventually reaches the sampling frequency, which leads to vector field directions that vary from pixel to pixel. The resulting checkerboard pattern that arises can be interpreted as two separate magnetisation distributions (on the "white" and "black" tiles of the checkerboard) with similar magnitudes but opposite directions. The frequency of the spatial variation for these two opposite distributions decreases until, for the last three singular values, they are reminiscent of the homogeneous distributions and the vortex from the three highest-valued singular values (see the second row in Fig. 4.8). This situation creates a symmetry, which reflects the symmetrical distribution of the singular values (marked green in Fig. 4.7). The opposite nature of the two checkerboard distributions for the lower-valued singular values creates phase distributions that nearly cancel each other out. In practice, the regularisation, which has to be chosen appropriately for the present level of noise, suppresses these singular vector contributions due to their high spatial frequencies. The determining factor for where this singular value "cut-off" takes place is equivalent to the resolution derived from the averaging kernel (*cf.* Section 4.4.1). The checkerboard patterns strongly conflict with the smoothness constraint and are energetically extremely unfavourable. It therefore
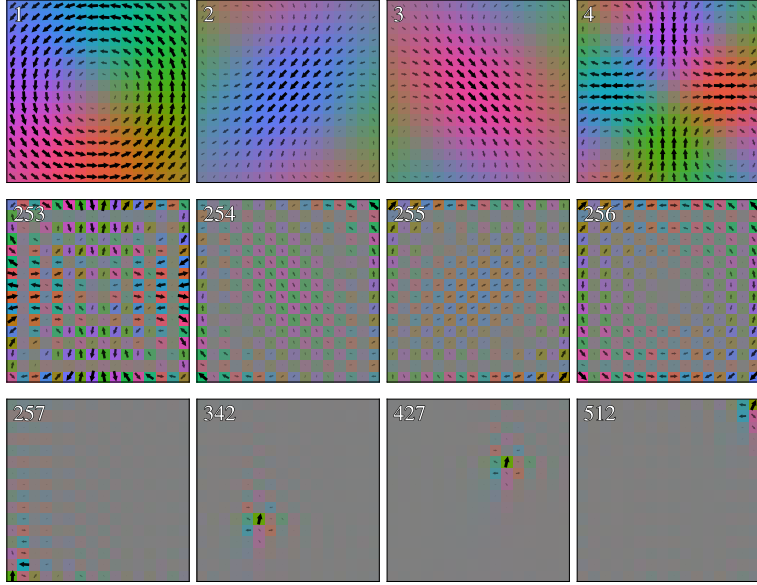
Figure 4.8.: Examples of singular vectors and null space basis vectors from the SVD of Fig. 4.7. The first row shows distributions that belong to the four highest-valued singular values. The second row shows distributions that belong to the four lowest-valued singular values, which show a distinct checkerboard pattern. The distributions on the "black" and "white" tiles of this pattern show similarities to distributions corresponding to the highest singular values. The last row shows four arbitrary reshaped basis vectors of the null space.

makes sense to prohibit them from mixing into the reconstructed distribution.

The null space of $\mathbf{Q}$ is independent of regularisation or noise and is determined by the basis that is spanned by the last N^2 columns of $\mathbf{V}$, some of which are illustrated in the last row of Fig. 4.8 in reshaped form. Even though the null space basis vectors look non-intuitive on their own, recognisable structures can be built by superposition. One example is that of a Halbach disc of first order [133, 134], whose magnetisation distribution points radially outwards from the centre and which is illustrated in Fig. 4.9a. The vectorised Halbach distribution $\boldsymbol{x}_{\mathrm{hal}}$ can be expressed as a superposition of the column vectors of $\mathbf{V}$. Figure 4.9b shows the coefficients $\boldsymbol{c}_{\mathrm{hal}}$ for the superposition, which can be calculated as:

$$\boldsymbol{x}_{\mathrm{hal}} = \mathbf{V}\boldsymbol{c}_{\mathrm{hal}} \quad \Leftrightarrow \quad \boldsymbol{c}_{\mathrm{hal}} = \mathbf{V}^T\boldsymbol{x}_{\mathrm{hal}}. \tag{4.46}$$

$\boldsymbol{x}_{\mathrm{hal}}$ can be expressed exclusively by the null space basis, *i.e.*, the Halbach distribution does not produce any phase contribution and is therefore invisible to the phase mapping matrix $\mathbf{Q}$. Mathematically, the null space can not enter the solution of

the reconstruction. The low-value singular values on the other hand will dominate the solution unless they are dampened by the regularisation. As such, the actual, regularised solution is an approximation of the "true solution", consisting only of the singular vectors.
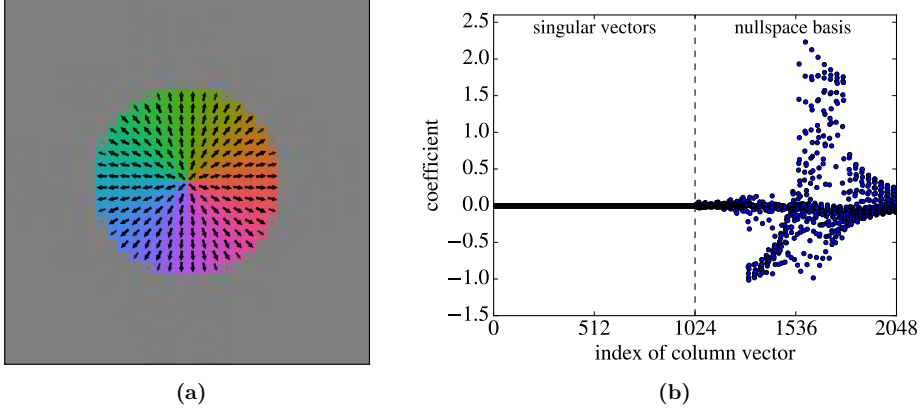
Figure 4.9.: (a) Magnetic configuration of a Halbach cylinder of first order (in which the magnetisation rotates once while going around the cylinder, causing it to always point radially outwards) with a radius of $8\,\mathrm{px}$ in a FOV of $32 \times 32\,\mathrm{px}$. **(b)** Decomposition of the vectorised Halbach cylinder distribution into a linear combination of singular vectors and the null space basis, showing the coefficients for the respective vectors. The distribution can be expressed exclusively by the null space basis, *i.e.*, it produces no phase.

4.6. Summary

In this chapter, the principles for the implementation of an efficient model-based, iterative reconstruction algorithm for solving the inverse problem of reconstructing a magnetisation distribution from a set of electron optical phase images were derived. The initially ill-posed problem was first replaced by a least-squares minimisation problem. First order Tikhonov regularisation, motivated by minimisation of the exchange energy of the magnetisation distribution, was applied. A mask was introduced to localise magnetised objects and to further decrease the number of unknowns. All of these measures were combined into a cost function, whose minimisation is facilitated by conjugate gradient methods and which replaces the original problem. Diagnostic tools were introduced to assess the quality of the reconstruction. Root mean square diagnostics can be used to examine the closeness of the solution to a reference state while optimal estimation linear diagnostics are employed to judge the goodness-of-fit at specific points of interest. An averaging

kernel **A** can be used to calculate the resolution of the reconstruction, which depends directly on the chosen regularisation strength. A gain matrix **G** determines the influence of measurement errors in specific phase image pixels on the reconstructed distribution. The retrievability of magnetisation distributions was evaluated by examining the null spaces of the projection matrix **P** and the phase mapping matrix **Q**. It was established that two (optimally orthogonal) tilt series are required to trivialise the null space of the projection, in particular if curls are present in the magnetisation vector field. The phase mapping matrix **Q** was examined by means of a SVD. Singular vectors that are linked to the lower values exhibit a checkerboard pattern. The corresponding magnetisation distributions produce only a minimal phase contribution and conflict strongly with the smoothness constraint of the regularisation. This situation emphasises the significant influence of the regularisation strength on the resolution of the reconstruction. A non-trivial null space of **Q** describes magnetisation distributions that cannot be reconstructed using the MBIR algorithm.

5. Magnetisation reconstruction in two dimensions

In general, two, optimally orthogonal, tilt series of magnetic phase images are necessary for a full, three-dimensional reconstruction of the magnetisation distribution in a given sample, as discussed in Section 4.5. However, even a single magnetic phase image provides insight into the magnetic state of the sample. Although spatial information in the projection direction and the vector component of the magnetisation that is oriented perpendicular to the projection plane are lost upon projection, the in-plane components of the projected magnetisation distribution can still, in principle, be reconstructed. For a two-dimensional material, *e.g.*, a lithographically patterned structure, a measurement of the projected in-plane magnetisation may be sufficient to understand the magnetic microstructure of the material. However, the fidelity of such a reconstructed magnetisation state depends on many parameters, including:

- the chosen regularisation strength and the associated averaging kernel;
- the measurement noise in the magnetic phase images;
- the chosen mask that defines position and size of the magnetised region;
- the presence of magnetisation sources outside the FOV;
- other artefacts in the magnetic phase images.

All of these factors can result in the presence of artefacts in the reconstruction or deviations from the true magnetic state if they are not addressed appropriately. This chapter discusses all of these parameters, assesses the nature of the corresponding artefacts and introduces measures that can be used to identify or suppress them. All of these influences affect both two-dimensional and three-dimensional reconstructions. Here, they are tackled for the two-dimensional case, because their visualisation in two dimensions is more intuitive and easier to interpret than in three dimensions. Chapter 6 deals with artefacts that are specific to the three-dimensional case.

For a single magnetic phase image, *i.e.*, for $N_b = 1$, with the projection direction chosen to be the z direction, the forward model is reduced to the expression

$$\boldsymbol{y} = \mathbf{Q}\boldsymbol{x}_{\mathrm{pr}} \tag{5.1}$$

and the retrieval target is the two-dimensional projected in-plane magnetisation $\boldsymbol{x}_{\mathrm{pr}}$. The phase mapping matrix $\mathbf{Q}$ consists of only one sub-matrix (*cf.* Eq. 3.16). The image index b can therefore be dropped and $\mathbf{Q}$ is obtained directly from Eq. 3.17 in the form

$$\mathbf{Q} = \begin{pmatrix} \mathbf{Q}_u & \mathbf{Q}_v \end{pmatrix}. \tag{5.2}$$

5.1. Resolution and reconstruction noise

As mentioned in Section 4.4, the resolution of a reconstruction is influenced significantly by the chosen regularisation strength. Stronger regularisation, which is controlled by the regularisation parameter λ, suppresses high frequency contributions to the reconstructed magnetisation distribution. On the one hand, strong regularisation diminishes noise in the reconstruction resulting from noise in the magnetic phase image (described as reconstruction noise $\mathbf{S}_{\mathrm{out}}$ in Eq. 4.32). On the other hand, over-regularisation risks smoothing out relevant features in the magnetisation distribution.

In this section, the dependence of both the spatial resolution and the noise in a reconstruction in dependence of the chosen regularisation parameter λ are assessed. As outlined in Section 4.4, the averaging kernel $\mathbf{A}$ does not depend on the measurements. For illustrative purposes, a magnetic phase image resulting from a simulated 180° magnetic domain boundary was used as an example of a magnetic feature, for which the resolution of the reconstruction is very important. The original magnetisation distribution and the resulting magnetic phase image, which was calculated by applying the RDFC phase mapping approach (*cf.* Section 3.2.4), are shown in Fig. 5.1. The magnetic phase image shown in Fig. 5.1b was used as input for the MBIR algorithm described in Chapter 4 while varying the regularisation parameter λ over several orders of magnitude from 10^{-8} to 10^{-2}.

The top row of Fig. 5.2 shows the resulting reconstructed projected in-plane magnetisation distributions for four different regularisation parameters λ. The middle row shows the corresponding averaging kernel rows (*cf.* Eq. 4.38) for the y component for a point in the centre of the FOV in their reshaped forms as vector fields. The relevant point is marked by a square. The resulting gain maps (*cf.* Eq. 4.37) are shown in the third row.

The vector fields of the corresponding averaging kernel rows are each very similar to the field of a magnetic dipole, *i.e.*, they exhibit closed field line loops on both sides of the orientation axis. For low values of λ, this dipole field is localised on the point of interest and quickly decays to zero. The FWHM of the averaging kernel rows in the x and y directions determine the best possible spatial resolution of the reconstruction (*cf.* Section 4.4.1). The spatial resolutions in x and y direction are visualised as the minor and major axes of an ellipse and increase with regularisation strength λ. This increase manifests itself as a smoothing of the originally sharp
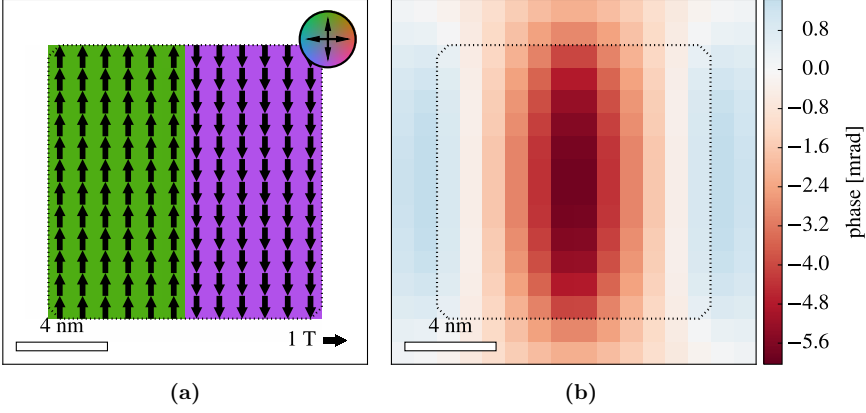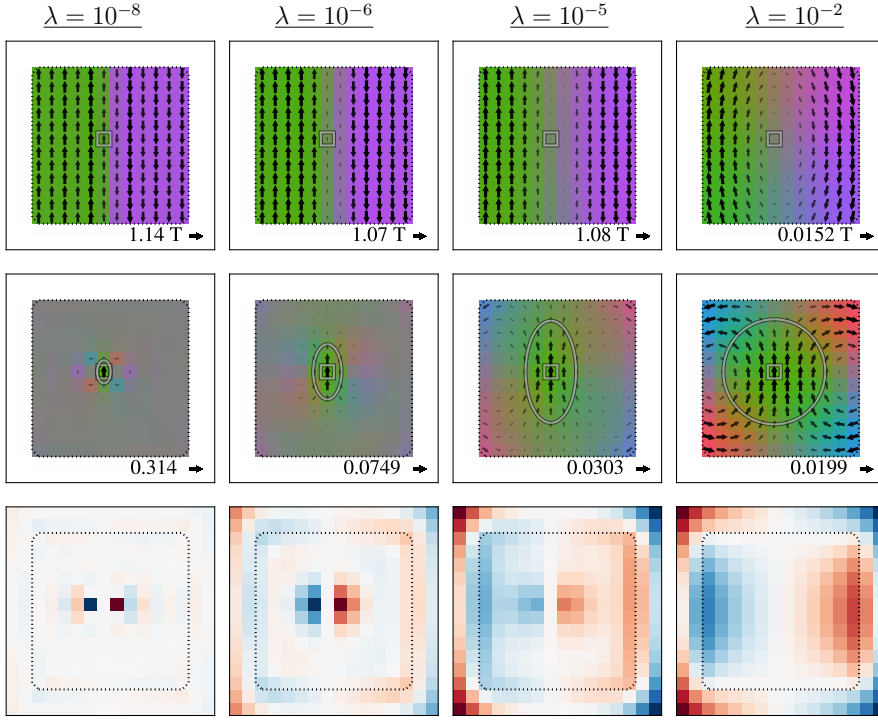
Figure 5.1.: (**a**) In-plane magnetisation distribution in a $12 \times 12 \times 1\,\mathrm{nm}^3$ slab, which contains a magnetic domain wall at its centre. The saturation magnetic induction was set to $1\,\mathrm{T}$ (*cf.* the arrow at the lower right corner). The FOV is 16×16 pixels with a grid spacing of $a = 1\,\mathrm{nm}$. (**b**) The resulting magnetic phase image, calculated using the forward model for the RDFC phase mapping approach.

domain wall along the y axis. The width of this region is proportional to the spatial resolution of the y component in the x direction in the reconstruction and can be seen in the first row of Fig. 5.2. As mentioned in Section 4.4.1, this smoothing effect can be regarded as a diffusion of information. For very high values of λ, such as 10^{-2}, the magnetisation distribution is completely smoothed away, as indicated by the low maximum magnetisation amplitude of $0.0152\,\mathrm{T}$ in the rightmost image of the first row of Fig. 5.2.

With increasing λ, the averaging kernel row size approaches the dimensions of the magnetised object. In contrast to the use of lower values of λ, the dipole field of the averaging kernel row can then not decay sufficiently before reaching the borders of the mask and the field lines cannot close properly. The averaging kernel row is then forced to compensate the missing regions outside the mask Ξ by increasing the vector field inside the mask near its borders. This compensation is visible as an increase in the vector field of the averaging kernel row for $\lambda = 10^{-5}$ at the corners and for $\lambda = 10^{-2}$ also along the edges.

A similar effect can be seen in the gain maps. For a low value of the regularisation parameter λ, the main information sources for the reconstruction of the chosen magnetisation vector component at each point of interest are the directly adjacent pixels. These pixels have the highest gain values, as can be seen, *e.g.*, in the first image in the last row of Fig. 5.2. A higher regularisation parameter results in a flatter gain distribution. Pixels that are further away from the point of interest are then included, effectively resulting in averaging over a larger region.

Figure 5.2.: Reconstructed magnetisation distributions for a simplified magnetic domain wall for four different regularisation parameters λ are shown in the first row. A central point of interest is marked by a square. Corresponding averaging kernel rows, calculated for the y vector component and reshaped into two-dimensional vector fields, are displayed in the second row. The axes of the marked ellipses define the FWHM of the averaging kernel, as described in Fig. 4.4. An increase of the regularisation parameter leads to an increase in the size of the averaging kernel and to a smoothing effect. The last row shows the gain maps, which determine the influence of the pixels in the magnetic phase image on the reconstruction of the point of interest. The gain maps are normalised to the highest value for each map and do not have the same scale. An arrow in the lower right corner of each vector field indicates the scale of the largest vector.
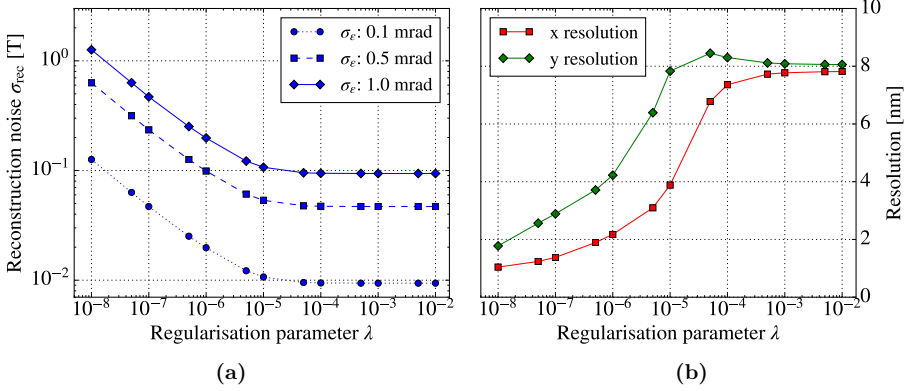
Figure 5.3.: Dependence of reconstruction noise and maximum spatial resolution on λ for the point of interest shown in Fig. 5.2. (**a**) Reconstruction noise σ_{rec} for three different levels of measurement noise σ_ϵ. (**b**) Maximum spatial resolution in the x and y directions for the y component of the vector field at the central point of interest, marked in Fig. 5.2. Both plots show saturation for larger values of the regularisation parameter λ.

Figure 5.3 plots the maximum spatial resolution in the x and y directions, determined from the averaging kernel row for the y component of the central point of interest shown in Fig. 5.2. The reconstruction noise σ_{rec} is also shown for three different levels of Gaussian measurement noise σ_ϵ (0.1, 0.5 and 1 mrad), according to Eq. 4.35.

An increase in the regularisation parameter leads to poorer spatial resolution of the reconstruction in the x and y directions. For higher regularisation parameters, the spatial resolution shows a saturation behaviour, as the averaging kernel row cannot expand any further (*cf.* the last image in the second row of Fig. 5.2). Here, saturation occurs at approximately $\lambda = 10^{-4}$ for the spatial resolution in the x direction. It already occurs at $\lambda = 10^{-5}$ for the spatial resolution in the y direction, as a result of the elliptical shape of the averaging kernel row, which has a larger half axis in y direction[1].

The reconstruction noise σ_{rec} is directly proportional to the measurement noise σ_ϵ and decreases linearly for lower regularisation parameters λ when plotted on a double logarithmic scale. Here, saturation of σ_{rec} begins at values of λ between 10^{-4} and 10^{-5}. The proportionality between the reconstruction noise σ_{rec} and the measurement error noise σ_ϵ is maintained, *i.e.*, the graphs in Fig. 5.3a stay equidistant from each other vertically.

---

[1] The small peak for the y direction at approximately $\lambda = 5 \cdot 10^{-5}$ appears to be an artefact that results from the way that the FWHM is calculated (*cf.* Fig. 4.4b).

Figures 5.2 and 5.3 show that an increase in regularisation parameter λ is accompanied by a decrease in reconstruction noise σ_{rec} and by poorer spatial resolutions. A trade-off between these quantities is required in order to achieve the best possible reconstruction. The reconstruction noise must be sufficiently low to guarantee a good signal-to-noise ratio in the reconstructed magnetisation distribution, without sacrificing too much spatial resolution by enforcing too much smoothness through the regularisation. The optimal regularisation parameter λ depends on the level of noise in the input phase images and must be identified on a case by case basis. The next section discusses the influence of noise on the reconstruction in greater depth and describes a method for finding an optimal value of λ.

Both, spatial resolution and reconstruction noise are limited by the size of the mask Ξ for large regularisation parameters. In practice, this situation should be avoided, because it usually signifies over-regularisation of the problem.

5.2. Influence of Gaussian measurement noise

As discussed above, finding the optimal regularisation parameter λ is not a trivial task. The required regularisation parameter primarily depends on the level of noise in the magnetic phase images that are used as input to the reconstruction. An approach that can be used to find an optimal value for λ is discussed in this section by examining the reconstruction for different levels of Gaussian noise. This and the following sections focus on two test cases, which are similar to those used in Section 3.3:

- A homogeneously magnetised disc in the xy plane with its magnetisation directed at an angle of 45° (or $\pi/4$) to the x axis (*cf.* Eq. 2.20);

- A disc that is magnetised in a counter-clockwise vortex state, with a smooth vortex core at its centre (*cf.* Eq. 2.29).

Each disc has a radius of $R = 8\,\mathrm{nm}$, a thickness of $t = 1\,\mathrm{nm}$ and is placed in a volume of size $32 \times 32 \times 1\,\mathrm{nm}^3$. The z axis is both the symmetry axis and the projection direction. The magnetisation distributions represent different possible behaviours of a vector field, *i.e.* curl-free and divergence-free fields, as described by a Helmholtz decomposition (*cf.* Section 4.5). They are displayed in Fig. 5.4 alongside corresponding magnetic phase images, which were calculated using the RDFC approach.

In order to assess the influence of noise on the dependence of the reconstruction on the regularisation parameter λ, Gaussian noise levels σ_ϵ of between 0 and $1.0\,\mathrm{mrad}$ in steps of $0.1\,\mathrm{mrad}$ were added to the magnetic phase images shown in Figs. 5.4b and 5.4d. For a maximum magnetic phase shift of roughly $10\,\mathrm{mrad}$ in Fig. 5.4d, these values for σ_ϵ correspond to up to 10% noise. Regularisation parameters of between $\lambda = 10^{-8}$ and $\lambda = 10^{-3}$ were used. Each combination of noise level σ_ϵ and
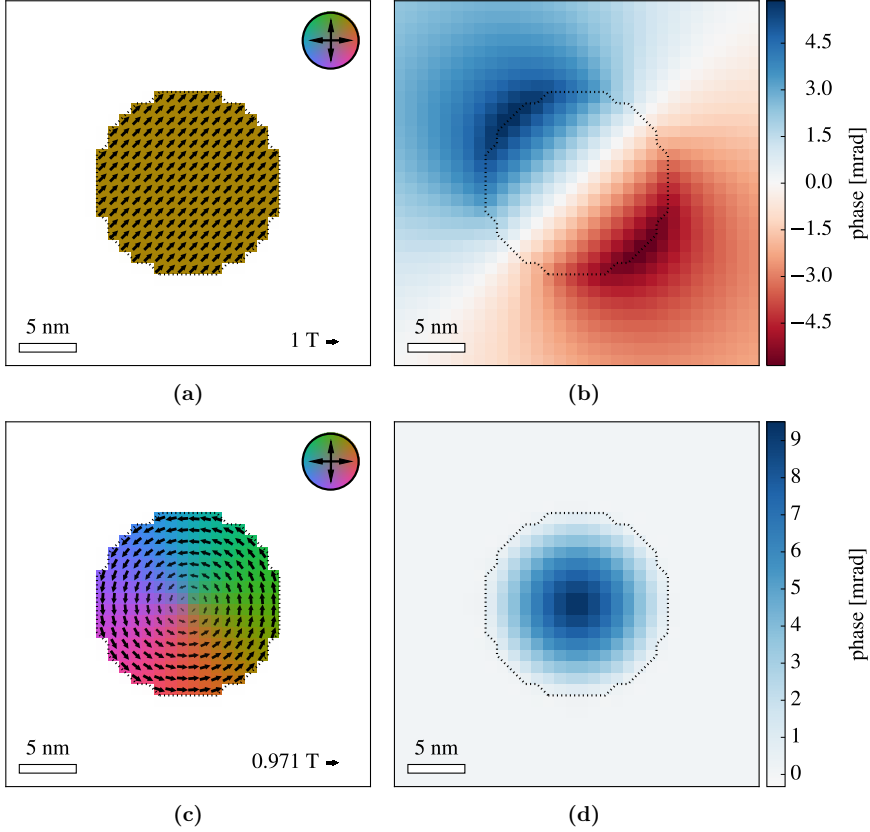
Figure 5.4.: Magnetisation distributions for the analysis of two-dimensional reconstructions of the projected in-plane magnetisation for (**a**) a homogeneously magnetised disc in the xy plane oriented at an angle of 45° to the x axis and (**c**) a disc that supports a counter-clockwise smooth magnetic vortex state. Corresponding magnetic phase images are shown in (**b**) and (**d**), respectively. Both discs have a radius of $R = 8$ nm and a thickness of $t = 1$ nm. The FOV has a size of 32×32 nm^2 and the grid spacing is $a = 1$ nm. The magnetisation amplitude of the largest arrow is indicated in the lower right corner of (**a**) and (**c**).

regularisation parameter λ was repeated ten times with different distributions of the same level of noise for statistical purposes.

The RMS quantities that were introduced in Section 4.4.2 were used to determine the goodness of fit of each reconstruction result. The directional error ϵ_{dir} and the RMS error in magnitude ϵ_{mag}, which are defined in Eqs. 4.42 and 4.41, respectively, were calculated by using the original magnetisation distributions shown in Figs. 5.4a and 5.4c as references. The results for both RMS error quantities and both magnetised discs are summarised in Fig. 5.5.

In all of the graphs for the homogeneously magnetised disc, both ϵ_{mag} and ϵ_{dir} increase with higher noise levels σ_ϵ. Increasing the regularisation strength λ then decreases both the directional error and the error in magnitude of the reconstructed vector field. The graphs for different values of λ do not intersect. For the magnetised disc that supports a vortex state, the situation is different. Looking at the noise-free case for $\sigma_\epsilon = 0\,\mathrm{mrad}$, an increase in λ leads to an increase in the magnitude error ϵ_{mag}, as the vortex distribution is in conflict with the smoothness constraint, especially at its centre, where large angles between the vectors occur. Increasing the regularisation enforces a smoother solution than that in the reference magnetisation distribution. For higher levels of noise, an increase in λ initially decreases ϵ_{mag}, as is the case for the homogeneously magnetised disc. This decrease is associated with the successful suppression of noise. However, if the regularisation parameter is increased too far, then over-regularisation occurs. A reversal in the behaviour of ϵ_{mag} can be observed and the magnitude error rises again. For the highest noise level of $\sigma_\epsilon = 1\,\mathrm{mrad}$, this reversal occurs for values of λ above 10^{-5}. The graphs for the three highest regularisation parameters (10^{-5}, 10^{-4} and 10^{-3}) are nearly flat. The magnitude errors for these values of λ are independent of the level of noise because the smoothing effect is so strong. These phenomena also occur for the directional error ϵ_{dir}, but are less pronounced. The amplitude of the vortex is smoothed out, while the direction is less strongly affected. This reversal does not occur for the homogeneously magnetised disc because it passes through the regularisation unpunished, as described in Section 4.3.

A balance between too much and too little regularisation must be found. According to Hansen [135], a so-called L-curve plot provides a heuristic method to discover the regularisation strength λ that provides the best balance between the compliance with the measurements and accordance to *a priori* information. Figure 5.6 shows the normalised regularisation term $\frac{1}{\lambda}\left\|\boldsymbol{x}\right\|^2_{\mathbf{S}_{\mathrm{a}}^{-1}}$ plotted on a double logarithmic scale against the cost of the residual vector, which is expressed by the norm $\left\|\mathbf{F}\boldsymbol{x} - \boldsymbol{y}\right\|^2_{\mathbf{S}_\epsilon^{-1}}$, in the form of an L-curve for the vortex distribution[2].

Figure 5.6 shows one L-curve per level of Gaussian noise σ_ϵ, with the regularisation parameter λ varied along each curve. The starting point for nearly negligible regularisation at $\lambda = 10^{-8}$, which is marked by a downward triangle, is very distinct for

---

[2]As discussed above, for the homogeneously magnetised disc, no trade-off happens because it passes through the regularisation unpunished. The corresponding plots are therefore omitted.
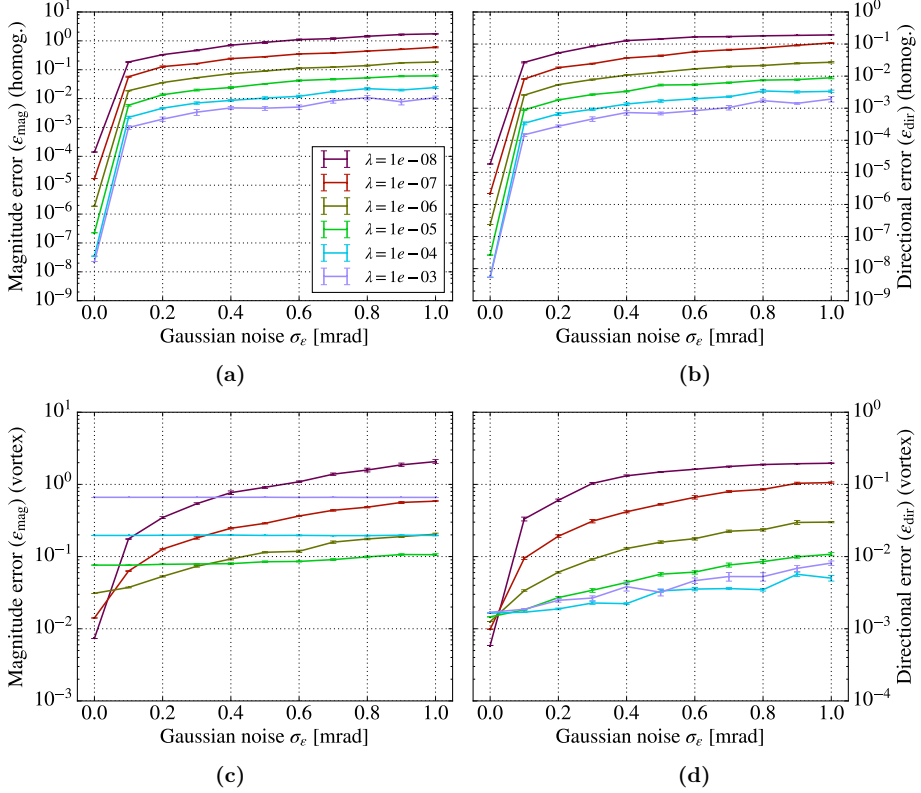
Figure 5.5.: (**a**, **b**) Error ϵ_{mag} in magnitude and directional error ϵ_{dir} for the homogeneously magnetised disc plotted as a function of the level of Gaussian noise σ_ϵ for different regularisation parameters λ. (**c**, **d**) show ϵ_{mag} and ϵ_{dir} for the magnetic vortex distribution. In each case, the original distributions shown in Figs. 5.4a and 5.4c are used as references. For the homogeneously magnetised disc, an increase in the regularisation parameter consistently decreases the noise. For low values of λ, the same behaviour can be observed for the magnetic vortex state. For higher values, however, over-regularisation occurs and smooths away features of the magnetisation distribution, which causes the RMS errors to rise again.
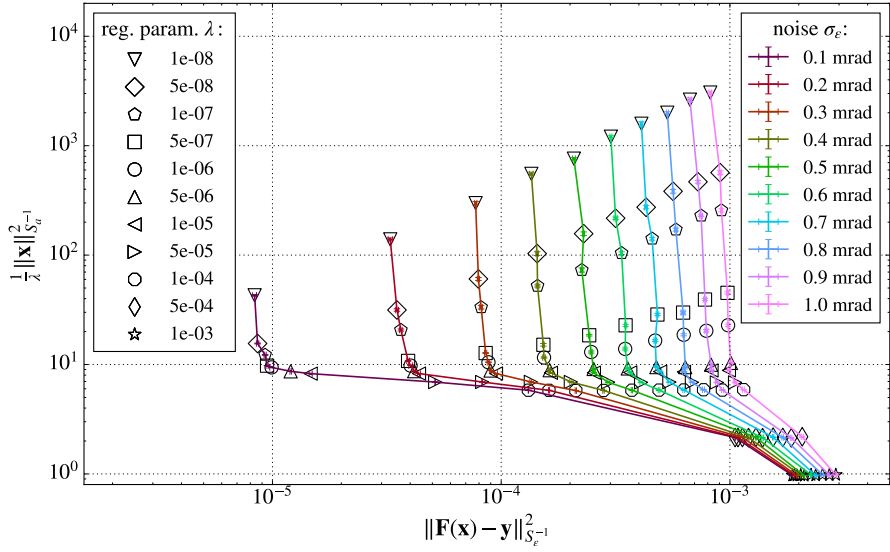
Figure 5.6.: L-curve overview for a magnetised vortex state. The normalised regularisation term is plotted on a double logarithmic scale against the norm of the residual vector. One L-curve is displayed for each Gaussian noise level σ_ϵ, with each curve plotted in a different colour, as indicated in the legend on the right. Black outlines of geometric shapes mark the point on each L-curve that corresponds to a reconstruction performed using a specific regularisation parameter λ, as indicated in the legend on the left.

all of the noise levels and moves away from the origin of the plot with increasing σ_ϵ. The origin is an unreachable "optimal", point where both the cost of the residual term and the regularisation term are zero.

All of the L-curves starts with a vertical slope nearly parallel to the ordinate. Solutions that lie on this vertical part are dominated by perturbation errors, which manifest in magnetisation vectors which vary considerably from pixel to pixel. These perturbations arise, because the MBIR algorithm tries to account for noise in the input magnetic phase images, which is not sufficiently punished by the weak regularisation. Increasing λ decreases the cost of the regularisation term by smoothing away these perturbations and therefore moving downwards along the L-curve. The position along the abscissa does not change significantly, *i.e.*, the cost of the residual term stays approximately the same. The L-curves then exhibit a flat part. If a reconstructed solution lies on this part of the curve, then λ is likely too large. Not all of the information can be extracted from the measurements and high spatial frequency features in the magnetisation are smoothed out. For even stronger regularisation, the end points of all L-curves (marked by stars in Fig. 5.6) converge. The corresponding solutions have a high cost of the residual vector term, as indicated by the position on the far right of the abscissa. A magnetic phase image calculated from this overly smooth solution may then not comply with the measured magnetic phase image at all.

A distinct corner separates the steep part and the flat part of the L-curve. The point of highest curvature at this corner is closest to the origin of the plot. It therefore corresponds to a regularisation parameter λ, for which there is a good trade-off between measurement compliance and smoothness. Nine L-curves, which show magnified regions of these corner points, are plotted in Fig. 5.7 for the magnetised disc that supports a vortex state. The L-curve corner coincides with a larger regularisation parameter λ for stronger noise levels σ_ϵ in the input magnetic phase images. For example, whereas a good trade-off for $\sigma_\epsilon = 0.1\,\mathrm{mrad}$ is reached for approximately $\lambda = 5 \cdot 10^{-7}$, a higher noise level of $\sigma_\epsilon = 0.9\,\mathrm{mrad}$ requires a one hundred times larger regularisation parameter[3] of $\lambda = 5 \cdot 10^{-5}$. As described in Section 5.1, stronger regularisation is accompanied by increased smoothing. The noise level therefore indirectly determines the spatial resolution of the reconstruction and should be decreased as far as possible during image acquisition.

In summary, the L-curve is a reliable heuristic tool that can be used to determine a good starting choice for the regularisation parameter λ for both two- and three-dimensional magnetisation reconstructions. The drawback is an increased time investment, as for each regularisation parameter that is evaluated along the L-curve one complete reconstruction is required (*cf.* the analysis in Section 5.6).

---

[3]This behaviour is consistent with Eq. 4.35. An increase in the input noise σ_ϵ goes quadratically into the calculation of the covariance matrix $\mathbf{S}_\mathrm{out}$. The regularisation therefore has to be adjusted accordingly.
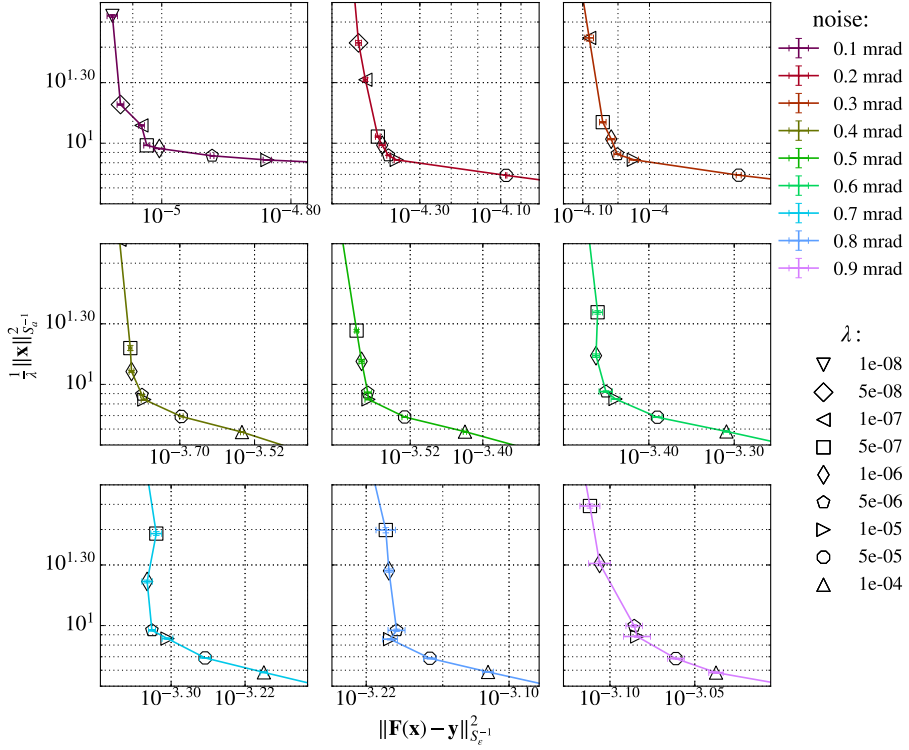
Figure 5.7.: Magnified views of the points of highest curvature in the L-curves in Fig. 5.6 for nine different Gaussian noise levels σ_ϵ. Each "corner" corresponds to the regularisation parameter λ, for which there is the best trade-off between compliance with the measurements and smoothness according to *a priori* information.

5.3. Influence of the mask

One of the greatest advantages of reconstructing the magnetisation $\boldsymbol{M}$ instead of the magnetic flux density $\boldsymbol{B}$ or the magnetic vector potential $\boldsymbol{A}$ is the significant reduction in unknown parameters that results from applying a mask Ξ, which specifies the positions of magnetised regions (*cf.* Section 4.2.2). The influence of the mask Ξ on the reconstruction is therefore very strong and is examined in this section. For this purpose, both of the test distributions from the previous section are reconstructed using different mask sizes. In each case, the disc shape of the test distributions allows a parametrisation, whereby the radius of the mask is varied relative to the radius of the disc $R = 8\,\mathrm{nm}$. The mask radius is increased in steps of $1\,\mathrm{px}$ (pixel), which corresponds to an increase in steps of $1\,\mathrm{nm}$. The variation ranges from $-4\,\mathrm{px}$, corresponding to a mask that is smaller than the particle, to $+14\,\mathrm{px}$, where the mask encompasses the entire FOV. The input phase images are noise-free and the regularisation strength is set to a low value of $\lambda = 10^{-8}$, so that the influence of the mask can be examined without being affected by the artefacts discussed above[4].
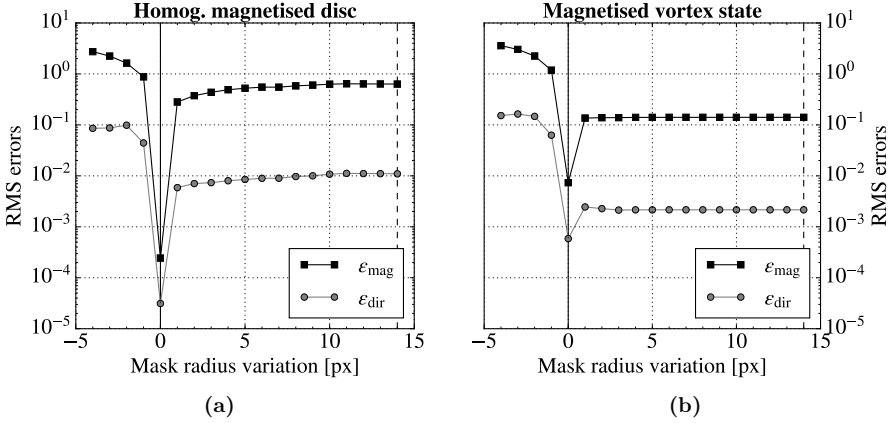
Figure 5.8.: Plots of magnitude error ϵ_{mag} and directional error ϵ_{dir} as a function of mask size. Results for the homogeneously magnetised disc and the vortex distribution are shown in (**a**) and (**b**), respectively. A solid vertical line indicates a mask that exactly fits the particle size. As expected, the errors are smallest for this radius. Dashed vertical lines at a mask radius variation of $+14\,\mathrm{px}$ correspond to masks that encompass the entire FOV.

In order to analyse the results, the error quantities ϵ_{mag} and ϵ_{dir} are displayed, as in the previous section. Both quantities are plotted in Fig. 5.8 for the homogeneously

---

[4]This value for λ is used in the following sections for the same reason, if not explicitly stated otherwise.

magnetised disc and the vortex state disc. Figure 5.9 shows a selection of reconstruction results for the two magnetisation distributions. As expected, both ϵ_{mag} and ϵ_{dir} reach their minimum values[5] for a mask size that exactly fits the disc size (marked at zero on the abscissa in Figs. 5.8a and 5.8b).
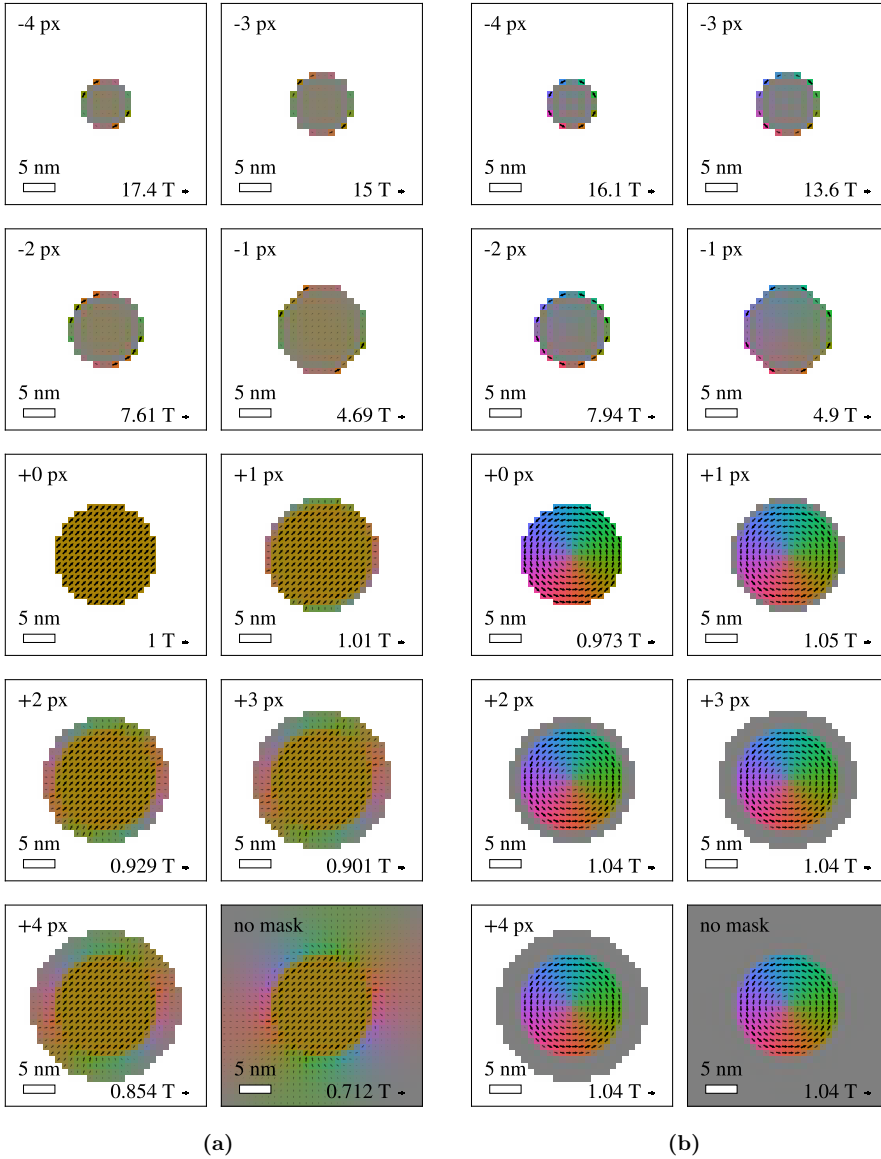
The use of a mask that is larger than the magnetised disc results in the MBIR algorithm trying to fit magnetisation in regions that do not belong to the disc. The magnetisation in this regions should ideally be reconstructed to zero. However, in particular for the homogeneously magnetised disc, this is not the case. In contrast to the vortex state, which does not result in a magnetic phase shift outside the disc, the homogeneously magnetised disc is associated with a smoothly decaying magnetic phase distribution outside its boundary (*cf.* Fig. 5.4b). As shown in the gain maps for a low regularisation parameter in Fig. 5.2 in Section 5.1, a phase shift will always be attributed primarily to the magnetisation of a neighbouring pixel, assuming this pixel lies inside the mask Ξ. A smoothly decaying phase shift therefore leads to a smoothly decaying magnetisation distribution inside the boundaries of the mask Ξ. As the regularisation only calculates the magnetisation derivative inside the mask (*cf.* Section 4.2.2), this smooth solution is chosen over the correct distribution shown in Fig. 5.4a (or Fig. 5.9a for +0 px). If the mask extends beyond the particle boundaries, then the derivatives at these positions are included and harshly punished by the regularisation if sudden jumps occur. Therefore, the smoother solutions that are seen in Fig. 5.9a for positive mask radius variations are retrieved instead. This smoothing effect occurs for both magnetic discs and results in a jump in the error quantities shown in Fig. 5.9 when the mask radius is increased by even a single pixel. The error levels for the homogeneously magnetised disc become higher for larger mask radii until they asymptotically approach a saturation level. The reason for this saturation level is the fact that every increase in mask radius adds pixels that have weaker and weaker magnetic phase contributions. For the vortex disc, which exhibits no stray magnetic phase outside its boundary, no further increase in the error quantities is observable after the mask radius has increased by one pixel[6].

A decrease in the mask size leads to the magnetisation of regions at the outer border of each magnetised disc being erroneously fixed to zero. The reconstruction therefore misses vital degrees of freedom and the magnetic phase contribution that the magnetisation of these pixels at the borders would produce has to be compensated. The MBIR algorithm achieves this compensation by increasing the magnetisation of the outermost pixels at the borders of the smaller mask. This effect can be seen in Fig. 5.9 for negative values of the mask radius variation. It is similar for both distributions and results in significantly larger errors than for a mask that is too big.

---

[5]The errors are smaller for the homogeneously magnetised distribution because it passes unpunished through the regularisation. This is not the case for the vortex distribution, as explained in Section 5.3.

[6]A stronger regularisation would increase the observed smoothing effect. The resolution of the averaging kernel (*cf.* Section 5.1) provides an estimate for how many pixels are affected outside the particle boundaries for a mask that is too large.

A good example is provided by the reconstruction of the homogeneously magnetised disc for a mask variation of -4 pixels, for which the magnetisation at the boundary pixels is increased by a factor of 17.4 when compared to the correct solution. Extreme care therefore has to be taken when assigning a mask. The results that are presented in this section indicate that it is better to choose a mask that is slightly too large than too small if its exact position is not known sufficiently well.

-4 px	-3 px
5 nm	5 nm
17.4 T	15 T

-2 px	-1 px
5 nm	5 nm
7.61 T	4.69 T

+0 px	+1 px
5 nm	5 nm
1 T	1.01 T

+2 px	+3 px
5 nm	5 nm
0.929 T	0.901 T

+4 px	no mask
5 nm	5 nm
0.854 T	0.712 T

(a)

-4 px	-3 px
5 nm	5 nm
16.1 T	13.6 T

-2 px	-1 px
5 nm	5 nm
7.94 T	4.9 T

+0 px	+1 px
5 nm	5 nm
0.973 T	1.05 T

+2 px	+3 px
5 nm	5 nm
1.04 T	1.04 T

+4 px	no mask
5 nm	5 nm
1.04 T	1.04 T

(b)

Figure 5.9.: Examples of reconstruction results for different mask radii for (**a**) the homogeneously magnetised disc and (**b**) the magnetised disc that supports a magnetic vortex state. The mask variation, relative to the true mask size, is denoted at the top left of each image. An arrow at the lower right of each image indicates the maximum magnetisation in that image.

5.4. Influence of magnetisation sources outside the FOV

An MBIR algorithm that is based on real space discretisation implicitly assumes that the area outside the FOV is devoid of sources of magnetisation (*cf.* Tab. 3.3). If, however, this assumption does not hold true and magnetisation sources outside the FOV exist, then the MBIR algorithm will falsely attribute magnetic phase contributions from these external sources to masked regions that lie inside the FOV. This incorrect attribution leads to artefacts that can be described by low spatial frequencies in the magnetisation if the sources are far enough away from the FOV. This section examines some of these artefacts and introduces different strategies that can be used to deal with them.

5.4.1. Fitting of a phase offset and ramp

If the magnetisation sources that are outside the FOV are far enough away from the measured region, then their magnetic phase contribution can usually be approximated using low order polynomials. As a first order approximation, this polynomial can take the form of a phase ramp. The MBIR algorithm can be extended to include a phase plane fit to each magnetic phase image. Each phase ramp can be described by three parameters,

1. A phase offset, given in rad;
2. A phase ramp in the u direction, given in $\frac{\text{rad}}{\text{nm}}$;
3. A phase ramp in the v direction, given in $\frac{\text{rad}}{\text{nm}}$.

As mentioned in Section 2.1, an incorrect value for the zero level of the phase outside the magnetised object can lead to an additional phase offset, which is also included in the proposed additional linear ramp and offset fit. The fit can furthermore account for phase ramps that may be present due to artefacts such as specimen charging or changes to the biprism wire over time.

In order to fit phase offsets and ramps, $3N_b$ unknown parameters are added to the vector $\boldsymbol{x}$ of retrieval targets for a magnetisation reconstruction from N_b images. Each set of three parameters describes the phase ramp for one phase image. The $3N_b$ additional parameters are unaffected by the projection matrix $\mathbf{P}$ or by the phase mapping matrix $\mathbf{Q}$ in the forward model. These calculation steps can therefore be bypassed. The phase plane for each image is then simply added at the end of each iteration step. The forward model is linear in the additional parameters, so the derivative and adjoint operators are equally easy to implement. Theoretically, polynomials of higher order could also be used for the fit. However, the use of such polynomials is not encouraged due to the risk of falsely attributing magnetic phase contributions from the magnetisation inside the FOV to these higher orders.
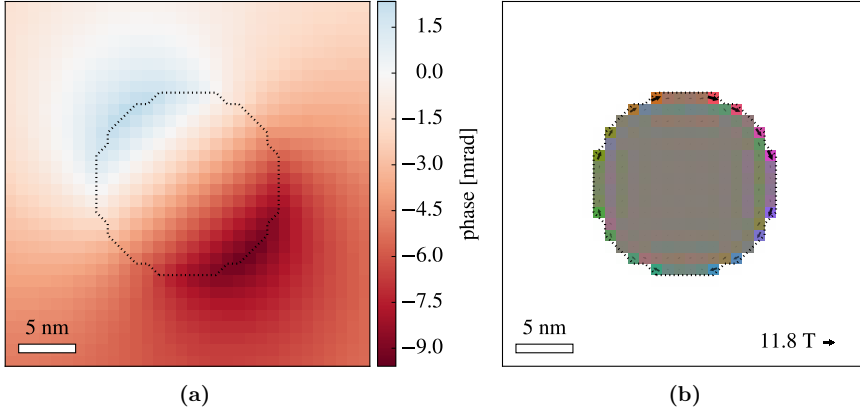
Figure 5.10.: (**a**) Magnetic phase image of a homogeneously magnetised disc (*cf.* Fig. 5.4b) with an additional phase offset of -5 mrad and additional phase slopes of $60 \frac{\mu\text{rad}}{\text{nm}}$ in the u direction and $40 \frac{\mu\text{rad}}{\text{nm}}$ in the v direction. (**b**) Reconstruction of the magnetisation without taking the additional phase ramp into account. The magnetisation amplitude, which is indicated by the scale on the lower right, is too high, when compared to the original magnetised disc.

Figure 5.10a shows a magnetic phase image generated by a homogeneously magnetised disc (*cf.* Fig. 5.4b) with an additional superimposed phase ramp with a phase offset of -5 mrad and phase slopes of $60 \frac{\mu\text{rad}}{\text{nm}}$ in the u direction and $40 \frac{\mu\text{rad}}{\text{nm}}$ in the v direction. Reconstruction without the inclusion of the ramp and offset results in the fitted magnetisation distribution shown in Fig. 5.4b. The magnetisation of the outermost pixels is up to twelve times higher than in the reference magnetisation distribution shown in Fig. 5.4a, leading to very high RMS error values of $\epsilon_{\text{mag}} = 2.38$ and $\epsilon_{\text{dir}} = 0.15$. The reason why the outermost pixels are particularly affected is similar to the effect that was observed in Section 5.3. The MBIR algorithm adds a magnetisation loop to the disc borders because a closed flux line with a constant magnetisation amplitude is associated with a constant phase offset in the enclosed area, as shown, *e.g.*, in [111]. Slight asymmetries in the magnetisation of the loop can be used to account for the slopes in the u and v directions. However, the algorithm is only able to correctly recreate the phase, including the offset and ramp, inside the disc. The additional phase across the complete FOV cannot be recreated by making use of only the degrees of freedom that are provided by the mask Ξ.

The fitting of a phase ramp and offset during reconstruction shown in Fig. 5.10 increases its quality and decreases the error quantities to $\epsilon_{\text{mag}} = 1.69 \cdot 10^{-4}$ and $\epsilon_{\text{dir}} = 1.94 \cdot 10^{-5}$, respectively. The ramp parameters can be retrieved perfectly. The fitted phase ramp is shown in Fig. 5.11a. The reconstructed magnetisation is visually indistinguishable from the original distribution (*cf.* Fig. 5.4a). Figure 5.11b shows

only the difference between these two distributions. The largest error in amplitude is smaller than approximately $0.5\,\mathrm{mT}$, which is less than $1\,\text{‰}$ of the saturation magnetic induction of $B_{\mathrm{sat}} = 1\,\mathrm{T}$ in the original magnetisation distribution.


(a)   **(b)**
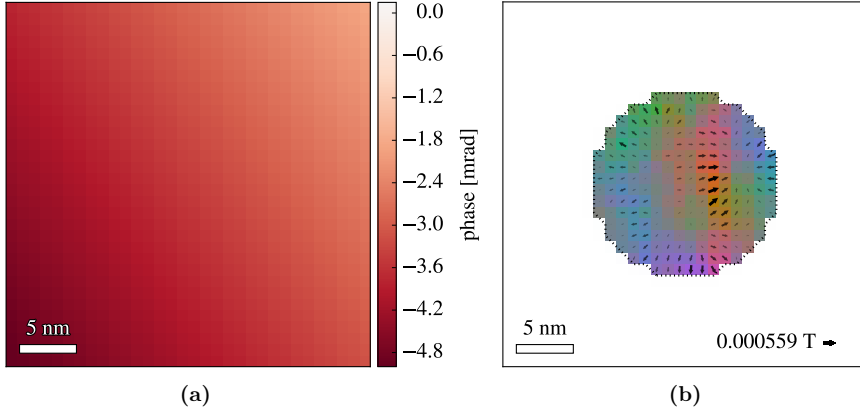
Figure 5.11.: (**a**) Reconstruction of the additional phase ramp with an exactly retrieved phase offset of $-5\,\mathrm{mrad}$ and slopes of $60\,\frac{\mu\mathrm{rad}}{\mathrm{nm}}$ in the u direction and $40\,\frac{\mu\mathrm{rad}}{\mathrm{nm}}$ in the v direction. (**b**) Difference between the original magnetisation distribution (*cf.* Fig. 5.4a) and the reconstruction result when the phase ramp is fitted. The maximum relative error in magnitude lies below $1\,\text{‰}$.

5.4.2. Magnetisation sources in the immediate vicinity

In the presence of magnetisation sources that are directly outside the FOV, the additional magnetic phase can no longer be approximated sufficiently well by the linear phase ramp that was introduced in Section 5.4.1. Figure 5.12a shows an example of an array of homogeneously magnetised discs next to a slab that is magnetised along the y axis. The phase image that is produced by this distribution is displayed in Fig. 5.12b. The green square marks the FOV and extent of the input magnetic phase image used in the reconstruction algorithm. For the purpose of the reconstruction, only the magnetic phase and the position and size of the magnetised regions inside the FOV in Fig. 5.12a are assumed to be known.

As expected, a "naive" reconstruction that does not consider external magnetisation sources provides an unsatisfying result, which is shown in Fig. 5.13a. As before (*cf.* Sections 5.3 and 5.4.1), the external sources are "buffered" by the nearest masked pixels that are available for the MBIR algorithm, resulting in a magnetisation loop in the outermost pixels of the disc. The use of a phase ramp fit, according to Section 5.4.1, improves the reconstruction result. However, it can only fit a phase offset and a linear phase ramp. All higher order phase contributions remain unaccounted
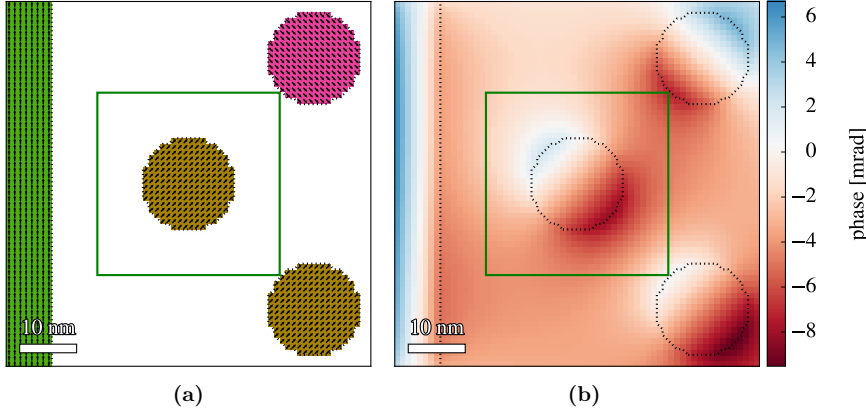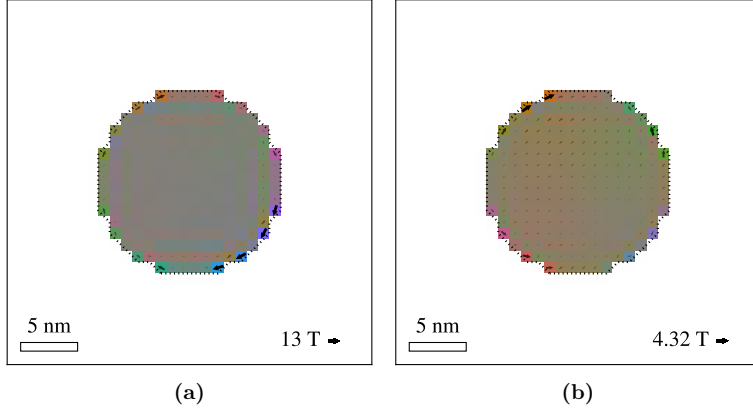
Figure 5.12.: (**a**) Magnetisation distribution with magnetisation sources outside the FOV, which is marked by a green square. (**b**) Resulting magnetic phase image. Only the region marked by the green square is used as the input magnetic phase image in the MBIR algorithm.

for, which leads to the reconstruction result shown in Fig. 5.13b. Even though the amplitude of the magnetisation loop around the disc is now decreased by a factor of three, the result is still unsatisfactory.

An alternative to the polynomial fit can be obtained if the magnetisation loop, which is created by the MBIR algorithm to counter outside sources, is not seen as an artefact but is made use of in another context. Instead of forcing the algorithm to use the outermost pixels of the masked region of interest, which is detrimental to the goodness of fit, an additional buffer region outside the borders of the FOV is constructed. This buffer can serve the same purpose, without influencing the retrieval targets. Figure 5.14a shows the reconstructed magnetisation distribution for the previous example for a buffer region that has a thickness of one pixel on all four edges of the FOV[7]. The buffer region, which contains fitted magnetisation amplitudes that are up to six times higher than the original value of 1 T, can be discarded after reconstruction in order to extract the original FOV that contains the region of interest. The original FOV with the reconstruction result is shown in Fig. 5.14b. It accurately reproduces the original magnetisation distribution shown in Fig. 5.4a, with RMS error quantities of just $\epsilon_{\mathrm{mag}} = 8.25 \cdot 10^{-4}$ and $\epsilon_{\mathrm{dir}} = 1.27 \cdot 10^{-4}$.

The use of buffer pixels is more flexible for two-dimensional reconstructions than fitting a linear phase ramp and offset. However, problems may arise for three-dimensional reconstructions. The phase ramp fits must be executed on an image-

---

[7]The buffer region does not necessarily have to correspond to a closed loop around the FOV. If some directions are known to not contain any magnetisation, then no buffer pixels on that edge are necessary. A closed loop is, however, recommended if such information is not known.

Figure 5.13.: Magnetisation distributions reconstructed from the region marked by the green square in Fig. 5.12b (**a**) without considering external magnetic sources and (**b**) fitting a linear phase ramp, as described in Section 5.4.1.
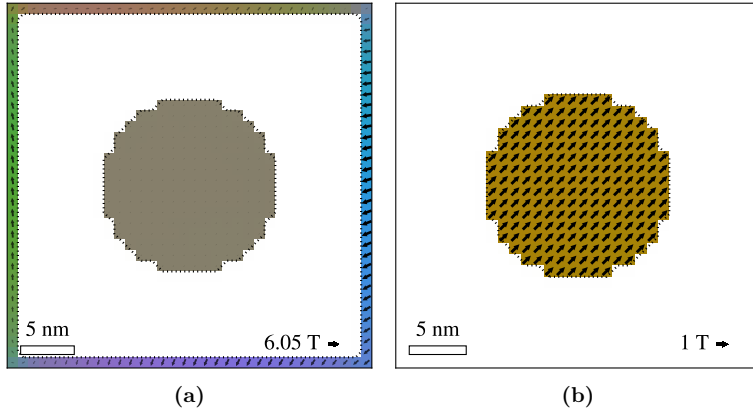
Figure 5.14.: (**a**) Magnetisation reconstruction for the example shown in Figs. 5.12 and 5.13 after including a buffer region of one pixel on each side of the FOV. Because the arrows are scaled to the highest amplitude, which is six times higher in the buffer region than in the disc, the magnetisation in the disc is not visible. The original FOV was extracted by cropping the buffer pixels and is shown in (**b**). The resulting magnetisation distribution accurately reproduces the original distribution (*cf.* Fig. 5.4a)

by-image basis and can therefore be used to account for artefacts that only appear in single phase images or vary from image to image, *e.g.*, with time. In contrast, buffered regions have to be applied to a three-dimensional reconstruction volume that is used for all images simultaneously. The image-by-image flexibility is then lost. For a single image, separation of the buffer region from the magnetised region inside the FOV is straightforward due to their spatial distance. For a three-dimensional reconstruction, a buffer region would have to enclose the complete three-dimensional volume in order to account for all projection directions. As a result of the relatively large number of degrees of freedom in the buffer region[8], features in the magnetisation distribution may then be falsely attributed to the buffer voxels by the MBIR algorithm.
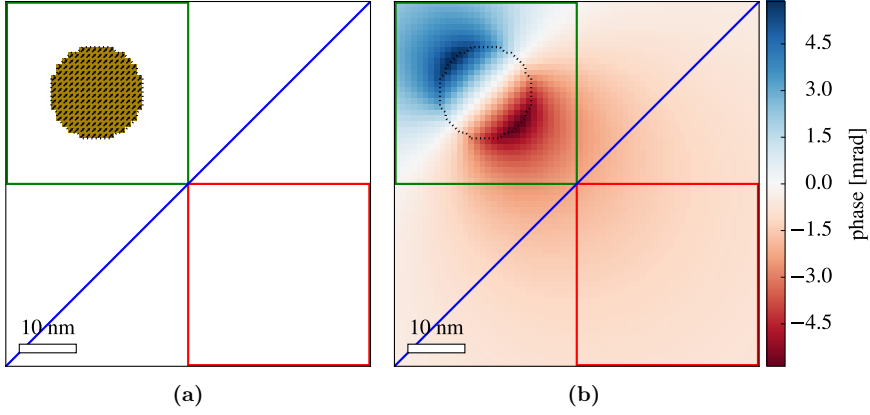
5.4.3. Inclusion of the perturbed reference wave

In Section 2.1, the assumption was tacitly made that the vacuum reference wave is an unperturbed plane wave. Even if no other magnetisation sources are present in or near the path of the object and reference beams, this assumption can, however, be violated. In particular, if the magnetic stray field of the magnetised regions of interest is strong enough and the vacuum reference wave is sufficiently close, then the magnetic stray field arising from the specimen may modulate the magnetic phase shift of the vacuum reference wave [103].

Figure 5.15 shows a schematic illustration of the formation of a perturbed reference wave. The object wave and the FOV of the magnetic phase image are marked by a green square, while the vacuum reference wave is marked by a red square. Both waves are oriented symmetrically to the biprism, whose position is marked by a blue line[9]. The recorded magnetic phase image is calculated by taking the difference between the magnetic phase of the object wave and that of the vacuum reference wave. The resulting magnetic phase image is shown in Fig. 5.16a. It contains a slight asymmetry due to the perturbed reference wave, in comparison to the unperturbed image shown in Fig. 5.4b. Attempting a naive reconstruction yields the magnetisation distribution shown in Fig. 5.16a. The effect on the reconstruction is similar to the influence of magnetisation distributions outside the FOV discussed above. However, in this case, the artefacts do not arise from external sources, but due to the influence of the magnetised disc on itself as a result of the perturbed reference wave. The RMS error quantities for the naive reconstruction are $\epsilon_{\mathrm{mag}} = 0.71$ and $\epsilon_{\mathrm{dir}} = 0.08$.

---

[8]In contrast to the phase ramp fits, where there are only $3N_b$ degrees of freedom.

[9]In practice, the waves are not positioned directly next to the biprism. The example is chosen to emphasize the phenomenon. In consequence, the artefacts that are described here are less pronounced in an actual experiment.

Figure 5.15.: Illustration of the concept of a perturbed vacuum reference wave. (**a**) The known magnetisation distribution of a homogeneously magnetised disc. (**b**) The corresponding magnetic phase shift. The object wave and the FOV of the phase image are marked by a green square. The vacuum reference wave, which is perturbed by the magnetic phase shift of the magnetised disc, is marked by a red square. The biprism orientation is indicated by a blue line.
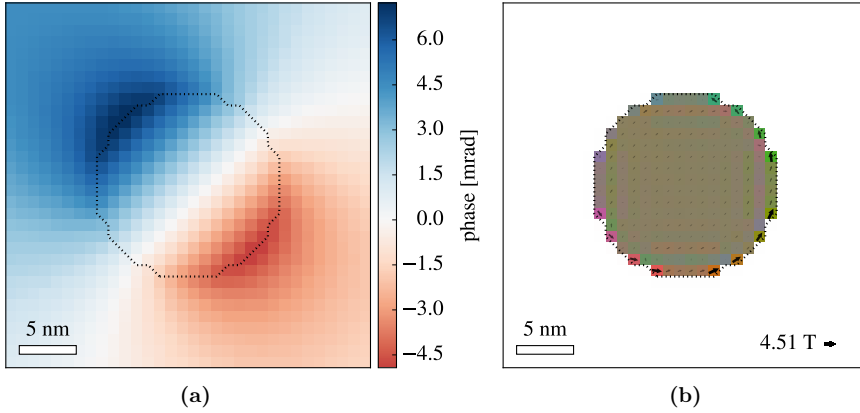

Figure 5.16.: (**a**) Magnetic phase image obtained by calculating the difference between the object wave and the perturbed reference wave shown in Fig. 5.15b. (**b**) Naive reconstruction of the magnetisation distribution containing artefacts due to the perturbed reference wave.

105

The most efficient way to account for the perturbed reference wave is to include it in the earliest possible stage of the reconstruction process, *i.e.*, the calculation of the convolution kernels. This procedure is illustrated in Figure 5.17a for a FOV of 3×3 pixels and for the convolution kernel for the magnetisation component in the y direction. As stated in Section 3.2.4, the convolution kernel then has to have a size of 5×5 pixels[10]. The object wave and the FOV are marked by a solid green square, while the convolution kernel is marked by a dashed green square. A similar red square is used to mark the vacuum reference wave. If the position of the biprism relative to the FOV is known, then a displacement vector can be constructed. This vector is marked in purple and is calculated by doubling the perpendicular vector onto the centre of the projected biprism, which is marked by a blue line. The displacement vector determines the distance between corresponding points in the object and reference waves. For the original convolution kernel (dashed green square) and its counterpart associated with the perturbed reference wave (dashed red square), the vector determines the displacement between their centre points. In order to include the perturbed vacuum reference wave in the reconstruction, this counterpart is simply subtracted from the original convolution kernel. The resulting perturbed convolution kernel is shown in Fig. 5.17b.

Due to the pre-computation, the inclusion of the perturbed vacuum reference wave does not increase the computation time during the reconstruction itself, making this method very efficient. The original magnetisation distribution (*cf.* Fig. 5.4a) can be reconstructed accurately by including the perturbed vacuum reference wave in the reconstruction for the example shown in Fig. 5.16a. The RMS error quantities are significantly reduced to $\epsilon_{\mathrm{mag}} = 6.62 \cdot 10^{-4}$ and $\epsilon_{\mathrm{dir}} = 9.26 \cdot 10^{-5}$, respectively. If the position of the biprism is known for each magnetic phase image, then the perturbed reference wave can also be included in three-dimensional reconstructions.

---

[10]The size would be 6×6 pixels after the zero-padding that is necessary for the convolution in Fourier space in the RDFC approach. It is not taken into account here because the padding takes place *after* pre-computation.
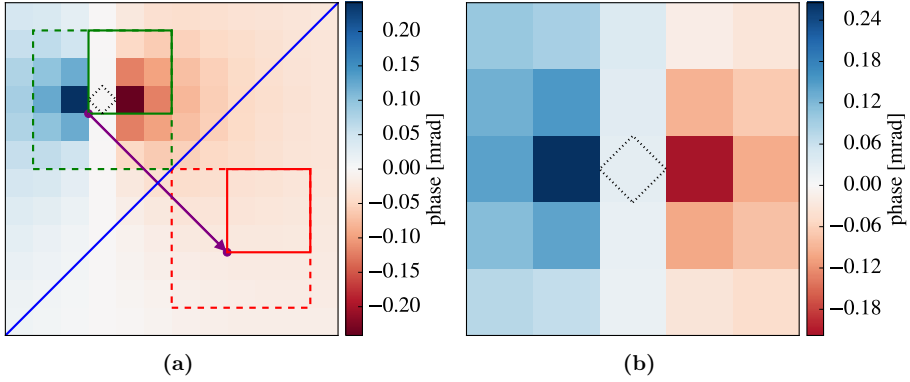
Figure 5.17.: (**a**) Schematic diagram illustrating the construction of a convolution kernel for a perturbed vacuum reference wave. The FOV is marked by a solid green square. The corresponding convolution kernel is marked by a dashed green line. The same markings in red are used for the reference wave and the corresponding counterpart of the convolution kernel. The displacement vector between the object and vacuum reference wave is marked by a purple arrow. The perturbed convolution kernel can be calculated by subtracting the red dashed square from the green dashed square. It is displayed in (**b**) and shows a slight asymmetry compared to the unperturbed kernel, which can be seen in the colorbar.

5.5. Use of a confidence array

The previous sections provided strategies to deal with external sources of magnet-isation and the perturbed vacuum reference wave in order to correct for some of the artefacts that can affect magnetic phase images. In some cases there are other artefact sources that can be detrimental to the reconstruction process. Examples include alignment errors during separation of the magnetic from the electrostatic contribution to the phase shift and phase unwrapping errors, both of which are described in Section 2.1. In order to account for these and other artefacts, a confidence array Γ, which was introduced in Section 4.1, can be utilised. The trust values in the affected regions of a magnetic phase image can be set to zero, so that they do not influence the reconstruction[11].

Figure 5.18a again shows a magnetic phase image of a homogeneously magnetised disc (*cf.* Fig. 5.4b). Three areas of 2×2 pixels are artificially set to erroneous values. The erroneous pixels inside the disc are set to 0 mrad, while those outside the disc are set to -6 mrad. Performing a reconstruction with a uniform confidence array $\Gamma[p, q] = 1$ results in the magnetisation distribution shown in Fig. 5.18b. The fact that the artefacts in the phase image have propagated to the reconstructed distribution is particularly visible in the area inside the disc, where a vortex with a nearly four times higher magnetisation amplitude is produced in the reconstruction to account for the erroneous phase values. Such vortices can arise to recreate small areas that vary significantly in phase when compared to their surroundings, because they are able to create a very localised change in phase (*cf.*, *e.g.*, Fig. 5.4d). The erroneous phase areas outside the disc result in less highly pronounced artefacts. The change in magnetisation is directly correlated to the distance to the masked region. The artefact on the right is stronger than that at the bottom, because it is closer to the magnetised disc. The RMS error quantities for this reconstruction are $\epsilon_{\mathrm{mag}} = 0.44$ and $\epsilon_{\mathrm{dir}} = 0.06$. In contrast, a reconstruction that takes the erroneous regions into account by setting their Γ values to zero accurately reconstructs the original magnetisation distribution. The RMS errors in this case are decreased to $\epsilon_{\mathrm{mag}} = 1.15 \cdot 10^{-4}$ and $\epsilon_{\mathrm{dir}} = 1.67 \cdot 10^{-5}$.

---

[11]Other values between 0 and 1 can also be chosen, if the trustworthiness of some magnetic phase image regions are questionable.
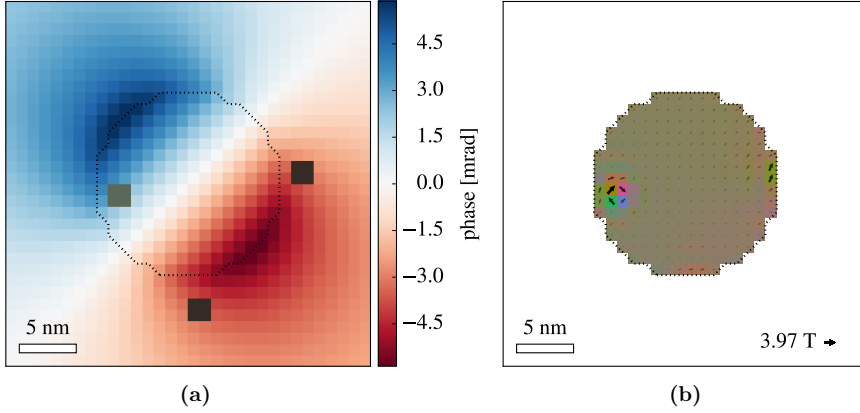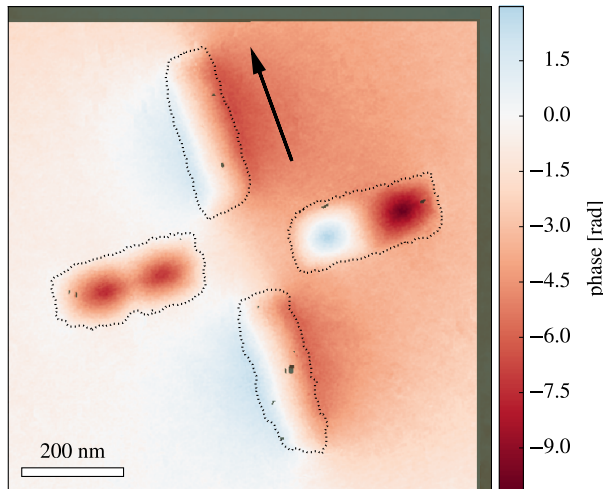
Figure 5.18.: (**a**) Magnetic phase image of a homogeneously magnetised disc with three areas of 2×2 pixels set to erroneous values. The erroneous area inside the disc is set to 0 mrad, while both areas outside the disc are set to -6 mrad. The erroneous regions are marked by dark squares. (**b**) Reconstruction for a confidence array that is uniformly $\Gamma\left[p, q\right] = 1$ and does not take the erroneous regions into account.

5.6. Reconstruction from an experimental phase image

In this section, all of the analysis techniques and procedures to deal with artefacts are applied to an experimentally acquired magnetic phase image to showcase the potential applications of the new MBIR algorithm. For this purpose, a lithographic cobalt structure was prepared. The structure was patterned by electron beam lithography on a 50 nm thick Si_3N_4 membrane. The cobalt and an 8 nm thick layer of aluminium as a protection layer were deposited by electron beam evaporation. Although the nominal thickness of the cobalt layer was 30 nm, shutter problems leading to a longer evaporation time were discovered after acquisition. The true thickness t was estimated to be 20% higher than the nominal thickness, *i.e.*, $t = 36$ nm, with an error of approximately 5%. Off-axis electron holograms were acquired in an FEI Titan 60-300 [44] at 300 kV using a biprism voltage of 92 V, resulting in a holographic interference fringe spacing of 3.1 nm. The sample was magnetised inside the electron microscope by using the magnetic field of the objective lens. After the first hologram was acquired, the magnetisation state of the sample was reversed and a second hologram was recorded. After reconstructing the recorded phase images (*cf.* Section 2.1), the electrostatic contribution to the phase shift was removed by taking half of the difference between the aligned phase images. The resulting magnetic phase image is shown in Fig. 5.19. A mask, which is visible as a dotted outline, was constructed by using the electrostatic (*i.e.*, mean inner potential) contribution to the

109

phase shift (*cf.* Section 2.1) to locate four approximately rectangular regions, which are oriented in a "plus" formation[12]. The two holograms that were used to generate the magnetic phase image had to be shifted with respect to each other so that they could be aligned before being subtracted. As a result of this alignment, regions at the upper and right border contained artefacts and the confidence value in these regions was set to zero, as marked in Fig. 5.19. The confidence values of regions corresponding to phase unwrapping errors in the magnetised regions were also set to zero. The grid spacing in the image and therefore in the reconstruction is $a = 1.85\,\text{nm}$. Preparation of the sample, acquisition of the holograms, reconstruction of the phase images and subsequent assessment of the magnetisation position and trustworthy phase regions were conducted by Patrick Diehle from the Ernst Ruska-Centre for Microscopy and Spectroscopy with Electrons in Forschungszentrum Jülich.
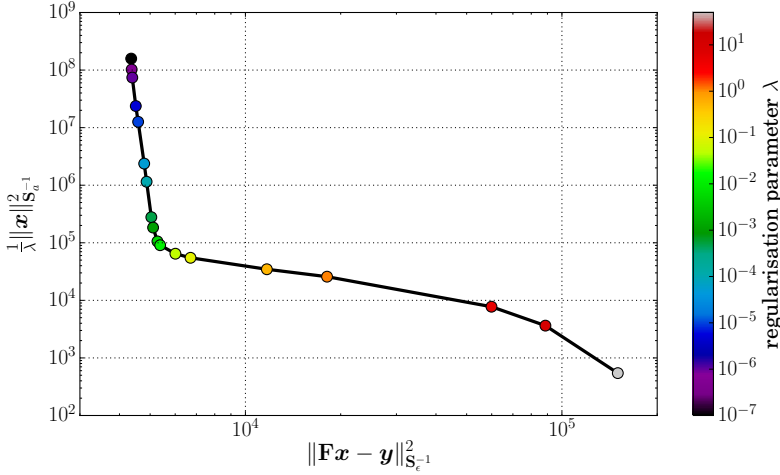

Figure 5.19.: Experimentally acquired magnetic phase image of a lithographically patterned structure. A 36 nm thick cobalt layer was deposited in a "plus" shape on a 50 nm thick Si_3N_4 membrane. The dotted lines mark the positions of the deposited magnetic regions. The dark regions mark untrustworthy regions, in which the confidence value was set to zero. The direction along which the sample was magnetised is indicated by the black arrow.

An L-curve analysis, as introduced in Section 5.2, was first conducted in order to determine an optimal value for the regularisation parameter λ. As described above, the choice of regularisation parameter depends on the level of measurement noise. The goal is to find a value for λ that results in a sufficiently smooth solution and also

---

[12]Identification of the correct mask can be challenging, especially in three dimensions. For example, oxidation of magnetic regions can lead to layers that are not magnetic but exhibit a change in mean inner potential, leading to a mask that is too large.

accurately reproduces the measured magnetic phase image. Reconstructions were performed for 18 regularisation parameters, ranging from very weak regularisation ($\lambda = 10^{-7}$) to very strong regularisation ($\lambda = 5$). The results, which are shown in Fig. 5.20, indicate that an adequate balance between smoothness and measurement compliance can be reached for a value of $\lambda = 0.01$. The reconstruction results do not vary drastically for regularisation parameters in the corner region of the L-curve, *i.e.*, for values between 0.001 and 0.1. The MBIR algorithm is not overly sensitive to λ in this region and all of these values lead to reasonable results.

Figure 5.20.: L-curve analysis of the experimentally acquired magnetic phase image shown in Fig. 5.19. The cost of the residual vector, which is expressed by the norm $\|\mathbf{F}\boldsymbol{x} - \boldsymbol{y}\|^2_{\mathbf{S}_\epsilon^{-1}}$, is plotted on a double logarithmic scale against the normalised regularisation term $\frac{1}{\lambda} \|\boldsymbol{x}\|^2_{\mathbf{S}_a^{-1}}$.

The resulting reconstructed projected in-plane magnetisation distribution is displayed in Fig. 5.21. In addition to the magnetisation, a linear phase ramp was fitted, as described in Section 5.4.1. This fit yielded a phase offset of -1.77 rad and a linear phase ramp of $1.42 \frac{\mathrm{mrad}}{\mathrm{nm}}$ in the u direction and $-1.46 \frac{\mathrm{mrad}}{\mathrm{nm}}$ in the v direction. The four rectangular magnetised regions contain a variety of different magnetic configurations. The upper and lower regions are nearly homogeneously magnetised along their long axes. The left region supports two clockwise vortices, while the right region shows a clockwise and a counter-clockwise vortex. The reconstruction result showcases the capability of the MBIR algorithm to simultaneously retrieve structures that have vastly differing magnetic configurations.

For such a two-dimensional reconstruction, the magnetisation is by default calculated for a slice of one pixel thickness (*i.e.*, $a = 1.85$ nm). Because the true thickness of the lithographically patterned structure is known to be $t = 36$ nm, a correction
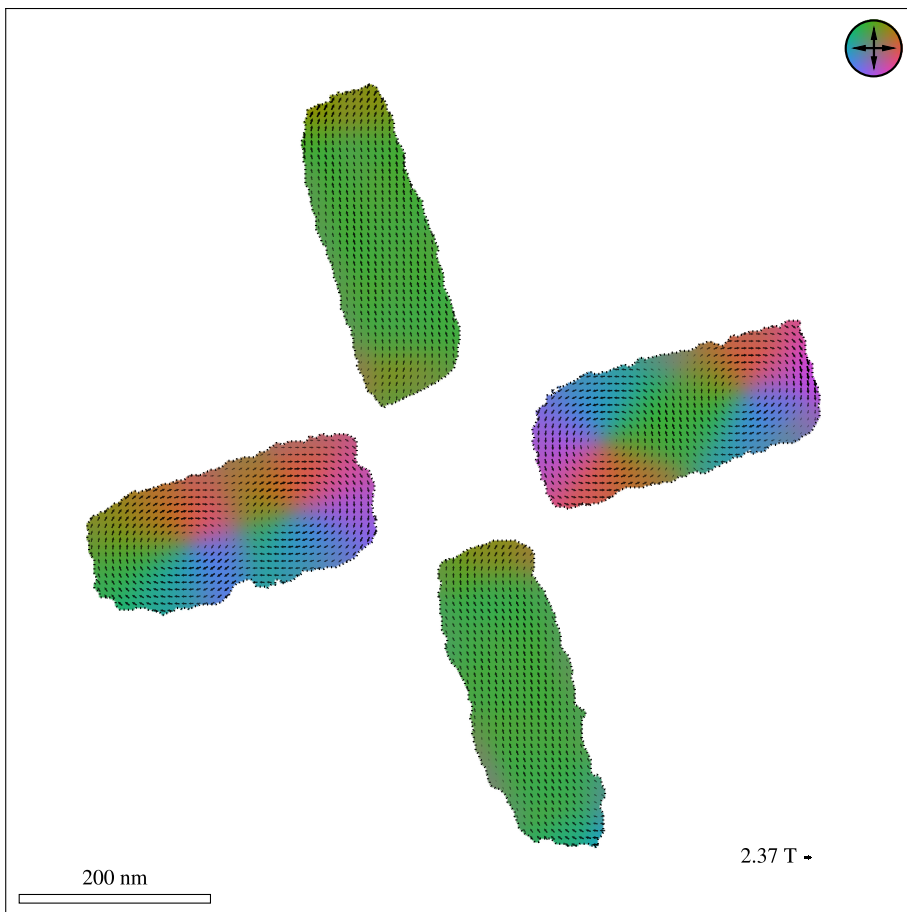
Figure 5.21.: Projected in-plane magnetisation distribution that was reconstructed from the experimentally acquired phase image shown in Fig. 5.19. A regularisation parameter of $\lambda = 0.01$ was used. For visualisation purposes, only every 4th arrow is displayed in the vector plot.

factor of $\frac{a}{t}$ has to be applied to obtain meaningful values for the magnetisation as a volume density of magnetic moments. The corrected maximum strength of the measured magnetisation is 2.37 T and is indicated by the arrow on the lower right of Fig. 5.21.

The magnitude of the reconstructed magnetisation and a corresponding histogram are show in Fig. 5.22. The peak of the magnitude histogram is in good agreement with the literature value for the saturation magnetic induction of 1.79 T [136]. Values on the left side of the histogram peak represent magnetised pixels which are not fully saturated in-plane. In particular the cores of the magnetic vortices and the regions between each pair of vortices are likely magnetised out-of-plane. Magnetised pixels, which have higher magnitudes than the saturation magnetic induction are likely caused by erroneously masked regions (*cf.* Section 5.3). This is indicated by the fact that the highest magnitude values were reconstructed at the borders of the mask (*cf.* Fig. 5.22a).

(a) (b)
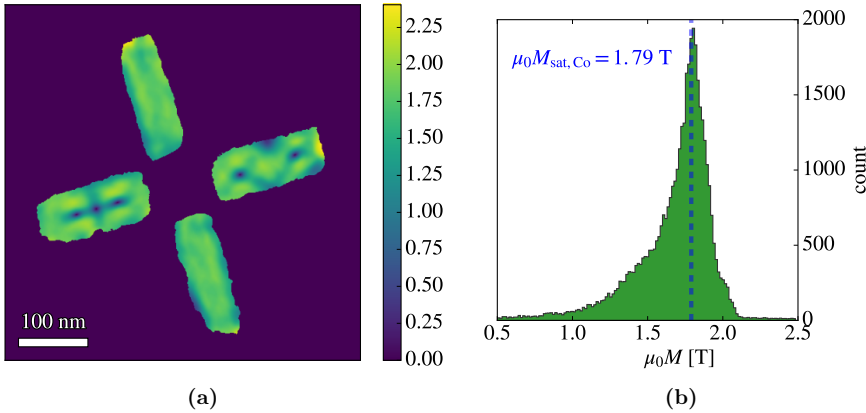
Figure 5.22.: (**a**) Plot of the magnitude of the reconstructed magnetisation distribution. (**b**) Correspoding histogram plot. The blue line indicates a literature value of $\mu_0 M_{sat} = 1.79$ T [136], which is in good agreement with the peak of the histogram. Only magnetised regions of the FOV were taken into account for the histogram.
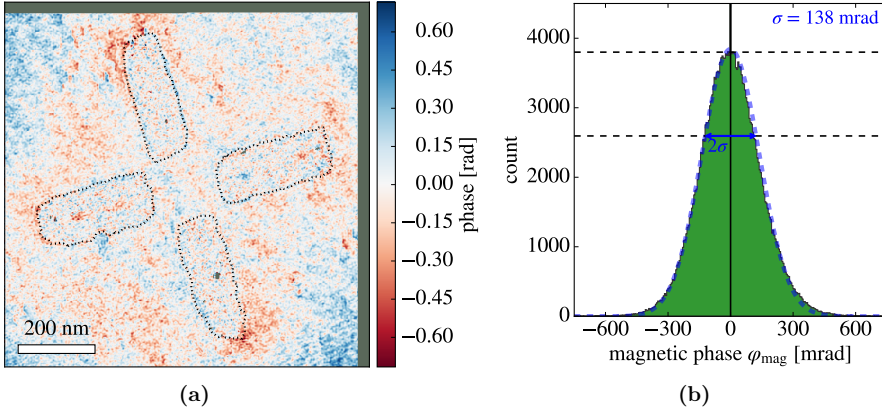
The reconstructed magnetisation distribution can be used to calculate a magnetic phase image by applying the RDFC forward model introduced in Section 3.2.4. The resulting image is displayed in Fig. 5.23a. The calculated phase reproduces the input phase image shown in Fig. 5.19 without measurement noise and without the phase ramp that was fitted. Subtraction of the phase ramp emphasises the phase symmetry around the homogeneously magnetised regions at the top and bottom. Figure 5.23b shows a magnetic induction map for the calculated magnetic phase image.

(a)   (b)
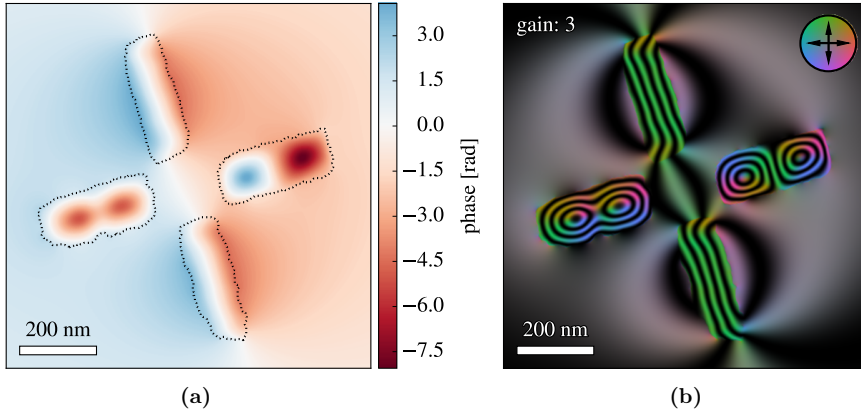
Figure 5.23.: (**a**) Magnetic phase image calculated by applying the forward model to the reconstructed magnetisation distribution shown in Fig. 5.21. (**b**) Corresponding magnetic induction map. The phase amplification factor is 3.

The calculated phase image shown in Fig. 5.23a can be used to retrospectively assess the measurement errors in the input phase image shown in Fig. 5.19. For this purpose, the input phase image was first ramp-corrected by subtracting the fitted phase ramp from it. The difference between the ramp-corrected input phase and the magnetic phase calculated from the reconstructed magnetisation is shown in Fig. 5.24a. Regions with a confidence value of zero are not taken into account. Plotting the resulting phase differences in a histogram, as depicted in Fig. 5.24b, reveals a Gaussian distribution, whose standard deviation of 138 mrad provides an estimate of the measurement noise.

For further analysis, the upper homogeneously magnetised region is shown separately in Fig. 5.25a. The averaging kernel row for the y component, which corresponds approximately to the magnetisation direction, was calculated as described in Section 5.1 for a central pixel. The spatial resolution of the reconstruction for the chosen parameters can be estimated from the FWHM of the reshaped averaging kernel row, which is shown in Fig. 5.25b and explained in Section 4.4.1. The spatial resolution in the y direction parallel to the magnetisation direction is approximately 34.1 nm, while the resolution in the x direction perpendicular to the magnetisation direction is approximately 16.1 nm. The relatively high values are caused by the applied regularisation and the corresponding smoothing effect to compensate for the noise in the input magnetic phase image. Both values are illustrated as an ellipse in Fig. 5.25b. Figure 5.25c shows the gain map of the chosen central pixel. It indicates which phase information has the biggest influence on the reconstructed y component of the magnetisation at the specified location.

Figure 5.24.: (**a**) Difference between the ramp-corrected input phase and the phase image calculated from the reconstructed magnetisation distribution shown in Fig. 5.21. (**b**) Histogram of the phase differences. The standard deviation of 138 mrad is an indicator for the measurement error of the phase image.

The mean value of the in-plane magnetisation in the upper magnetised region is calculated to be 1.73 ± 0.20 T on the assumption of a magnetic specimen thickness of $t = 36$ nm. The error in the thickness t of 5% can be propagated to the magnetisation and yields another uncertainty of ± 0.09 T. The estimate of the measurement error in the phase image of 138 mrad can be converted to an error in the reconstructed magnetisation of 0.22 T by using the gain matrix according to Eq. 4.39 in its simplified form (*cf.* Eq. 4.35). In order to account for the known thickness, this reconstruction noise has to be multiplied by the correction factor $\frac{a}{t}$. The result is a value of 0.01 T. By using error propagation as a summation of variances, the mean magnetisation and the corresponding error are calculated to be 1.73 ± 0.22 T, which is in good agreement with the literature value for cobalt of 1.79 T [136]. The standard deviation of 0.22 T is much higher than the reconstruction noise of 0.01 T, which only takes the noise of the input magnetic phase image into account. The reason for this difference may result from the out-of-plane moments and erroneously masked regions, which were already mentioned above. The total magnetic moment of the upper magnetised region is calculated to be $1.592 \cdot 10^{-15}$ Am$^2 = 1.715 \cdot 10^8 \, \mu_B$, with μ_B being the Bohr magneton, by summing up the magnetic moments of all involved voxels.

40 nm

(a)   (b)   (c)
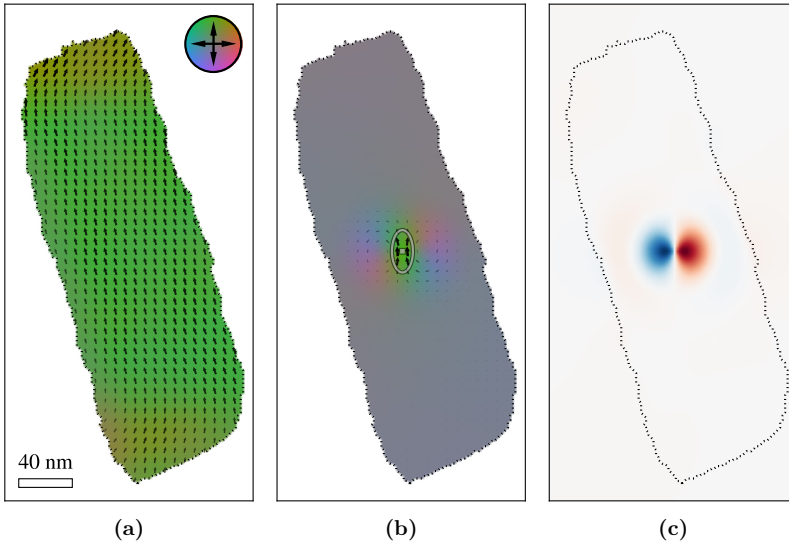
Figure 5.25.: (**a**) Reconstruction of the upper magnetised region in Fig. 5.21. (**b**) Averaging kernel row, calculated for the y component of a pixel that is positioned in the centre of the magnetised region. (**c**) Corresponding gain map for the same position. For visualisation purposes, only every 4th arrow is displayed in the vector plots shown in (**a**) and (**b**).

5.7. Summary

The aim of this chapter was the reconstruction of two-dimensional projected magnetisation distributions. The influence of the regularisation parameter on the reconstruction was evaluated by examining the associated averaging kernel. By calculating the FWHM of the averaging kernel rows, the resolution of the reconstruction can be estimated. The determination of an optimal regularisation parameter λ that balances compliance with the measurements and the smoothness of the solution was tackled by introducing the L-curve method, which was conducted for different test distributions and different levels of Gaussian noise. The importance of the choice of mask was emphasized and artefacts resulting from variations in mask size were evaluated. It was found that masks that underestimate the size of the magnetised regions lead to larger artefacts than masks whose size is overestimated. Methods to account for sources of magnetisation outside the FOV were proposed. The fit of a phase ramp in two- and three-dimensional reconstructions yields a phase offset and a linear phase ramp for each phase image in the MBIR algorithm. However, for very close magnetisation sources, a phase ramp does not sufficiently reproduce the additional contributions to the phase. In order to account for such magnetisation sources, buffer pixels were introduced in order to "shield" the reconstruction inside the FOV from the external sources. This method is more flexible than the use of a phase ramp. However, its application to three-dimensional reconstructions is significantly more complicated, if not unfeasible. Perturbation of the vacuum reference wave, as a result of the presence of long-range stray magnetic fields of the magnetised object itself, was addressed by modifying the convolution kernels. For other artefacts, a confidence array, which was introduced in Section 4.3, was used successfully to exclude erroneous regions from the reconstruction process. A two-dimensional reconstruction was performed successfully on an experimentally acquired phase image and was analysed quantitatively, using strategies developed in this chapter.

6. Magnetisation reconstruction in three dimensions

The reconstruction of three-dimensional magnetisation distributions from tilt series of phase images poses a set of unique challenges, which are tackled in this chapter. First, three test magnetisation distributions are introduced. These distributions are utilised to assess the dependence of the reconstruction results on the maximum tilt angle and the angular sampling of the tilt series of magnetic phase images, which are used as input for the MBIR algorithm. The importance of the mask in three dimensions is then examined. A reconstruction from phase images that include Gaussian noise, as well as random phase ramps and offsets, is conducted for one of the magnetisation distributions. This reconstruction and the subsequent analysis demonstrate the capabilities of the MBIR algorithm in three dimensions under realistic conditions.

6.1. Test magnetisation distributions

Three test magnetisation distributions were each placed in a volume of $N_x \times N_y \times N_z = 32 \times 32 \times 32$ voxels. The grid spacing was chosen as $a = 5\,\mathrm{nm}$, resulting in a spatial volume of $160 \times 160 \times 160\,\mathrm{nm}^3$. The magnetic phase images are therefore comparable to the experimental results presented in Section 5.6. Each of the three test magnetisation distributions was used to construct two simulated orthogonal tilt series of magnetic phase images by applying the new RDFC forward model for tilts about both the x and the y axis. The resulting simulated magnetic phase images were used as input for a magnetisation reconstruction using the MBIR algorithm. Each image had a size of $N_u \times N_v = 64 \times 64$ pixels, corresponding to a FOV of $320 \times 320\,\mathrm{nm}^2$. The saturation magnetic induction in each of the test magnetisation distributions was set to a value of $B_\mathrm{sat} = 1\,\mathrm{T}$.

The first test distribution is a magnetic disc with a radius $R = 80\,\mathrm{nm}$ and a thickness of $t = 80\,\mathrm{nm}$, which supports a clockwise magnetic vortex state in the xy plane. This distribution is shown in Fig. 6.1a in the form of a vector plot. The colour scheme for this and all of the following three-dimensional vector plots is explained in the appendix in Section A.5. As stated in Section 4.5.1, homogeneous magnetisation distributions and magnetic vortex states result in two different behaviours that can be compared to the Helmholtz decomposition of a vector field into a curl-free and

a divergence-free part. In order to assess whether the MBIR algorithm is able to successfully reconstruct both a vortex state and a homogeneously magnetised region, the core of the disc was magnetised out-of-plane in positive z direction. The radius of the core was chosen to be 20 nm, so that the phase contributions of the vortex and the core would be of the same order of magnitude. The magnetisation direction of the core is marked with white arrows in Fig. 6.1a. When approaching the homogeneously magnetised core from the surrounding vortex state, the magnetic moments gradually rotate out of the xy plane, according to Eq. 2.29. Along the z axis, each xy slice of the magnetisation distribution is equal, $i.e.$, that the distribution does not vary along the z direction in magnitude or direction of the magnetisation. In general, the most information about the variation in the z direction of a magnetic object is obtained for projections with high tilt angles about the x or the y axis. Reconstruction of the magnetic vortex state in the xy plane therefore should not change significantly when these hight tilt angles are missing, which is examined in the next section. Figure 6.1b shows a magnetic phase image that corresponds to a projection along the z direction, while Fig. 6.1c corresponds to a projection along the y direction. The homogeneously magnetised core lies in the null space of the z projection and therefore does not contribute to the magnetic phase in this direction. In turn, the vortex does not contribute to the magnetic phase when projected along any direction that is perpendicular to the z axis. In order to reconstruct all of the important features of the magnetisation distribution, tilt series of magnetic phase images are therefore absolutely necessary.

The second test distribution is constructed similarly to the previous vortex structure, but is oriented in the yz plane, instead of the the xy plane. The corresponding vector plot of the magnetisation is shown in Fig. 6.2a. The homogeneously magnetised core is now magnetised along the positive x direction, as indicated by red arrows. In contrast to the first test distribution, the vortex in the yz plane varies strongly in magnetisation magnitude and direction along the z direction. Reconstruction of the magnetic vortex state in the yz plane should therefore be more sensitive to missing high tilt angles. Figure 6.2b shows a magnetic phase image for a projection along the z direction, while Fig. 6.2c corresponds to a projection along the x direction.

The third test distribution is chosen to be difficult to reconstruct, in order to explore the capabilities and limits of the MBIR algorithm. As for the previous distributions, the geometrical shape is again a disc with a radius of $R = 80$ nm, but with a greater thickness of $t = 90$ nm and without a homogeneously magnetised core. The disc is now built out of three layers. The uppermost layer is 30 nm thick and supports a clockwise magnetic vortex state, similar to the first test distribution. The magnetic moments rotate to an out-of-plane orientation in positive z direction when approaching the vortex core, according to Eq. 2.29. The lowermost layer contains the same vortex structure, but turned over in the xy plane. The vortex therefore spins counter-clockwise and the magnetisation in the centre points in negative z direction. The two vortices are separated by a non-magnetic layer of the same thickness and radius. The resulting stack is illustrated in Figs. 6.3a and 6.3b. The experi-

mental identification of such a non-magnetic layer is likely to be very challenging. If the mask is constructed using the mean inner potential contribution, it may be difficult to distinguish between magnetised and non-magnetised regions, in particular if the mean inner potentials of the three layers are similar. In order to assess this difficulty, the non-magnetic layer is included in the three-dimensional mask for the reconstruction below. The MBIR algorithm is therefore allowed to falsely fit magnetisation in this region. The magnetisation distributions of the two vortices sum up to zero for a projection along the z direction. The vortices therefore lie in the null space of a z projection and no magnetic phase is produced. Furthermore, each vortex separately adds up to zero for any projection perpendicular to the z axis. Only the small component along the z axis in the vortex cores produces any magnetic phase when it is projected in these directions. The resulting magnetic phase is shown in Fig. 6.3c and is significantly smaller than that produced by the previous distributions. Information about the vortices can only be obtained from projections in directions that are oblique to the three major axes. Out of the three presented distributions, this vortex stack poses the biggest challenge for the MBIR algorithm.
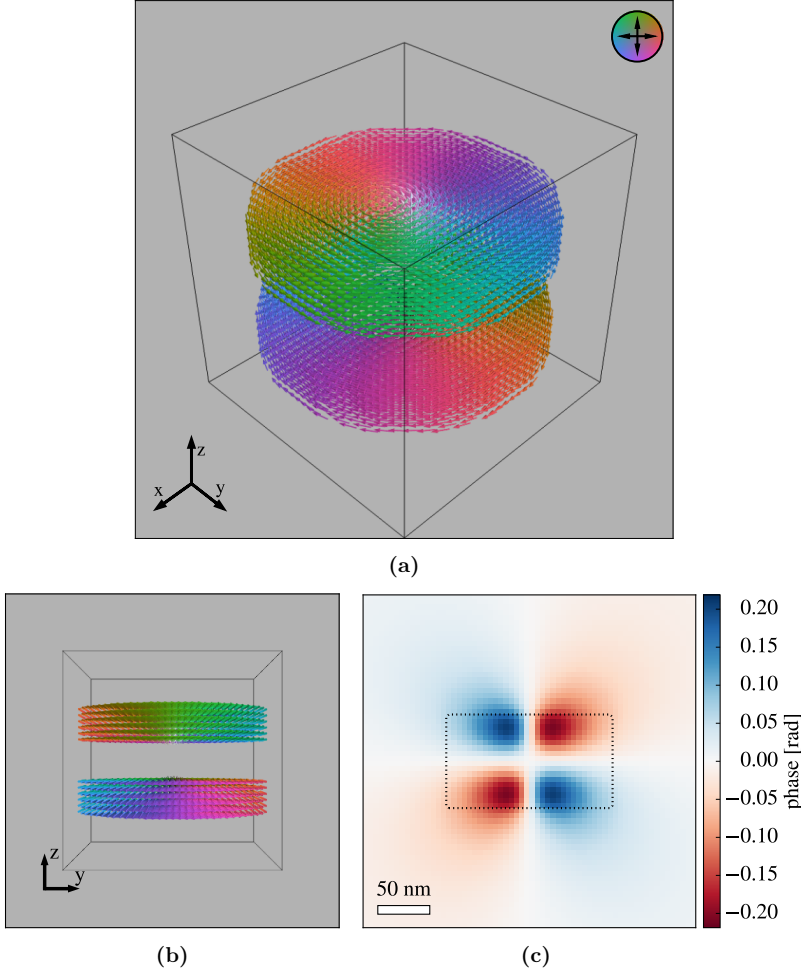
(a)

(b)

(c)
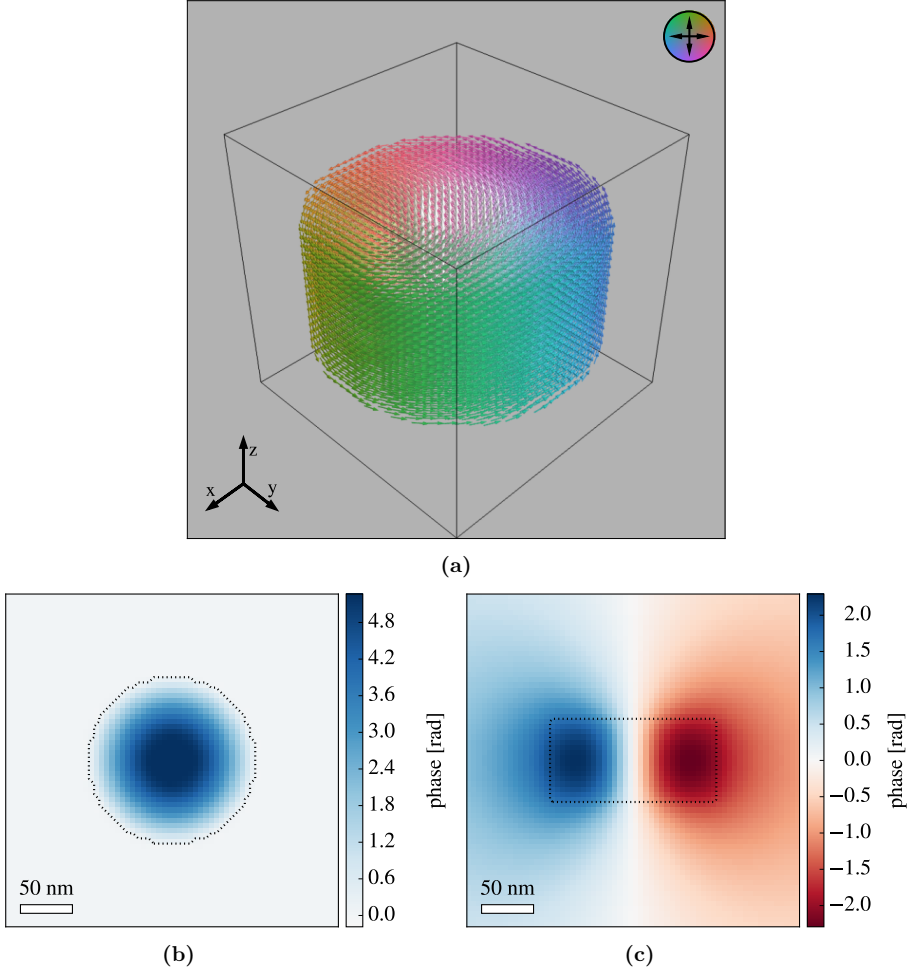
Figure 6.1.: (**a**) Vector plot of the magnetisation of a magnetised disc of radius $R = 80\,\mathrm{nm}$ and thickness $t = 80\,\mathrm{nm}$ in a volume of $160 \times 160 \times 160\,\mathrm{nm}^3$. The disc supports a clockwise vortex state in the xy plane. The grid spacing is $a = 5\,\mathrm{nm}$, which results in a size of $N_x \times N_y \times N_z = 32 \times 32 \times 32$ pixels along the axes. The core of the disc has a radius of $20\,\mathrm{nm}$ and is magnetised out-of-plane in the positive z direction. The colour wheel in the upper right corner describes the direction of magnetisation in the xy plane. White arrows point in the positive z direction, while black arrows point in the negative z direction. The coordinate system at the lower left indicates the x, y and z axes. (**b**) Magnetic phase image for a projection along the z direction. (**c**) Magnetic phase image for a projection along the y direction. Both magnetic phase images are calculated for a FOV of $320 \times 320\,\mathrm{nm}^2$, corresponding to $N_u \times N_v = 64 \times 64$ pixels.

(a)

(b)

(c)
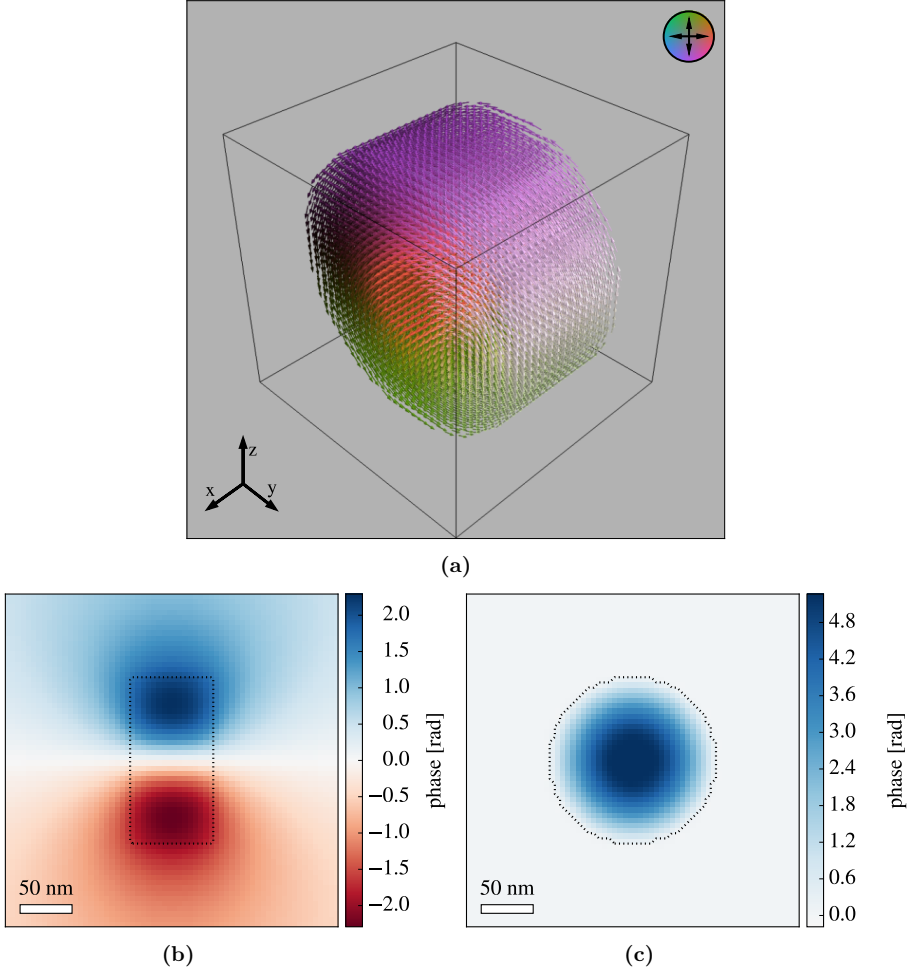
Figure 6.2.: (**a**) Vector plot of the magnetisation of a magnetised disc of radius $R = 80\,\mathrm{nm}$ and thickness $t = 80\,\mathrm{nm}$ in a volume of $160 \times 160 \times 160\,\mathrm{nm}^3$. The disc supports a clockwise vortex state in the yz plane. The grid spacing is $a = 5\,\mathrm{nm}$, which results in a size of $N_x \times N_y \times N_z = 32 \times 32 \times 32$ pixels along the axes. The core of the disc has a radius of $20\,\mathrm{nm}$ and is magnetised in the positive x direction, as indicated by red arrows. The colour wheel in the upper right corner describes the direction of magnetisation in the xy plane. White arrows point in the positive z direction, while black arrows point in the negative z direction. The coordinate system at the lower left indicates the x, y and z axes. (**b**) Magnetic phase image for a projection along the z direction. (**c**) Magnetic phase image for a projection along the x direction. Both magnetic phase images are calculated for a FOV of $320 \times 320\,\mathrm{nm}^2$, corresponding to $N_u \times N_v = 64 \times 64$ pixels.

(a)

(b)

(c)

Figure 6.3.: (**a**) Vector plot of the magnetisation of a magnetised disc of radius $R = 80\,\text{nm}$ and thickness $t = 90\,\text{nm}$ in a volume of $160\times160\times160\,\text{nm}^3$. The grid spacing is $a = 5\,\text{nm}$, which results in a size of $N_x \times N_y \times N_z = 32 \times 32 \times 32$ pixels along the axes. The disc is built out of three layers, each of which has a thickness of $30\,\text{nm}$. The uppermost layer supports a clockwise magnetic vortex with a smooth core. The magnetisation of the core points in the positive z direction. The lowermost layer supports a counter-clockwise magnetic vortex with a smooth core, whose magnetisation points in the negative z direction. The two vortices are separated by a $30\,\text{nm}$ thick non-magnetic layer. The colour wheel in the upper right corner describes the direction of magnetisation in the xy plane. (**b**) shows the same vector plot viewed along the negative x direction. (**c**) Magnetic phase image for a projection along the negative x direction. The image was calculated for a FOV of $320 \times 320\,\text{nm}^2$, corresponding to $N_u \times N_v = 64 \times 64$ pixels.

6.2. Influence of the maximum tilt angle

Ideally, the two tilt series of magnetic phase images that are used as input for the MBIR algorithm, should cover the full range of tilt angles from $+90°$ to $-90°$ in order to collect information about the sample from all projection directions. However, in practice the maximum tilt angle is often limited by the capabilities of the sample stage of the microscope, as well as by the geometry of the sample and the holder inside the TEM, which may result in shadowing at high tilt angles. Furthermore, the effective thickness of the sample and its substrate can increase significantly for tilts approaching $±90°$. A realistic practical tilt range reaches maximum angles of between $60°$ and $75°$.

The influence of the maximum tilt angle on the reconstruction using the MBIR algorithm is assessed in this section. For this purpose, the maximum tilt angle is varied between $±10°$ and $±90°$ in steps of $10°$. Reconstructions are performed for all three test distributions, which were introduced in Section 6.1. 27 magnetisation distributions are therefore retrieved in total. The angular sampling is chosen to be $5°$ for all of the reconstructions. As a result, the number of magnetic phase images per reconstruction also varies from reconstruction to reconstruction. For a maximum tilt angle of $±10°$, 10 input magnetic phase images (5 per tilt series) are required, while for a maximum tilt angle of $±90°$ this number rises to 74 input magnetic phase images (37 per tilt series). Variations in angular sampling are analysed separately in Section 6.3. The three-dimensional mask Ξ, which determines the position of the magnetised disc, is assumed to be known exactly. The influence of the mask was assessed for the two-dimensional case in Section 5.3 and is discussed briefly for the three-dimensional case in Section 6.4. The regularisation parameter is set to a relatively low value[1] of $\lambda = 10^{-5}$ in order to isolate the influence of the maximum tilt angle on the reconstruction from regularisation effects. It is important to note that values for λ cannot be simply transferred from the two- to the three-dimensional case.

The RMS error quantities, which were introduced in Section 4.4.2, are employed for the evaluation of the reconstruction results and displayed in Fig. 6.4 as a function of the maximum tilt angle. RMS errors are calculated from the differences between the reconstructions and their corresponding original distributions from Section 6.1. Figure 6.4a shows the magnitude error ϵ_{mag} for the two vortex structures with homogeneously magnetised core. The according directional error is shown in Fig. 6.4b.

For the disc that supports a magnetic vortex state in the xy plane, no significant dependence on maximum tilt angle is observed. As a result of the orientation of the magnetic vortex in the xy plane, it lies in the null space of projections that are perpendicular to the z axis, $i.e.$, for tilt angles of exactly $±90°$ about the x or y axis, as discussed in Section 4.5.1. Projections along angles that are close to $±90°$ only produce weak magnetic phase images. These angles are in the tilt range

---

[1]An L-curve analysis that justifies this choice is conducted in Section 6.5.

of the missing wedge for lower maximum tilt angles, such as $\pm 60°$. Most of the information about the magnetic vortex is obtained from projections along the z axis, which explains why the reconstruction works well even for maximum tilt angles of only $\pm 10°$. The opposite situation holds for the homogeneously magnetised vortex core in the same test magnetisation distribution, which lies in the null space for a projection parallel to the z axis and produces no magnetic phase. The magnetic phase contribution of the core is greatest at tilts angles of $\pm 90°$ (*cf.* Fig. 6.2b). Nevertheless, it was found that the vortex core is reconstructible even if only weak phase contributions (*e.g.* for $\pm 10°$) are available, as the first test distribution does not change along the z axis, as mentioned in Section 6.1

For the second test distribution, which supports a vortex state in the yz plane (*cf.* Fig. 6.2), a significant dependence on the maximum tilt angle was found, as can be seen in the form of plots of ϵ_{mag} and ϵ_{dir} in Figs. 6.4a and 6.4b, respectively. The magnetic vortex lies in the null space of projections in the z direction and its reconstruction therefore relies on the tilts about the x and the y axis. A significant decrease in the RMS error quantities is already apparent when relatively low maximum tilt angles of $\pm 30°$ are available. In order to illustrate the influence of the maximum tilt angle, reconstructed magnetisation distributions for maximum tilt angles of $\pm 10°$ and $\pm 90°$ are shown in Fig. 6.5. By increasing the maximum tilt angle from $\pm 10°$ to $\pm 90°$, the RMS error quantities were reduced from $\epsilon_{\mathrm{mag}} = 0.043$ and $\epsilon_{\mathrm{dir}} = 0.016$ to $\epsilon_{\mathrm{mag}} = 0.008$ and $\epsilon_{\mathrm{dir}} = 0.002$.

Reconstruction results for the third test distribution, which contains the stack of two opposing vortices separated by a non-magnetic layer, are shown in Figs. 6.4c and 6.4d. They are displayed separately because ϵ_{mag} and ϵ_{dir} are larger than for the first two distributions. The errors are larger because the MBIR algorithm is allowed to erroneously fit magnetisation within the non-magnetic layer, which is included in the masked region, as stated in Section 6.1. In order to correctly identify the non-magnetic layer, magnetic phase images recorded perpendicular to the z axis are of utmost importance. These projections correspond to tilts of $\pm 90°$ about the x or y axis. For all other projection directions, the non-magnetic region is at least partly shadowed by the two vortex layers. When compared with the test distribution that contains a vortex in the yz plane, the most significant improvement in ϵ_{mag} for the vortex stack occurs when the highest tilt angles of $\pm 90°$ are included (*cf.* Fig. 6.4c). The choice of maximum tilt angle does not affect the directional error ϵ_{dir} noticeably. The erroneous assignment of magnetisation to non-magnetic regions emphasises the importance of the mask Ξ, which is further examined in Section 6.4.
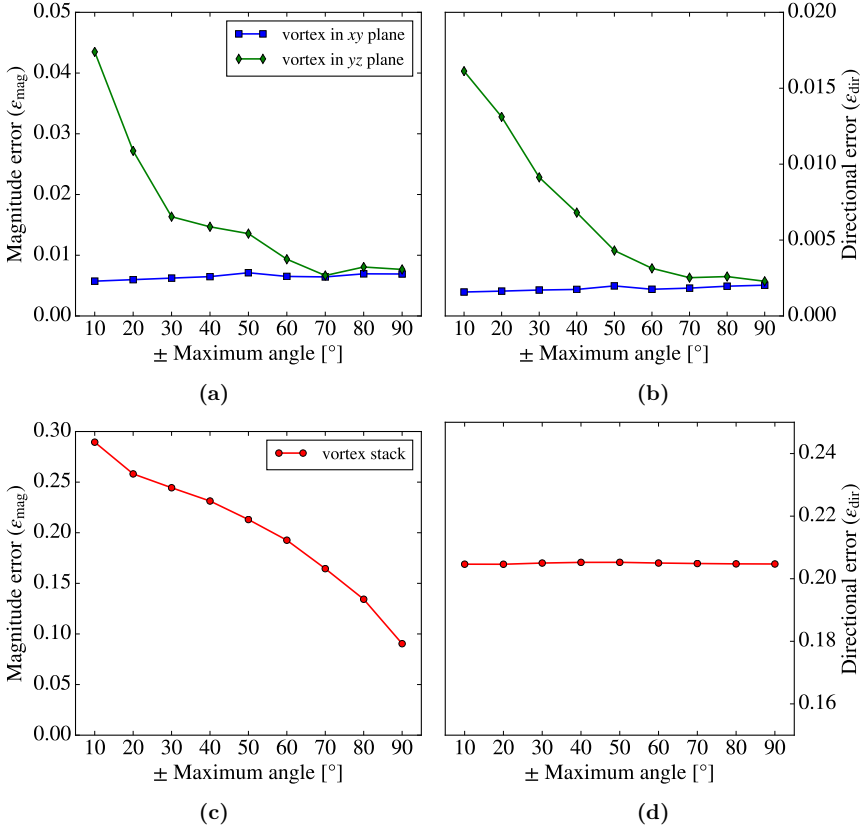
Figure 6.4.: RMS error quantities plotted as a function of maximum tilt angle for three-dimensional magnetisation reconstructions. (**a**) Magnitude error ϵ_{mag} for the vortex distribution in the xy plane (marked in blue) and the vortex in the yz plane (marked in green). (**b**) Corresponding directional error ϵ_{dir}. The results for the vortex stack distribution are shown separately in (**c**) and (**d**) (marked in red). No significant dependence of the errors on the maximum tilt angle can be inferred for the vortex in xy plane. For the other two test distributions, a higher maximum tilt angle leads to a significant improvement of the goodness of fit.

(a)   (b)

(c)   (d)
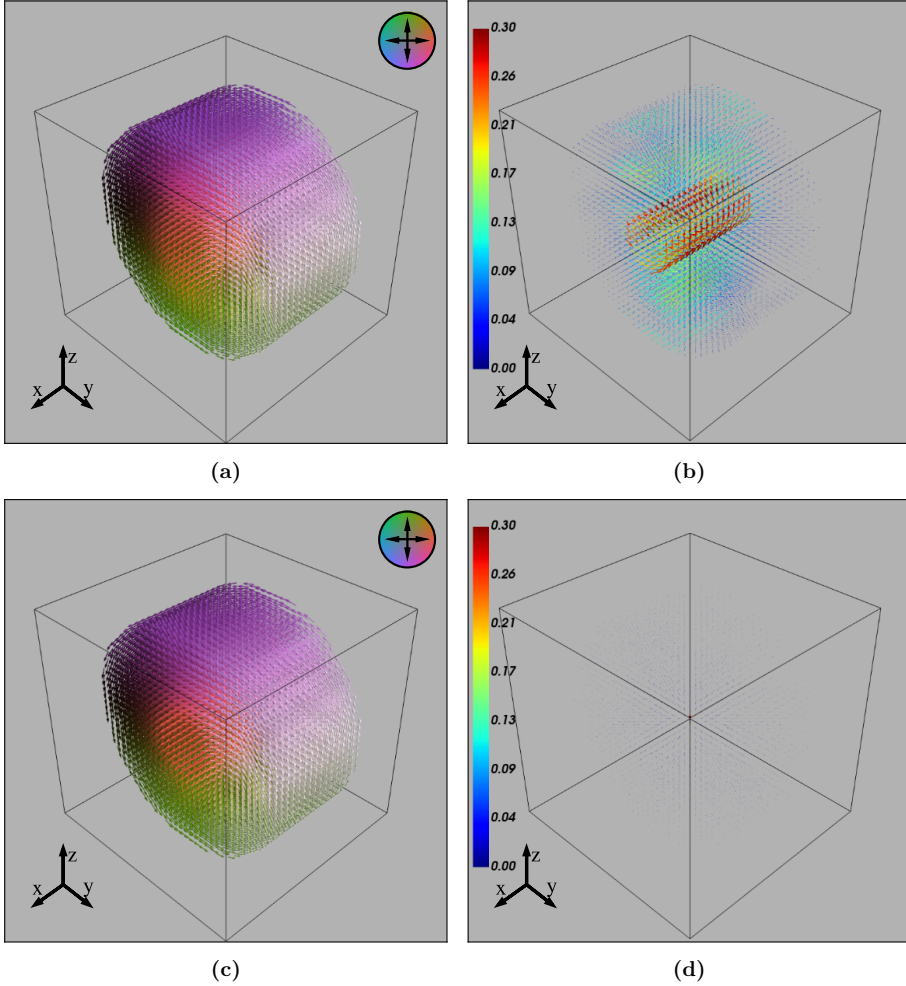
Figure 6.5.: (**a**) 3D vector plot of the reconstructed magnetisation distribution of the disc that supports a magnetic vortex state in the yz plane with a maximum tilt angle of $\pm 10°$ and an angular sampling of 5°. The colour wheel encodes the magnetisation direction in the xy plane. (**b**) 3D vector plot of the difference between the original magnetisation distribution and its reconstruction. The amplitude of the arrows is colour-coded according to the colour bar on the left side. (**c**) and (**d**) show corresponding plots for a reconstruction with a maximum tilt angle of $\pm 90°$ and an angular sampling of 5°. The higher maximum tilt angle significantly improves the reconstruction results. The difference plots are shown with the same scale and a maximum value of 0.3 T, which causes the arrows in (**d**) to be barely visible.

6.3. Influence of the angular sampling

This section focuses on the influence of the angular sampling on the reconstruction results. Two sets of reconstructions are performed for each test distribution: one for the ideal case of a maximum tilt angle of $\pm 90°$ and one for the more realistic case of a maximum tilt angle of $\pm 60°$. Reconstruction results for both maximum tilt angles are obtained for angular samplings of $1°$, $2°$, $5°$, $10°$ and $20°$. The number of input phase images varies from 14 for angles of $\pm 60°$ and an angular sampling of $20°$ to 362 for angles of $\pm 90°$ and an angular sampling of $1°$. The three-dimensional mask Ξ is assumed to be known exactly and the regularisation parameter is set to a relatively low value of $\lambda = 10^{-5}$. As in the previous section, the RMS error quantities ϵ_{mag} and ϵ_{dir} are used to assess the reconstruction results.

Figures 6.6a and 6.6b show that the reconstruction results depend only slightly on angular sampling for the first test distribution, which supports a vortex state in the xy plane, as a result of the fact that the magnetisation distribution does not vary along the z axis. Even when coarse angular sampling is used, the important features of the magnetisation distribution can be effectively reproduced. The same lack of dependence on angular sampling can be observed for the second test distribution, which supports a vortex state in the yz plane, for a maximum tilt angle of $\pm 90°$ (*cf.* Figs. 6.6a and 6.6b). However, the reconstruction results do show a dependence on angular sampling if the maximum tilt angle is decreased to $\pm 60°$. As shown in the last section, a reduction in maximum tilt angle leads to a decrease in reconstruction quality, due to the loss of information along the missing projection directions. Finer angular sampling can only partly compensate for this loss of information. Results for the vortex stack distribution are shown in Fig. 6.6c. Here, finer angular sampling leads to an improvement in ϵ_{mag} for both maximum tilt angles of $\pm 60°$ and $\pm 90°$. The angular sampling has no significant effect on the directional error ϵ_{dir} (*cf.* Fig. 6.6d). The influence of angular sampling on the reconstructed magnetisation distribution of the vortex stack is shown in Fig 6.5 for a maximum tilt angle of $\pm 90°$ and angular samplings of $\pm 20°$ and $\pm 1°$. The magnitude error was reduced from $\epsilon_{\mathrm{mag}} = 0.197$ to $\epsilon_{\mathrm{mag}} = 0.085$, by changing the angular sampling from $\pm 20°$ to $\pm 1°$.

In conclusion, the maximum tilt angle is more important for the quality of the reconstruction than the angular sampling for the presented test magnetisation distributions. An angular sampling of $5°$ proved to be enough to produce acceptable reconstruction results in all three cases. The orientation of the magnetic features of the sample relative to the tilt axes also plays an important role on the quality of the reconstruction.
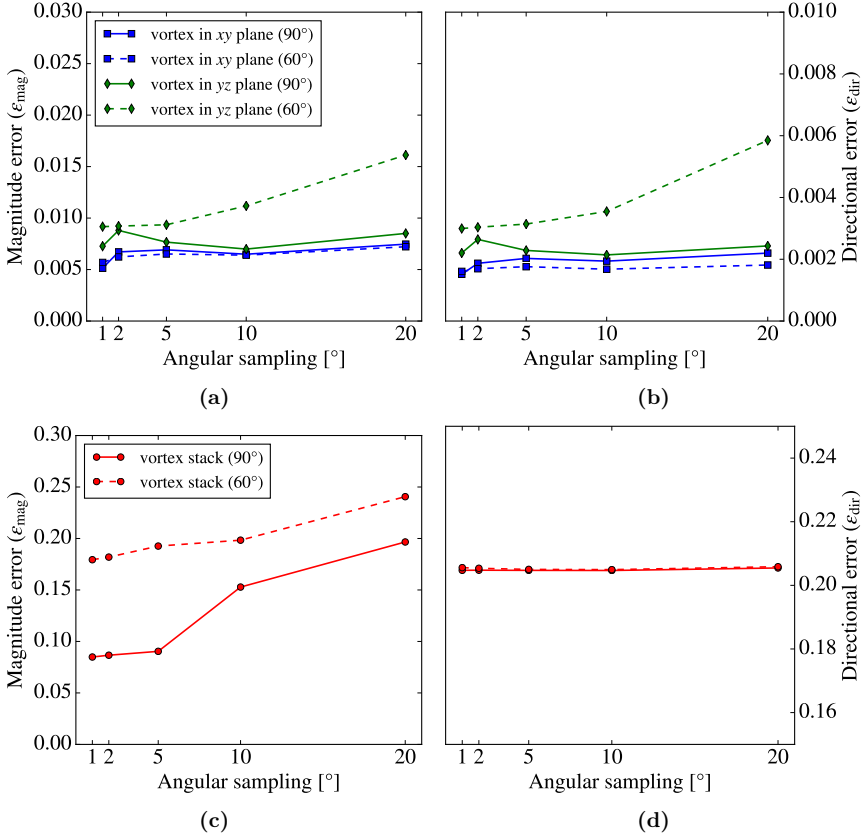
Figure 6.6.: RMS error quantities plotted as functions of angular sampling for three-dimensional magnetisation reconstructions. (**a**) Magnitude error ϵ_{mag} for the vortex distribution in the xy plane (marked in blue) and the vortex in yz plane (marked in green). (**b**) Corresponding directional error ϵ_{dir}. Larger errors occur for the reconstruction of the vortex stack distribution, for which the results are shown separately in (**c**) and (**d**) (marked in red). All of the displayed plots contain results for a maximum tilt angle of $\pm 90°$ (marked with solid lines) and for a maximum tilt angle of $\pm 60°$ (marked with dashed lines).

(a)　　　　　　　　　　　　　　**(b)**

(c)　　　　　　　　　　　　　　**(d)**
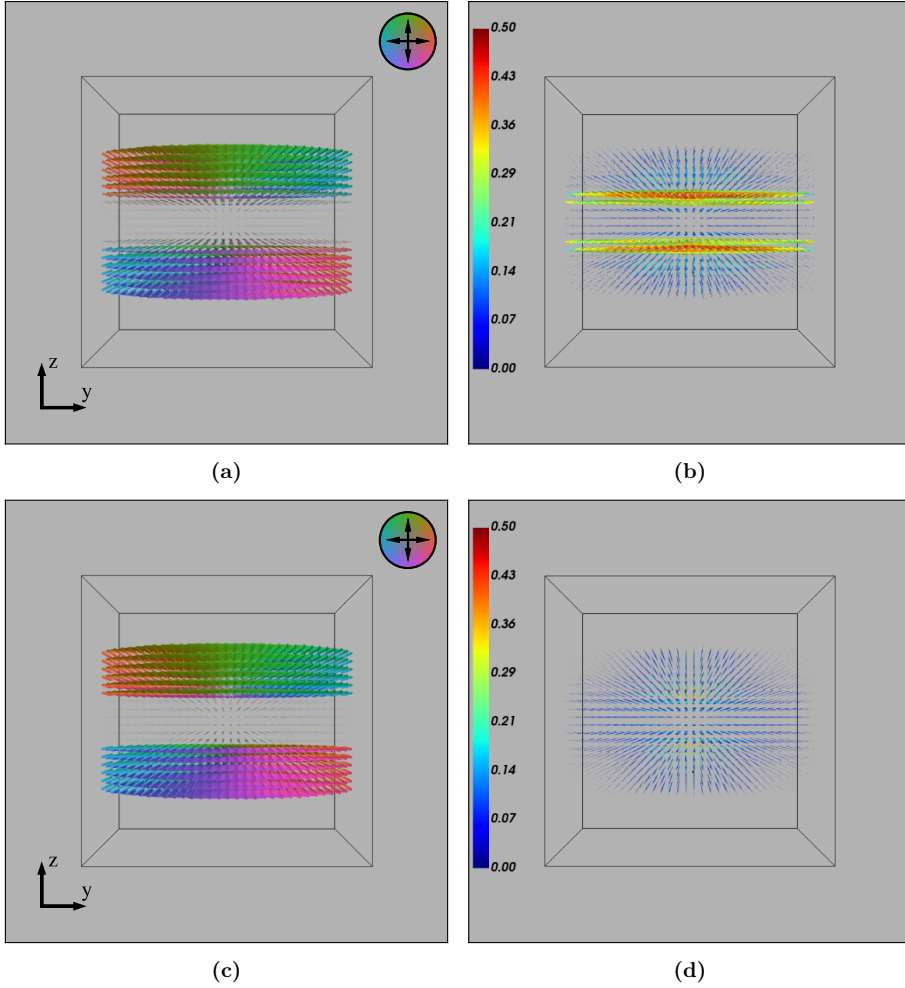
Figure 6.7.: (**a**) 3D vector plot of the reconstructed magnetisation distribution of the vortex stack for a maximum tilt angle of ±90° and an angular sampling of 20°, viewed along the x axis. The colour wheel encodes the magnetisation direction in the xy plane. (**b**) 3D vector plot of the difference between the original magnetisation distribution and its reconstruction. The amplitude of the arrows is colour-coded according to the colour bar on the left side. (**c**) and (**d**) show corresponding plots for a reconstruction with a maximum tilt angle of ±90° and an angular sampling of 1°. The finer angular sampling improves the reconstruction results. Both difference plots use the same colour bar scale with a maximum value of 0.5 T

6.4. Influence of the three-dimensional mask

As discussed above, a mask that does not accurately reflect the position of the magnetic object can lead to artefacts. The two-dimensional case was assessed in depth in Section 5.3. A mask that is too small increases the magnetisation in the outermost voxels, while a mask that is too large leads to a diffusion of magnetisation from correctly to erroneously masked regions. Equivalent artefacts also occur in three dimensions and are exacerbated by the fact the construction of a three-dimensional mask is not a trivial task. Although the mean inner potential contribution to the phase can in principle be used to obtain insight about the projected positions of magnetised objects, finding the three-dimensional mask is ultimately a tomographic problem in itself. Depending on the tomographic approach that is used to construct the mask, the presence of a missing wedge can lead to elongation of the mask in the corresponding direction. In order to assess the extent of the problem, two reconstructions of the magnetised disc that supports a vortex state in the xy plane were performed with different masks. Two tilt series of magnetic phase images about the x and y axes with a maximum tilt angle of $\pm 90°$ and an angular sampling of $5°$ were created by applying the forward model to this magnetisation distribution. The tilt series were used for both reconstructions with a regularisation parameter of $\lambda = 10^{-5}$. The first reconstruction used the optimal mask, which was given by the known shape of the magnetised disc. The mask for the second reconstruction was constructed by applying a simple discrete tomography algorithm[2] to the two-dimensional masks for all angles between $\pm 60°$ (*cf.* [51, 52]). The missing angles cause the mask to be extended in the form of pyramid-shaped structures above and below the magnetised disc along the z direction.
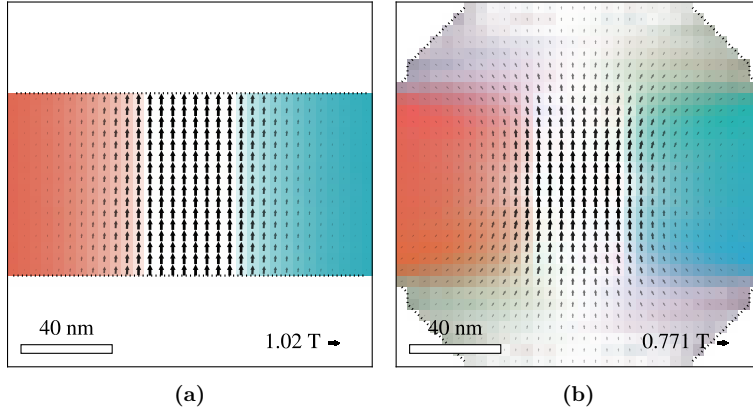
Three-dimensional vector plots of both reconstructions are shown in Fig. 6.8. Corresponding central slices perpendicular to the x axis are shown in Fig. 6.9. The reconstruction performed using the optimal mask is in very good agreement with the original magnetisation distribution, with RMS errors that are calculated to be $\epsilon_{\mathrm{mag}} = 0.007$ and $\epsilon_{\mathrm{dir}} = 0.002$. When using the imperfect mask, the magnetisation in the homogeneous core diffuses into the erroneously masked, pyramid-shaped structures above and below the disc. The RMS error values rise to $\epsilon_{\mathrm{mag}} = 0.29$ and $\epsilon_{\mathrm{dir}} = 0.035$. The maximum magnetisation in the centre of the vortex core is reduced by approximately 25% in comparison to the original distribution. Similar outward diffusion of homogeneous magnetisation distributions when using masks that are too large was observed for two-dimensional reconstructions in Section 5.3 (*cf.* Fig. 5.9a). The vortex state only diffuses into the nearest neighbouring voxels, which is also in agreement with the results for the two-dimensional reconstructions.

---

[2]The discrete tomography algorithm uses the transposed projection matrices $\mathbf{P}_b$ to calculate three-dimensional back-projections of the two-dimensional masks. These back-projections are then summed up and a threshold is used to define which voxels lie inside and outside the mask. The strictest setting defines the mask as the three-dimensional region where all back-projections overlap.
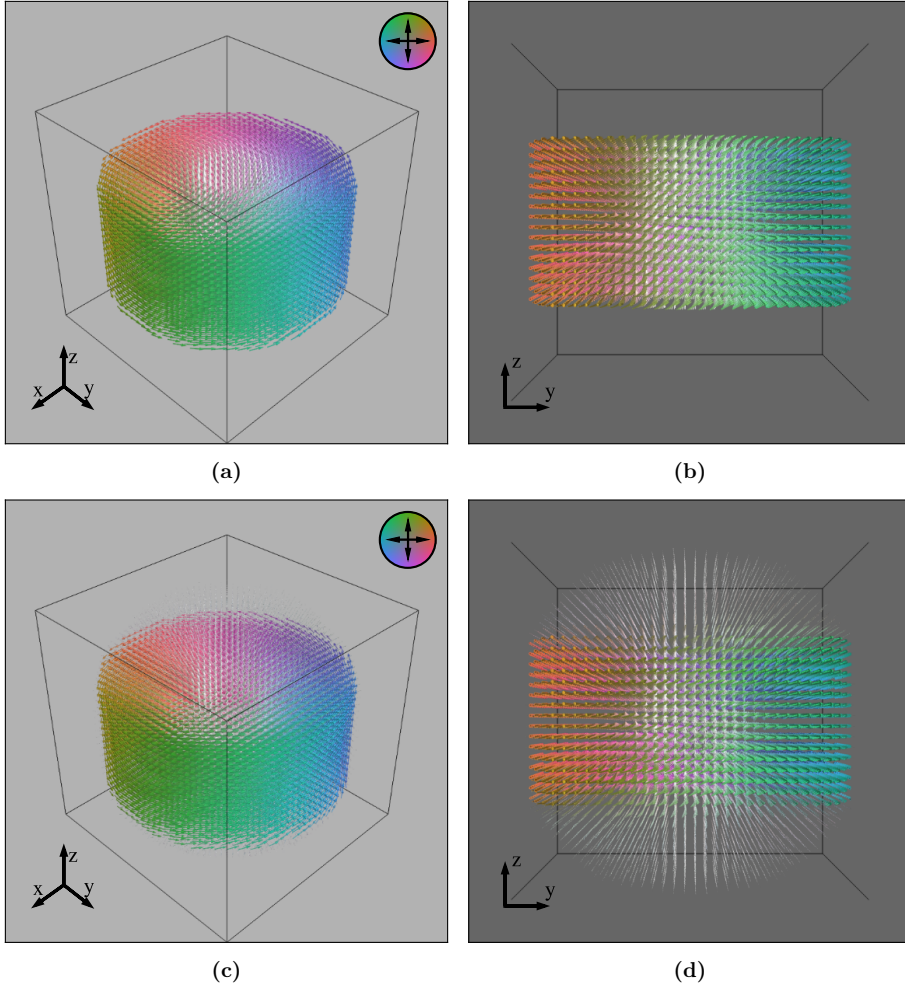
Figure 6.8.: (**a**) 3D Vector plot of the reconstructed magnetisation distribution of the vortex state in the xy plane for an optimal mask. The colour wheel encodes the magnetisation direction in the xy plane, while white arrows point in the positive z direction. A view along the x axis is shown in (**b**). Equivalent plots are shown in (**c**) and (**d**) for a reconstruction performed using a mask that was generated by applying a simple discrete tomography algorithm to the two-dimensional masks available for all angles between $\pm60°$. The magnetisation of the homogeneous core diffuses into the erroneously masked regions. This diffusion is visible in (**d**) as small white arrows above and below the magnetised disc. The vortex does not diffuse significantly. The backgrounds of the views along the x axis in (**c**) and (**d**) are set to a darker tone to increase visibility of the white arrows.

The results once more emphasise the importance of a correctly assigned mask for the reconstruction process.

Figure 6.9.: (**a**) Central slice viewed along the x direction of the vector plot shown in Fig. 6.8b for the optimal mask. The colours are encoded in the same way as in the three-dimensional vector plot, with white pointing in the positive z direction, red pointing in the positive x direction and blue pointing in the negative x direction. The arrows only show the magnetisation in the yz plane and not in x direction, which would be out of plane for the slice. (**b**) shows the same slice for the reconstruction with an imperfect mask, which was generated by applying discrete tomography to the two-dimensional masks for an incomplete range of angles (*cf.* Fig 6.8d). The magnetisation in the homogeneous core diffuses into the erroneously masked regions, reducing the maximum magnetisation in the centre of the core by approximately 25% (denoted by the arrow at the lower right). The input phase images for both reconstructions were calculated for a maximum tilt angle of $\pm 90°$ in steps of $5°$.

6.5. Reconstruction in three dimensions with noise and phase ramps

In this section, a realistic three-dimensional reconstruction that is affected by Gaussian noise, phase offsets and ramps is conducted for the first test distribution, which supports a vortex state in the xy plane and a homogeneous core pointing in the z direction. It is assumed that the mask is known accurately for the following reconstructions. Input phase images were constructed by applying the forward model based on the RDFC approach to the chosen magnetisation distribution for a limited angular range between $\pm 60°$ and an angular sampling of $5°$ about both the x and the y axis. Gaussian noise with $\sigma_\epsilon = 100$ mrad was added to all magnetic phase images to emulate experimental conditions. This level of noise is representative of

that measured in the experimental phase image in Section 5.6. In addition, a phase offset and a phase ramp were added to each magnetic phase image. The offsets were chosen randomly from a uniform distribution with a range of ± 5 rad, while the slopes of the ramp in the u and the v directions were chosen independently from ranges of $\pm 10 \frac{\text{mrad}}{\text{nm}}$. Figure 6.10 shows a resulting input magnetic phase image for a projection along the z axis to illustrate the level of noise. Figure 6.11 displays a selection of other phase images of the same tilt series about the x axis, in order to show the variation in phase offsets and phase ramps.
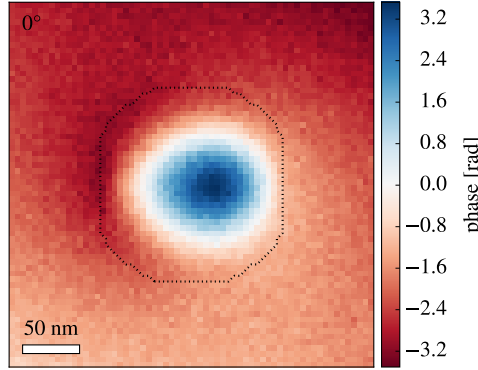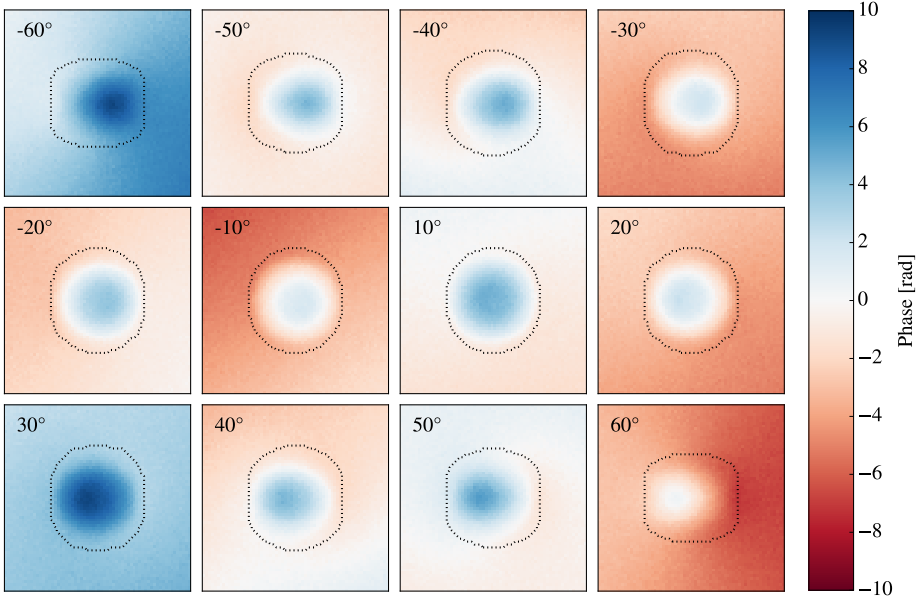

Figure 6.10.: Simulated input magnetic phase image for the three-dimensional magnetisation reconstruction of a vortex state in the xy plane for a tilt angle of 0° about the x axis. Gaussian noise with $\sigma_\epsilon = 100$ mrad has been added, as well as a phase offset of 3.5 rad and phase slopes of $-8.0 \frac{\text{mrad}}{\text{nm}}$ in the u direction and 5.1 $\frac{\text{mrad}}{\text{nm}}$ in the v direction. The two-dimensional projection of the mask is marked by a dashed line.

An L-curve analysis was performed for the three-dimensional reconstruction in order to determine an optimal regularisation parameter λ, as described in Section 5.6. The reconstructions included fits of phase ramps and offsets. Figure 6.12 shows the resulting L-curve, which suggests values between $\lambda = 0.1$ and $\lambda = 10$. A regularisation parameter of $\lambda = 1$, approximately at the point of the maximum curvature, was therefore chosen for the reconstruction.

The resulting reconstructed magnetisation distribution is displayed as a vector plot in Fig. 6.13a. Figure 6.13b shows the difference between the reconstructed and original magnetisation distribution in the form of a vector plot. The corresponding RMS measures of $\epsilon_{\text{mag}} = 0.035$ and $\epsilon_{\text{dir}} = 0.010$ are indicative of the quality of the reconstruction (*cf.*, *e.g.*, Fig. 6.4).

The centre of the homogeneously magnetised core of the vortex structure was chosen as a point of interest for further analysis. The averaging kernel rows for the x, y and z components of the chosen voxel were calculated and the resolution of the reconstruction was determined by analysing the corresponding FWHM. Figure 6.14 shows slices through the averaging kernel rows, which provide a visual representation of the

Figure 6.11.: Simulated input magnetic phase images the for three-dimensional magnetisation reconstruction of a vortex state in the xy plane for tilts about the x axis. Only every other phase image (in 10° steps) is displayed, with the exception of the 0° tilt image, which is shown in Fig. 6.10 instead. Gaussian noise with $\sigma_\epsilon = 100\,\mathrm{mrad}$ has been added to all of the magnetic phase images. Phase offsets were chosen randomly from a uniform distribution with a range of $\pm 5\,\mathrm{rad}$. Phase ramps with slopes in the u and the v directions were chosen from ranges of $\pm 10\,\frac{\mathrm{mrad}}{\mathrm{nm}}$. All of the images are displayed with the same phase range, as indicated by the colour bar. The two-dimensional projections of the mask are marked by dashed lines.
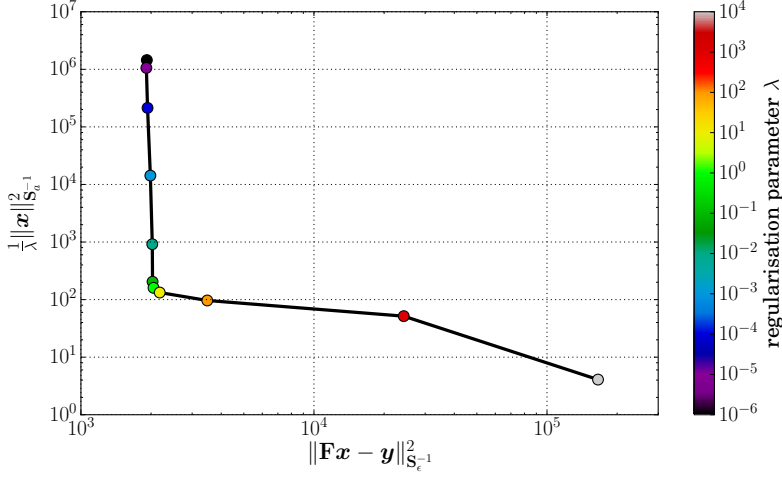
Figure 6.12.: L-curve analysis for the three-dimensional reconstruction of a magnetised disc that supports a magnetic vortex state in the xy plane under the influence of noise, phase offsets and phase ramps. Regularisation parameters of $\lambda = 0.1$ to $\lambda = 10$ at the corner of the curve provide optimal reconstruction results.
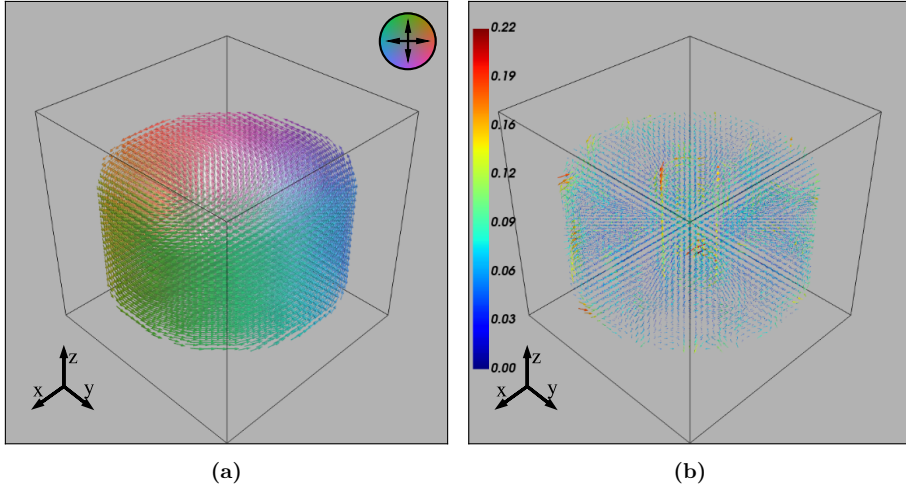

Figure 6.13.: (**a**) 3D vector plot of the reconstructed magnetisation distribution of a disc that supports a magnetic vortex state in the xy plane under the influence of noise. The colour wheel encodes the magnetisation direction in the xy plane. (**b**) 3D vector plot of the difference between the original magnetisation distribution and its reconstruction. The amplitude of the arrows is colour coded according to the colour bar on the left side.

reconstruction resolution. The reconstruction resolution for all spatial directions of the three components is listed in Tab. 6.1. The resolution ranges from 12.1 nm (*ca.* 2.5 pixels) to 31.9 nm (*ca.* 6.5 pixels). It is striking that each component exhibits its worst resolution along its corresponding axis. This phenomenon can be explained by the shape of the averaging kernel rows, which resemble the magnetic field of a dipole, as mentioned in Section 5.1.

The mean saturation magnetic induction of the reconstructed magnetisation distribution is calculated to be 0.911 ± 0.045 T, which is close to the value of $B_{\mathrm{sat}} = 1$ T that was used in the original distribution. A calculation of the reconstruction noise from the input noise level σ_ϵ, according to Eq. 4.39 in its simplified form (*cf.* Eq. 4.35), yields a value of 0.021 T. The reconstruction noise accounts for approximately half of the standard deviation of the reconstructed saturation magnetic induction. The difference may be explained by the missing tilt angles and by the phase offsets and ramps, which are not taken into account in the calculation of the reconstruction noise, but increase the standard deviation in the reconstruction. Just as for the two-dimensional case, the ability of the MBIR algorithm to retrieve features of a magnetisation distribution depends on the geometry of the object, the available magnetic phase images and the noise that they contain.

Table 6.1.: Overview of the resolution of the reconstruction at a central point of interest, summarising the resolution values for all three components in all spatial dimensions. Each row is calculated from the FWHM values of an averaging kernel row, which corresponds to the respective vector component.

Vector-component	x resolution	y resolution	z resolution
x component	20.8 nm	12.1 nm	12.1 nm
y component	12.1 nm	20.8 nm	12.1 nm
z component	17.2 nm	17.2 nm	31.9 nm

(a)

(b)

(c)
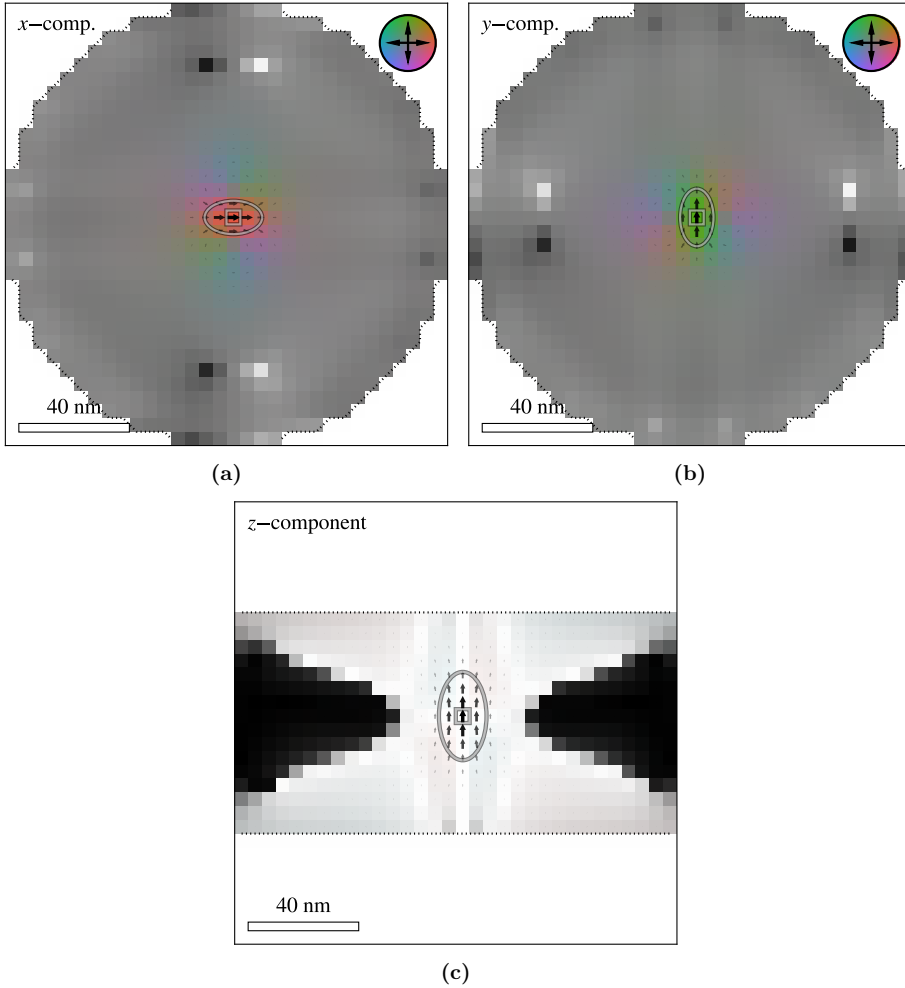
Figure 6.14.: (**a**) Slice in the xy plane of the averaging kernel row of the x component of a central point of interest for the reconstruction shown in Fig. 6.13. The colour wheel encodes the magnetisation direction in the xy plane. White indicates magnetisation pointing in the positive z direction, while black indicates magnetisation pointing in the negative z direction. (**b**) Equivalent slice for the y component for the same point of interest. (**c**) Slice in the xz plane of the averaging kernel row for the z component for the same point of interest. The arrows only show the in-plane magnetisation of the corresponding slices and not the out-of-plane component.

6.6. Summary

In this chapter, the reconstruction of three-dimensional magnetisation distributions was assessed and discussed. Most of the techniques that were previously used to address artefact sources in two dimensions could be transferred to three dimensions. However, unique challenges had to be solved for reconstructions from tilt series of phase images. The influence of the maximum tilt angle and the angular sampling were analysed with the aid of three test distributions, which incorporated magnetisation distributions that were introduced in earlier chapters. The maximum tilt angle had the greatest influence on the reconstruction results. Magnetic features in or near the null space of the projections along missing angles were found to be particularly difficult to reconstruct. Finer angular sampling was shown to improve reconstruction, but could not be used to recover features that were lost due to missing angles. Missing angles also influenced the three-dimensional mask, which was not as easy to determine as in two dimensions. A diffusion of magnetisation into erroneously masked regions was observed for masks that were too large. This artefact is equivalent to the one discussed in Section 5.3. In order to guarantee the best reconstruction results, the use of specialised discrete tomography algorithms should be explored in the future. The chapter closed with a reconstruction from two simulated tilt series with a limited tilt angle range and phase images that were affected by noise and random phase offsets and phase ramps to emulate experimental circumstances. Despite these artefacts, the MBIR algorithm proved to be able to accurately reconstruct magnetisation distributions, confirming the capabilities of the technique. The algorithm should now be applied to experimental data sets that are affected by additional sources of error, such as the misalignment of the original phase images and an imprecise knowledge of the sample tilt directions. The diagnostic techniques that have been developed within this thesis are promising tools for addressing these issues and overcoming the resulting challenges.

7. Summary and Outlook

In this thesis, a new model-based iterative reconstruction (MBIR) algorithm was developed for the retrieval of two-dimensional projected in-plane magnetisation distributions from individual magnetic phase images and three-dimensional magnetisation distributions from tilt series of magnetic phase images. An optimised forward model was developed to map a magnetisation distribution onto one or more phase images at each iteration step. This model satisfies the demands of the MBIR algorithm for fast computation speed and a precise representation of the underlying physics. By utilising the linear nature of the underlying equations, the forward model was expressed as a matrix equation and split into sub-problems for each phase image. The matrix for each sub-problem was further separated into the projection of the three-dimensional magnetisation distribution onto a two-dimensional vector field and a subsequent calculation of the magnetic phase image. The latter calculation was described by a phase mapping matrix, which involves convolutions for each of the two vector field components of the projected magnetisation. An efficient implementation of the projection was achieved by applying sparse matrix calculations.

The dense nature of the phase mapping matrix necessitated a more sophisticated technique. In this RDFC ("real space discretisation, Fourier space convolution") approach, the magnetisation distribution and the convolution kernels are discretised in real space to avoid Fourier related artefacts. Known analytical solutions for pixel-sized magnetic discs were employed to pre-compute look-up tables for the convolution kernels and to define an efficient phase mapping operator. In a comparison with an approach based on Fourier space discretisation, the clear superiority of the RDFC approach was demonstrated in terms of both computation time and the accuracy of the resulting phase images. Equivalently optimised implementations were derived for the derivative and the adjoint of the forward model. These operators are essential for the development of the MBIR algorithm.

In a first step, the originally ill-posed inverse problem of reconstructing magnetisation distributions from phase images was substituted by a least square minimisation problem to guarantee the existence of a solution. In addition, several regularisation techniques were employed to select the most reasonable reconstruction result from a pool of possible solutions. *A priori* knowledge about the position and size of the magnetised regions was incorporated in the form of a three-dimensional mask, in order to significantly reduce the number of retrieval targets. Tikhonov regularisation of first order was modelled after the macroscopic expression for the magnetic exchange energy of the magnetisation distribution, effectively searching for

a smooth solution. The MBIR algorithm then searches for a magnetic state that minimises a cost function, which combines least square minimisation with all of the mentioned regularisation techniques. The strength of the regularisation then balances the agreement of the reconstructed solution with the measurements against the *a priori* constraints. By making use of the linearity of the forward model, the minimisation of the cost function was facilitated by employing conjugate gradient methods.

In order to evaluate the quality of the reconstructed magnetisation distributions, diagnostic tools based on optimal estimation were introduced. One such tool is the averaging kernel, which describes how a true solution is distorted by the reconstruction and which can be used to quantify the resolution of the reconstructed magnetisation. Another tool is the gain matrix, which determines the effect of errors in the recorded magnetic phase images on the reconstructed magnetisation distribution.

An examination of the null space of the projection matrix revealed that two optimally orthogonal tilt series are required to reconstruct all of the features in a three-dimensional magnetisation distribution. If only one tilt series is available, then curls around the tilt axis lie in the null space of the system matrix and cannot be recovered. Singular value decomposition was used to examine the phase mapping matrix. A non-trivial null space was found, confirming the existence of non-retrievable projected magnetisation distributions, such as a Halbach disc.

In the course of this thesis, a software package was written in the Python programming language to include implementations of the MBIR algorithm, the optimised forward model, as well as the diagnostic tools for the assessment of reconstructed magnetisation distributions.

The MBIR algorithm was applied to simulated phase images for the reconstruction of two- and three-dimensional magnetisation distributions. Artefacts resulting from magnetisation sources outside the field of view were assessed for two-dimensional reconstructions. Phase offsets and ramps in each magnetic phase image were fitted, providing a flexible and computationally cheap way of dealing with sufficiently distant sources of magnetisation. This approach was shown to work in both, the two- and the three-dimensional case. It can also account for phase offsets that are introduced during the reconstruction of a magnetic phase image from off-axis electron holograms. Furthermore, it deals with phase ramps from specimen charging or changes to the biprism wire over time. For magnetisation sources in the close vicinity of the field of view, buffer pixels were introduced to provide additional degrees of freedom to compensate for the magnetic fields which can influence the magnetic phase in the field of view. If the position of the biprism is known, then the algorithm can also take into account the influence of the perturbed reference wave. Other artefacts in magnetic phase images could be tackled by setting their confidence value to zero, effectively excluding them from the MBIR algorithm.

For three-dimensional reconstructions from tilt series of simulated magnetic phase images, the influence of maximum tilt angle and angular sampling was assessed. For a test distribution that did not exhibit a variation along the z axis, accurate reconstruction could be achieved even for low maximum tilt angles and angular sampling. For two other test distributions in which there was a stronger variation along the z axis, the reconstruction results were more sensitive to the maximum tilt angle than to the angular sampling.

Both, two- and three-dimensional magnetisation distributions were successfully reconstructed from simulated phase images under the influence of Gaussian noise. Regularisation parameters, which adequately balanced agreement with the measurements and with *a priori* constraints, were found using L-curve analyses. The power of the applied regularisation lies in its ability to suppress noise. However, strong regularisation can lead to over-smoothing of magnetic features of interest. In order to assess the severity of this effect, diagnostic tools were utilised to estimate the maximum sizes of resolvable magnetic features.

Incorrect assignment of the mask that defines the size and position of the magnetised regions was identified as one of the main sources of error in both two and three dimensions. Diffusion of magnetisation into erroneously masked regions was observed for overestimated mask sizes. In contrast, reconstruction with an underestimated mask suffers from compression of magnetisation at the borders of the masked regions, leading to locally overestimated values. In three dimensions, accurate determination of the position and size of magnetised regions is particularly challenging. In future studies, discrete tomography algorithms, which are dedicated to the detection of magnetised regions, could be applied in combination with the MBIR algorithm.

Reconstruction of the projected in-plane magnetisation from an experimental magnetic phase image of a two-dimensional lithographically patterned cobalt structure was successfully conducted. The reconstructed magnetisation strength was in agreement with the literature. The feasibility of the MBIR algorithm for three-dimensional experimental studies was demonstrated by reconstructing a three-dimensional magnetisation distribution from a set of simulated phase images with a limited angular range under the influence of Gaussian noise and random phase offsets and phase ramps, to emulate experimental limitations.

Future improvements to the MBIR algorithm that has been developed in this thesis include the use of feedback loops between the algorithm and micromagnetic simulations, in order to further ensure that the reconstruction is consistent with known physical laws. Whereas this thesis used the Euclidean norm L2, which was motivated by exchange energy minimisation, other forms of regularisation could be explored. Examples include the zero norm L0 and the Manhattan norm L1, which are better at handling sharp boundaries and could reduce the diffusion in the case of overestimated masks. However, these norms would necessitate more complicated minimisers for the MBIR algorithm. The next step for three-dimensional recon-

structions is the application of the MBIR algorithm to experimental phase images. Additional sources of errors, such as the misalignment of different phase images, errors in the determination of the correct tilt angles, specimen charging or dynamical diffraction, should be examined and the MBIR algorithm will have to be adapted accordingly. The algorithm and the accompanying diagnostics presented by this thesis will provide valuable tools for the examination of magnetisation distributions with off-axis electron holography in the future.

A. Appendix

A.1. Fringe spacing of an electron hologram
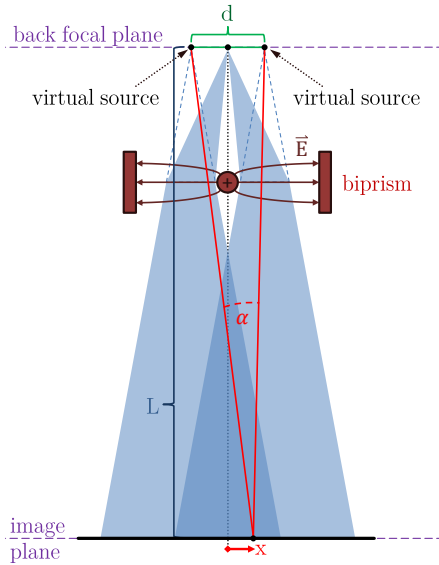
Figure A.1.: Schematic illustration for the derivation of the interference fringe spacing in an electron hologram. The beam paths between the back-focal plane and the image plane with distance L are displayed as blue cones. The beams are deflected by the biprism, which results in two virtual electron sources with distance d. The virtual beam paths for a point with distance x from the optical axis are marked in red. Their difference yields the path difference Δs.

In this section, the interference fringe spacing in an electron hologram is derived. In the off-axis electron holography scheme, the object and reference waves are deflected by a (usually positively) biased biprism. The deflection results in two virtual electron sources and causes the waves to interfere in the image plane under the superposition angle α. The according geometry is schematically illustrated in Fig. A.1. The path difference Δs can be determined by following the steps described by Reimer and

Kohl [137]. For a point with distance x to the optical axis, a distance d between the virtual sources and a distance L between the back focal plane and the image plane, Δs is calculated to:

$$\Delta s = \sqrt{L^2 + \left(x + \frac{d}{2}\right)^2} - \sqrt{L^2 + \left(x - \frac{d}{2}\right)^2} \tag{A.1}$$

$$= L\left[\sqrt{1 + \left(\frac{x + d/2}{L}\right)^2} - \sqrt{1 + \left(\frac{x - d/2}{L}\right)^2}\right] \tag{A.2}$$

$$\approx L\left[\frac{1}{2}\left(1 + \left(\frac{x + d/2}{L}\right)^2\right) - \frac{1}{2}\left(1 - \left(\frac{x - d/2}{L}\right)^2\right)\right] \tag{A.3}$$

$$= \frac{L}{2L^2}\left[x^2 + xd + \frac{d^2}{4} - \left(x^2 - xd + \frac{d^2}{4}\right)\right] \tag{A.4}$$

$$= \frac{xd}{L} \approx \alpha x. \tag{A.5}$$

A Taylor expansion can be applied in the third step, because $x, d \ll L$, to simplify the two square roots[1]. In the last step, a small-angle approximation $\frac{d}{L} = \sin(\alpha) \approx \alpha$ can be applied. Constructive interference can be observed when the path difference is $\Delta s = n\lambda$, with $n \in \mathbb{N}$. The interference fringe spacing is therefore given by[2]:

$$\Delta x = \frac{\lambda}{\sin(\alpha)} \approx \frac{\lambda}{\alpha} = \frac{2\pi}{k\alpha}, \tag{A.6}$$

with k being the wave number of the electron wave.

A.2. Setup of weighting and projection matrices

This section provides instructions on how to implement the projection matrices $\mathbf{P}_b$ and the corresponding weighting matrices $\mathbf{W}_b$ that are used in the RDFC approach. Projections along the major axes of the three-dimensional coordinate system and projections with tilts about the x or y axis are discussed.

A.2.1. Projections along the major axes

The simplest projections are performed along one of the three major axes x, y or z. The vector components in three dimensions are then mapped onto the projected components in two dimensions without intermixing them. The coefficients for the

---

[1]$\sqrt{1 + x^2} \approx \frac{1}{2}\left(1 + x^2\right)$

[2]A small-angle approximation is used, which is valid for small deflections by the biprism.

weighting matrices in Eq. 3.13 are therefore either one or zero, which leads to the following expressions for the projection matrices[3]:

$$\mathbf{P}_{b,z} = \begin{pmatrix} \mathbf{W}_{b,z} & \mathbf{0} & \mathbf{0} \\ \mathbf{0} & \mathbf{W}_{b,z} & \mathbf{0} \end{pmatrix}, \tag{A.7}$$

$$\mathbf{P}_{b,y} = \begin{pmatrix} \mathbf{W}_{b,y} & \mathbf{0} & \mathbf{0} \\ \mathbf{0} & \mathbf{0} & \mathbf{W}_{b,y} \end{pmatrix}, \tag{A.8}$$

$$\mathbf{P}_{b,x} = \begin{pmatrix} \mathbf{0} & \mathbf{0} & \mathbf{W}_{b,x} \\ \mathbf{0} & \mathbf{W}_{b,x} & \mathbf{0} \end{pmatrix}. \tag{A.9}$$

The weighting matrix $\mathbf{W}_b$ is very sparse and has only $N_x N_y N_z$ non-zero entries, that is exactly one value of 1 for each voxel in the three-dimensional space. When projecting along the major axes, each voxel is mapped to exactly one pixel of the projected coordinate system, *i.e.*, the magnetisation of one voxel is not spread over several pixels. If the number of voxels along the chosen projection direction is denoted by N_{proj}, then each row of $\mathbf{W}_b$ has exactly N_{proj} entries with a value of one, that is one for each slice along the projection direction. Due to the sparsity of $\mathbf{W}_b$, it can be described in terms of a sparse sorted row matrix, defined by three arrays:

data: An array that contains $N_x N_y N_z$ entries with value 1.

indices: An array with the same length as *data* that contains indices denoting the columns where the non-zero-entries of the *data* array reside. This array depends on the projection direction (see below).

indptr: An array of pointers, where two consecutive values determine the index range of *data* and *indices* for a given row. The column indices and data entries of row r are therefore given by $indices\,[indptr\,[r]:indptr\,[r+1]]$ and $data\,[indptr\,[r]:indptr\,[r+1]]$, respectively. Here, it is given as $[0, N_{\text{proj}}, 2N_{\text{proj}}, \ldots, N_x N_y N_z]$.

For the sake of simplicity, it is assumed that the projection dimensions u and v have the same length as their three-dimensional counterparts x, y, and z. A relaxation of this assumption, *i.e.*, an increase in the projected FOV, would just lead to a trivial addition of rows full of zeros that correspond to pixels not hit by the projection of the magnetisation[4].

Below, the *indices* array will be described for all three major axis projections. The index $r \in \mathbb{N}_0 < N_u N_v$ is used to iterate over the rows of $\mathbf{W}_b$, while index i is used to iterate over the entries in each row (Fig. A.2 shows examples of the resulting matrices).

---

[3]The intuitive notion that the x component will map to the u component and the y component to the v component of the projected in-plane magnetisation was preserved. The z component is therefore mapped to the u component for a projection $\mathbf{P}_{b,x}$ along the x axis.

[4]Two equal consecutive numbers in *indptr* mean that this row has no non-zero entries.

- For a projection along the z axis, the projection direction is defined by $N_{\mathrm{proj}} = N_z$ and the two projected dimensions are given by $N_u = N_x$ and $N_v = N_y$. The indices for a specific row r are given by:

$$[r + i \cdot N_x N_y, \quad \text{for } i \in \mathbb{N}_0 < N_z] . \tag{A.10}$$

- For a projection along the y axis, the projection direction is defined by $N_{\mathrm{proj}} = N_y$ and the two projected dimensions are given by $N_u = N_x$ and $N_v = N_z$. The indices for a specific row r are given by[5]:

$$[r \bmod N_x + \lfloor r/N_x \rfloor \cdot N_x N_y + i \cdot N_x, \quad \text{for } i \in \mathbb{N}_0 < N_y] \tag{A.11}$$

- For a projection along the x axis, the projection direction is defined by $N_{\mathrm{proj}} = N_x$ and the two projected dimensions are given by $N_u = N_z$ and $N_v = N_y$. The indices for a specific row r are given by:

$$[(r \bmod N_z) \cdot N_x N_y + \lfloor r/N_z \rfloor \cdot N_x + i, \quad \text{for } i \in \mathbb{N}_0 < N_x] \tag{A.12}$$

The sparsity of $\mathbf{W}_b$ is critical for the performance of the reconstruction algorithm. In the case of a major axis projection, a total of $N_x N_y N_z$ non-zero entries, scattered in a matrix of size $N_u N_v \times N_x N_y N_z$, leads to a density (defined as the inverse of the sparsity) of $1/N_u N_v$. If all axes have, *e.g.*, a length of 256 pixels, the density is just 0.0015%.

A.2.2. Projections with tilts about the x or y axis

For the reconstruction of three-dimensional magnetisation distributions, projections along the major axes alone are generally not sufficient. In practice, the projection direction is fixed to the negative z direction by the experimental setup of the electron microscope. It is the sample which is tilted about the x or y axes, perpendicular to the projection direction. To facilitate this tomographic approach, projection matrices $\mathbf{P}_{b,x-\mathrm{tilt}}$ and $\mathbf{P}_{b,y-\mathrm{tilt}}$ have to be constructed, which can be expressed as

$$\mathbf{P}_{b,x-\mathrm{tilt}} = \begin{pmatrix} \mathbf{W}_b & \mathbf{0} & \mathbf{0} \\ \mathbf{0} & \cos(\phi)\,\mathbf{W}_b & \sin(\phi)\,\mathbf{W}_b \end{pmatrix}, \tag{A.13}$$

$$\mathbf{P}_{b,y-\mathrm{tilt}} = \begin{pmatrix} \cos(\phi)\,\mathbf{W}_b & \mathbf{0} & \sin(\phi)\,\mathbf{W}_b \\ \mathbf{0} & \mathbf{W}_b & \mathbf{0} \end{pmatrix}. \tag{A.14}$$

These two matrices are very similar to $\mathbf{P}_{b,z}$ in Eq. A.7. For $\mathbf{P}_{b,x-\mathrm{tilt}}$, the difference lies in the fact that the z component in three-dimensional space (which is lost in $\mathbf{P}_{b,z}$) is mixed into the resulting v component by cosines and sines of the tilting angle ϕ. For $\mathbf{P}_{b,y-\mathrm{tilt}}$, the z component is mixed into the u component of the projection instead.

---

[5] $\lfloor x \rfloor$ is the "floor" function, which maps a real number to the greatest preceding integer.

(a)

(b)

(c)
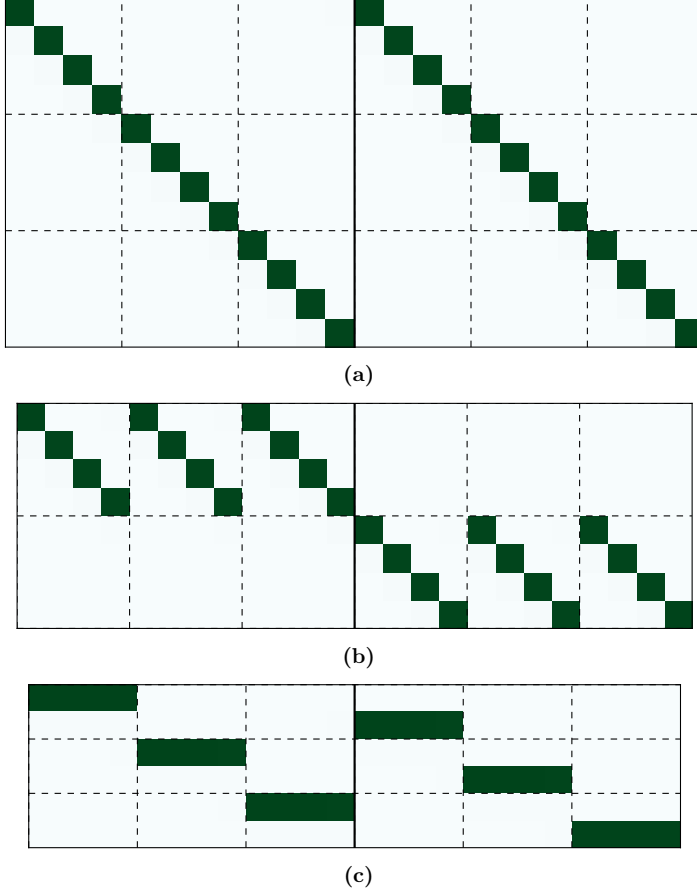
Figure A.2.: Weighting matrices (**a**)$\mathbf{W}_{b,z}$, (**b**)$\mathbf{W}_{b,y}$ and (**c**)$\mathbf{W}_{b,x}$ for a three dimensional volume with $N_z = 2$, $N_y = 3$ and $N_x = 4$. Elements with value one are marked in green, the rest of the matrix contains zeros. Vertical dashed lines indicate a jump in the y coordinate, the vertical solid line indicates a jump from $z = 0$ to $z = 1$. The horizontal dashed lines indicate a jump in the v coordinate.
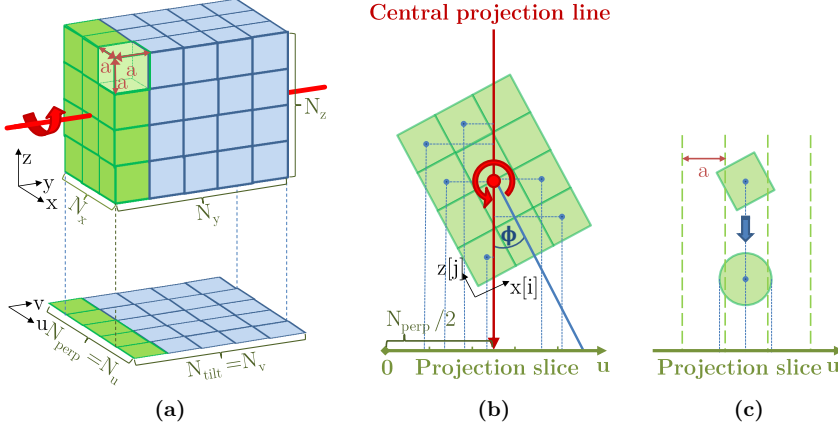
Figure A.3.: Schematic diagram illustrating a projection for a tilt about the y axis. (**a**) shows the three-dimensional problem, which can be reduced to an assortment of two-dimensional problems, by slicing the 3D volume and its 2D projection perpendicular to the tilting axis (one such slice is marked in green). (**b**) shows one slice, viewed along the tilt axis and perpendicular to the xz plane. The centre point of each pixel is projected down onto the pixel slice. In the case of a tilt about the y axis, this is the u axis of the projection (further explained in the main text). (**c**) A cubic voxel is approximated by a cylinder (viewed here along its symmetry axis) with the same volume. This approximation is then used to find the impacted pixels in the projection slice and to calculate how the three-dimensional magnetisation is distributed among these impacted pixels, as further described in Fig. A.4.

The dependence of the weighting matrix $\mathbf{W}_b$ on the tilting angle ϕ is discussed below. It is assumed that the rotation axis goes through the centre of the three-dimensional volume (*cf.* Fig. A.3a). The number of pixels along the tilting axis in the projected coordinate system is denoted N_{tilt}, the number of pixels along the second, perpendicular axis is denoted N_{perp}. N_{perp} should be larger than N_y (for a tilt about x) or N_x (for a tilt about y), so that no magnetisation is possibly projected outside of bounds. For a rotation around the x axis $N_{\text{tilt}} = N_u$ and $N_{\text{perp}} = N_v > N_y$ and for a rotation around the y axis, the situation is reversed, *i.e.*, $N_{\text{tilt}} = N_v$ and $N_{\text{perp}} = N_u > N_x$. The 2D and 3D grids stay aligned along the tilting axis, even after tilting. Subsequently, each slice of voxels (the "voxel slice") of the three-dimensional distribution is projected onto exactly one strip of pixels of the two-dimensional projection, which is termed the "projection slice" (marked in green in Fig. A.3a). The weights of the voxels onto the pixels is the same for each slice, effectively reducing the calculation of the weighting matrix $\mathbf{W}_b$ to a two-dimensional problem.

To calculate the weights, the positions of the projections of the voxel centres along the projection slice have to be determined first. For this purpose, a set of vectors $\boldsymbol{\nu}\,[i, j]$ which point from the voxel slice centre (marked in red in Fig. A.3b) to each voxel centre with indices ij in the slice is introduced. The distance of those voxels to a central projection line with direction $\boldsymbol{e}_{\text{proj}} = \big(\cos(\phi), -\sin(\phi)\big)$ through the voxel slice centre is given by $\|\boldsymbol{e}_{\text{proj}} \times \boldsymbol{\nu}\,[i, j]\|$. Because the distance calculation does not distinguish between voxels left or right from the central projection line, the value of the out-of-plane component of the cross product $[\boldsymbol{e}_{\text{proj}} \times \boldsymbol{\nu}\,[i, j]]_\perp$ is taken instead of the norm, so that the sign is preserved. This way, positions on the left of the central projection line are negative and positions on the right are positive. To correctly relate the positions to the origin of the projected coordinate system, the term $\frac{N_{\text{perp}}}{2}a$ with grid spacing a has to be added, assuming the three-dimensional distribution and the projected two-dimensional distribution are symmetrically centred around the tilt axis. This leads to the following formula for the positions $p\,[i, j]$ along the projection slice for each voxel with indices ij:

$$p\,[i, j] = [\boldsymbol{e}_{\text{proj}} \times \boldsymbol{\nu}\,[i, j]]_\perp + \frac{N_{\text{perp}}}{2}a \tag{A.15}$$

In contrast to a projection along a major axis, where each voxel only impacts one pixel of the projected distribution, a voxel of a tilted distribution could impact several pixels at once. To identify which pixels are hit by the projection of a voxel, the voxel volume is approximated by a cylinder that is oriented along the tilt axis, because its projection is mathematically easier to describe than that of a tilted cube (*cf.* Fig. A.3c). The magnetisation and therefore the volume of this approximation have to be preserved. For a radius R of the cylinder, this means:

$$V_{\text{voxel}} \equiv a^3 \stackrel{!}{=} \pi R^2 a \quad \Leftrightarrow \quad R = \frac{a}{\sqrt{\pi}} \approx 0.56a. \tag{A.16}$$

The leftmost impacted pixel is defined by the left border of the projection of the cylinder at $p - R$ and has index $h = \left\lfloor \frac{p-R}{a} \right\rfloor$. The rightmost impacted pixel is defined

by the right border at $p + R$ and has index $h = \left\lfloor \frac{p+R}{a} \right\rfloor$. This means that one voxel can impact at most three pixels (*cf.*. Fig. A.4). The density of $\mathbf{W}_b$ is therefore at most $3/N_u N_v$. If the centre of an impacted pixel lies at position u_h along the u axis, then its borders can be found at positions $u_h \pm \frac{a}{2}$[6].

In a reference frame centred around the projected position p of a voxel (*cf.* Eq. A.15) along the u axis, the borders of the impacted pixel (relative to p) are given by

$$u_\pm \equiv u_h \pm \frac{a}{2} - p. \tag{A.17}$$

In this reference frame, the formula for a half circle with radius R and area $A_{\scriptsize\textcircled{}} = \frac{\pi R^2}{2}$ is given by the expression

$$f(u) = \sqrt{R^2 - u^2} \qquad u \in [-R, R] \tag{A.18}$$

The weight of a voxel, that is projected onto position p, on an impacted pixel at position u_{imp} is then given by the normalised integral over $f(u)$ along its diameter:

$$w(u_l, u_r) = \frac{1}{A_{\scriptsize\textcircled{}}} \int_{u_l}^{u_r} f(u) \, du \tag{A.19}$$

$$= \frac{2}{\pi R^2} \int_{u_l}^{u_r} \sqrt{R^2 - u^2} \, du \tag{A.20}$$

$$= \frac{2}{\pi R^2} \left[\frac{1}{2} \left(u\sqrt{R^2 - u^2} + R^2 \arctan\left(\frac{u}{\sqrt{R^2 - u^2}} \right) \right) \right]_{u_l}^{u_r} \tag{A.21}$$

$$= \frac{1}{\pi} \left[\frac{u}{R}\sqrt{1 - \left(\frac{u}{R}\right)^2} + \arctan\left(\frac{u}{R} \frac{1}{\sqrt{1 - \left(\frac{u}{R}\right)^2}} \right) \right]_{u_l}^{u_r} \tag{A.22}$$

$$\equiv w_r(u_r) - w_l(u_l). \tag{A.23}$$

Because $f(u)$ is only defined on the interval $[-R, R]$, special care has to be taken of the integration borders, which are given by the expressions

$$u_l = \max\left(u_h - \frac{a}{2} - p, -R \right), \qquad u_r = \min\left(u_h + \frac{a}{2} - p, R \right). \tag{A.24}$$

If the left border of an impacted pixel does not intersect the cylinder, the left integration border u_l is set to the leftmost point $u_l = -R$ of the cylinder, leading to a minimal value of $w_l(-R) = -\frac{1}{2}$. Similarly, if the right border of an impacted pixel does not intersect the cylinder, the right integration border u_r is set to the rightmost point $u_r = R$, leading to a maximum value of $w_r(R) = \frac{1}{2}$. Both situations can't occur simultaneously for the same pixel, because the cylinder diameter $2R > a$

---

[6]The u axis is chosen here as an example for a tilt about y. Similarly, the v axis could have been chosen for a tilt about x.
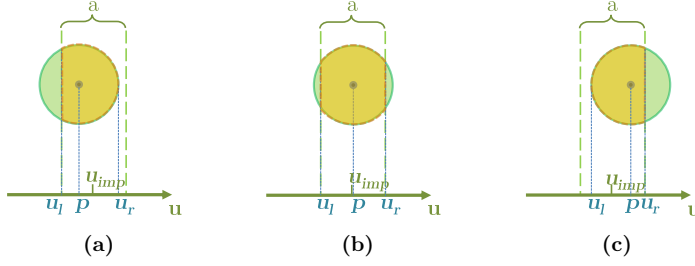
Figure A.4.: Weight calculation via integration over a circle segment, which is marked by the orange area. The normalised areas of the marked segments indicate the weights of a voxel onto the impacted pixels. u_l and u_r denote the left and right integration borders, while p denotes the "impact" coordinate of the projected voxel centre onto the projection slice. u_{imp} denotes the centre of the impacted pixel of width a, whose borders are indicated by the vertical dashed lines. (**a**) shows a case where only the left border of an impacted pixel intersects the circle, in (**b**), both borders and in (**c**), only the right border intersects it.

(*cf.* Eq. A.16), *i.e.*, $w\left(u_l, u_r\right) < w_r\left(R\right) - w_l\left(-R\right) = 1$ (a projected voxel can never influence only one pixel).

After calculating the weights for all voxels of one slice, all other slices can be filled with the same values. The corresponding matrix is sparse and can be defined by three arrays:

data: An array of all non-zero data entries, which contain the calculated weights that were derived above.

columns: An array of the column indices c, representing all three-dimensional voxels of the magnetisation distribution.

rows: An array of row indices r, representing all two-dimensional pixels of the projection.

In summary, the entries of the weighting matrix $\mathbf{W}_b$ are calculated following these instructions:

- Iteration over all voxels of one slice. A slice is determined by an index $s \in \mathbb{N}_0 < N_{\mathrm{tilt}}$. The voxels contained within are indexed by j along the projection axis and i along the axis perpendicular to the tilt axis. Each voxel corresponds to a column in $\mathbf{W}_b$ with an index given by the expressions

$$c_{x-\mathrm{tilt}}\left[i, j, s\right] = j \cdot N_x \cdot N_y + i \cdot N_x + s, \tag{A.25}$$
$$c_{y-\mathrm{tilt}}\left[i, j, s\right] = j \cdot N_x \cdot N_y + s \cdot N_x + i. \tag{A.26}$$

153

- Determination of the impacted pixels, which are indicated by index h along the projection slice, for each voxel of the slice. Each pixel corresponds to a row in $\mathbf{W}_b$ with a row index given by the expressions

$$r_{x-\text{tilt}}[h, s] = h \cdot N_u + s, \tag{A.27}$$
$$r_{y-\text{tilt}}[h, s] = s \cdot N_u + h. \tag{A.28}$$

- Calculate the weight for each impacted pixel like described above and write it into the sparse matrix at row index $r_{x-\text{tilt}}/r_{y-\text{tilt}}$ and column index $c_{x-\text{tilt}}/c_{y-\text{tilt}}$ for all slices s.

By using the fact that weights for all slices are equal, the number of weight calculations can be reduced by a factor of N_x for tilts about the x axis and by a factor of N_y for a tilt about the y axis, which significantly improves the performance of the algorithm. Examples for the weighting matrix $\mathbf{W}_b$ are shown in Fig. A.5.

(a)

(b)
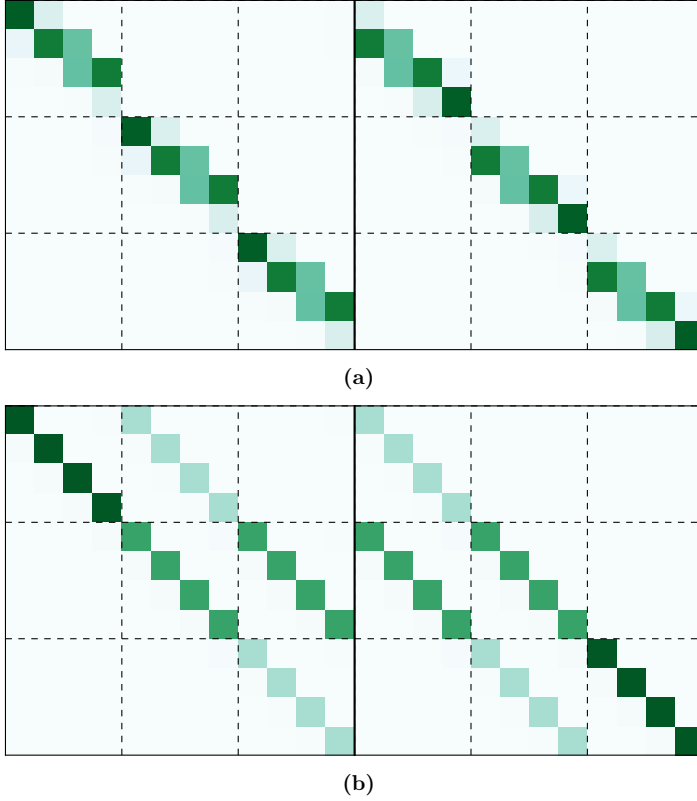
Figure A.5.: Weighting matrices for (**a**) a 45° tilt about the y axis and (**b**) a 45° tilt about the x axis. Non-zero elements are marked in green, with the saturation indicating their values. White elements of the matrix contains zeros. Vertical dashed lines indicate a jump in the y coordinate, the vertical solid line indicates a jump from $z = 0$ to $z = 1$. The horizontal dashed lines indicate a jump in the v coordinate.

A.3. Optimal estimation and Bayesian interpretation

In this section, the Bayesian interpretation that leads to optimal estimation linear diagnostics is illuminated. The norm weights $\mathbf{S}_\epsilon^{-1}$ and $\mathbf{S}_a^{-1}$ are interpreted as inverse covariance matrices (see Eq. 4.14). Optimal estimation diagnostics are mainly used in geosciences, particularly atmospheric sounding and the following derivation closely follows Rodgers [116] (also see [72] for a comprehensive summary). Under the assumption that Gaussian statistics are applicable to the measurements $\boldsymbol{y}$ and the retrieved magnetisation state $\boldsymbol{x}$, multidimensional Gaussian probability density functions (PDF) can be defined[7]:

$$P\left(\boldsymbol{y}|\boldsymbol{x}\right) = \frac{1}{\left(2\pi\right)^{m/2}\left|\mathbf{S}_\epsilon\right|}\exp\left[-\frac{1}{2}\left(\mathbf{F}\boldsymbol{x}-\boldsymbol{y}\right)^T\mathbf{S}_\epsilon^{-1}\left(\mathbf{F}\boldsymbol{x}-\boldsymbol{y}\right)\right] \tag{A.29}$$

$$P\left(\boldsymbol{x}\right) = \frac{1}{\left(2\pi\right)^{n/2}\left|\mathbf{S}_a\right|}\exp\left[-\frac{1}{2}\boldsymbol{x}^T\mathbf{S}_a^{-1}\boldsymbol{x}\right] \tag{A.30}$$

$$P\left(\boldsymbol{x}|\boldsymbol{y}\right) = \frac{1}{\left(2\pi\right)^{n/2}\left|\mathbf{S}_x\right|}\exp\left[-\frac{1}{2}\left(\boldsymbol{x}-\boldsymbol{x}_{\text{rec}}\right)^T\mathbf{S}_x^{-1}\left(\boldsymbol{x}-\boldsymbol{x}_{\text{rec}}\right)\right] \tag{A.31}$$

which are multidimensional generalisations of the one-dimensional PDF $P\left(x\right) = \frac{1}{\left(2\pi\right)^{1/2}\sigma}\exp\left[-\frac{\left(x-\bar{x}\right)^2}{2\sigma^2}\right]$ with mean value $\bar{x}$ and variance σ^2:

- $P\left(\boldsymbol{y}|\boldsymbol{x}\right)$ describes the probability of measuring a set of phase images $\boldsymbol{y}$, generated from a magnetisation state $\boldsymbol{x}$.

- $P\left(\boldsymbol{x}\right)$ describes the probability of the existence of a magnetisation state $\boldsymbol{x}$ with covariance matrix $\mathbf{S}_a$, independent of and before (*i.e.*, *a priori*) any phase images $\boldsymbol{y}$ are measured. $\mathbf{S}_a$ (more precisely its inverse, which is used in the regularisation) describes constraints mirroring physical laws, which ensure that nonsensical magnetisation states have a low probability.

- $P\left(\boldsymbol{x}|\boldsymbol{y}\right)$ describes the probability of the magnetic state $\boldsymbol{x}$ being present, under the prerequisite that the phase images $\boldsymbol{y}$ have been measured (*a posteriori*). This is the important quantity for inverse problem solving.

- $P\left(\boldsymbol{y}\right)$ describes the probability of a measurement $\boldsymbol{y}$, independent of the magnetic state $\boldsymbol{x}$. In practice, this is only a constant normalising factor and is therefore not needed in the following discussion.

Bayes's theorem states that

$$P\left(\boldsymbol{x}|\boldsymbol{y}\right) = \frac{P\left(\boldsymbol{y}|\boldsymbol{x}\right)P\left(\boldsymbol{x}\right)}{P\left(\boldsymbol{y}\right)} \tag{A.32}$$

---

[7]In the general case, the exponent of Eq. A.30 should be $-\frac{1}{2}\left(\boldsymbol{x}-\boldsymbol{x}_a\right)^T\mathbf{S}_a^{-1}\left(\boldsymbol{x}-\boldsymbol{x}_a\right)$, containing an a priory distribution $\boldsymbol{x}_a$, which is implicitly set to the zero vector in this case. This assumption has to be kept in mind for all further discussion.

and describes the relation between the different PDFs. It provides an approach for calculating the important quantity $P(\boldsymbol{x}|\boldsymbol{y})$ for inverse problem solving. Inserting equations A.29, A.30 and A.31 into Eq. A.32 and taking the natural logarithm results in the expression

$$\ln\left(P\left(\boldsymbol{x}|\boldsymbol{y}\right)\right) = \ln\left(P\left(\boldsymbol{y}|\boldsymbol{x}\right)\right) + \ln\left(P\left(\boldsymbol{x}\right)\right) - \ln\left(P\left(\boldsymbol{y}\right)\right) \quad \text{(A.33)}$$

$$\Leftrightarrow \left(\boldsymbol{x} - \boldsymbol{x}_{\text{rec}}\right)^T \mathbf{S}_x^{-1} \left(\boldsymbol{x} - \boldsymbol{x}_{\text{rec}}\right) = \left(\mathbf{F}\boldsymbol{x} - \boldsymbol{y}\right)^T \mathbf{S}_\epsilon^{-1} \left(\mathbf{F}\boldsymbol{x} - \boldsymbol{y}\right) + \boldsymbol{x}^T \mathbf{S}_a^{-1} \boldsymbol{x} - c, \tag{A.34}$$

with c containing all terms that are independent of $\boldsymbol{x}$. Calculating the first derivative of both sides with respect to $\boldsymbol{x}$ yields the expression

$$\mathbf{S}_x^{-1}\left(\boldsymbol{x} - \boldsymbol{x}_{\text{rec}}\right) = \mathbf{F}^T \mathbf{S}_\epsilon^{-1}\left(\mathbf{F}\boldsymbol{x} - \boldsymbol{y}\right) + \mathbf{S}_a^{-1}\boldsymbol{x} \tag{A.35}$$

and taking the second derivate results in

$$\mathbf{S}_x^{-1} = \mathbf{F}^T \mathbf{S}_\epsilon^{-1} \mathbf{F} + \mathbf{S}_a^{-1}. \tag{A.36}$$

Finally, substituting $\mathbf{S}_x^{-1}$ in Eq. A.35 by using Eq. A.36 yields

$$\left(\mathbf{F}^T \mathbf{S}_\epsilon^{-1} \mathbf{F} + \mathbf{S}_a^{-1}\right)\left(\boldsymbol{x} - \boldsymbol{x}_{\text{rec}}\right) = \mathbf{F}^T \mathbf{S}_\epsilon^{-1}\left(\mathbf{F}\boldsymbol{x} - \boldsymbol{y}\right) + \mathbf{S}_a^{-1}\boldsymbol{x} \tag{A.37}$$

Due to the fact that this equation has to be valid for all magnetic states $\boldsymbol{x}$, we evaluate it for an arbitrary state $\boldsymbol{x} = \boldsymbol{x}_0$, solve for the mean $\boldsymbol{x}_{\text{rec}}$ of the PDF. The result is a formula equivalent to Eq. 4.20:

$$\boldsymbol{x}_{\text{rec}} = \boldsymbol{x}_0 - \left(\mathbf{F}^T \mathbf{S}_\epsilon^{-1} \mathbf{F} + \mathbf{S}_a^{-1}\right)^{-1} \cdot \mathbf{F}^T \mathbf{S}_\epsilon^{-1}\left(\mathbf{F}\boldsymbol{x}_0 - \boldsymbol{y}\right) + \mathbf{S}_a^{-1}\boldsymbol{x}_0 \tag{A.38}$$

$$\equiv \boldsymbol{x}_0 - \qquad 2\left(\mathbf{C}''\right)^{-1} \qquad \cdot \qquad \frac{1}{2}\boldsymbol{C}'\left(\boldsymbol{x}_0\right), \tag{A.39}$$

where the covariance matrix of the magnetisation state can be expressed by the inverse of the Hessian matrix of the costfunction as

$$\mathbf{S}_x = 2\left(\mathbf{C}''\right)^{-1}. \tag{A.40}$$

A.4. Null space of a single projection matrix

This section provides a mathematical description for the (purely theoretical) split of a projection matrix $\mathbf{P}_b$ to illustrate the different contributions to its null space and to complement the discussion in Section 4.5.1. The matrix $\mathbf{P}_b$ describing the projection process for one image can be expressed as a combination of a projection matrix $\mathbf{P}_{b,LA}$ in a linear algebraic sense and a matrix $\mathbf{P}_{b,CS}$, which conducts a coordinate system transformation[8]:

$$\mathbf{P}_b = \mathbf{P}_{b,CS}\mathbf{P}_{b,LA}. \tag{A.41}$$

---

[8]Note that these matrices are never constructed explicitly, they are just used as a theoretical construct to explain the null space of $\mathbf{P}_b$.

The null space of the linear algebraic projection matrix $\mathbf{P}_{b,LA}$ is comprehensible in a very intuitive way. Following Werner [138], a vector-space endomorphism[9] $\mathbf{P}$ is called a projection if it is idempotent, *i.e.*, $\mathbf{P}^2 = \mathbf{P}$. The only two eigenspaces of a projection are the range (or "image") range $(\mathbf{P})$, assigned to eigenvalue 1, and the null space null $(\mathbf{P})$, assigned to eigenvalue 0. The range and the null space are complementary, which means the domain of $\mathbf{P}$ can be expressed as the direct sum range $(\mathbf{P}) \oplus$ null $(\mathbf{P})$ and every vector $\boldsymbol{x}$ from the domain can be decomposed uniquely into a linear combination of $\boldsymbol{x}_r + \boldsymbol{x}_n$ with $\boldsymbol{x}_r \in$ range $(\mathbf{P})$ and $\boldsymbol{x}_n \in$ null $(\mathbf{P})$.

Figuratively speaking, $\mathbf{P}$ is a parallel projection onto the image range $(\mathbf{P})$ along the null space null $(\mathbf{P})$, *i.e.*, that all information parallel to the projection direction is annihilated ($\mathbf{P}\boldsymbol{x}_n = \mathbf{0}$), while leaving components parallel to the projection plane invariant ($\mathbf{P}\boldsymbol{x}_r = \boldsymbol{x}_r$). In the special case of an orthogonal projection, range and null space are perpendicular (and with them $\boldsymbol{x}_r \perp \boldsymbol{x}_n$). For two orthogonal projections with perpendicular projection directions, this has the implication that the null space of one lies in the image of the other and vice versa.

In this case, $\mathbf{P}_{b,LA}$ is an endomorphism of the vectorised three-component, three-dimensional vector space $\mathbb{R}^{3N_x N_y N_z}$, *i.e.*, $\mathbf{P}_{b,LA} \in \mathbb{R}^{3N_x N_y N_z \times 3N_x N_y N_z}$, but the range only lies in a subspace of lower dimensionality (the three-component, two-dimensional space $\mathbb{R}^{3N_u N_v}$). A lot of the space is therefore empty after the projection. As a simple example for a projection along the z direction for a small three-dimensional volume of $2 \times 2 \times 2$ voxels, the projection matrix would be given by the expression

$$\mathbf{P}_{z,LA} = \begin{pmatrix} \mathbf{W}_{z,LA} & 0 & 0 \\ 0 & \mathbf{W}_{z,LA} & 0 \\ 0 & 0 & \mathbf{W}_{z,LA} \end{pmatrix}, \tag{A.42}$$

with

$$\mathbf{W}_{z,LA} = \begin{pmatrix} 1 & 0 & 0 & 0 & 1 & 0 & 0 & 0 \\ 0 & 1 & 0 & 0 & 0 & 1 & 0 & 0 \\ 0 & 0 & 1 & 0 & 0 & 0 & 1 & 0 \\ 0 & 0 & 0 & 1 & 0 & 0 & 0 & 1 \\ 0 & 0 & 0 & 0 & 0 & 0 & 0 & 0 \\ 0 & 0 & 0 & 0 & 0 & 0 & 0 & 0 \\ 0 & 0 & 0 & 0 & 0 & 0 & 0 & 0 \\ 0 & 0 & 0 & 0 & 0 & 0 & 0 & 0 \end{pmatrix}, \tag{A.43}$$

where $\mathbf{W}_{z,LA}$ is the linear algebraic form of the weighting matrix defined in Eq. 3.13. In this example, the magnetised volume was projected onto the first z slice. The idempotence of the weighting matrix $\mathbf{W}_{z,LA}^2 = \mathbf{W}_{z,LA}$, and therefore the idempotence of the projection matrix $\mathbf{P}_{z,LA}^2 = \mathbf{P}_{z,LA}$ can be easily shown.

---

[9]A linear transformation of a vector space onto itself.

To optimise the computational efficiency, another matrix $\mathbf{P}_{b,CS}$ is applied afterwards to discard all dimensions along which the projection took place. This matrix effectively changes the coordinate system to the subspace defined by the image range $(\mathbf{P}_{b,LA}) \in \mathbb{R}^{3N_u N_v}$. In addition, the perpendicular component of the projected distribution is also discarded, which reduces the target subspace even further to $\mathbb{R}^{2N_u N_v}$. Keeping the perpendicular component would waste computational effort, because it does not contribute to the phase mapping (see section 3.1.4) and therefore would always lie in the null space of the corresponding matrix $\mathbf{Q}_b$. The information loss of the third vector component is shifted from the phase mapping matrix $\mathbf{Q}_b$ to the projection matrix $\mathbf{P}_b$, because it makes the computation more efficient.

For the example of a simple z-projection above, the coordinate system conversion can be described by

$$\mathbf{P}_{z,CS} = \begin{pmatrix} \mathbf{W}_{z,CS} & 0 & 0 \\ 0 & \mathbf{W}_{z,CS} & 0 \end{pmatrix}, \tag{A.44}$$

with

$$\mathbf{W}_{z,CS} = \begin{pmatrix} 1 & 0 & 0 & 0 & 0 & 0 & 0 & 0 \\ 0 & 1 & 0 & 0 & 0 & 0 & 0 & 0 \\ 0 & 0 & 1 & 0 & 0 & 0 & 0 & 0 \\ 0 & 0 & 0 & 1 & 0 & 0 & 0 & 0 \end{pmatrix}. \tag{A.45}$$
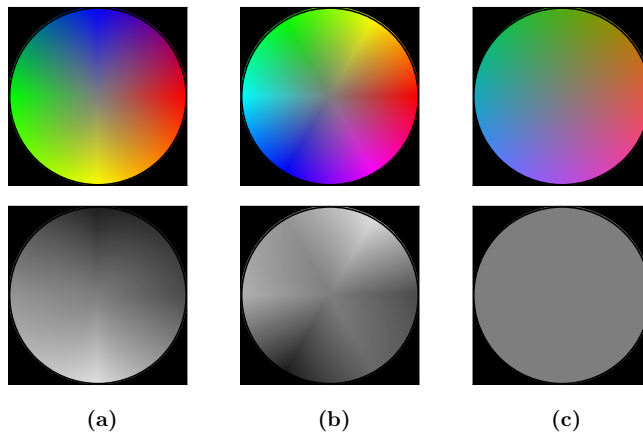
In this simple case, $\mathbf{W}_{z,CS}$ simply picks the first z slice (the target subspace of the projection) as the new coordinate system by containing suitable standard basis vectors in the first four columns. All other z slices, that do not contain any information after the projection anyway, are discarded. $\mathbf{P}_{z,CS}$ additionally discards the z component of the vector field, as motivated above. For projections that are not parallel to the main axes, the according matrices are more complicated.

After examining the theoretical split of a projection matrix $\mathbf{P}_b$, the two contributions to its null space can be listed as:

- The loss of information along the projection direction, described by the linear algebraic projection $\mathbf{P}_{b,LA}$.

- The loss of information about the vector component perpendicular to the projection direction, facilitated by the matrix $\mathbf{P}_{b,CS}$ that changes the coordinate system.

A.5. Visualisation of directional properties

In this section, a colour scheme for the visualisation of vector fields and directional properties in general is presented, which is used for vector plots in two and three dimensions, as well as for magnetic induction maps throughout this thesis. Two dimensional vector fields are often visualised with polar coordinates by using a colour wheel. The azimuth angle is encoded by hue and the amplitude is encoded by the radial component, which usually varies in saturation from the grey centre (*i.e.*, zero saturation) to the fully coloured borders of the wheel (*i.e.*, full saturation). Figure A.6a shows a colour wheel with four primary colours at angles of 90°, that is often found in publications concerning electron holography, where it encodes magnetic induction maps. Another type of colour wheel, which is based on the HSL colour space (*i.e.*, hue, saturation, lightness), is also quite common and is shown in Fig. A.6b.

(a)   (b)   (c)

Figure A.6.: (**a**) Colour wheel with four primary colours at angles of 90°, that is often used for magnetic induction maps. (**b**) Colour wheel, which is based on the HSL (hue, saturation, lightness) colour space. (**c**) The optimised isoluminant colour wheel based on the cubehelix colour map. A corresponding greyscale image is shown below each colour wheel.

The extension of these colour schemes to the visualisation of three-dimensional vector fields can be achieved by extending the polar coordinates to cylindrical coordinates, with the z axis being used to encode the out-of-plane component of the vector field. The colour property that is associated with this out-of-plane component is the brightness. Brightness is defined as an attribute of visual sensation according to which an area appears to emit more or less light [139]. It is a perceptual quantity and as such has no firm measure. Many colour spaces vary in brightness along their third dimension and nearly every one of them uses a different name and definition of

brightness. The mentioned HSL colour space, *e.g.*, defines the "lightness" as the average of the highest and lowest component of an RGB (red, green, blue) tuple, while the related HSV (hue, saturation, value) space defines it as the RGB-component average, both of which do not correspond very well to the human perception of brightness. This poses a problem for the use in the encoding of three-dimensional vector fields, as is revealed, when converting the colour wheels in Figs. A.6a and A.6b to greyscale. The perceived brightness of the colour wheel is not homogeneous for the whole colour wheel, which is especially noticeable for the HSL colour wheel, which appears brighter for the secondary colours yellow, cyan and magenta. In an images that is encoded with the HSL colour wheel, these differences in brightness may be mistaken for features by an unaware observer. For three-dimensional visualisation, the brightness difference in the colour wheel leads to a visual intermixture of vector components in- and out-of-plane.

In order to address this problem, the "cubehelix" colour map which was developed by Dave Green [140] is adapted to be used as an optimised, isoluminant colour wheel. The original cubehelix colour map is shown in Fig. A.7a and exhibits a linear increase in brightness, as indicated by the black straight line through the origin. This behaviour is achieved by letting the three RGB colour components rotate along helical paths around the desired path for the brightness in the RGB cube. In the original cubehelix, each colour rotates 1.5 times around the brightness path. The different amplitudes of the three helices compensate for the difference in human brightness perception for different colours[10]. For the adaptation as a colour wheel, three modifications have to be made: The brightness path is changed to a flat line at exactly 50% brightness, the number of rotations is set to one and the helix amplitudes are increased to optimally use the available brightness range. The resulting colour map is shown in Fig. A.7b.

Because it starts and ends with the same colour, the colour map can be turned into the colour wheel shown in Fig. A.6c. The greyscale image confirms a flat, isoluminant brightness level. The optimised colour wheel is used throughout this thesis for encoding the in-plane components of a three-dimensional vector field. As described above, the out-of-plane component is encoded by brightness, so that vectors that point in positive z direction are coloured white, while vectors that point in negative z direction are coloured black. An example for a simple vector field is shown in Fig. A.8.

For more information about colour theory, especially the different definitions of brightness, the two online PDFs of Charles Poynton are highly recommended (see [139, 141] at www.poynton.com).

---

[10]The receptor cells with a sensitivity peak at green wavelengths in the human eye are much more sensitive to light than the other two types. Therefore, the according helix has a smaller amplitude to attenuate the green contribution to the resulting colour.
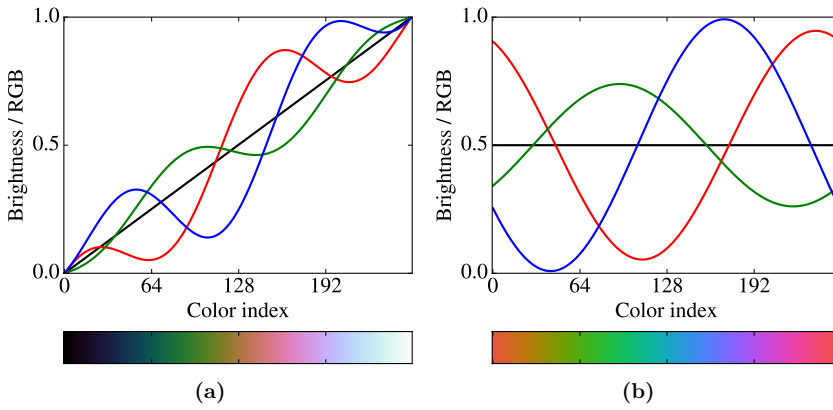
Figure A.7.: (**a**) Original cubehelix colour map, developed by Dave Green. Above the map, the brightness and the three RGB colour components are shown as functions of a colour index, which iterates from 0 to 255. (**b**) Modified cubehelix colour map that produces isoluminant colours of constant brightness. In order to generate a colour wheel, the colour map starts and ends with the same shade of red.
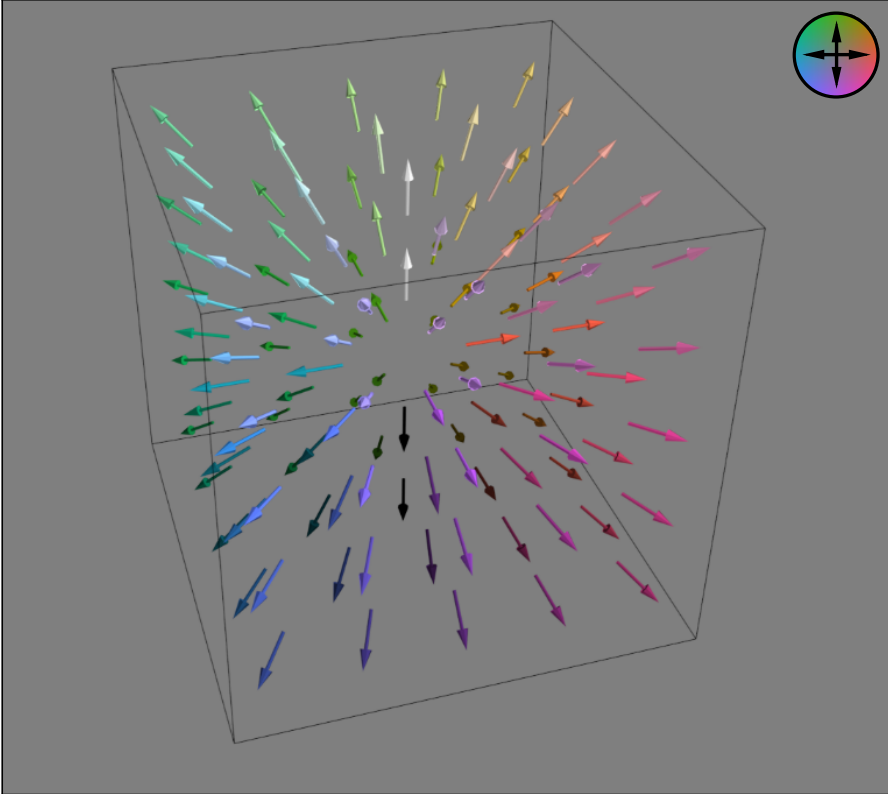
Figure A.8.: Vector field plot with in-plane components encoded with the optimised colour wheel. White arrows point in the positive z direction, black arrows point in the negative z direction.

Bibliography

[1] W. F. Brown, "Single-domain particles: New uses of old theorems," *American Journal of Physics*, vol. 28, no. 6, pp. 542–551, 1960.
(Cited on page 1)

[2] N. Nagaosa and Y. Tokura, "Topological properties and dynamics of magnetic skyrmions," *Nature Nanotechnology*, vol. 8, no. 12, pp. 899–911, 2013.
(Cited on page 1)

[3] Z.-A. Li, F. Zheng, A. H. Tavabi, J. Caron, C. Jin, H. Du, A. Kovács, M. Tian, M. Farle, and R. E. Dunin-Borkowski, "Magnetic skyrmion formation at lattice defects and grain boundaries studied by quantitative off-axis electron holography," *Nano Letters*, vol. 17, no. 3, pp. 1395–1401, 2017.
(Cited on page 1)

[4] C. Jin, Z.-A. Li, A. Kovács, J. Caron, F. Zheng, F. N. Rybakov, N. S. Kiselev, H. Du, S. Blügel, M. Tian, Y. Zhang, M. Farle, and R. E. Dunin-Borkowski, "Control of morphology and formation of highly geometrically confined magnetic skyrmions," *Nature Communications*, vol. 8, p. 15569, 2017.
(Cited on page 1)

[5] N. A. Frey and S. Sun, "Chapter 3 - Magnetic Nanoparticle for Information Storage Applications," in *Inorganic Nanoparticles*, ser. Nanomaterials and their applications, C. Altavilla and E. Ciliberto, Eds. Boca Raton: CRC Press, 2010, pp. 33–68.
(Cited on page 1)

[6] N. Romming, C. Hanneken, M. Menzel, J. E. Bickel, B. Wolter, K. von Bergmann, A. Kubetzka, and R. Wiesendanger, "Writing and deleting single magnetic skyrmions," *Science*, vol. 341, no. 6146, pp. 636–639, 2013.
(Cited on page 1)

[7] A.-H. Lu, W. Schmidt, N. Matoussevitch, H. Bonnemann, B. Spliethoff, B. Tesche, E. Bill, W. Kiefer, and F. Schuth, "Nanoengineering of a magnetically separable hydrogenation catalyst," *Angewandte Chemie (International ed. in English)*, vol. 43, no. 33, pp. 4303–4306, 2004.
(Cited on page 1)

[8] A. K. Gupta and M. Gupta, "Synthesis and surface engineering of iron oxide nanoparticles for biomedical applications," *Biomaterials*, vol. 26, no. 18, pp. 3995–4021, 2005.
(Cited on page 1)

[9] M. Colombo, S. Carregal-Romero, M. F. Casula, L. Gutierrez, M. P. Morales, I. B. Bohm, J. T. Heverhagen, D. Prosperi, and W. J. Parak, "Biological applications of magnetic nanoparticles," *Chemical Society Reviews*, vol. 41, no. 11, pp. 4306–4334, 2012.
(Cited on page 1)

[10] M. Javidi, M. Heydari, A. Karimi, M. Haghpanahi, M. Navidbakhsh, and A. Razmkon, "Evaluation of the effects of injection velocity and different gel concentrations on nanoparticles in hyperthermia therapy," *Journal of Biomedical Physics & Engineering*, vol. 4, no. 4, pp. 151–162, 2014.
(Cited on page 1)

[11] J. Estelrich, E. Escribano, J. Queralt, and M. A. Busquets, "Iron oxide nanoparticles for magnetically-guided and magnetically-responsive drug delivery," *International Journal of Molecular Sciences*, vol. 16, no. 4, pp. 8070–8101, 2015.
(Cited on page 1)

[12] A. Elaissari, J. Chatterjee, M. Hamoudeh, and H. Fessi, "Advances in the preparation and biomedical applications of magnetic colloids," in *Structure and Functional Properties of Colloidal Systems*, ser. Surfactant Science Series, R. Hidalgo-Álvarez, Ed. Boca Raton: CRC Press, 2010, pp. 315–337.
(Cited on page 1)

[13] X. Meng, H. C. Seton, T. Le Lu, I. A. Prior, N. T. K. Thanh, and B. Song, "Magnetic CoPt nanoparticles as MRI contrast agent for transplanted neural stem cells detection," *Nanoscale*, vol. 3, no. 3, pp. 977–984, 2011.
(Cited on page 1)

[14] R. E. Dunin-Borkowski, "Magnetic microstructure of magnetotactic bacteria by electron holography," *Science*, vol. 282, no. 5395, pp. 1868–1870, 1998.
(Cited on pages 1 and 2)

[15] M. Haider, H. Rose, S. Uhlemann, E. Schwan, B. Kabius, and K. Urban, "A spherical-aberration-corrected 200kV transmission electron microscope," *Ultramicroscopy*, vol. 75, no. 1, pp. 53–60, 1998.
(Cited on page 1)

[16] A. Tonomura, *Electron Holography: 2nd edition*, ser. Springer Series in Optical Sciences. Springer, 1999.
(Cited on page 2)

[17] R. E. Dunin-Borkowski, M. R. McCartney, B. Kardynal, D. J. Smith, and M. R. Scheinfein, "Switching asymmetries in closely coupled magnetic nanostructure arrays," *Applied Physics Letters*, vol. 75, no. 17, pp. 2641–2643, 1999.
(Cited on page 2)

[18] R. E. Dunin-Borkowski, M. R. McCartney, and D. J. Smith, "Electron holography of nanostructured materials," in *Encyclopedia of Nanoscience and Nanotechnology*, H. Nalwa, Ed. American Scientific Publishers, 2004, vol. 3, pp. 41–100.
(Cited on page 2)

[19] M. R. McCartney and D. J. Smith, "Electron holography: phase imaging with nanometer resolution," *Annual Review of Material Research*, vol. 37, no. 1, pp. 729–767, 2007.
(Cited on page 2)

[20] H. Lichte and M. Lehmann, "Electron holography – basics and applications," *Reports on Progress in Physics*, vol. 71, no. 1, p. 016102, 2008.
(Cited on pages 2 and 9)

[21] P. A. Midgley and R. E. Dunin-Borkowski, "Electron tomography and holography in materials science," *Nature Materials*, vol. 8, no. 4, pp. 271–280, 2009.
(Cited on pages 2 and 3)

[22] E. Völkl, L. F. Allard, and D. C. Joy, Eds., *Introduction to Electron Holography*. New York: Springer Science & Business Media, 1999.
(Cited on page 2)

[23] G. Pozzi, M. Beleggia, T. Kasama, and R. E. Dunin-Borkowski, "Interferometric methods for mapping static electric and magnetic fields," *Comptes Rendus Physique*, vol. 15, no. 2, pp. 126–139, 2014.
(Cited on page 2)

[24] R. E. Dunin-Borkowski, T. Kasama, M. Beleggia, and G. Pozzi, "Lorentz microscopy and electron holography of magnetic materials," in *Handbook of Nanoscopy*, G. Van Tendeloo, D. Van Dyck, and S. J. Pennycook, Eds. Weinheim: Wiley–VCH, 2012, pp. 221–251.
(Cited on page 2)

[25] N. H. Dekkers and H. de Lang, "Differential phase contrast in a STEM," *Optik*, vol. 41, no. 4, pp. 452–456, 1974.
(Cited on page 2)

[26] J. N. Chapman, I. R. McFadyen, and S. McVitie, "Modified differential phase contrast Lorentz microscopy for improved imaging of magnetic structures," *IEEE Transactions on Magnetics*, vol. 26, no. 5, pp. 1506–1511, 1990.
(Cited on page 2)

[27] K. J. Kirk, J. N. Chapman, S. McVitie, P. R. Aitchison, and C. D. W. Wilkinson, "Switching of nanoscale magnetic elements," *Applied Physics Letters*, vol. 75, no. 23, pp. 3683–3685, 1999.
(Cited on page 2)

[28] T. Uhlig and J. Zweck, "Recording of single-particle hysteresis loops with differential phase contrast microscopy," *Ultramicroscopy*, vol. 99, no. 2, pp. 137–142, 2004.
(Cited on page 2)

[29] M. Lohr, R. Schregle, M. Jetter, C. Wächter, T. Wunderer, F. Scholz, and J. Zweck, "Differential phase contrast 2.0 - Opening new "fields" for an established technique," *Ultramicroscopy*, vol. 117, pp. 7–14, 2012.
(Cited on page 2)

[30] A. Lubk and J. Zweck, "Differential phase contrast: An integral perspective," *Physical Review A*, vol. 91, no. 2, p. 023805, 2015.
(Cited on page 2)

[31] J. M. Rodenburg, "Ptychography and related diffractive imaging methods," *Advances in Imaging and Electron Physics*, vol. 150, no. 07, pp. 87–184, 2008.
(Cited on page 2)

[32] F. Hüe, J. M. Rodenburg, A. M. Maiden, F. Sweeney, and P. A. Midgley, "Wave-front phase retrieval in transmission electron microscopy via ptychography," *Physical Review B*, vol. 82, no. 12, p. 121415, 2010.
(Cited on page 2)

[33] J. N. Chapman, "The investigation of magnetic domain structures in thin foils by electron microscopy," *Journal of Physics D: Applied Physics*, vol. 17, no. 4, p. 623, 1984.
(Cited on page 2)

[34] R. C. Doole, A. K. Petford-Long, and J. P. Jakubovics, "Improved Foucault imaging of magnetic domains with a modified 400 kV transmission electron microscope," *Review of Scientific Instruments*, vol. 64, no. 4, pp. 1038–1043, 1993.
(Cited on page 2)

[35] A. B. Johnston and J. N. Chapman, "The development of coherent Foucault imaging to investigate magnetic microstructure," *Journal of Microscopy*, vol. 179, no. 2, pp. 119–128, 1995.
(Cited on page 2)

[36] S. McVitie and M. Cushley, "Quantitative Fresnel Lorentz microscopy and the transport of intensity equation," *Ultramicroscopy*, vol. 106, no. 4, pp. 423–431, 2006.
(Cited on page 2)

[37] E. Humphrey, C. Phatak, A. K. Petford-Long, and M. de Graef, "Separation of electrostatic and magnetic phase shifts using a modified transport-of-intensity equation," *Ultramicroscopy*, vol. 139, pp. 5–12, 2014.
(Cited on page 2)

[38] R. J. Harrison, "Direct imaging of nanoscale magnetic interactions in minerals," *Proceedings of the National Academy of Sciences*, vol. 99, no. 26, pp. 16 556–16 561, 2002.
(Cited on page 2)

[39] T. Kasama, R. E. Dunin-Borkowski, and M. Beleggia, "Electron holography of magnetic materials," in *Holography - Different Fields of Application*, F. Monroy, Ed. InTech, 2011, pp. 53–80.
(Cited on page 2)

[40] D. Gabor, "A new microscopic principle," *Nature*, vol. 161, no. 4098, pp. 777–778, 1948.
(Cited on pages 2 and 7)

[41] D. Gabor, "Microscopy by reconstructed wave-fronts," *Proceedings of the Royal Society of London A: Mathematical, Physical and Engineering Sciences*, vol. 197, no. 1051, pp. 454–487, 1949.
(Cited on pages 2 and 7)

[42] E. N. Leith and J. Upatnieks, "Reconstructed wavefronts and communication theory," *Journal of the Optical Society of America*, vol. 52, no. 10, p. 1123, 1962.
(Cited on page 2)

[43] G. Möllenstedt and H. Düker, "Fresnelscher Interferenzversuch mit einem Biprisma für Elektronenwellen," *Die Naturwissenschaften*, vol. 42, no. 2, p. 41, 1955.
(Cited on pages 2 and 7)

[44] Ernst Ruska-Centre for Microscopy and Spectroscopy with Electrons, "FEI Titan G2 60-300 HOLO," *Journal of Large-scale Research Facilities*, vol. 2, 2016.
(Cited on pages 2 and 109)

[45] Y. Aharonov and D. Bohm, "Significance of electromagnetic potentials in the quantum theory," *Physical Review*, vol. 115, no. 3, pp. 485–491, 1959.
(Cited on pages 3 and 12)

[46] W. Ehrenberg and R. E. Siday, "The refractive index in electron optics and the principles of dynamics," *Proceedings of the Physical Society. Section B*, vol. 62, no. 1, p. 8, 1949.
(Cited on pages 3 and 12)

[47] G. T. Herman, *Fundamentals of Computerized Tomography: Image Reconstruction from Projections*, ser. Advances in Pattern Recognition. London: Springer-Verlag London, 2009.
(Cited on page 3)

[48] A. Alpers, R. J. Gardner, S. König, R. S. Pennington, C. B. Boothroyd, L. Houben, R. E. Dunin-Borkowski, and K. Joost Batenburg, "Geometric reconstruction methods for electron tomography," *Ultramicroscopy*, vol. 128C, pp. 42–54, 2013.
(Cited on page 3)

[49] R. S. Pennington, S. König, A. Alpers, C. B. Boothroyd, and R. E. Dunin-Borkowski, "Reconstruction of an InAs nanowire using geometric and algebraic tomography," *Journal of Physics: Conference Series*, vol. 326, p. 012045, 2011.
(Cited on page 3)

[50] R. J. Gardner, *Geometric Tomography.* Cambridge: Cambridge University Press, 2006.
(Cited on page 3)

[51] G. T. Herman and A. Kuba, *Discrete Tomography: Foundations, Algorithms, and Applications.* Boston: Birkhäuser Boston, 1999.
(Cited on pages 3 and 132)

[52] G. T. Herman and A. Kuba, Eds., *Advances in Discrete Tomography and its Applications*, ser. Applied and Numerical Harmonic Analysis. Boston: Birkhäuser, 2007.
(Cited on pages 3 and 132)

[53] S. Lade, D. Paganin, and M. Morgan, "3-D vector tomography of Doppler-transformed fields by filtered-backprojection," *Optics Communications*, vol. 253, no. 4-6, pp. 382–391, 2005.
(Cited on pages 3 and 76)

[54] S. Lade, D. Paganin, and M. Morgan, "Electron tomography of electromagnetic fields, potentials and sources," *Optics Communications*, vol. 253, no. 4-6, pp. 392–400, 2005.
(Cited on page 3)

[55] G. Lai, T. Hirayama, A. Fukuhara, K. Ishizuka, T. Tanji, and A. Tonomura, "Three-dimensional reconstruction of magnetic vector fields using electron-holographic interferometry," *Journal of Applied Physics*, vol. 75, no. 9, pp. 4593–4598, 1994.
(Cited on page 3)

[56] J. B. Elsbrock, W. Schroeder, and E. Kubalek, "Evaluation of three-dimensional micromagnetic stray fields by means of electron-beam tomography," *IEEE Transactions on Magnetics*, vol. 21, no. 5, pp. 1593–1595, 1985.
(Cited on page 3)

[57] J. Matsuda, K. Aoyagi, Y. Kondoh, M. Iizuka, and K. Mukasa, "A three-dimensional measuring method for magnetic stray fields," *IEEE Transactions on Magnetics*, vol. 26, no. 5, pp. 2061–2063, 1990.
(Cited on page 3)

[58] R. P. Ferrier, Y. Liu, J. L. Martin, and T. C. Arnoldussen, "Electron beam tomography of magnetic recording head fields," *Journal of Magnetism and Magnetic Materials*, vol. 149, no. 3, pp. 387–397, 1995.
(Cited on page 3)

[59] R. P. Ferrier, S. McVitie, A. Gallagher, and Nicholson, W A P, "Characterisation of MFM tip fields by electron tomography," *IEEE Transactions on Magnetics*, vol. 33, no. 5, pp. 4062–4064, 1997.
(Cited on page 3)

[60] H. Suzuki, T. Shimakura, K. Itoh, and K. Nakamura, "Magnetic head field over the air-bearing surface as visualized by the projection of a patterned electron beam," *IEEE Transactions on Magnetics*, vol. 36, no. 5, pp. 3614–3617, 2000.
(Cited on page 3)

[61] C. Phatak, M. Beleggia, and M. de Graef, "Vector field electron tomography of magnetic materials: Theoretical development," *Ultramicroscopy*, vol. 108, no. 6, pp. 503–513, 2008.
(Cited on page 3)

[62] A. Lubk, D. Wolf, P. Simon, C. Wang, S. Sturm, and C. Felser, "Nanoscale three-dimensional reconstruction of electric and magnetic stray fields around nanowires," *Applied Physics Letters*, vol. 105, no. 17, p. 173110, 2014.
(Cited on page 3)

[63] C. Phatak and D. Gürsoy, "Iterative reconstruction of magnetic induction using Lorentz transmission electron tomography," *Ultramicroscopy*, vol. 150, pp. 54–64, 2015.
(Cited on page 3)

[64] D. Wolf, L. A. Rodriguez, A. Beche, E. Javon, L. Serrano, C. Magen, C. Gatel, A. Lubk, H. Lichte, S. Bals *et al.*, "3D magnetic induction maps of nanoscale materials revealed by electron holographic tomography," *Chemistry of Materials*, vol. 27, no. 19, pp. 6771–6778, 2015.
(Cited on page 3)

[65] P. Simon, D. Wolf, C. Wang, A. A. Levin, A. Lubk, S. Sturm, H. Lichte, G. Fecher, and C. Felser, "Synthesis and three-dimensional magnetic field mapping of Co2FeGa Heusler nanowires at 5 nm resolution," *Nano Letters*, vol. 16, no. 1, pp. 114–120, 2016.
(Cited on page 3)

[66] T. Tanigaki, Y. Takahashi, T. Shimakura, T. Akashi, R. Tsuneta, A. Sugawara, and D. Shindo, "Three-dimensional observation of magnetic vortex cores in stacked ferromagnetic discs," *Nano Letters*, vol. 15, no. 2, pp. 1309–1314, 2015.
(Cited on page 3)

[67] C. Phatak, L. de Knoop, F. Houdellier, C. Gatel, M. J. Hytch, and A. Masse-boeuf, "Quantitative 3D electromagnetic field determination of 1D nanostructures from single projection," *Ultramicroscopy*, vol. 164, pp. 24–30, 2016.
(Cited on page 3)

[68] C. Phatak, A. K. Petford-Long, and M. de Graef, "Three-dimensional study of the vector potential of magnetic structures," *Physical Review Letters*, vol. 104, no. 25, p. 253901, 2010.
(Cited on page 3)

[69] R. P. Yu, M. J. Morgan, and D. M. Paganin, "Lorentz-electron vector tomography using two and three orthogonal tilt series," *Physical Review A*, vol. 83, no. 2, p. 023813, 2011.
(Cited on page 3)

[70] Z. D. C. Kemp, T. C. Petersen, D. M. Paganin, K. M. Spiers, M. Weyland, and M. J. Morgan, "Analysis of noise-induced errors in vector-field electron tomography," *Physical Review A*, vol. 90, no. 2, p. 023859, 2014.
(Cited on pages 3 and 73)

[71] E. Humphrey and M. de Graef, "On the computation of the magnetic phase shift for magnetic nano-particles of arbitrary shape using a spherical projection model," *Ultramicroscopy*, vol. 129, pp. 36–41, 2013.
(Cited on pages 4, 15, and 47)

[72] J. Ungermann, *Tomographic Reconstruction of Atmospheric Volumes from Infrared Limb-Imager Measurements (Ph.D. Thesis)*. Jülich: Forschungszentrum Jülich, Zentralbibliothek, 2011.
(Cited on pages 4, 30, 61, 62, 69, 72, and 156)

[73] L. Liu, "Model-based iterative reconstruction: A promising algorithm for today's computed tomography imaging," *Journal of Medical Imaging and Radiation Sciences*, vol. 45, no. 2, pp. 131–136, 2014.
(Cited on page 4)

[74] K. Harada, A. Tonomura, T. Matsuda, T. Akashi, and Y. Togawa, "High-resolution observation by double-biprism electron holography," *Journal of Applied Physics*, vol. 96, no. 11, pp. 6097–6102, 2004.
(Cited on page 7)

[75] C. B. Carter and D. B. Williams, *Transmission Electron Microscopy: A Textbook for Materials Science*. New York: Springer Science & Business Media, 2016.
(Cited on pages 7, 9, and 10)

[76] K. Keimpema, *Electron Holography of Nanoparticles (Ph.D. Thesis)*. Enschede and Groningen: PrintPartners Ipskamp and University Library Groningen [Host], 2008.
(Cited on pages 7, 10, 13, and 14)

[77] R. E. Dunin-Borkowski, T. Kasama, A. Wei, S. L. Tripp, M. J. Hytch, E. Snoeck, R. J. Harrison, and A. Putnis, "Off-axis electron holography of magnetic nanowires and chains, rings, and planar arrays of magnetic nanoparticles," *Microscopy Research and Technique*, vol. 64, no. 5-6, pp. 390–402, 2004.
(Cited on page 12)

[78] M. Gajdardziska-Josifovska, M. R. McCartney, W. J. De Ruijter, D. J. Smith, J. K. Weiss, and J. M. Zuo, "Accurate measurements of mean inner potential of crystal wedges using digital electron holograms," *Ultramicroscopy*, vol. 50, no. 3, pp. 285–299, 1993.
(Cited on page 12)

[79] M. O'Keeffe and J. C. H. Spence, "On the average Coulomb potential and constraints on the electron density in crystals," *Acta Crystallographica Section A: Foundations of Crystallography*, vol. 50, no. 1, pp. 33–45, 1994.
(Cited on page 12)

[80] D. K. Saldin and J. C. H. Spence, "On the mean inner potential in high- and low-energy electron diffraction," *Ultramicroscopy*, vol. 55, no. 4, pp. 397–406, 1994.
(Cited on page 12)

[81] J. Li, M. R. McCartney, R. E. Dunin-Borkowski, and D. J. Smith, "Determination of mean inner potential of germanium using off-axis electron holography," *Acta Crystallographica Section A: Foundations of Crystallography*, vol. 55, no. 4, pp. 652–658, 1999.
(Cited on page 12)

[82] P. Kruse, M. Schowalter, D. Lamoen, A. Rosenauer, and D. Gerthsen, "Determination of the mean inner potential in III–V semiconductors, Si and Ge by density functional theory and electron holography," *Ultramicroscopy*, vol. 106, no. 2, pp. 105–113, 2006.
(Cited on page 12)

[83] R. S. Pennington, C. B. Boothroyd, and R. E. Dunin-Borkowski, "Surface effects on mean inner potentials studied using density functional theory," *Ultramicroscopy*, vol. 159, pp. 34–45, 2015.
(Cited on page 12)

[84] P. G. Merli, G. F. Missiroli, and G. Pozzi, "Transmission electron microscopy observations of p–n junctions," *Physica Status Solidi (a)*, vol. 30, no. 2, pp. 699–711, 1975.
(Cited on page 12)

[85] S. J. Lloyd, R. E. Dunin-Borkowski, and C. B. Boothroyd, "The determination of the ionicity of sapphire using energy-filtered high resolution electron microscopy," *Institute of Physics Conference Series*, vol. 153, pp. 113–116, 1997.
(Cited on page 12)

[86] W. D. Rau, P. Schwander, F. H. Baumann, W. Höppner, and A. Ourmazd, "Two-dimensional mapping of the electrostatic potential in transistors by electron holography," *Physical Review Letters*, vol. 82, no. 12, p. 2614, 1999. (Cited on page 12)

[87] M. A. Gribelyuk, M. R. McCartney, J. Li, C. S. Murthy, P. Ronsheim, B. Doris, J. S. McMurray, S. Hegde, and D. J. Smith, "Mapping of electrostatic potential in deep submicron CMOS devices by electron holography," *Physical Review Letters*, vol. 89, no. 2, p. 025502, 2002. (Cited on page 12)

[88] M. R. McCartney, M. A. Gribelyuk, J. Li, P. Ronsheim, J. S. McMurray, and D. J. Smith, "Quantitative analysis of one-dimensional dopant profile by electron holography," *Applied Physics Letters*, vol. 80, no. 17, pp. 3213–3215, 2002. (Cited on page 12)

[89] K. H. Downing, M. R. McCartney, and R. M. Glaeser, "Experimental characterization and mitigation of specimen charging on thin films with one conducting layer," *Microscopy and Microanalysis*, vol. 10, no. 6, pp. 783–789, 2004. (Cited on page 12)

[90] A. C. Twitchett-Harrison, T. J. V. Yates, S. B. Newcomb, R. E. Dunin-Borkowski, and P. A. Midgley, "High-resolution three-dimensional mapping of semiconductor dopant potentials," *Nano Letters*, vol. 7, no. 7, pp. 2020–2023, 2007. (Cited on page 12)

[91] D. Wolf, A. Lubk, A. Lenk, S. Sturm, and H. Lichte, "Tomographic investigation of Fermi level pinning at focused ion beam milled semiconductor surfaces," *Applied Physics Letters*, vol. 103, no. 26, p. 264104, 2013. (Cited on page 12)

[92] S. Frabboni, G. Matteucci, G. Pozzi, and M. Vanzi, "Electron holographic observations of the electrostatic field associated with thin reverse-biased p-n junctions," *Physical Review Letters*, vol. 55, no. 20, p. 2196, 1985. (Cited on page 12)

[93] M. Beleggia, R. Capelli, and G. Pozzi, "A model for the interpretation of holographic and Lorentz images of tilted reverse-biased p-n junctions in a finite specimen," *Philosophical Magazine B*, vol. 80, no. 5, pp. 1071–1082, 2000. (Cited on page 12)

[94] D. Cooper, C. Ailliot, J.-P. Barnes, J.-M. Hartmann, P. Salles, G. Benassayag, and R. E. Dunin-Borkowski, "Dopant profiling of focused ion beam milled semiconductors using off-axis electron holography; reducing artifacts, extending detection limits and reducing the effects of gallium implantation," *Ultramicroscopy*, vol. 110, no. 5, pp. 383–389, 2010.
(Cited on page 12)

[95] G. Matteucci, G. F. Missiroli, M. Muccini, and G. Pozzi, "Electron holography in the study of the electrostatic fields: the case of charged microtips," *Ultramicroscopy*, vol. 45, no. 1, pp. 77–83, 1992.
(Cited on page 12)

[96] B. G. Frost and E. Völkl, "A study of electric charging using low-magnification electron holography," *Materials Characterization*, vol. 42, no. 4, pp. 221–227, 1999.
(Cited on page 12)

[97] G. Matteucci, G. F. Missiroli, and G. Pozzi, "Electron holography of long-range electrostatic fields," in *Advances in Imaging and Electron Physics*, P. W. Hawkes, Ed. Elsevier, 2002, vol. 122, pp. 173–249.
(Cited on page 12)

[98] J. Cumings, A. Zettl, M. R. McCartney, and J. C. H. Spence, "Electron holography of field-emitting carbon nanotubes," *Physical Review Letters*, vol. 88, no. 5, p. 056804, 2002.
(Cited on page 12)

[99] J. J. Kim, D. Shindo, Y. Murakami, W. Xia, L.-J. Chou, and Y.-L. Chueh, "Direct observation of field emission in a single TaSi2 nanowire," *Nano Letters*, vol. 7, no. 8, pp. 2243–2247, 2007.
(Cited on page 12)

[100] M. Beleggia and G. Pozzi, "Phase shift of charged metallic nanoparticles," *Ultramicroscopy*, vol. 110, no. 5, pp. 418–424, 2010.
(Cited on page 12)

[101] C. Gatel, A. Lubk, G. Pozzi, E. Snoeck, and M. Hytch, "Counting elementary charges on nanoparticles by electron holography," *Physical Review Letters*, vol. 111, no. 2, p. 025501, 2013.
(Cited on page 12)

[102] M. Beleggia, T. Kasama, D. J. Larson, T. F. Kelly, R. E. Dunin-Borkowski, and G. Pozzi, "Towards quantitative off-axis electron holographic mapping of the electric field around the tip of a sharp biased metallic needle," *Journal of Applied Physics*, vol. 116, no. 2, p. 024305, 2014.
(Cited on page 12)

[103] G. Matteucci, G. F. Missiroli, E. Nichelatti, A. Migliori, M. Vanzi, and G. Pozzi, "Electron holography of long-range electric and magnetic fields," *Journal of Applied Physics*, vol. 69, no. 4, pp. 1835–1842, 1991.
(Cited on pages 12 and 104)

[104] R. E. Dunin-Borkowski, S. B. Newcomb, T. Kasama, M. R. McCartney, M. Weyland, and P. A. Midgley, "Conventional and back-side focused ion beam milling for off-axis electron holography of electrostatic potentials in transistors," *Ultramicroscopy*, vol. 103, no. 1, pp. 67–81, 2005.
(Cited on page 12)

[105] M. Beleggia, T. Kasama, R. E. Dunin-Borkowski, S. Hofmann, and G. Pozzi, "Direct measurement of the charge distribution along a biased carbon nanotube bundle using electron holography," *Applied Physics Letters*, vol. 98, no. 24, p. 243101, 2011.
(Cited on page 12)

[106] V. Migunov, A. London, M. Farle, and R. E. Dunin-Borkowski, "Model-independent measurement of the charge density distribution along an Fe atom probe needle using off-axis electron holography without mean inner potential effects," *Journal of Applied Physics*, vol. 117, no. 13, p. 134301, 2015.
(Cited on page 12)

[107] J. M. Thomas, E. T. Simpson, T. Kasama, and R. E. Dunin-Borkowski, "Electron holography for the study of magnetic nanomaterials," *Accounts of Chemical Research*, vol. 41, no. 5, pp. 665–674, 2008.
(Cited on page 12)

[108] M. Mansuripur, "Computation of electron diffraction patterns in Lorentz electron microscopy of thin magnetic films," *Journal of Applied Physics*, vol. 69, no. 4, p. 2455, 1991.
(Cited on pages 12 and 14)

[109] K. Keimpema, H. De Raedt, and J. De Hosson, "Electron holography image simulation of nanoparticles," *Journal of Computational and Theoretical Nanoscience*, vol. 3, no. 3, pp. 362–374, 2006.
(Cited on pages 13, 14, 33, and 46)

[110] M. De Graef, N. T. Nuhfer, and M. R. McCartney, "Phase contrast of spherical magnetic particles," *Journal of Microscopy*, vol. 194, no. 1, pp. 84–94, 1999.
(Cited on page 14)

[111] M. Beleggia and Y. Zhu, "Electron-optical phase shift of magnetic nanoparticles I. Basic concepts," *Philosophical Magazine*, vol. 83, no. 8, pp. 1045–1057, 2003.
(Cited on pages 14, 15, and 100)

[112] M. Beleggia, Y. Zhu, S. Tandon, and M. de Graef, "Electron-optical phase shift of magnetic nanoparticles II. Polyhedral particles," *Philosophical Magazine*, vol. 83, no. 9, pp. 1143–1161, 2003.
(Cited on pages 14 and 15)

[113] M. Beleggia, M. A. Schofield, Y. Zhu, M. Malac, Z. Liu, and M. Freeman, "Quantitative study of magnetic field distribution by electron holography and micromagnetic simulations," *Applied Physics Letters*, vol. 83, no. 7, p. 1435, 2003.
(Cited on page 17)

[114] R. E. Dunin-Borkowski, M. R. McCartney, D. J. Smith, and S. S. Parkin, "Towards quantitative electron holography of magnetic thin films using in situ magnetization reversal," *Ultramicroscopy*, vol. 74, no. 1, pp. 61–73, 1998.
(Cited on page 17)

[115] H. W. Engl, M. Hanke, and A. Neubauer, *Regularization of inverse problems*. Dordrecht and Boston: Kluwer Academic Publishers, 1996.
(Cited on pages 18, 19, 60, and 62)

[116] C. D. Rodgers, *Inverse Methods for Atmospheric Sounding: Theory and Practice*, ser. Series on Atmospheric, Oceanic and Planetary Physics. Singapore and River Edge: World Scientific, 2000, vol. 2.
(Cited on pages 19, 61, 69, and 156)

[117] A. Tarantola, *Inverse Problem Theory and Methods for Model Parameter Estimation*. Philadelphia: Society for Industrial and Applied Mathematics, 2005.
(Cited on pages 19 and 62)

[118] W. H. Press, *Numerical Recipes: The Art of Scientific Computing*, 3rd ed. Cambridge and New York: Cambridge University Press, 2007.
(Cited on pages 19, 64, 65, and 72)

[119] J. Claerbout, "Adjoint operators," 16.03.2009. [Online]. Available: http://www.reproducibility.org/RSF/book/bei/conj/paper.pdf
(Cited on page 31)

[120] S. K. Walton and S. Felton, "MALTS: A tool to simulate Lorentz transmission electron microscopy from micromagnetic simulations," *IEEE Transactions on Magnetics*, vol. 49, no. 8, pp. 4795–4800, 2013.
(Cited on page 34)

[121] J. F. J. Bryson, T. Kasama, R. E. Dunin-Borkowski, and R. J. Harrison, "Ferrimagnetic/ferroelastic domain interactions in magnetite below the Verwey transition: Part II. Micromagnetic and image simulations," *Phase Transitions*, vol. 86, no. 1, pp. 88–102, 2013.
(Cited on page 34)

[122] M. Frigo and S. G. Johnson, "The Design and Implementation of FFTW3," *Proceedings of the IEEE*, vol. 93, no. 2, pp. 216–231, 2005.
(Cited on page 41)

[123] A. N. Tikhonov and V. I. Arsenin, *Solutions of Ill-Posed Problems*, ser. Scripta Series in Mathematics.   Washington and New York: Halsted Press, 1977.
(Cited on page 62)

[124] S. Twomey, *Introduction to the Mathematics of Inversion in Remote Sensing and Indirect Measurements*.   Mineola: Dover Publications, 1996.
(Cited on page 62)

[125] K. M. Krishnan, *Fundamentals and Applications of Magnetic Materials*, 1st ed. Oxford: Oxford University Press, 2016.
(Cited on page 63)

[126] T. J. Ypma, "Historical development of the Newton–Raphson method," *SIAM Review*, vol. 37, no. 4, pp. 531–551, 1995.
(Cited on page 67)

[127] J. Nocedal and S. J. Wright, *Numerical Optimization*, 2nd ed., ser. Springer Series in Operations Research.   New York: Springer, 2006.
(Cited on page 68)

[128] M. Hanke, *Conjugate Gradient Type Methods for Ill-posed Problems*, ser. Pitman Research Notes in Mathematics Series.   Harlow and New York: Longman Scientific & Technical, 1995, vol. 327.
(Cited on page 68)

[129] J. Nocedal, "Updating quasi-Newton matrices with limited storage," *Mathematics of Computation*, vol. 35, no. 151, p. 773, 1980.
(Cited on page 68)

[130] J. Radon, "On the determination of functions from their integral values along certain manifolds," *IEEE Transactions on Medical Imaging*, vol. 5, no. 4, pp. 170–176, 1986.
(Cited on page 76)

[131] A. Hauck, *Tomographie von Vektorfeldern (Ph.D. Thesis)*.   Düsseldorf: VDI Verlag, 1990.
(Cited on page 76)

[132] T. Fließbach, *Elektrodynamik*.   Heidelberg: Spektrum Akademischer Verlag, 2012.
(Cited on page 76)

[133] K. Halbach, "Design of permanent multipole magnets with oriented rare earth cobalt material," *Nuclear Instruments and Methods*, vol. 169, no. 1, pp. 1–10, 1980.
(Cited on page 80)

[134] R. Bjørk, A. Smith, and C. Bahl, "Analysis of the magnetic field, force, and torque for two-dimensional Halbach cylinders," *Journal of Magnetism and Magnetic Materials*, vol. 322, no. 1, pp. 133–141, 2010.
(Cited on page 80)

[135] P. C. Hansen, "Analysis of Discrete Ill-Posed Problems by Means of the L-Curve," *SIAM Review*, vol. 34, no. 4, pp. 561–580, 1992.
(Cited on page 90)

[136] S.-A. Zhou, *Electrodynamics of Solids and Microwave Superconductivity*, ser. Wiley Series in Microwave and Optical Engineering. New York: John Wiley & Sons, 1999.
(Cited on pages 113 and 115)

[137] L. Reimer and H. Kohl, *Transmission Electron Microscopy: Physics of Image Formation.* New York: Springer Science & Business Media, 2008.
(Cited on page 146)

[138] D. Werner, *Funktionalanalysis*, 7th ed., ser. Springer-Lehrbuch. Berlin and New York: Springer, 2011.
(Cited on page 158)

[139] C. Poynton, "Frequently Asked Questions about Color," 13.12.2000. [Online]. Available: http://www.poynton.com/PDFs/ColorFAQ.pdf
(Cited on pages 160 and 161)

[140] D. A. Green, "A colour scheme for the display of astronomical intensity images," *Bulletin of the Astronomical Society of India*, no. 39, pp. 289–295, 2011.
(Cited on page 161)

[141] C. Poynton, "Frequently Asked Questions about Gamma," 13.12.2000. [Online]. Available: http://www.poynton.com/PDFs/GammaFAQ.pdf
(Cited on page 161)

List of publications

Publications that are included in this thesis in a modified version are marked with asterisks (**).

[P1] J. Caron, J. Ungermann, M. Riese and R. Dunin-Borkowski, "Model-based reconstruction of magnetisation from electron-optical phase images: I. A fast and accurate forward model," *Submitted to Ultramicroscopy*, 2016.**

[P2] D. Song, Z.-A. Li, J. Caron, A. Kovács, H. Tian, C. Jin, H. Du, M. Tian, J. Li, J. Zhu, and R. E. Dunin-Borkowski, "Quantification of magnetic surface and edge states in an FeGe nanostripe by off-axis electron holography," *Physical Review Letters*, vol. 120, no. 16, p. 167204 , 2018.

[P3] F. Zheng, F. N. Rybakov, A. B. Borisov, D. Song, S. Wang, Z.-A. Li, H. Du, N. S. Kiselev, J. Caron, A. Kovács, M. Tian, Y. Zhang, S. Blügel and R. E. Dunin-Borkowski, "Experimental observation of chiral magnetic bobbers in B20-type FeGe," *Nature Nanotechnology*, vol.13, pp. 451-455, 2018.

[P4] Z.-A. Li, F. Zheng, A. H. Tavabi, J. Caron, C. Jin, H. Du, A. Kovács, M. Tian, M. Farle and R. E. Dunin-Borkowski, "Magnetic skyrmion formation at lattice defects and grain boundaries studied by quantitative off-axis electron holography," *Nano Letters*, vol. 17, no. 3, pp. 1395–1401, 2017.

[P5] A. Kovács, J. Caron, A. Savchenko, N. S. Kiselev, K. Shibata, Z.-A. Li, N. Kanazawa, Y. Tokura, S. Blügel and R. E. Dunin-Borkowski, "Mapping the magnetization fine structure of a lattice of Bloch-type skyrmions in an FeGe thin film," *Applied Physics Letters*, vol 19, no. 19, p. 192410, 2017.

[P6] C. Jin, Z.-A. Li, A. Kovács, J. Caron, F. Zheng, F. N. Rybakov, N. S. Kiselev, H. Du, S. Blügel, M. Tian, Y. Zhang, M. Farle, and R. E. Dunin-Borkowski, "Control of morphology and formation of highly geometrically confined magnetic skyrmions," *Nature Communications*, vol. 8, p. 15569, 2017.

[P7]   F. de la Peña, T. Ostasevicius, V. T. Fauske, P. Burdet, P. Jokubauskas, M. Nord, M. Sarahan, D. N. Johnstone, E. Prestat, J. Taillon, J. Caron, T. Furnival, K. E. MacArthur, A. Eljarrat, S. Mazzucco, V. Migunov, T. Aarholt, M. Walls, F. Winkler, B. Martineau, G. Donval, E. R. Hoglund, L. F. Zagonel, A. Garmannslund, C. Gohlke and H.-W. Chang, "HyperSpy/HyperSpy V1.2 [Dataset]," 2017.

[P8]   J. Caron, J. Ungermann, P. Diehle, A. Kovács, M. Riese and R. E. Dunin-Borkowski, "Iterative model-based tomographic reconstruction of 3D magnetisation distributions using electron holography on the nanoscale," *Poster presented at the PICO 2017: Frontiers of Aberration Corrected Electron Microscopy Conference*, Kasteel Vaalsbroek, the Netherlands, 30. April – 4. May 2017.

[P9]   J. Caron, J. Ungermann, Z.-A. Li, P. Diehle, A. Kovács, M. Riese and R. E. Dunin-Borkowski, "Towards electron holography of 3D magnetization distributions in nanoscale materials using a model-based iterative reconstruction technique," *Poster presented at the PICO 2015: Frontiers of Aberration Corrected Electron Microscopy Conference*, Kasteel Vaalsbroek, the Netherlands, 19. April – 23. April 2015.

[P10]   J. Caron, J. Ungermann, Z.-A. Li, M. Riese and R. E. Dunin-Borkowski, "Towards the reconstruction of 3D magnetic distributions on the nanoscale via model-based iterative techniques," *Talk at the 18th International Microscopy Congress*, Prague, Czech Republic, 9. September 2014.

[P11]   P. Diehle, J. Caron and R. E. Dunin-Borkowski, "Towards model-based reconstruction of 3D magnetic distributions," *Talk at the Holo Workshop Dresden*, 11. Juni 2014.

Acknowledgements

I'd like to express my sincerest gratitude to all members of the PGI-5 / Ernst Ruska-Centre. I thoroughly enjoyed the discussions, the working atmosphere and the time I spent at this institute. In particular, I want to thank:

- Prof. Dr. Rafal Dunin-Borkowski for giving me the opportunity to work on this interesting topic, his suggestions and his support.

- Prof. Dr. Joachim Mayer for kindly accepting the role as co-assessor of this thesis.

- Dr. Jörn Ungermann for his supervision, his advice concerning Python, his open door and many discussions which represent a substantial contribution to this thesis.

- Patrick Diehle, with whom I worked closely together during this thesis and who made sure that I'd keep the experimental point of view in mind.

- Dr. András Kovács, Dr. Zi-An Li, Dr. Ahmir Tavabi and Dr. Nikolai Kiselev for providing me with interesting data sets and practical advice.

- Dr. Vadim Migunov and Florian Winkler for the interesting discussions about Python and HyperSpy.

- Prof. Dr. Giulio Pozzi and Dr. Marco Beleggia for valuable discussions about my work.

- Gabriele Waßenhoven, Ingrid Rische-Radloff, Werner Pieper and Dr. Karsten Tillmann for all of their administrative work.

- Dr. Andreas Thust, Dr. Juri Barthel and Dr. Markus Lentzen for theoretical discussions and showing me that there's always something new to learn about the Fourier space.

- Teresa Weßels for her proofreading skills and Michael Schnedler for his last minute help.

- Dr. Hongchu Du, Dr. Xiankui Wei and Dr. Paul Paciok for the pleasant office climate.

- My family and my girlfriend for their support and encouragement throughout my study.

Schriften des Forschungszentrums Jülich
Reihe Schlüsseltechnologien / Key Technologies

Schriften des Forschungszentrums Jülich
Reihe Schlüsseltechnologien / Key Technologies

Weitere *Schriften des Verlags im Forschungszentrum Jülich* unter
http://wwwzb1.fz-juelich.de/verlagextern1/index.asp

Mitglied der Helmholtz-Gemeinschaft

JÜLICH
Forschungszentrum